Faculty of Science
Department of Physics

Precipitation behavior and heat resistance properties of Al-Cu-Mg-Ag-(Si) Alloys

PhD thesis submitted for the degree of Physics at the University of Antwerp to be defended by Qiang Lu

Supervisor(s):
University of Antwerp
Prof. Dominique Schryvers

Central South University
Prof. Liya Li
Prof. Kai Li

Antwerp, 2024

Defence jury

Chairman:

Prof. Dr. Min Song, Central South University – China

Members:

Prof. Dr. Zhenggang Wu, Hunan University - China

Prof. Dr. Jie Pan, Huazhong University of Science and Technology- China

Prof. Dr. Hailin Yang, Central South University - China

Prof. Dr. Jianguo Tang, Central South University – China

Secretary:

Prof. Dr. Jiong Wang, Central South University – China

Promoters:

Prof. Dr. Dominique Schryvers, University of Antwerp, Antwerp - Belgium

Prof. Dr. Liya Li, Central South University - China

Prof. Dr. Kai Li, Central South University - China

Contact information:

Qiang Lu, PhD candidate,
State Key Laboratory of Powder Metallurgy,
Central South University,
Changsha Hunan, 410083, China
Phone: +86 13187056409
e-mail: luqiangsdly@163.com

Precipitation behavior and heat resistance properties of Al-Cu-Mg-Ag-(Si) Alloys

Abstract: With the rapid increase in the speed of new-generation aerospace vehicles, conventional heat-resistant aluminum alloys cannot meet the long-term service of the equipment. Therefore, the development of new high-strength heat-resistant aluminum alloys is of great strategic for the sustainable and high-quality development of industries. Al-Cu-Mg-Ag alloy is an age-hardenable heat-resistant aluminum alloy and has high strength and heat resistance. The addition of alloying elements such as Si and Sc to Al-Cu-Mg-Ag alloy introduces a competitive relationship among the σ-$Al_5Cu_6Mg_2$, θ′-Al_2Cu, and Ω phases. Therefore, a systematic investigation of precipitation behavior and heat resistance of Al-Cu-Mg-Ag-(Si) is essential for guiding the design of high-strength heat-resistant aluminum alloys. Combined characterization testing methods such as scanning electron microscopy, transmission electron microscopy, atom probe tomography, microhardness testing, and tensile testing with simulation calculation methods such as calculation of phase diagram, first-principles calculations, and Ab initio molecular dynamics, the effects of heat treatment processes and element content on the precipitation behavior, mechanical properties, and heat resistance of Al-Cu-Mg-Ag-(Si) alloys were systematically investigated. Furthermore, a multiple interface segregation structure was constructed at the θ′/Al interface, and a new Al-Cu-Mg-Ag-Si-Sc alloy with synergistically improved strength and heat resistance

was developed. The main conclusions are as follows:

(1) Based on the Kampmann-Wagner-Numerical theory, the relationship between the coarsening rate of the Ω phase and the aging process was analyzed, revealing for the first time that the critical size of Ω phase ($r^*_{thermal}$) under thermal exposure temperature was the key factor determining the coarsening rate of Ω phase during long time thermal exposure heat treatment. After artificial ageing, when the size of Ω phase was smaller than the critical size $r^*_{thermal}$, the dissolution of smaller Ω phase leaded to a rapid decrease in the number density of Ω phases, thereby reducing the heat resistance of the alloy. When the size of Ω phase was greater than or equal to the critical size $r^*_{thermal}$, the coarsening rate of Ω phase was consistent, but a larger initial size would result in a larger final size after long-term thermal exposure. Therefore, the closer the size of Ω phase in the alloy is to the critical size under heat exposure temperature, the better the heat resistance of the alloy.

(2) A concept of constructing a multiple interface segregation structure at the precipitate/matrix interface was proposed, and based on this concept, a multiple interface segregation structure containing the C/L-AlMgSiCu interfacial phase, newly discovered χ-AgMg interfacial phase, and Sc segregation layer was successfully constructed at the θ′/Al interface. The existence of the multiple interface segregation structure ensured that the designed Al-Cu-Mg-Ag-Si-Sc alloy maintains a yield strength of 400 MPa after thermal exposure at 200 °C for 100 h, with a strength retention rate of 97%, creating a new record for the synergistic improvement of strength and heat resistance in aluminum alloys. In addition, combining transmission electron microscopy ex-situ/in-situ characterization

with first-principles calculations, it is shown that the χ-AgMg interface phase will be destroyed due to the diffusion of the outer Ag layer during thermal exposure, and gradually dissolve into the matrix, but it can still delay the coarsening behavior of θ′-Al_2Cu phase.

(3) The criteria for determining whether Ω phase can precipitate are updated in Al-Cu-Mg-Ag-Si alloys with low Mg/Si ratio based on phase diagram thermodynamic calculations and multi-scale structural characterization. When W(Mg)/W(Si) > 1.4 and X(Ag)/X(Mg_{excess}) > 1, Ω phase can precipitate in Al-Cu-Mg-Ag-Si alloys, where X(Mg_{excess}) represents the atomic percentage of residual Mg elements after the formation of the AlMgSiCu quaternary precipitate phase C/L phase in the supersaturated solid solution, and the W(Mg) is the mass fraction of Mg in the supersaturated solid solution before artificial ageing.

(4) The effects of alloy element content on precipitation behavior and heat resistance of Al-Cu-Mg-Ag-Si alloys were systematically analyzed. Critical conditions for the precipitation of σ-$Al_5Cu_6Mg_2$ and Ω phase in Al-Cu-Mg-Ag-Si alloys are revealed. Based on calculation of phase diagram results, the conditions for precipitating σ-$Al_5Cu_6Mg_2$ phase in the alloy are: ① W(Mg)/W(Si) > 1.8; ② W(Cu) > 2.7W(Mg) - 5W(Si). When W(Mg)/W(Si) < 1.8, the alloy is mainly precipitated with C/L/Q′-AlMgSiCu. When W(Cu) < 2.7W(Mg) - 5W(Si), the alloy will generate GPB zone. In addition, W(Ag)/W(Si) > 4 is the critical condition which the Ω phase can the main precipitates in Al-Cu-Mg-Ag-Si alloys. Furthermore, the correlation between precipitate types and heat resistance was summarized, showing that Al-Cu-Mg-Ag-(Si) alloys with Ω phase as the main strengthening phase are more suitable for the preparation

of structures with short service time but high temperature, while Al-Cu-Mg-Ag-(Si) alloys with low Mg content and multiple segregation structures are more suitable for structures requiring long-term service at medium to high temperatures.

This study, for the first time, combines calculation of phase diagram with multi-scale microstructure characterization, systematically unraveling the effects of element content on precipitation behavior, strength, and heat resistance of Al-Cu-Mg-Ag-(Si) alloys. In addition, a concept of constructing a multiple interface segregation structure at the precipitate/matrix interface was proposed to synergistically improve alloy strength and heat resistance. This work provides theoretical guidance for optimizing the composition and processing of Al-Cu-Mg-Ag-(Si) alloy and regulating the microstructure. Furthermore, it also offers new ideas and theoretical guidance for the development of novel high-strength heat-resistant alloys in other systems.

Keywords: Al-Cu-Mg-Ag-Si; heat resistance; segregation structure; χ-AgMg interface phase

Table of contents

Chapter 1. Introduction

1.1 Foreword

Aluminum alloys have high specific strength, excellent conductivity, thermal conductivity, and corrosion resistance, as well as outstanding formability. They have been widely used as lightweight materials in the transportation industry, including high-speed trains, and automobiles, improving their carrying capacity, and speed[1]. According to whether they be strengthened by ageing heat treatment, aluminum alloys can be divided into non- age-hardenable aluminum alloys and age-hardenable aluminum alloys. The strengthening phase in non- age-hardenable aluminum alloys mainly consists of micron to submicron scale second phases added during casting or formed in situ during solidification, such as the AlFeSi eutectic phase and TiB_2 particles shown in Fig. 1-1. As for the age-hardenable aluminum alloys, the main strengthening phase is rod-like, plate-like, and other nanoscale precipitate formed during heat treatment. High-density nanoscale precipitates can effectively hinder the motion of dislocations, significantly improving the room temperature mechanical properties of aluminum alloys. Therefore, age-hardenable aluminum alloys have been widely used in weight-sensitive industries such as aerospace and automotive transportation due to their excellent comprehensive mechanical properties and broad tunability of performance.

To better meet the demand for high-performance aluminum alloys in high-end sectors fields such as aerospace, the aluminum alloys must develop in the direction of high specific strength, heat resistance, and corrosion resistance. As for the heat-resistant aluminum alloys, the rapid increase in the speed of next-generation aerospace has led to the service

temperatures of aircraft skin and structural components near the engine exceeding 150 °C. However, heat-resistant aluminum alloys that are currently in common use such as 2618 and 2D70 have long-term application temperatures below 150 °C[2]. Therefore, the development of new high-strength heat-resistant aluminum alloys is of great significance for the sustainable and high-quality development of industries such as aerospace.

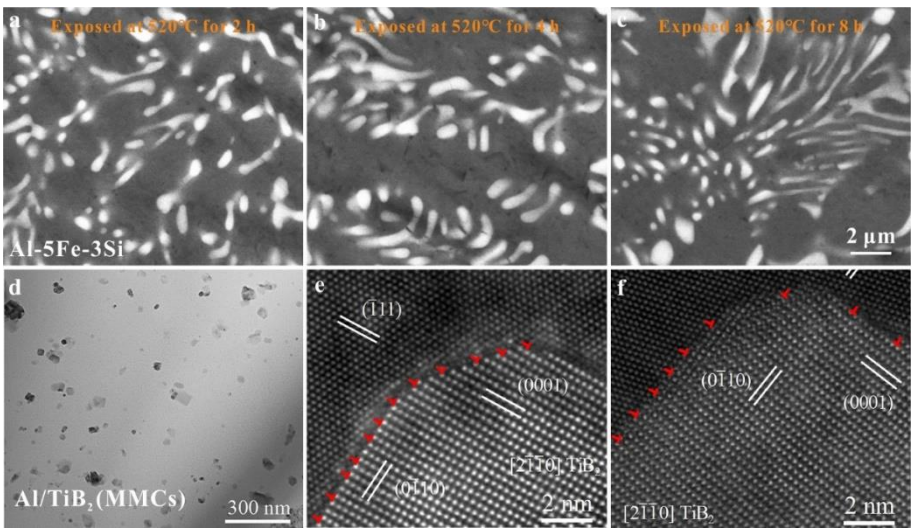

Figure 1-1 (a-c) The size change of second phase in Al-Fe-Si cast alloy after thermally exposed at 520 ℃ for different time[3]. (d) Low magnification image of Al/TiB_2 metal matrix composite[4]. (e-f) The images of misfit dislocations at the Al/TiB_2 interface in the Al/TiB_2 metal matrix composite [4]

1.2 Design strategy for heat-resistant aluminum alloys

Ceramic particles, eutectic phases, and nanoscale precipitates with high thermal stability are widely used as strengthening phases in the heat resistance aluminum alloys. Fig. 1-1 illustrates the structures of eutectic

phases in Al-Fe-based alloys and TiB_2 ceramic particles in aluminum-based composites. Fig. 1-1a-c demonstrated that the Al-Fe-based eutectic phase exhibited high thermal stability, with no significant change in phase size after thermal exposure at 520 °C for 8 hours. However, the relatively large size of ceramic particles and eutectic phases leads to the low strength of the aluminum alloys, resulting in limitations in strength improvement. Therefore, to achieve a synergistic improvement in the strength and heat resistance of aluminum alloys, the premise is to ensure that they have sufficiently high room temperature strength.

Age-hardenable aluminum alloys can effectively achieve the goal of lightweight and high strength at room temperature due to the high-density nano-scale precipitates. However, the strength of age-hardenable aluminum alloys decreases significantly when they are exposed to temperatures in the medium to high range[5]. This is mainly because nano-scale precipitates tend to coarsen rapidly at high temperatures, resulting in a significant decrease in the number density and volume fraction of precipitate, thus unable to effectively hinder the movement of dislocation, thereby shortening the service life of age-hardenable aluminum alloys. Therefore, improving the thermal stability of nano-scale precipitates under high-temperature is crucial for achieving a synergistic enhancement of strength and heat resistance in aluminum alloys.

Segregation structure at the precipitate/matrix interface can stabilize the precipitate interface during high-temperature service of age-hardenable aluminum alloys, thereby enhancing the thermal stability of the precipitates. Researchers have attempted to construct different segregation structures at θ′/Al interfaces to improve the stability of θ′-Al_2Cu phases by adding different microalloying elements. Fig. 1-2 shows the atom probe tomography (APT) characterization results of Mn/Zr elements segregated

at the θ′/Al interface. APT results indicated that during long time thermal exposure, Mn and Zr elements segregated at the θ′/Al interface, thereby inhibiting the coarsening of θ′-Al_2Cu and significantly improving the alloy's heat resistance[6].

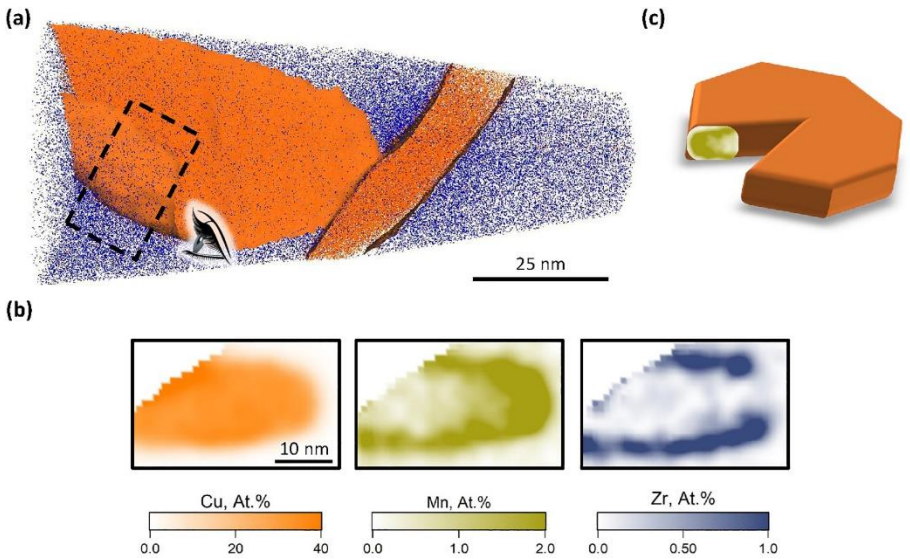

Figure 1-2 The APT results of Al-Cu-Mn-Zr alloy after thermal exposure at 300 ℃ for 5000 h[6]. (a) Low magnification APT result. (b) Concentration distribution maps for Cu, Mn, and Zr. (c) Schematic distribution map for Mn in the θ′-Al_2Cu

In addition, when Mg/Ag elements are simultaneously added to Al-Cu-based alloys, the main strengthening precipitates will transform from θ′-Al_2Cu to Ω phase with a AgMg segregation layer at the Ω/Al interface[7, 8]. The regular AgMg segregation layer at the Ω/Al interface can effectively suppress the coarsening of Ω phase during thermal exposure, thereby improving the thermal stability of Ω phase. However, when the service temperature of the Al-Cu-Mg-Ag alloys exceeds 200 °C, the presence of ledge at the Ω/Al interface accelerates its coarsening rate, leading to a rapid

decrease in the strength of the alloys[9]. Therefore, further research is needed to investigate whether the heat resistance of Al-Cu-Mg-Ag alloys can be further enhanced through the control of heat treatment processes and the addition of microalloying elements.

1.3 Strengthen mechanisms of Al-Cu-Mg-Ag alloy

The main strengthening mechanisms of aluminum alloys include solid solution strengthening, grain boundary strengthening, deformation strengthening, dispersion strengthening, and precipitation strengthening. Solid solution strengthening[10] is carried out by adding solid solution elements that lead to lattice distortion in the matrix, hindering dislocation motion and increasing the strength of the alloy. Grain boundary strengthening, also known as fine grain strengthening, involves refining the aluminum alloy grains through processes such as rolling, extrusion, or by adding alloying elements. According to the Hall-Petch relationship[11], when grain size is in the micro and sub-micro scale, smaller grain size and higher grain boundary density result in stronger hindrance to dislocation movement. However, when the grain size reaches the nano scale, further reduction in grain size may lead to alloy softening[12]. Deformation strengthening is achieved by deformation, introducing dislocations into the alloy and increasing the density of grain boundaries, thereby enhancing the alloy's strength[13]. Precipitation strengthening[14], similar to dispersion strengthening, involves dispersing strengthening phases throughout the matrix to impede dislocation movement. The solute elements such as Cu and Mg will dissolve into the Al matrix during high-temperature solution heat treatment, while they gradually precipitate as nano scale strengthening phases with regular crystal structures during the low-temperature artificial aging treatment, and using these uniformly

distributed nano scale precipitates as the main strengthening phase is the precipitation strengthening mechanism. As for dispersion strengthening, the strengthening phases mainly consist of micron and submicron scale dispersods formed during casting and homogenization processes. However, due to the large size of dispersods, their contribution to improving the strength of the alloy is not significant[15, 16].

Al-Cu-Mg-Ag alloy, as an age-hardenable aluminum alloy, undergoes solution heat treatment followed by aging heat treatment, during which solute elements are fully precipitated from the supersaturated solid solution, resulting in a reduced content of supersaturated solute elements in the matrix and thus less solid solution strengthening effects. That is, the main strengthening mechanism of Al-Cu-Mg-Ag alloy is precipitation strengthening, where the size, number density, and volume fraction of precipitates after artificial aging significantly influence the strength and heat resistance of Al-Cu-Mg-Ag alloys. In addition, there are multiple solute elements in Al-Cu-Mg-Ag-(Si) alloys, different precipitates may compete after artificial aging, resulting in complex alloy precipitation behavior. Moreover, different precipitates may have different effect on the strength and heat resistance of the alloys. Therefore, an in-depth analysis of the effects of heat treatment processes and the addition of elements on alloy precipitation behavior is important for process adjustments and composition optimization in industrial production.

1.4 Precipitation behavior of Al-Cu-Mg-Ag alloy

Age-hardenable Al-Cu-Mg alloys are widely used in transportation and other fields due to their excellent specific strength, good toughness, fatigue strength, and heat resistance[17]. Studies have shown[18-21] that the precipitation sequence in Al-Cu-Mg alloys is correlated with the content

and ratio of Cu/Mg elements, but the main precipitation sequence includes: supersaturated solid solution → GP zone/θ″/GPB zone/S″ → θ′-Al_2Cu/S′-Al_2CuMg → θ-Al_2Cu/S-Al_2CuMg. The high-angle annular dark-field scanning transmission electron microscope (HAADF-STEM) images shown in Fig. 1-3a and c displays the atomic resolution structure of GP zones and GPB zones along the $[001]_{Al}$ zone axis, which are the precursors to θ′-Al_2Cu and S-Al_2CuMg, respectively. θ′-Al_2Cu and S-Al_2CuMg phases are the main strengthening precipitates in the Al-Cu-Mg alloys, and they exhibit good thermal stability and strengthening effects when the service temperatures are below 150 °C and 200 °C. However, when the operating temperature exceeds 150 °C and 200 °C, θ′-Al_2Cu and S-Al_2CuMg phases rapidly coarsen, leading to a rapid decrease in the mechanical properties of Al-Cu-Mg alloys[22, 23].

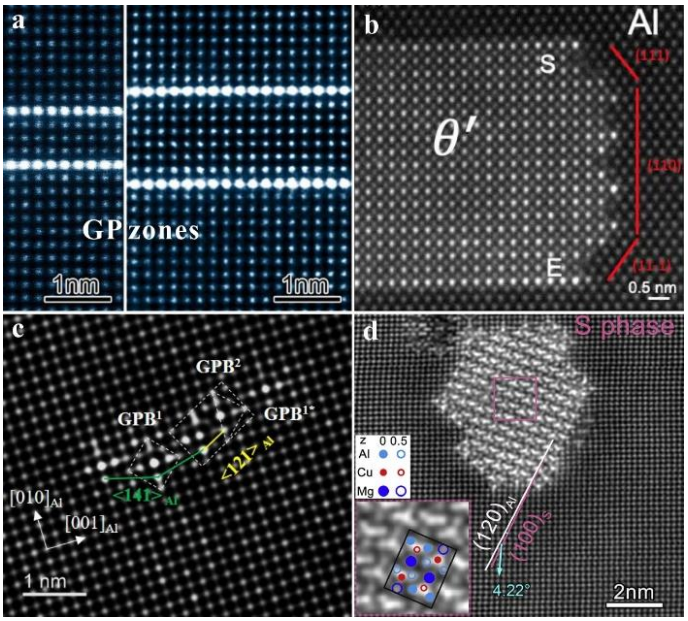

Figure 1-3 Atomic resolution HAADF-STEM images of (a) GP zones[24], (b) θ′-Al_2Cu[25], (c) GPB zones[26] and (d) S-Al_2CuMg[27] phases in Al-Cu-Mg alloys

To further improve the heat resistance of Al-Cu-Mg alloys, researchers attempted to promote the formation of Ω phases with regular AgMg segregation layers by adding small amounts of Ag to Al-Cu-Mg alloys with high Cu/Mg ratios[28-33]. As shown in Fig. 1-4, the APT results showed that the Mg-Ag co clusters formed during early-stage aging were the precursors to the Ω phase[34-38], which could gradually transform into Ω phases with prolonged aging time[39-41]. According to the atomic resolution HAADF-STEM images and energy-dispersive X-ray spectroscopy (EDX) of the Ω phase shown in Fig. 1-5, the habit plane of the Ω phase is the $\{111\}_{Al}$ plane, which is a slip plane of the aluminum matrix. Therefore, the presence of Ω phases on this plane effectively impedes dislocation movement, thereby enhancing the strength of Al-Cu-Mg-Ag alloys[42-45].

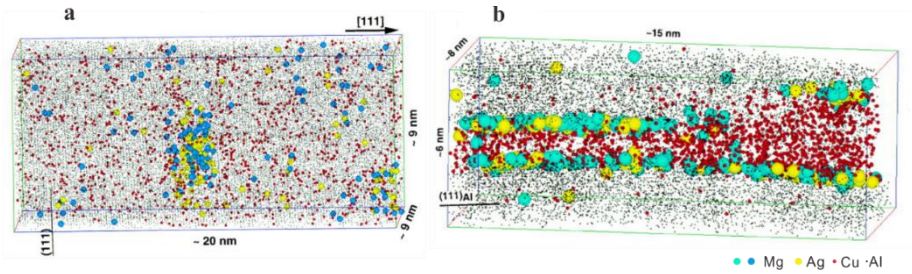

Figure 1-4 The APT results of Al-Cu-Mg-Ag alloy aged at 180 ℃ for (a) 15 s and (b) 36000 s [35]. The blue and green atoms represent Mg element, while the yellow atoms represent Ag element

The structure of the Ω phase had been extensively analyzed using techniques such as X-Ray Diffraction (XRD) and High-Resolution Transmission Electron Microscopy (HRTEM)[46]. Auld[47] constructed the structure of the Ω phase as monoclinic (a = b = 0.496 nm, c = 0.848 nm, γ = 120°) by XRD. In addition, the research of Auld[47] indicated that after prolonged aging at 200 ℃, the Ω phase would be replaced by the

equilibrium phase θ-Al_2Cu, suggesting that the Ω phase serves as a precursor to the equilibrium phase θ-Al_2Cu. Therefore, the precipitation sequence in Al-Cu-Mg-Ag alloys is: supersaturated solid solution → AgMg atomic clusters → Ω phase → θ-Al_2Cu. Knowles et al.[48] checked the monoclinic structure constructed by Auld using HRTEM and showed that the monoclinic structure should actually be orthorhombic (space group Fmmm, a = 0.496 nm, b = 0.859 nm, c = 0.848 nm). The optimized orthorhombic structure is the currently widely accepted Ω phase structure[49, 50], and the orientation relationship of it with the aluminum matrix is confirmed to the $[010]_{\Omega}$ // $[101]_{Al}$ and $(001)_{\Omega}$ // $(111)_{Al}$.

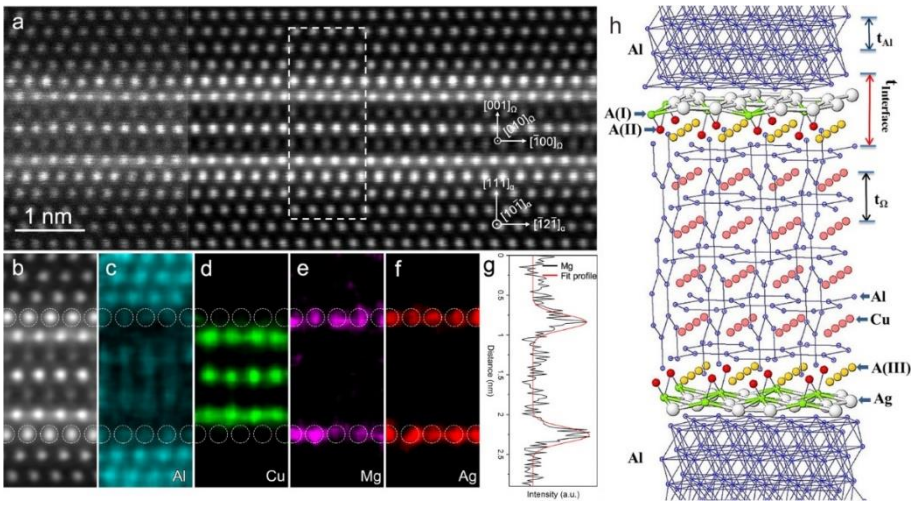

Figure 1-5 (a) Original and filtered HAADF-STEM images of the Ω phase[51]. (b) Region selected for energy-dispersive X-ray spectroscopy (EDX) spectrum acquisition[51]. (c-f) EDX mapping results for Al, Cu, Mg, and Ag[51]. (g) Line distribution of Mg element in the EDX acquisition region[51]. (h) 3D atomic structure of the Ω phase[52]

However, Garg et al. [53] reported that the symmetry of the Ω phase was tetragonal based on Convergent Beam Electron Diffraction (CBED),

which differed from the structure proposed by Knowles et al.[48], but they did not deeply investigate the reasons behind this discrepancy. Recently, Yang et al.[54] reported that the orthorhombic structure proposed by Knowles et al.[48] is a variant of the tetragonal structure of θ-Al_2Cu (space group I4/mcm, a = 0.607 nm, c = 0.487 nm) based on the results of Density Functional Theory (DFT) calculations. When the tetragonal θ-Al_2Cu structure is embedded as a thin plate in the aluminum matrix, the elastic strain exerted by the surrounding aluminum matrix causes it to transition from tetragonal symmetry to orthorhombic symmetry, resulting in an orthorhombic structure.

AgMg co-clusters formed at the early stages of aging will gradually segregate at the Ω/Al coherent interface, forming a regular structure known as the AgMg segregation layer[55]. Fig. 1-5 shows an HAADF-STEM image of the AgMg segregation structure along with the corresponding EDX spectrum, where the positions of Ag and Mg elements overlap at the interface, with Mg elements located closer to the inner θ-Al_2Cu core. Combining DFT calculations with HAADF-STEM image, Kang et al.[52, 56] constructed a complete Ω phase model as shown in Fig. 1-5h. In this model, the AgMg segregation layer between the θ-Al_2Cu core and the aluminum matrix is a bilayer structure, with the outermost layer adjacent to the aluminum matrix composed of hexagonal-packed Ag atoms, while the inner layer adjacent to the θ-Al_2Cu core is composed of Cu and Mg atoms. DFT results further confirmed that the AgMg bilayer segregation structure could stabilize the interface structure and promote the precipitation of the Ω phase on the $\{111\}_{Al}$ plane. In addition, the AgMg segregation layer effectively inhibits the coarsening of the Ω phase, enhancing its thermal stability and thereby improving the heat resistance of Al-Cu-Mg-Ag alloys.

1.5 Effect of heat treatment processes on the mechanical properties of Al-Cu-Mg-Ag Alloy

Al-Cu-Mg-(Ag) alloy is an age-hardenable aluminum alloy[57], and the number density and volume fraction of precipitates after artificial aging heat treatment significantly affect the comprehensive mechanical properties of the alloy. Common heat treatment processes for age-hardenable aluminum alloys include homogenization, solution heat treatment, and artificial aging heat treatment[58-62]. Solid solution heat treatment is achieved by raising the temperature to dissolve the unstable micro-scale second phases formed during the casting into the matrix. Subsequent rapid quenching process preserves the solute atoms in the aluminum matrix, creating a supersaturated solid solution to facilitate subsequent precipitation[63]. To ensure sufficient dissolution of micro and sub-micron second phases, the temperature of solution heat treatment generally needs to be higher than the solubility curve of the second phase but lower than the eutectic temperature of the alloy. Therefore, the solution heat treatment temperature for 2XXX aluminum alloys is typically between 500 to 550 ℃. After quenching, the alloys are subjected to artificial aging at 160~200 ℃ to obtain high-density precipitates, ensuring rapid improvement in the mechanical properties of the alloy.

The flow of the heat treatment process significantly affects the precipitation driving force, thereby influencing the number density of precipitates in the alloy[64-69]. Zhao et al.[70] introduced pre-annealing between cold rolling and solution heat treatment, refining the size of Ω phase and then significantly increasing the number density of Ω phase under peak aging state, thus improving the room temperature mechanical properties of the alloy. Sadeghi et al.[71] introduced pre-rolling before artificial aging of Al-Cu-Mg alloy, increasing the heterogeneous

nucleation sites for the precipitates in the alloy, and significantly improving the yield strength of the alloy. In addition, the heating curves during artificial aging also affect the precipitation behavior of Al-Cu-Mg-Ag alloy. Tang et al.[72] studied the effect of non-isothermal heat treatment and isothermal heat treatment on the mechanical properties of Al-Cu-Mg-Ag alloy. The research showed that non-isothermal heat treatment could promote nucleation of Ω phase, thereby improving the number density of Ω phase and enhancing the strength of the alloy. However, non-isothermal heat treatment would result in widening of precipitate free zones (PFZ) at grain boundaries, reducing the elongation of the alloy. Wang et al.[73] also demonstrated that compared to isothermal heat treatment at 160 ℃, heating from 100 ℃ to 250 ℃ at a rate of 40 ℃/h can significantly refine the size of Ω phase and improve the mechanical properties of the alloy. However, the size of Ω phase will increase when the heating rate is 60 ℃/h, thereby decreasing the strength of the Al-Cu-Mg-Ag alloy.

When the heat treatment process is consistent, the temperature of aging heat treatment also affects the strength and heat resistance of Al-Cu-Mg(-Ag) alloy[74]. Alexopoulos et al.[75] studied the effect of aging temperatures on the yield strength of Al-Cu-Mg alloy, and the result showed that the yield strength of the alloy decreased by 6 MPa as the artificial aging temperature increased by 10 ℃ within the range of 170 ℃ and 210 ℃, indicating that excessively high heat treatment temperatures lead to coarsening of precipitates and reduced yield strength of the alloy. Moreover, Teleshov et al.[76] also demonstrated that increasing the aging temperature results in coarsening of Ω phase in Al-Cu-Mg-Ag alloys, decreasing the number density of c and, thus, reducing the mechanical properties of the alloy at room temperature. Therefore, it is necessary to select the appropriate artificial aging temperature to obtain the optimum

mechanical properties of the alloy.

When the heat treatment process and temperature are consistent, the extent of heat treatment, namely under-aging, peak-aging, and over-aging, also affects the properties of Al-Cu-Mg-Ag alloy. Liu et al.[57] demonstrated that the corrosion resistance of Al-Cu-Mg-Ag alloy gradually decreases with increasing aging time, primarily due to widening of PFZ at grain boundaries caused by prolonged heat treatment, leading to a significant decrease in corrosion resistance. The extent of heat treatment not only affects the corrosion resistance but also influences the heat resistance of the alloy. Lumley et al.[42, 77] studied the effect of under-aging and peak aging states on the creep properties of Al-Cu-Mg-(Ag) alloy aged at 185 ℃. When Al-Cu-Mg-Ag alloy was subjected to creep testing at 130 ℃ and 150 ℃, under aged alloy exhibited a lower creep rate compared to the peak aged alloy. In addition, the creep performance of under-aged 2024 aluminum alloy was also higher than that of the peak-aged state. Furthermore, Liu et al.[78] investigated the effect of aging state on the creep properties and long-term high-temperature service performance of Al-Cu-Mg-Ag alloy. As shown in Fig. 1-6, the yield strength of the peak-aged alloy decreased with increasing exposure time, while that of the under-aged alloy initially increased and then decreased. That is, the final yield strength of the under-aged alloy is significantly higher than that of the peak-aged alloy after thermal exposure for 100 h. This phenomenon is mainly attributed to the presence of many supersaturated solute atoms in the under-aged alloy, which can promote nucleation and growth of Ω phase, increasing the number density and volume fraction of Ω phase in the alloy. Then, when the supersaturated solute atoms in the alloy are depleted, the Ω phase enters the coarsening stage, causing the dissolution of smaller Ω phase and the growth of larger Ω phase, thereby reducing the number

density of Ω phase. However, current studies on the effect of extent of heat treatment have used single Al-Cu-Mg-Ag alloys and have not investigated whether it can be applied to Al-Cu-Mg-Ag alloys with different solute element contents. Furthermore, whether the over-aging state similarly affect the heat resistance of the alloy as the under-aging state requires further research.

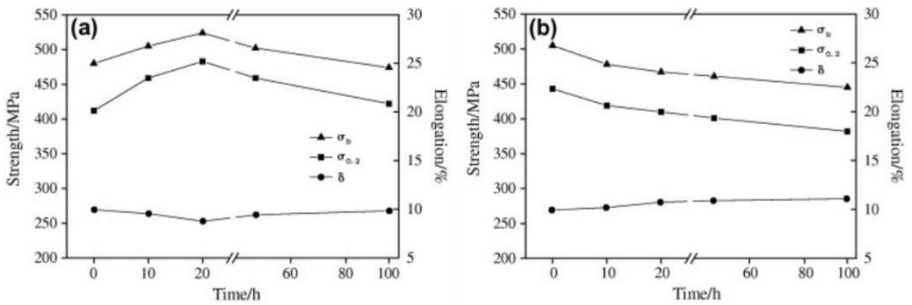

Figure 1-6 Tensile properties of (a) under aged and (b) peak aged Al–Cu–Mg–Ag alloy thermally exposed at 150 °C for different time[78]

1.6 Effect of microalloying element on the microstructure and mechanical properties of Al-Cu-Mg-Ag Alloy

1.6.1 Effect of Mg and Ag

Adding a small amount of Ag element in Al-Cu-Mg alloys with high Cu/Mg ratio can promote the precipitation of Ω phase with AgMg segregation layer, thereby increasing the strength and heat resistance of the alloy[79]. Yang et al.[54] demonstrated that the AgMg segregation layer could reduce the interfacial energy between the Ω phase, and the aluminum matrix based on the DFT results, thereby promoting the precipitation of the Ω phase. Therefore, the content of Ag and Mg elements will affect the number density and volume fraction of Ω phase, thus influencing the

alloy's performance. Bai et al.[80] investigated the effect of Ag contents on the strength and heat resistance of Al-Cu-Mg-Ag alloys. As shown in Fig. 1-7, the rate of decrease in strength during thermal exposure was significantly reduced in Al-Cu-Mg-Ag alloys with high Ag content. Therefore, increasing the Ag content can not only improve the room temperature mechanical properties of the alloy but also enhance its heat resistance during long-term thermal exposure. The studies by Bai et al.[81] show that increasing the Ag content can effectively improve the high-temperature mechanical properties and high-temperature creep resistance of the alloy. When the content of Ag is increased to 1 wt.%, the tensile strength of the alloy at 300 ℃ can exceed 200 MPa.

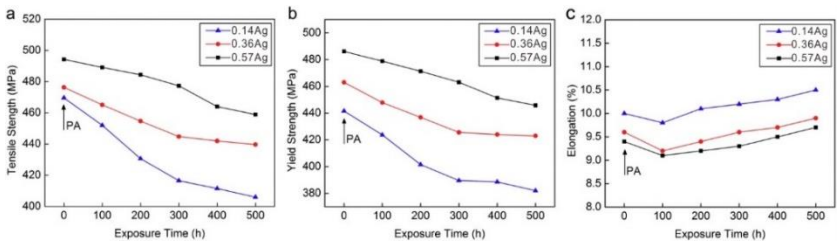

Figure 1-7 (a) tensile strength, (b) yield strength and (c) elongation of the peak-aged alloys with different Ag content after exposure at 150 °C for various times[31]

Furthermore, Bai et al.[82] used APT to analyze the reasons for increasing the strength of the alloy by increasing the Ag content. APT results show that increasing the Ag content can increase the AgMg clusters while inhibiting the formation of GP zones and CuMg atomic clusters in the alloy after artificial aging at 180 ℃ for 10 min. AgMg clusters serve as precursors for the Ω phase, while GP zones and CuMg atomic clusters serve as precursors for θ′-Al_2Cu and S-Al_2CuMg, respectively. Therefore, increasing the Ag content can promote the generation of the Ω phase while suppressing the formation of θ′-Al_2Cu and S-Al_2CuMg which will

consume Cu, thereby increasing the number density and volume fraction of the Ω phase and thus improving the mechanical properties of Al-Cu-Mg-Ag alloys.

Mg content also significantly influences the comprehensive properties of Al-Cu-Mg-Ag alloys[83]. As shown in Fig. 1-8, Bai et al.[38, 84] demonstrated that appropriately increasing the Mg content could significantly improve the mechanical properties of the alloy. However, when Mg content was excess, the mechanical properties decreased again, although they remained higher than those of low-Mg content alloys. APT and transmission electron microscopy (TEM) results showed that GP zones were the main cluster type in the under-aged low-Mg alloys, leading to the subsequent generation of θ′-Al_2Cu during aging. In contrast, the formation of GP zones is significantly suppressed, and AgMg atomic clusters become the main cluster type in high-Mg alloys. In addition, TEM bright-field images also confirmed that the number density of θ′-Al_2Cu in low-Mg alloys is significantly higher than in high-Mg alloys. Therefore, increasing the Mg content can promote the formation of AgMg atomic clusters in the early stages of aging, increase the number of nucleation sites for the Ω phase, thereby promoting the generation of the Ω phase during subsequent aging, increasing the number density and volume fraction of the Ω phase, and improving the mechanical properties of the alloy.

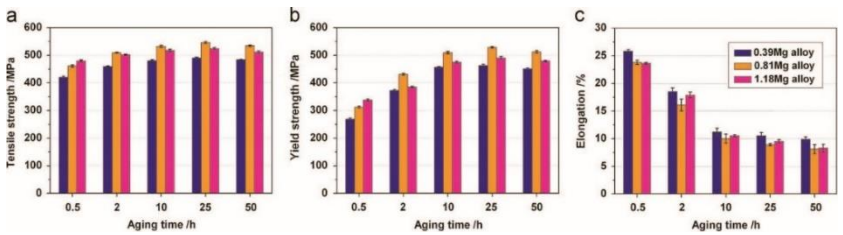

Figure 1-8 (a) tensile strength, (b) yield strength and (c) elongation of the alloys with different Ag content aged at 165 °C for various times[84]

1.6.2 Effect of Sc addition

The addition of Sc and other rare earth elements can improve the solidification structure and change aging precipitation sequence of aluminum alloys[85-89]. Adding a small amount of Sc to aluminum alloys can significantly optimize the microstructure of the alloy at multiple scales, from micro to nano levels[90, 91]. At the micro scale, primary Al_3Sc particles act as heterogeneous nucleation sites during solidification, refining the grain size. At the nano scale, Sc promotes the precipitation of fine Al_3Sc phases which are coherent and uniformly distributed within the aluminum matrix[92]. These nanoscale Al_3Sc phases effectively hinder dislocation movement, thereby enhancing the strength of the aluminum alloy[93]. In addition, due to the low diffusion rate of Sc in the aluminum matrix, the thermal stability of Al_3Sc particles is significantly improved, leading to enhanced heat resistance of the alloy[94]. Therefore, Sc is an important microalloying element in the development of heat-resistant aluminum alloys.

In the Al-Cu alloy system, the nanoscale Al_3Sc particles not only serve as strengthening phases to improve the alloy's strength and heat resistance[90, 95] but also act as heterogeneous nucleation sites, thereby promoting the precipitation of nanoscale θ′-Al_2Cu phases[96-98]. This leads to an increase in the number density of θ′-Al_2Cu, consequently enhancing the strength of the alloys. Besides enhancing room temperature strength, Sc can also enhance the heat resistance of the alloys by segregating at the θ′/Al interface, thereby inhibiting the coarsening of θ′-Al_2Cu[86]. Based on APT results obtained from Al-Cu-Sc alloys aged at 250 °Cfor 3 h, Chen et al.[97] demonstrated that Sc segregated at the θ′/Al interface significantly inhibit the diffusion of solute atoms from the aluminum matrix to the θ′-Al_2Cu phase, thereby improving the thermal stability of the θ′-Al_2Cu phase

under high-temperature and consequently enhancing the heat resistance of the alloy. On this basis, Gao et al.[99, 100] proposed a multi-step aging heat treatment to increase Sc segregation at θ′/Al interface. As shown in Fig. 1-9, Step-I, Step-II, Step-III, and Step-IV represent artificial ageing at 250 ℃ for 8 h, regression heat treatment at 450 ℃ for 20 min, re-aging at 250 ℃ for 6 h, and creep testing at 300 ℃ for 350 h, respectively.

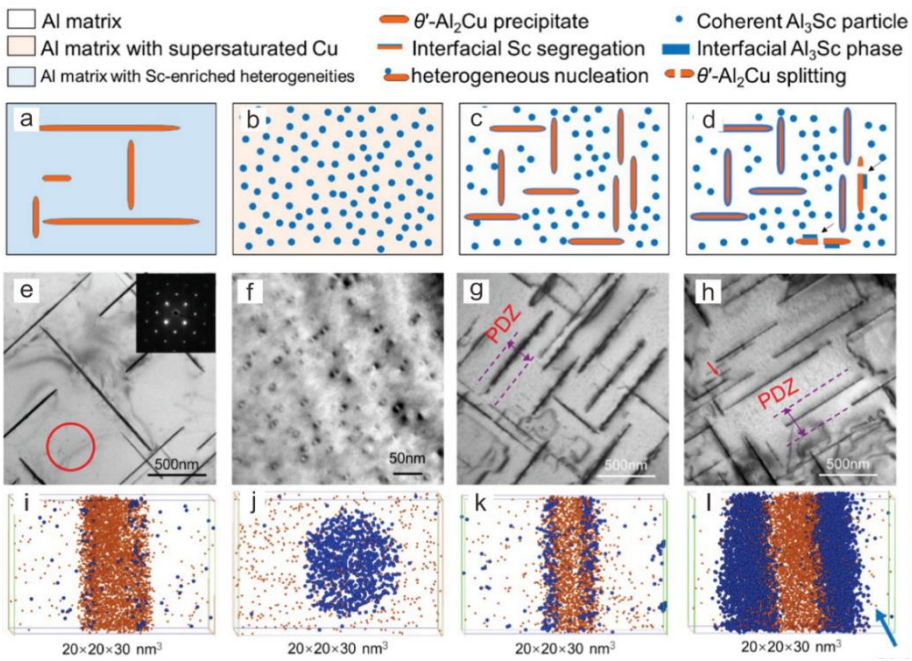

Figure 1-9 Microstructure of the Al-Cu-Sc alloy after each heat-treatment step and after creep test[99]. (a-d) Schematic of the microstructure developed in Step-I, Step-II, Step-III and Step-IV, respectively. (e-h) TEM images in Step-I, Step-II, Step-III and Step-IV, respectively. (i), (k) and (l) APT maps of Sc segregation at the Al/θ′ interface in Step-I, Step-III and Step-IV, respectively. (g) APT maps of Al_3Sc in Step-II

After artificial ageing heat treatment, enough θ′-Al_2Cu and nanoscale Sc-clusters precipitated in the aluminum matrix. Subsequently, during

regression heat treatment, the θ′-Al_2Cu phases formed during artificial ageing completely dissolve, and the Sc clusters gradually transform into nanoscale Al_3Sc particles, which can act as heterogeneous nucleation sites during re-aging heat treatment, promoting the formation of θ′-Al_2Cu phases. This multi-step aging heat treatment promote the segregation of Sc at θ′/Al interface, greatly improving the thermal stability of the θ′-Al_2Cu phase and thus enhancing the thermal stability of the alloy.

In Al-Cu-Mg-Ag alloys, Bai et al.[101] investigated the influence of Sc on the strength and heat resistance of the alloy. As shown in Fig. 1-10, the addition of Sc reduces the microhardness of Al-Cu-Mg-Ag alloys after artificial ageing. EDX results in Fig. 1-10b indicate that the addition of Sc promotes the formation of Al_8Cu_4Sc intermetallic in the alloy during casting and homogenization processes, consuming Cu solute atoms used for the precipitation of Ω phase. Therefore, excessive addition of Sc leads to the consumption of solute atoms in the alloy, reducing the number density and volume fraction of the Ω phase, and thus decreasing the room temperature mechanical properties of the alloy.

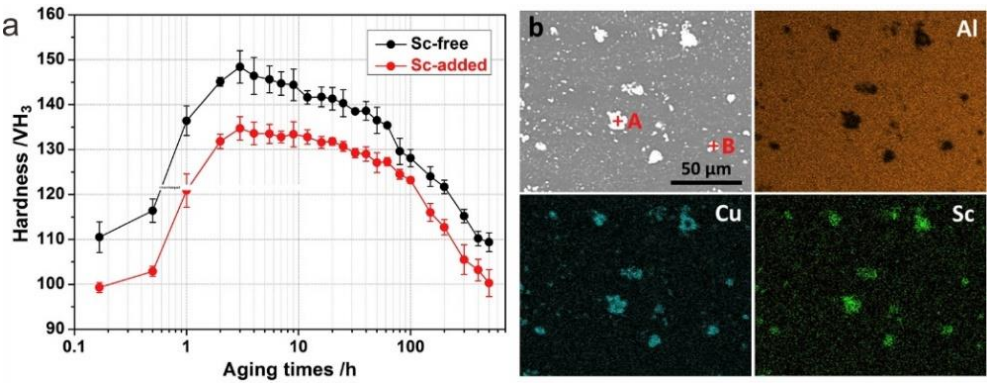

Figure 1-10 (a) Microhardness of Al-Cu-Mg-Ag(-Sc) alloys[101]. (b) Microstructure and EDX maps of the Al-Cu-Mg-Ag-Sc alloy after homogenization heat treatment[101]

Xue et al.[102] investigated the influence of excessive Sc addition on the precipitation behavior and mechanical properties of Al-Cu-Mg-Ag alloys under ultra-high temperature. After adding 0.3 wt.% Sc to the Al-Cu-Mg-Ag alloy, its yield strength exceeded 100 MPa at 400 ℃, significantly higher than other high-strength aluminum alloy systems. The results in Fig. 1-11 show that the addition of Sc promotes the transformation of the Ω phase into a more heat-resistant nanoscale V-AlCuSc phase at 400 ℃, which can stably exist at this temperature and significantly improve the high-temperature mechanical properties of the Al-Cu-Mg-Ag-Sc alloy.

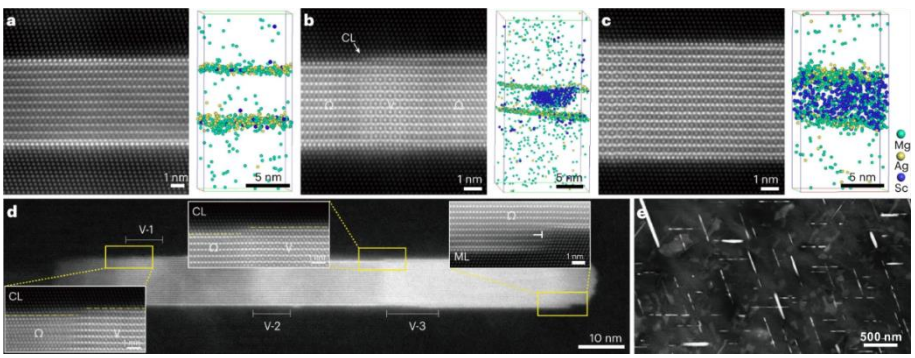

Figure 1-11. (a-c) HAADF images and corresponding APT images with different stages of the Ω-to-V transformation in the Al–Cu–Mg–Ag–Sc alloy exposed to 400 °C for 10 min, 30 min and 4 h, respectively. (d) HAADF image with multiple V phases simultaneously formed within a large Ω nanoprecipitate[102]. (e) TEM image of Al-Cu-Mg-Ag-Sc alloy during phase transformation[102]

Atomic-resolution HAADF-STEM and APT results shown in Fig. 1-11a-c indicate that the diffusion of Sc in the Ω phase promotes the formation of the V-AlCuSc phase. When the alloy was thermally exposed at 400 ℃ for 30 min, Sc diffused into the Ω phase and initiated the formation of the V phase internally, which grew gradually with prolonged exposure time. As shown in Fig. 1-11e, the portion of the Ω phase that had

not transformed into the V phase gradually dissolved due to low thermal stability at high temperature, resulting in point-like splitting within the Ω phase. It is worth noting that neither of the two strategies for adding Sc has resulted in the formation of a Sc segregation layer at the Ω/Al interface. Therefore, whether a multiple segregation structure containing both Sc and AgMg segregation layer can be obtained in Al-Cu-Mg-Ag alloys remains to be further investigated.

1.6.3 Effect of Si addition

Silicon is the primary alloying element in Al-Si and Al-Mg-Si systems, which is used to form Si particles or β″ and other nano scale precipitates to improve the strength of the alloy[103-106]. In Al-Cu based alloys, Si acts as a heterogeneous nucleation site, promoting the precipitation of θ′-Al_2Cu and refining its size, thereby improving alloy strength[107-111]. Mitlin et al.[107, 108] reported that the Si particles preferentially formed during artificial ageing would serve as heterogeneous nucleation sites for θ′-Al_2Cu in the alloy with higher Si content, thus enhancing the mechanical properties of the alloy after artificial ageing. As shown in Fig. 1-12a-b, Liu et al.[112] investigated the effect of Si on the precipitation sequence and mechanical properties of Al-Cu-Mg alloys with high Cu/Mg ratios. The results show that Si promotes the early-stage precipitation of Q″/L/C-AlMgSiCu phases in Si-containing alloys, where the preferentially precipitated Q″ phase further acts as a heterogeneous nucleation site, promoting the precipitation of θ′-Al_2Cu. In addition, the presence of the Q″ phase inhibits the thickening of θ′-Al_2Cu. In the peak-aged state, the width of most θ′-Al_2Cu in Si-containing alloys is $2C_{\theta'}$, which is much smaller than the thickness of θ′-Al_2Cu in Al-Cu-Mg alloys without Si addition. Gazizov et al.[113] investigated the precipitation behavior of Al-Cu-Mg-Si

alloys using HAADF-STEM. As shown in Fig. 1-12c, TEM characterization results indicate that the addition of Si not only promotes the formation of Q″/L precipitates at the θ′/Al semi-coherent interface but also precipitates the C-AlMgSiCu interfacial phase at the θ′/Al coherent interface, effectively inhibiting the coarsening of θ′-Al_2Cu and enhancing the heat resistance of Al-Cu-Mg-Si alloys.

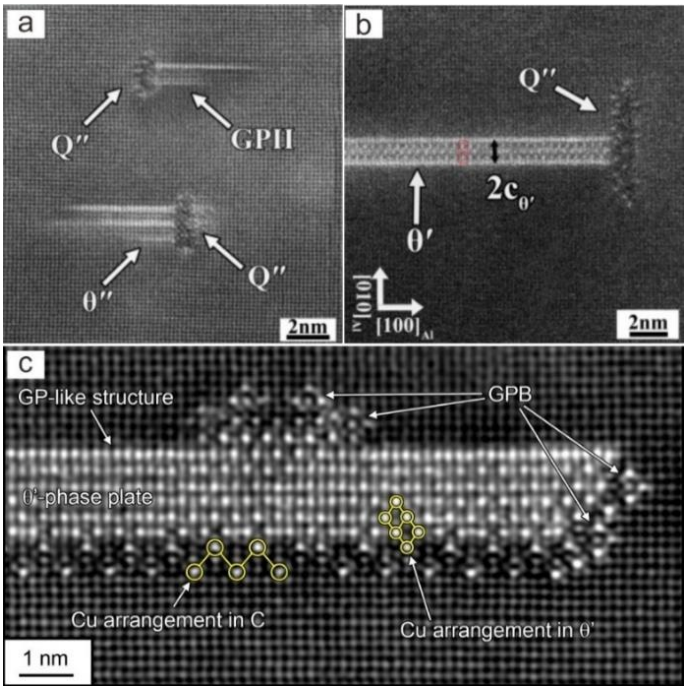

Figure 1-12 Atomic resolution HAADF-STEM images of Q″ phase[112] and C-AlMgSiCu interface phase at θ′/Al interface[113] in the (a) under aged and (b-c) peak aged Al-Cu-Mg-Si alloy

In addition to serving as heterogeneous nucleation sites to promote the precipitation of θ′-Al_2Cu, Si can also segregate at the θ′/Al interface, hindering the coarsening of the θ′-Al_2Cu phase and improving the heat resistance of the alloy[114-117]. According to the APT results, Biswas et al.[114] demonstrated that Si could segregate at the θ′/Al interface in high-Si

content alloys (Al - 7.38Si - 1.54Cu - 0.17Fe - 0.35Mg). The Si segregation at the θ′/Al interface is non-localized, with the concentration gradually decreasing from the interface to the interior of the θ′-Al_2Cu phase. That is, in addition to segregating at the θ′/Al interface, Si is also slightly enriched within the θ′-Al_2Cu phase. Further combined with DFT calculation results, it was found that Si tended to replace Cu atomic sites at the θ′/Al coherent interface, theoretically verifying the experimental results of Si segregation at the θ′/Al coherent interface and within the θ′-Al_2Cu phase. As shown in Fig. 1-13, Gao et al.[115] also found that the Si, Sc, and Fe could synergistically segregate at the θ′/Al interface using APT in the Al-Cu alloys with low Si and high Cu content.

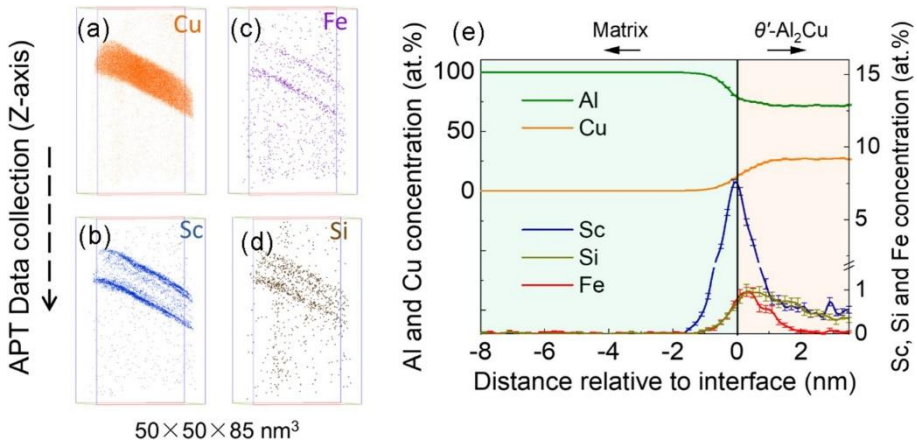

Figure 1-13 APT results of θ′-Al_2Cu/matrix interface with multiple segregation in Al–Cu–Sc–Fe–Si alloy after crept at 300 °C for 450 h[115]. (a) Iso-surface of Cu. (b) Iso-surface of Sc. (c) Iso-surface of Fe. (d) Iso-surface of Si. (e) Distribution of Sc, Si and Fe cross the θ′/Al interface

The APT results shown in Fig. 1-13 indicate that the Al-Cu-Sc-Fe-Si alloy exhibited a multiple segregation layer of Si-Sc-Fe at the θ′/Al coherent interface after creep testing at 300 °C. In this multiple segregation

structure, Sc and Fe elements tended to segregate at the θ′/Al coherent interface, while Si elements segregated both at the θ′/Al coherent interface and within the θ′-Al_2Cu phase, consistent with the results of Biswas et al.[114] in high-Si alloys. The presence of the Si-Sc-Fe multiple segregation layer effectively inhibited the coarsening behavior of the θ′-Al_2Cu phase during high-temperature creep, ensuring that the alloy could serve for over 1000 h under creep conditions of 300 ℃ and 30 MPa.

The addition of Si in the Al-Cu-Mg system can promote the precipitation of θ′-Al_2Cu by forming heterogeneous nucleation sites, thereby improving the mechanical properties of the alloy[112]. However, when Si elements are added to the Al-Cu-Mg-Ag alloys, the precipitation sequence in the alloy is altered, with the suppression of the formation of Ω phase and the promotion of the precipitation of θ′-Al_2Cu, S-Al_2CuMg, and σ-$Al_5Cu_6Mg_2$ phases[118-122]. Abis et al.[120] and Gao et al.[118] combined Differential Scanning Calorimetry (DSC) and TEM characterization to analyze the effect of Si addition on the precipitation sequence of Al-Cu-Mg-Ag alloys, showing that Si promotes the formation of precipitates containing MgSi elements in Al-Cu-Mg-Ag alloys, leading to the consumption of Mg elements in the supersaturated solid solution and thus inhibiting the precipitation of the Ω phase. As shown in Fig. 1-14, Gable et al.[119] demonstrated that the Mg/Si mass ratio is an important factor controlling the precipitation of the Ω phase in Al-Cu-Mg-Ag-Si alloys. When the Mg/Si mass ratio is less than 2, the precipitation of the Ω phase is completely suppressed, and the main precipitate in the alloy changes from the Ω phase to the θ′-Al_2Cu phase.

Gable et al.[119] attributed the inhibitory effect of Si on the Ω phase to the high binding energy between Si and Mg elements, which prevents the formation of Mg-Ag atomic clusters in the alloy, thereby inhibiting the

precipitation of the Ω phase, and the excess Cu alloy element generates precipitated phases such as θ′-Al_2Cu. Therefore, the addition of Si inhibits the precipitation of the Ω phase and promotes the formation of the θ′-Al_2Cu phase in Al-Cu-Mg-Ag-Si alloys. However, the increase in Ag content can suppress the formation of the θ′-Al_2Cu phase and promote the precipitation of the Ω phase. Therefore, when Si and Ag elements are simultaneously added to the alloy, their competitive effects on the precipitation of the Ω phase need further investigate. Further research is needed to determine whether increasing the Ag content can alter the precipitation sequence in low Mg/Si mass ratio Al-Cu-Mg-Ag-Si alloys.

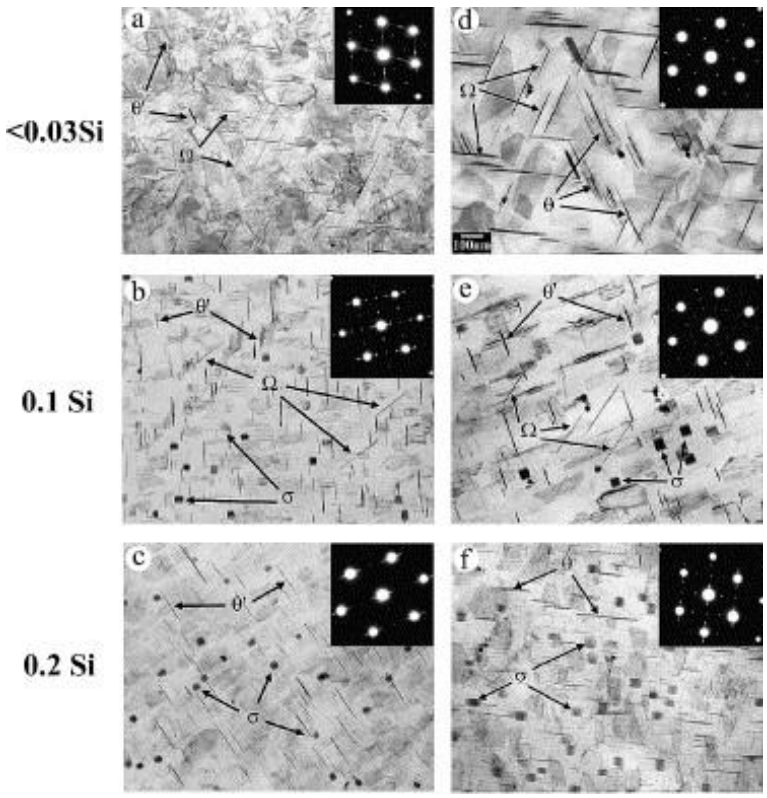

Figure 1-14 TEM bright field of Al - 4.0Cu - 0.4Mg - 0.3Ag - xSi alloys after artificial aging at 250 °C[119]. (a-c) Aged 30 min. (d–f) Aged 2 h

1.7 Challenges in Al-Cu-Mg-Ag Alloy

1.7.1 Synergistic enhancement of Alloy strength and heat resistance

As mentioned above, to meet the demand for high-performance aluminum alloys in sectors such as aerospace, it is necessary to develop aluminum alloy materials with synergistically improved strength and heat resistance. Currently, the main research focus for high-strength, heat-resistant aluminum alloys lie in the Al-Cu-Mg-Ag alloys, where the main strengthening phase is the Ω phase with a bi-AgMg segregation layer at the Ω/Al interface. When the service environment temperature of the alloy is lower than 200 °C, the AgMg segregation layer at the Ω/Al interface can effectively inhibit the coarsening of the Ω phase and improve the heat resistance of the alloy. However, when the service environment temperature is higher than 200 °C, the hindrance of Ω phase coarsening by the AgMg interface segregation layer diminishes due to elemental redistribution, making the Ω phase susceptible to coarsening during thermal exposure[9]. That is, the Ω phase with a single segregation layer is difficult to serve for a long time in an environment above 200 °C. Therefore, it is necessary to design heat-resistant aluminum alloy materials that can serve for a longer time at higher temperatures. The addition of alloying elements such as Si and Sc can induce different types of segregation structures in Al-Cu-Mg base alloys, such as Sc segregation layers, Si segregation layers, and C-AlMgSiCu interface phases. If these different types of segregation structures can be combined with the AgMg segregation layer through reasonable composition design, it may be possible to design an Al-Cu-Mg-Ag alloy with multiple segregation structures, thereby further enhancing the heat resistance of Al-Cu-Mg-Ag

alloy and improving its long-term service properties at high temperatures.

The addition of Si, Sc, and other elements in Al-Cu-Mg-Ag alloys complicates the phase equilibrium at homogenization and ageing temperatures[123]. Excessive Sc addition will consume Cu during homogenization heat treatment, leading to a decrease in Cu content in the supersaturated solid solution and, consequently, a decrease in the alloy's room temperature mechanical properties. Therefore, the key to achieving a synergistic improvement in strength and heat resistance is to reasonably select the content of various alloy elements, ensuring that the added elements are utilized to form precipitates or multiple segregation structures. Compared to traditional trial-and-error methods, computational thermodynamic calculations using the Calculation of Phase Diagrams (CALPHAD) approach offer a more efficient and accurate means of controlling phase equilibria, thereby avoiding the formation of detrimental phases. The CALPHAD method, proposed by Kaufman et al.[124] in 1970, is based on solution theory, statistical thermodynamics, and computational techniques, and it is currently the most widely used and mature material genome engineering technology worldwide. Fig. 1-15 illustrates a study on the synergistic enhancement of strength and plasticity in Al-Mg-Si-Cu alloys by reasonable control of multi-scale microstructures using CALPHAD[125]. The Mg/Si element ratio is reasonably controlled through the phase diagram, and the most suitable Mg/Si ratio and content are selected in combination with the precipitation driving force of the precipitation phase to rapidly promote the precipitation of β″ phase, thereby improving the strength of the alloy. In addition, the Mn element content is reasonably controlled to avoid the formation of harmful β-AlFeSi in the alloy, improve the plasticity of the alloy, and ultimately achieve a synergistic improvement in the strength and plasticity of the alloy.

Therefore, in this study, the CALPHAD method can be used to reasonably control the content and ratio of each element in the alloy, inhibit the formation of harmful phases, and attempt to promote the precipitation of strengthening phases and multiple interface structures, thereby achieving synergistic enhancement of alloy strength and heat resistance.

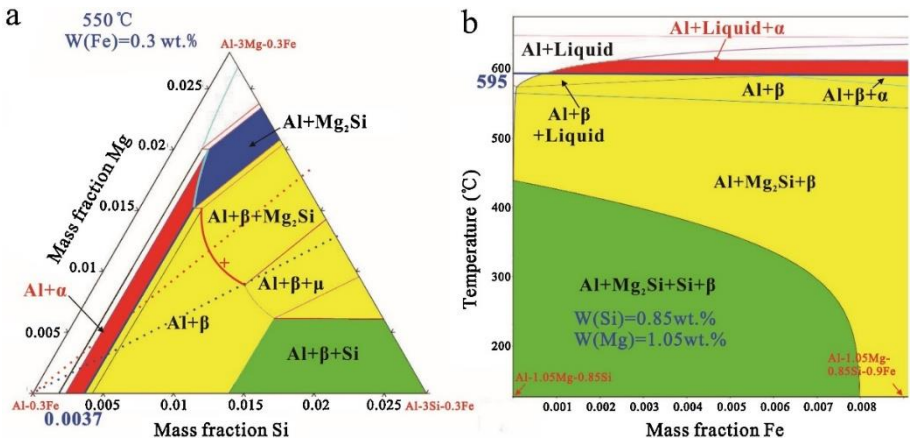

Figure 1-15 (a) Isothermal section of Al-Mg-Si-Fe alloy with fixed iron content of 0.3 wt.% at 550 ℃; (b) Vertical section of the Al-Mg-Si-Fe alloy[125]

1.7.2 Relationship between precipitation behavior and alloying elements

The addition of Si significantly alters the precipitation behavior and mechanical properties of Al-Cu-Mg(-Ag) alloys. Barlow et al.[109] investigated the effect of Si on the precipitation behavior of Al-Cu-Mg alloys with low Cu/Mg ratio. As shown in Fig. 1-16, the addition of Si promotes the precipitation of the σ-$Al_5Cu_6Mg_2$ phase with excellent thermal stability[126-128], while inhibiting the formation of the S-Al_2CuMg phase. As for Al-Cu-Mg-Ag alloys, the results in Fig. 1-14 indicate that the addition of Si not only suppresses the precipitation of the Ω phase but also promotes the formation of the σ-$Al_5Cu_6Mg_2$ phase[119]. Therefore, the

precipitation behavior under different alloy compositions is relatively complex in Al-Cu-Mg-Ag-Si alloys.

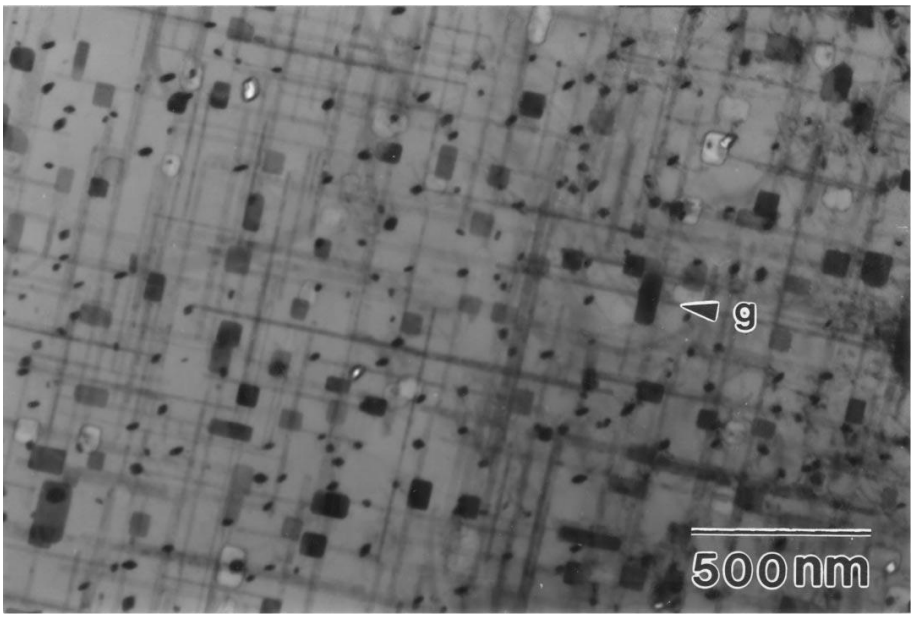

Figure 1-16 TEM images of S and σ-$Al_5Cu_6Mg_2$ phases in Al-3.62Cu-1.66Mg-0.5Si alloy[109]

Firstly, the research of Gable et al.[119] suggests that increasing Si content inhibits the formation of the Ω phase, but increasing Ag content in Al-Cu-Mg-Ag alloys promotes Ω phase precipitation. Thus, whether increasing Ag content can further promote Ω phase precipitation in low Mg/Si ratio Al-Cu-Mg-Ag-Si alloys needs further validation. Secondly, Barlow et al.[109] found that increasing Mg content in Al-Cu-Mg-Si alloys promotes the formation of the σ-$Al_5Cu_6Mg_2$ phase. As for the Al-Cu-Mg-Ag-Si alloys, increasing Mg content implies an increase in the Mg/Si ratio, which promotes the generation of the Ω phase. Therefore, whether increasing Mg content in Al-Cu-Mg-Ag-Si alloys leads to competition between the σ-$Al_5Cu_6Mg_2$ phase and the Ω phase also requires further

investigation. Finally, the impact of changes in precipitation behavior resulting from the addition of different alloying elements on the room temperature mechanical properties and heat resistance of the alloy is also unclear and requires further study. Clarifying the relationship between various element contents and proportions and the precipitation behavior, mechanical properties, and heat resistance of Al-Cu-Mg-Ag-Si alloys will deepen the understanding of the influence of different types of precipitates on heat resistance. It will also aid in designing alloy compositions based on service conditions to construct alloys with different proportions of precipitates.

1.8 Research content and research approach

Based on the unresolved problems mentioned above, this work maily investigates the effects of aging heat treatment and alloy element content and ratio on the precipitation behavior and heat resistance of Al-Cu-Mg-Ag-(Si) alloys, and couples the CALPHAD to achieve the synergistic improvement of aluminum alloy strength and heat resistance. In terms of mechanical properties, methods such as microhardness testing and tensile testing are employed to analyze the effects of aging parameters and alloy elements on the room temperature mechanical properties and heat resistance of Al-Cu-Mg-Ag-(Si) alloys. Regarding precipitation behavior, scanning electron microscopy (SEM), aberration-corrected transmission electron microscopy (TEM), APT, and electron probe tomography techniques are utilized to analyze the effects of aging processes and alloy element content on the types, sizes, number densities, volume fractions, and interface segregation structures of precipitates from micrometer to atomic scales. In addition, first-principles calculations, and Ab initio molecular dynamics (AIMD) methods are employed to analyze the reasons

for elemental segregation or structural stability. The overall research strategy of this work is illustrated in Fig. 1-17.

(1) Effect of aging heat treatment process on the heat resistance of Al-Cu-Mg-Ag alloy. Based on TEM characterization and quantitative results from tensile testing, the effects of alloy element content and aging heat treatment on the room temperature mechanical properties and heat resistance of Al-Cu-Mg-Ag alloys were studied, providing guidance for selecting aging parameters for structural parts in medium and high temperature service.

(2) Achieving a synergistic improvement in the strength and heat resistance of Al-Cu-Mg-Ag-Si-Sc alloys by adding Si/Sc elements to Al-Cu-Mg-Ag alloys to construct multiple interface structures at the precipitate/matrix interface. Based on CALPHAD, the content and ratio of each element in Al-Cu-Mg-Ag-Si-Sc alloy were reasonably controlled, and multiple interface structures were constructed at θ′/Al, which effectively inhibited the coarsening of θ′-Al_2Cu and achieved a synergistic improvement in strength and heat resistance. The concept of constructing multiple segregation structures including interfacial phases and segregation layers at precipitate interfaces was proposed, providing new strategies for the design of other heat-resistant materials.

(3) Effect of Ag on the precipitation behavior of the Ω phase in low Mg/Si ratio Al-Cu-Mg-Ag-Si alloys. Based on TEM characterization, the promotion effect of Ag on the precipitation of the Ω phase in low Mg/Si ratio Al-Cu-Mg-Ag-Si alloys is verified, and the precipitation criteria for the Ω phase in Al-Cu-Mg-Ag-Si alloys are updated.

(4) Effect of Mg/Ag content on the competitive behavior of Ω/σ/θ′ phase precipitation and heat resistance of Al-Cu-Mg-Ag-Si alloy. Based on TEM characterization and mechanical properties testing, the effects of

changes in Mg/Ag content on the precipitation sequence of Ω phase, θ′-Al_2Cu phase, and σ-$Al_5Cu_6Mg_2$ phase in the alloy are analyzed. In addition, the contributions of different precipitate types to the long-term high-temperature service and instantaneous high-temperature service strength of the alloy are summarized, providing theoretical guidance for alloy composition design based on service conditions.

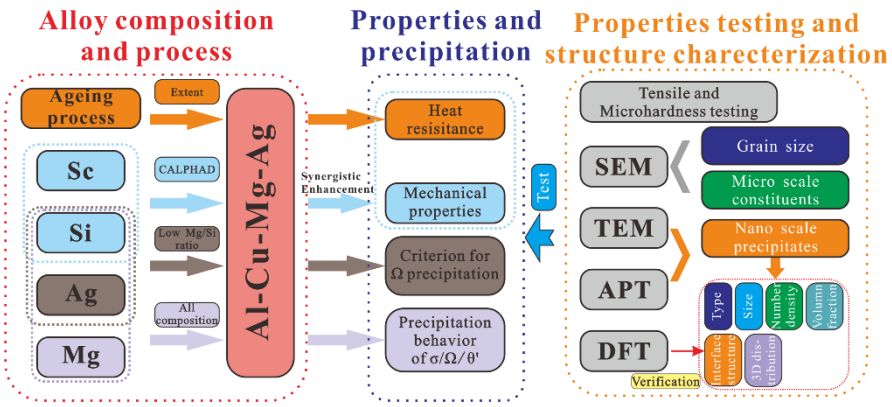

Figure 1-17 Schematic diagram of the research methodology in this work

Chapter 2. Research methods

2.1 Sample preparation

2.1.1 Alloy melting and rolling process

This work investigates the effects of aging heat treatment processes and alloy elements on the heat resistance and precipitation behavior of Al-Cu-Mg-Ag alloys. The alloy compositions used in each chapter are shown in Tab. 2-1.

Table 2-1 Nominal/determined chemical compositions of the alloys and the corresponding chapters (wt.%)

	Cu	Mg	Ag	Si	Sc	Al	Chapter	Label
1	4/3.91	0.3/0.30	0.4/0.38	\	\	Bal.	3	1#
2	4/3.87	0.3/0.29	0.6/0.57	\	\	Bal.		2#
3	6/5.95	0.45/0.42	0.6/0.59	\	\	Bal.		3#
4	4/4.15	0.315/0.3	0.5/0.47	0.21/0.17	0.09/0.10	Bal.	4	\
5	4/3.89	0.4/0.40	0.5/0.49	0.2/0.24	\	Bal.	5	0.5Ag
6	4/3.66	0.4/0.38	0.8/0.76	0.2/0.22	\	Bal.		0.8Ag
7	4/3.95	0.3/0.28	0.5/0.47	0.2/0.20	0.09/0.09	Bal.	6	3M5A
8	4/3.89	0.5/0.49	0.5/0.47	0.2/0.24	0.09/0.09	Bal.		5M5A
9	4/3.85	0.8/0.80	0.5/0.48	0.2/0.20	0.09/0.09	Bal.		8M5A
10	4/4.03	0.8/0.78	0.8/0.75	0.2/0.19	0.09/0.09	Bal.		8M8A

During alloy melting, the following raw materials were used: high-purity aluminum particles with a purity of 99.999%, high-purity magnesium particles with a purity of 99.99%, high-purity silver powder with a purity of 99.99%, and intermediate alloys of Al-50Cu, Al-20Si, and Al-5Sc with purities higher than 99.9%. Melting was conducted using a Chixin CXZG-0.5 vacuum induction melting furnace, with argon gas introduced into the furnace chamber as a protective atmosphere to reduce element oxidation and impurities. After the raw materials are completely

melted and kept for 3~5 min, the molten liquid is cast into a 20 mm × 100 mm iron mold. The cast rods were subjected to homogenization heat treatment at 520-540 ℃ using a Kejing KSL-1200 furnace, followed by immediate water quenching. The homogenized rods were then hot- and cold-rolled from rods to approximately 1-2 mm-thick sheets. The determined chemical compositions were detected by a SPECTRO BLUE inductively coupled plasma optical emission spectrometer (ICP-OES).

2.1.2 Heat treatment process

After the rolling process, the aluminum alloy sheets were processed into different specimens according to different testing requirements. The alloy specimens were subjected to solution heat treatment in a Kejing KSL-1200 furnace, followed by water quenching after the solution heat treatment. Subsequently, the specimens underwent aging heat treatment at different parameters. After artificial ageing, some of the specimens were subjected to thermal exposure for 100 h to assess the heat resistance of the alloy. The solution heat treatment, artificial aging heat treatment, and thermal exposure parameters used for the alloys in each chapter are presented in Tab. 2-2.

Table 2-2 The heat treatment parameters of the alloys in the corresponding chapters

	Solution temperature	Solution time	Ageing temperature	Thermal exposure temperature	Chapter
1	520 ℃	2 h	200 ℃	225 ℃	3
2	540 ℃	1 h	175 ℃	200/210 ℃	4
3	530 ℃	2 h	180 ℃	210 ℃	5
4	520 ℃	4 h	180 ℃	210 ℃	6

2.2 SEM characterization

The Hitach Regulus 8230 cold field emission SEM equipped with an EDX probe was employed to analyze the morphology and composition of micron-scale constituents in the alloy. The operating voltage was set to 15 kV, and the working mode was backscattered electron (BSE) mode. In addition, the FEI Helios Nanolab G3 UC dual-beam SEM, equipped with an electron backscatter diffraction (EBSD) probe, was used to analyze the grain size of the alloy. The collected EBSD data were analyzed using the OIM software.

2.3 TEM characterization

2.3.1 Ex-situ TEM characterization

After undergoing the corresponding heat treatment processes, TEM samples were thinned from both sides to ensure a final thickness of 50-100 μm. Subsequently, the thin samples were punched into circular pieces with a diameter of Φ3 mm using a DERVEE 1700-3A puncher. For TEM observation, the observation area needed to reach the nanoscale (30-100 nm). In this study, the convenient electropolishing method was mainly employed to prepare samples for ex situ TEM characterization. For specific samples, a combination of electropolishing and ion thinning methods was used. The detailed procedures and parameters are as follows:

(1) Electropolishing method: The electropolishing instrument used in this study was the STRUERS Tenupol-5, and the electrolyte was a mixture of 30 vol.% nitric acid (HNO3) and 70 vol.% methanol (CH4O). The voltage was set to 16 V, the instrument sensitivity was 120, and the electrolyte column flow rate was 50. Liquid nitrogen was used to cool the electrolyte during the electropolishing process to maintain a temperature of around -30 ℃. After the electropolishing process, the samples were

immediately removed, washed three times with alcohol, and then placed on filter paper to air dry, preventing further corrosion by the electrolyte. The prepared samples were stored under vacuum to prevent oxidation.

(2) Ion thinning method: Ion thinning uses an accelerated ion beam (usually Ar ions) to bombard atoms on the surface of the sample to achieve sample thinning. This method is highly versatile but less efficient than electropolishing method. In this work, samples after thermal exposure were first prepared using the electropolishing methods. However, there were no well-thinned areas suitable for observing atomic resolution interface structures. Therefore, small-angle ion thinning was performed on samples prepared using electropolishing. The ion thinning instrument used was the Gatan 695. The samples prepared using electropolishing were placed in the instrument, and the position of the sample is adjusted to ensure that the sample hole prepared by electropolishing is in the center. Subsequently, low voltage (2 kV) and small angle (2°) thinning were performed for approximately 10 minutes. After thinning, the samples were removed and placed in a high-elasticity film box, and vacuum using a vacuum pump for storage.

The transmission electron microscopes used in this work were as follows: (1) FEI Tecnai G2 F20, operating at 200 kV, mainly used for collecting selected area electron diffraction (SAED) spectra, TEM bright-field images, CBED, and HRTEM. CBED was used to measure the sample thickness in the observed area, bright-field images were used to count the size and number of precipitates, and HRTEM was mainly used to measure the length and thickness of precipitates. (2) FEI Titan G2 60-300, operating at 300 kV and equipped with an objective spherical aberration corrector and a super-X high resolution EDX spectrometry system, mainly used for collecting HRTEM, HAADF-STEM, and EDX. (3) Thermo Fisher Titan

Cubed Themis G2 300, operating at 80 kV and equipped with objective and probe spherical aberration correctors and super-X high-resolution EDX system, mainly used for collecting atomic resolution HAADF-STEM images and EDX spectra of multiple interface structures. The atomic resolution HAADF-STEM images collected using this equipment were obtained by recording 50 frames of rapid scanning images using the drift-corrected frame integration (DCFI) technique, which significantly reduces the impact of sample drift and increases the signal-to-noise ratio to ensure the accuracy of the image information. (4) Thermo Fisher Titan Spectra 300, operating at 300 kV and equipped with objective and probe spherical aberration correctors and super-X high-resolution EDX system, mainly used for collecting atomic resolution HAADF-STEM images and EDX spectra of alloys after thermal exposure. (5) FEI Tecnai Osiris, operating at 200 kV and equipped with a super-X EDX system, mainly used for collecting HAADF-STEM images and EDX spectra and conducting electron tomography experiments. (6) FEI Titan G2, operating at 300 kV and equipped with objective and probe spherical aberration correctors, mainly used for acquiring atomic resolution HAADF-STEM images.

To improve the signal-to-noise ratio of HRTEM images, some HRTEM images were filtered using the HRTEM Filter plugin[129] in the DigitalMicrograph software. The atomic resolution HAADF-STEM images collected using the DCFI technique were obtained by overlaying images in the Velox software without filtering. For atomic resolution HAADF-STEM images collected without the DCFI technique, the outer signals were filtered out using the Fourier transform (FFT) function in the DigitalMicrograph software to enhance the signal-to-noise ratio. Atomic scale image simulations were performed using the QSTEM software[130] based on different interface structure models. Parameters such as

experimental voltage and collection angle were set to match the experimental conditions.

The atomic resolution EDX spectra were background-corrected and peak-fitted using the Velox software, and the Intensity Profile tool in the software was used to obtain the corresponding element line scan data. For EDX spectra collected using the FEI Tecnai Osiris and FEI Titan G2, quantitative data processing was performed using the ESPRIT software, and the EDX mapping data were quantitatively calculated using the Qmap function in the software. After quantitative processing, line segments were drawn on the EDX mapping data to obtain the element line scan data in the corresponding regions.

2.3.2 In-situ TEM characterization

To observe the phase transformation of interface phases in real time during thermal exposure, in-situ TEM heating experiments were conducted using a combination of aberration-corrected TEM and the DENS solutions in situ system. The DENS solutions in situ double-tilt sample holder[131] used for in-situ heating experiments is shown in Fig. 2-1a-b, and the DENS solutions Wildfire heating chip is illustrated in Fig. 2-1c-d. The DENS solutions in situ heating double-tilt sample holder allows tilting of both α and β angles up to ±25° in the TEM, providing a large range of rotation angles and enabling direct integration with the Thermo Fisher transmission electron microscope. The Wildfire heating chip ensures uniform temperature distribution in the sample observation area during heating, thereby guaranteeing the set temperature is reached throughout the entire sample. In addition, the in-situ heating chip exhibits high stability, preventing any bending or drifting even during rapid temperature changes in in-situ experiments. This ensures that real-time

observation of phase transformations with atomic resolution can be achieved.

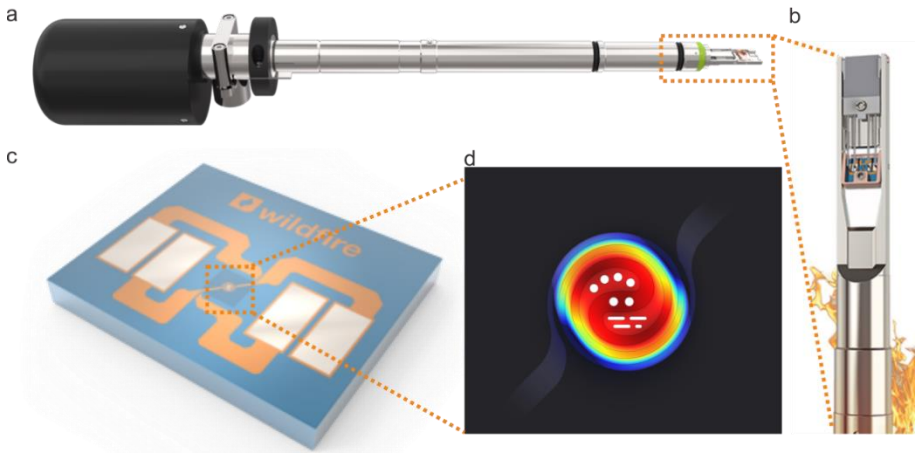

Figure 2-1 (a-b) In-situ heating double-tilt holder. (c-d) In-situ heating chip

For in-situ heating sample preparation, TEM was first used to select an electropolishing sample that could reach $[001]_{Al}$ zone axis by a small tilt angle, and the position of the observable area of the sample was marked. Subsequently, the FEI Helios NanoLab 650 dual-beam SEM was used to prepare the in-situ sample using focused ion beam (FIB) techniques. The FIB sample preparation process is illustrated in Fig. 2-2. Fig. 2-2a shows that the selected area at the edge of the sample prepared by electropolishing, and the area is cut by Ga ion beam. Fig. 2-2b shows the extracted region using a Pt needle, which was then placed on a DENS solutions in-situ heating chip. The final prepared sample is shown in Fig. 2-2c-d. During in-situ heating experiments, temperature was controlled by the Impulse software. Fig. 2-2e shows a screenshot of the software interface. In the Temperature Control section, the Temperature option represents the temperature for conducting in-situ heating experiments, while the Ramp rate indicates the heating rate. The real-time temperature of the chip can

be observed on the right-hand side in the red box, facilitating adjustment of the control program based on the real-time temperature.

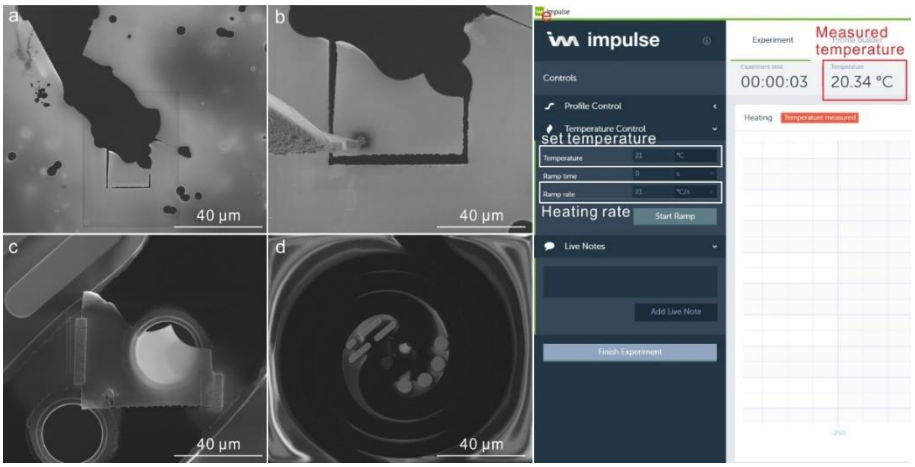

Figure 2-2 (a-d) The preparation process of in-situ heating sample. (e) The in-situ heating control software impulse developed by DENS solutions company

2.4 Electron tomography characterization

Electron tomography, a novel technique based on electron microscopy and computational algorithms, holds significant potential applications, and is widely used for nanoparticle reconstruction[132], characterization of dislocation density[133-135], and more. When combined with in situ TEM experiment, it enables real-time observation of phase transformation processes in fields such as catalysis and alloy phase transitions[136, 137].

In this work, electron tomography characterization was employed to analyze the crystallographic orientation relationships of different precipitate phases in the 8M5A alloy. As shown in Fig. 2-3, to avoid obstruction of the observation area by the slice-shaped samples prepared by electropolishing during the rotation process, the sample used in the tomography experiment is a needle-shaped sample. The needle-shaped

sample was prepared using the FIB method in the FEI Helios NanoLab 650 dual-beam SEM, and sampling was directly performed at the edge of the sample prepared by electropolishing (as indicated by the red box in Fig. 2-3a), and then the sample was further thinned to a tip diameter of approximately 40 nm using the ion beam (as shown in Fig. 2-3b). The prepared needle-shaped sample was used for data collection with a single tilt sample holder as shown in Fig. 2-4.

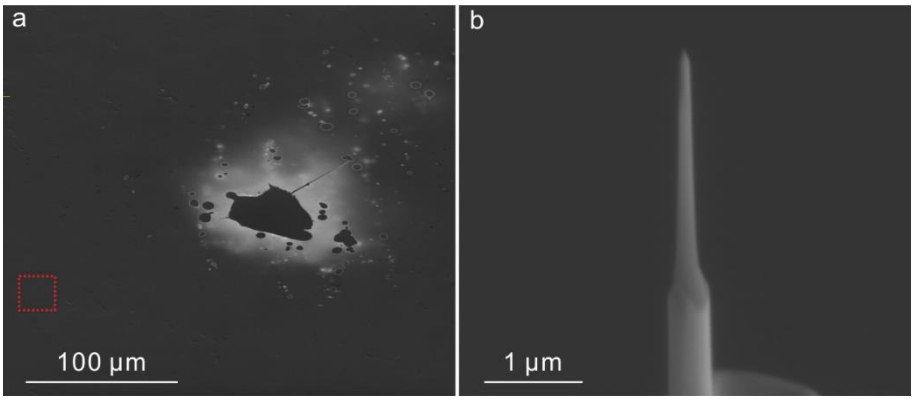

Figure 2-3 (a) Low-magnification image of TEM sample prepared by twin-jet electro-polishing. (b) The prepared needle-shaped sample used for electron tomography testing

Electron tomography experiment was conducted using the Fischione Model 2050 single-tilt rotation sample holder. The needle-shaped sample prepared by FIB is placed on the sample stage as shown in Fig. 2-4a, and then secured to the retractable sample holder using a clip. Before inserting the sample holder into the TEM, to prevent damage to the sample during transfer, the sample needs to be retracted into the interior of the sample holder by rotating the knob shown in Fig. 2-4a. Once the sample holder is inserted into the TEM, the sample is extended using the same knob. Finally, the rotation angle is controlled using the microscope software.

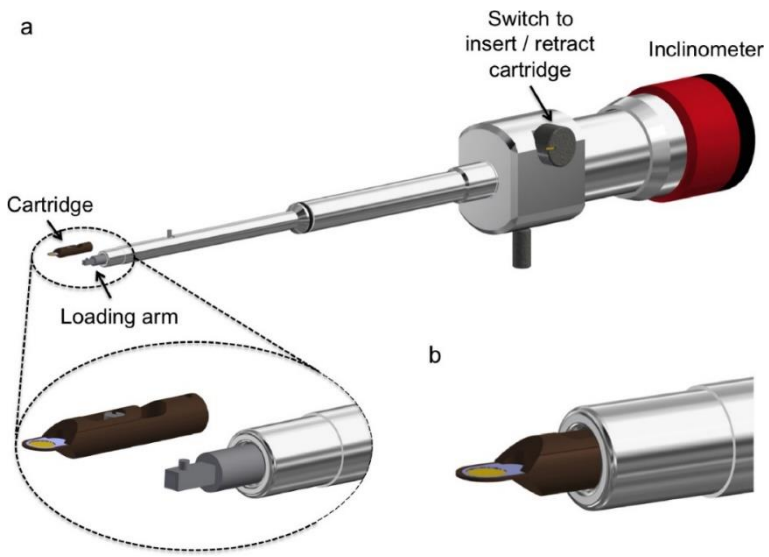

Figure 2-4 Schematic diagram of Fischione model 2050 tomography specimen holder[138]. (a) Schematic diagram showing the cartridge, the on-axis tomography specimen holder and the inclinometer unit. (b) The position of the cartridge in the specimen holder during a TEM experiment

2.5 APT characterization

APT is a commonly used method in materials science for quantitative analysis of the three-dimensional spatial distribution of elements in materials. The operating principle of APT is illustrated in Fig. 2-5. Under ultra-low temperature (20-70 K) and ultra-high vacuum conditions, a nanoscale needle-shaped sample is bombarded with pulsed laser beams. Atoms of different elements at the tip of the sample are ejected in the form of positive ions, which are further detected by an element detector to determine their elemental types and record the spatial positions. By bombarding the sample layer by layer, the entire three-dimensional

distribution of elements in the sample is obtained, and then the reconstruction software is used to reconstruct and analyze the data.

For metal materials such as aluminum alloys, the most suitable method for preparing APT samples is electropolishing[139]. Firstly, samples with dimensions of 0.5 mm × 0.5 mm × 20 mm are cut from the artificially aged plate using wire cutting. After cleaning with alcohol, the samples are electropolished. During rough polishing, the electrolyte consists of 70 vol.% glacial acetic acid and 30 vol.% perchloric acid, with a polishing voltage of 20 V. After rough polishing, the rod-shape samples are further polished to obtain a fine tip. To obtain samples with a curvature radius suitable for testing of less than 100 nm, a fine polishing process is required to produce nanoscale needle tips. The electrolyte for fine polishing consists of 95 vol.% ethylene glycol dimethyl ether and 5 vol.% perchloric acid, with a voltage of 25 V.

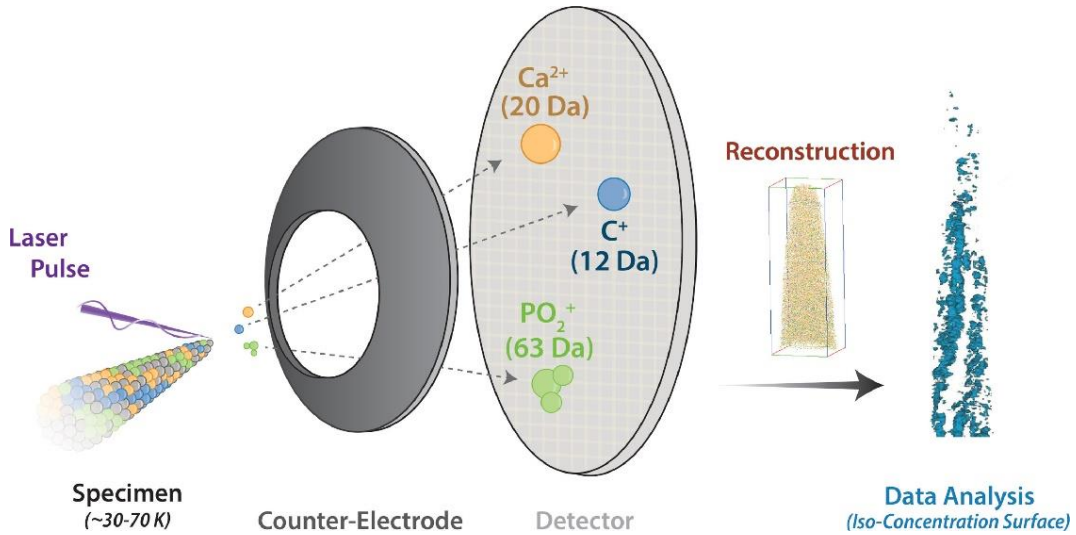

Figure 2-5 Operating principle of APT[140]

In this work, the composition of precipitates and multiple interface segregation structures in under-aged and peak-aged Al-Cu-Mg-Ag-Si-Sc

alloys were investigated using the CAMECA LEAP 4000X SI three-dimensional atom probe. The sample detection temperature was 20 K, with a pulse voltage of 50 pJ, a frequency of 200 kHz, and a detection efficiency of 0.6%. The collected data were reconstructed and analyzed using IVAS 3.8.2 software.

2.6 Mechanical properties testing

2.6.1 Microhardness

The microhardness samples are square specimens of approximately 10 mm × 10 mm. After heat treatment, the samples are polished to ensure smooth surfaces for microhardness testing. The SIOMM HV-1000IS automatic turret microhardness tester is used for the microhardness tests, with a testing load of 100 g and a dwell time of 10 s after loading. To reduce measurement errors, ten tests are taken from each sample, and the highest and lowest points are excluded before averaging to determine the microhardness of the samples.

2.6.2 room temperature mechanical properties

An Instron 3369 mechanical testing machine was used to conduct the tensile tests at a constant speed of 2 mm/s. The bar geometry and dimensions of room temperature tensile sample are shown in Fig. 2-6. Each group of samples consists of 3 parallel specimens, and the average values of yield strength, ultimate tensile strength, and elongation are taken from these 3 parallel specimens. If one of the parallel specimens deviates significantly from the other two, the average value of the data from the remaining two parallel specimens is used as the experimental value.

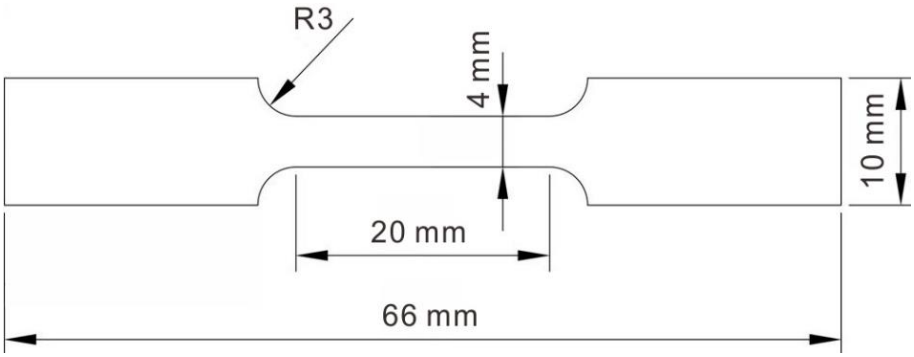

Figure 2-6 The size of tensile specimen tested at room temperature

2.6.3 High temperature mechanical properties

High temperature mechanical properties testing is conducted at 210 ℃ using an INSTRON 3369 universal testing machine. The bar geometry and dimensions of high temperature tensile sample are shown in Fig. 2-7. The samples are heated from room temperature to the test temperature, and after holding for 10 minutes at the test temperature, tensile testing is performed with a constant speed of 2 mm/s. Each group of samples consists of 3 parallel specimens, and the average values of yield strength, ultimate tensile strength, and elongation are taken from these 3 parallel specimens as the experimental values for the respective test samples.

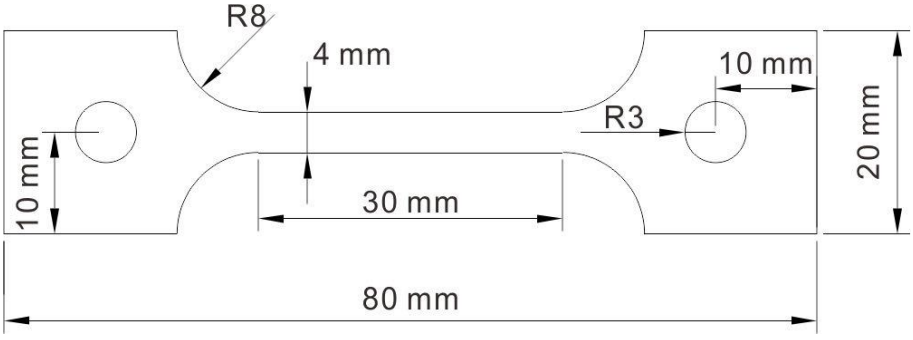

Figure 2-7 The size of tensile specimen tested at high temperature

2.7 Computational simulation

2.7.1 CALPHAD

In this work, CALPHAD was employed in alloy design to effectively control the content and proportion of each element, thereby avoiding the formation of harmful phases, and constructing multiple segregation structures at the interface between precipitates and the matrix. The calculation software used in the alloy design part was Thermo-Calc (TC) software, with the multicomponent aluminum alloy database (TCAL)[141]. For detailed calculation procedures, please refer to Chapter 4. In Chapters 3 and 6, the Pandat calculation software and the multicomponent aluminum alloy database were used for equilibrium phase diagram calculations of alloys with different compositions.

2.7.2 First-principles calculations

All first-principles calculations have been performed within the framework of density functional theory (DFT), as implemented in the Vienna *ab initio* Simulation Package (VASP) code[142]. Projector-augmented wave (PAW) potentials[143] and Perdew-Burke-Ernzerhof (PBE) within generalized gradient approximation (GGA)[144] were used to treat the ion-electron interaction and electron exchange-correlation effects, respectively. The cut-off energy was set to be 500 eV for plane-wave expansion for wave function. Models containing θ′ and C phases were constructed based on the experimental matrix/precipitate orientation relationship $(0\ 0\ 1)_{\theta'}//(0\ 0\ 1)_{Al}$, $[1\ 0\ 0]_{\theta'}//[1\ 0\ 0]_{Al}$; $(010)_C//(0\ 0\ 1)_{Al}$, $(001)_C//(1\ 0\ 0)_{Al}$[145]. The dimensions of each model parallel to the interfacial plane (cell vectors **a** and **b**) were expanded, resulting in a 2 × 2 geometry with dimensions $|\mathbf{a}| = 2a_{Al}$ and $|\mathbf{b}| = 2a_{Al}$. In this condition, the mismatch of θ′ with aluminum matrix is 1.18%, indicating the constructed

interface is reliable. The Brillouin zone was sampled with Gamma-center scheme using the *k*-points grid of 17×17×17 for bulk, 3×3×1 and 5×5×1 for relaxation calculation and total energy calculations, respectively.

In addition, the formation energy per atom were calculated used the following formula:

$$\Delta E_{ss}^{form}(ModelX) = \frac{E_t - \Sigma N_i E_i}{N} \quad (2\text{-}1)$$

where E_t is the total energy of supercell model, N_i (i = Al, Cu, Mg, Ag and Si) is the number of each type of atoms in the model, E_i represents the energy per atom of pure Al, Cu, Mg, Ag or Si in their standard states, respectively. N is the total number of atoms in the model.

2.7.3 Ab initio molecular dynamics calculations

Formation energy can only compare the formation tendencies of different interface structures and cannot analyze the evolution process of interface structures with different interface structure during thermal exposure. Molecular dynamics simulations can provide insights into the diffusion processes of atoms within interface structures and analyze the evolution of interface structures at high temperatures. Due to the presence of a wide variety of elemental elements in different interface structures in this work, traditional molecular dynamics methods cannot find suitable empirical potentials. Therefore, Ab Initio Molecular Dynamics (AIMD) were employed to analyze the structural evolution process of different interface structures at high temperatures.

As for the AIMD simulations, the time step was 2.0 fs. The structures used for AIMD calculation of AgMg and C interface phases contained 512 and 464 atoms, respectively. The *k*-points grid for the AIMD simulations was set as 1×1×1 due to the large dimensions of the supercell. The melting temperature calculated by AIMD usually differs from the actual melting

temperature[146, 147]. Therefore, the melting temperature of pure Al was predicted through AIMD. The AIMD simulations were performed at different temperatures using 4×4×4 supercell (the total number of Al atom is 256). The results show that the predicted melting temperature of pure Al is between 1073 K (800°C) and 1173 K (900°C). Thus, the temperature used to simulate the structural evolution of the AgMg and C interface phase by AIMD was set as 1073 K, which is close to the actual melting temperature of Al.

Chapter 3. Effect of ageing temper on the heat resistance of Al-Cu-Mg-Ag alloy with different compositions

3.1 Foreword

The Al-Cu-Mg-Ag alloy is an important heat-resistant aluminum alloy material, and its excellent heat resistance mainly originates from the Ω phase with AgMg segregation layer[148]. Artificial ageing heat treatment process not only affects the size and distribution of the Ω phase, altering the room temperature mechanical properties of the Al-Cu-Mg-Ag alloy, but also influences the coarsening rate of the Ω phase, thereby changing the heat resistance of the alloy. Liu et al.[83] indicated that the under-aged Al-Cu-Mg-Ag alloy exhibits superior heat resistance compared to the peak-aged alloy due to the secondary precipitation behavior of Ω phase during high-temperature thermal exposure. However, there has been no investigation on whether over-ageing affects the heat resistance of alloys, and whether varying degrees of over-ageing have different effects on the heat resistance of alloys.

In this study, three groups of Al-Cu-Mg-Ag alloys with different solute contents were employed to investigate the impact of over-ageing heat treatment on alloys with different compositions. The results show that, compared with peak ageing, slight over ageing heat treatment improves the heat resistance of Al-Cu-Mg-Ag alloys, while server over ageing decrease it. Through systematic quantitative characterization, it is demonstrated that the relationship between the size of Ω phase after artificial aging and the critical size of Ω phase at the thermal exposure

temperature ($r^{*}_{thermal}$) is the key factor determining the varying effects of over-aging on heat resistance.

3.2 Mechanical properties of alloys under different ageing conditions

The mechanical properties of the alloys under different ageing conditions are shown in Fig. 3-1. According to the yield strength shown in the Fig. 3-1 and the microhardness of 3# alloy shown in the Fig. 3-2, the 1# and 2# alloy reached peak aging after 2 h of aging at 200°C, while the 3# alloy reached the peak aging after 0.5 h. As illustrated in Fig. 3-1a, the yield strength of 3# alloy in peak-aged state is much higher than that of the other alloys, while the peak-aged strength of 2# alloy with 0.6Ag is slightly higher than that of 1# alloys with 0.4Ag. After thermally exposed at the elevated temperature of 225°C, the trends of yield strength in different alloys remain unchanged. Zhou et al.[149] and Bai et al.[84] reported that properly increasing Ag and Mg could promote the precipitation of Ω phase, thereby synergistically improving the strength and heat resistance of the alloys, which is consistent with the results in this research. In addition, Al-Cu-Mg-Ag alloy is a typical precipitation-strengthened aluminum alloy. The nanoscale strengthening precipitates undergo rapid coarsening during high temperature thermal exposure (above 200°C), leading to the decrease in the strength of the alloys. The faster the coarsening rate of precipitates, the quicker the decrease in both precipitates' number density and volume fraction, resulting in a more pronounced decline in alloy strength. For an alloy with low heat resistance, an abrupt decrease in yield strength can be observed after thermal exposure.

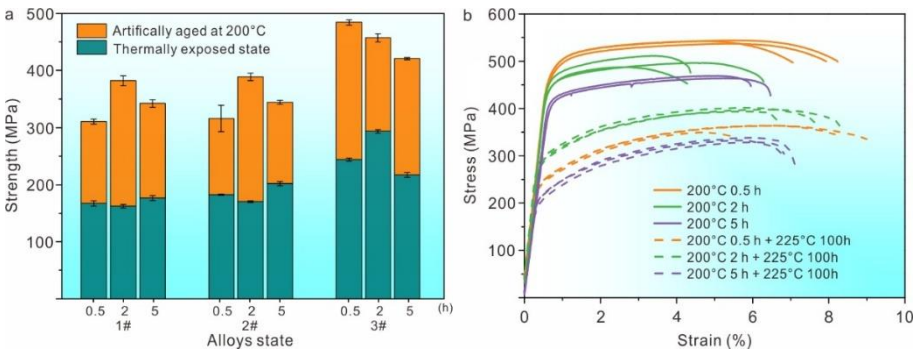

Figure 3-1 Mechanical properties of different alloys under different ageing conditions. (a) The yield strength of the alloys aged at 200℃ (for 30, 120 and 300 min) before and after thermal exposure at 225℃. (b) The typical stress-strain curves of the 3# alloy aged at 200℃ before and after thermal exposure.

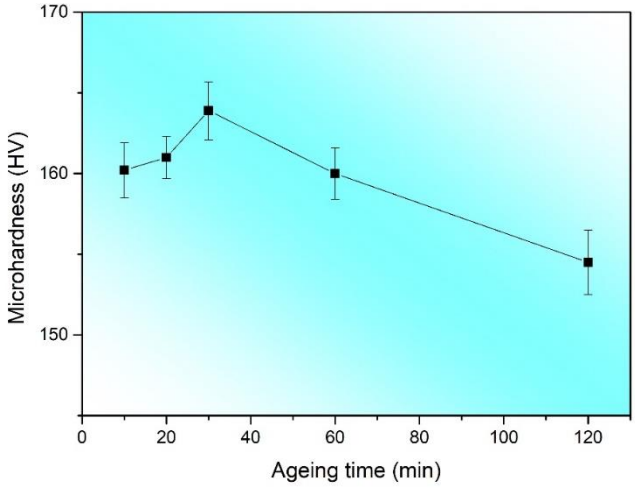

Figure 3-2 Microhardness of 3# alloy aged at 200 ℃ for different times

The strength values of the alloys before and after thermal exposure demonstrate that ageing condition impacts the heat resistance of the alloys. Fig. 3-1a manifests that the yield strength values determined after thermal exposure of the under-aged and slightly over-aged alloys are both higher than those of the peak-aged alloys. However, Fig. 3-1a-b shows that

different extents of over-ageing have different effects on the heat resistance of 3# alloy. That is, after thermal exposure, the slightly over-aged alloy has higher yield strength than the peak-aged alloy, while seriously over-aged state yields lower yield strength compared with the slightly over-aged and peak-aged state. Liu et al.[78] reported that under-aged heat treatment could improve the heat resistance of the alloys compared to peak-aged heat treatment due to secondary precipitations of the precipitate when thermally exposed at a lower temperature than artificial ageing process. In this work, although the thermal exposure temperature is higher than the aging temperature, the presence of excess solute in solid solution also ensures that the under-aged alloy has better thermal stability (in terms of strength) than the peak-aged alloy.

3.3 Nano scale precipitates of different alloys under peak-aged state

In Fig. 3-3, the precipitates of different alloys in peak-aged state along $[110]_{Al}$ zone axis are shown, while Fig. 3-4 displays the atomic resolution HAADF-STEM images of the precipitates.

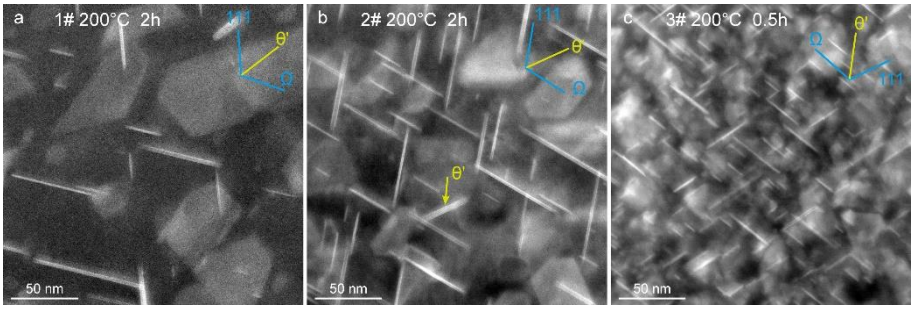

Figure 3-3 HAADF-STEM images of different alloys under peak-aged state. (a) 1# alloy aged at 200℃ for 2 h. (b) 2# alloy aged at 200℃ for 2 h. (c) 3# alloy aged at 200℃ for 0.5 h.

According to the growth direction and atomic arrangement of the precipitates, there are Ω phase with regular AgMg bi-layer at interfaces and θ′-Al_2Cu phase in the alloys under peak-aged state. However, the Ω phase is dominant, namely the size and distribution of Ω phase significantly affect the mechanical property and heat resistance of different alloys.

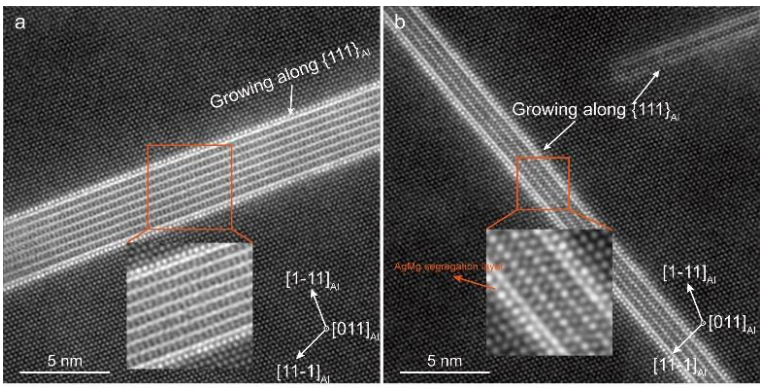

Figure 3-4 Atomic resolution HAADF images of 2# alloy aged at 200℃ for 5 h.

The diameter and thickness of the main strengthening precipitate Ω are statistically shown in Fig. 3-5. The histograms illustrate that increasing Ag content can slightly decrease the size of Ω phase, while increasing the contents of Cu and Mg can significantly decrease the size of Ω phase, thereby increasing the strength of the alloys. To compare the size and quantity of Ω phase more quantitatively in different alloys, the number density and volume fraction of Ω phase were calculated. As shown in Fig. 3-6, according to the $\{111\}_{Al}$ habit plan of Ω phase and $[-110]_{Al}$ zone axis of the observed area, only half of the Ω phase precipitated on $(111)_{Al}$ and $(11\text{-}1)_{Al}$ crystallographic plans, which belong to the {111} crystallographic plane family, is cut vertically by the $(-110)_{Al}$ plane. That is, the other half of Ω phase precipitated on $(-111)_{Al}$ and $(1\text{-}11)_{Al}$ crystallographic planes can

only be observed as an irregular disc shape.

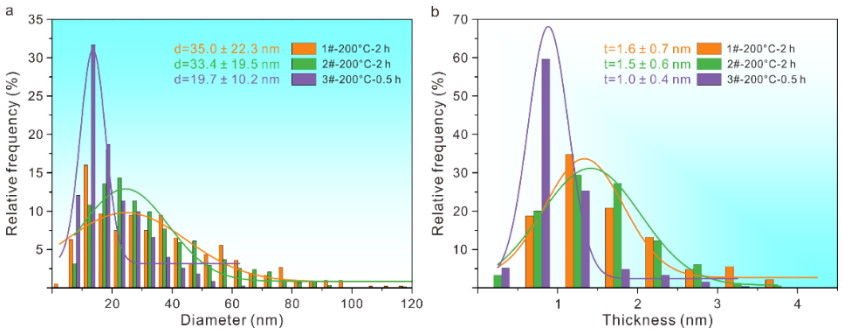

Figure 3-5 Size distribution of Ω phase in different alloys under peak-aged state. The (a) diameter and (b) thickness distribution of Ω phase.

The number of Ω phase (marked with N) cut vertically by the $(-110)_{Al}$ plane can be counted directly through TEM images, while the other part of Ω phase in an irregular shape is difficult to count directly due to weak contrast and overlapping. According to the work of Li et al.[150] and Nie et al.[151], by considering the difference between the thickness of the thin foil TEM sample (T) and the area of the field of view (A_{fov}), the part of Ω phase (marked with $N1$) difficult to count directly can be determined using the following Eq.3-1, and then the number density and volume fraction of Ω phase can be calculated using Eq.3-2 and Eq.3-3.

$$N1 = N\frac{T+d}{\sqrt{A_{fov}}} \tag{3-1}$$

$$n = \frac{N+N1}{A_{fov}(T+d)} = \frac{N(1+\frac{T+d}{\sqrt{A_{fov}}})}{A_{fov}(T+d)} \tag{3-2}$$

$$f_v = nt\frac{\pi d^2}{4} \tag{3-3}$$

where the n and f_v are the number density and volume fraction of Ω phase,

respectively. N and d represent the number and diameter of Ω phase counted in the field of view, respectively, while A_{fov} denotes the area of the field of view. t is the thickness of Ω phase counted in the alloy, which can be seen in Fig. 3-7d. T is the thickness of the field of view in the TEM sample, which is calculated based on the CBED shown in Fig. 3-7a.

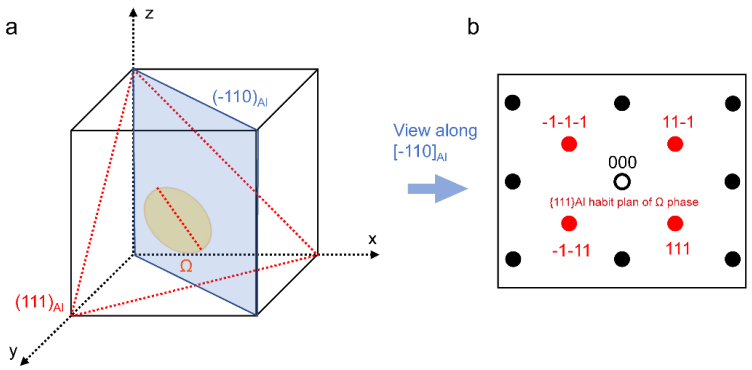

Figure 3-6 Schematic diagram of the orientation relationship of Ω phase in the matrix. (a) The relationship between habit plan of Ω phase and $[-110]_{Al}$ zone axis of the observed area. (b) The simulated diffraction pattern along $[-110]_{Al}$ zone axis.

The number density, volume fraction and corresponding parameters of Ω phase in different alloys under peak-aged state are listed in Tab. 3-1.

Table 3-1 The number density, volume fraction and corresponding parameters of Ω phase in peak-aged state

	1#	2#	3#
d (nm)	35.0 ± 22.3	33.4 ± 19.5	19.7 ± 10.2
t (nm)	1.6 ± 0.7	1.5 ± 0.6	1.0 ± 0.4
T (nm)	102 ± 3.1	129 ± 3.9	137 ± 4.1
n (nm^{-3})	$4.6 \pm 0.6 \times 10^{-6}$	$5.5 \pm 0.5 \times 10^{-6}$	$3.1 \pm 0.1 \times 10^{-5}$
f_v (%)	0.71 ± 0.09	0.72 ± 0.07	0.94 ± 0.05

The number density and volume fraction of Ω phase slightly increase with the increase of Ag content from 0.4% to 0.6%, while a remarkable

increase was observed with the increase of Cu and Mg contents. The trend is contrary to that for the size, in other words, precipitate refinement occurred due to increasing solute contents.

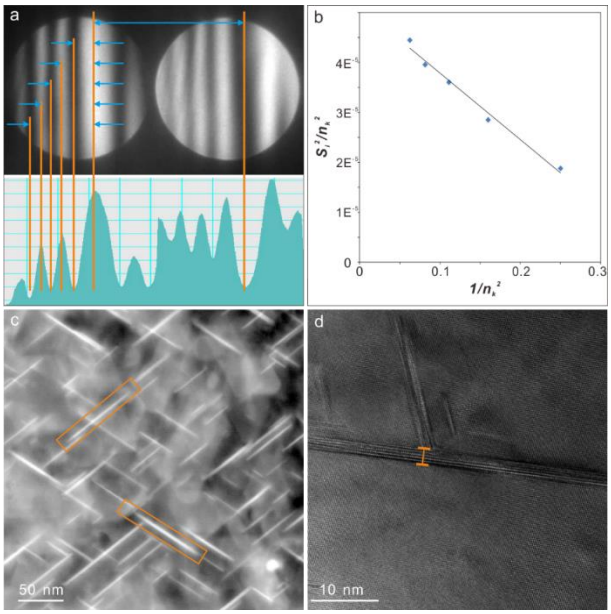

Figure 3-7 (a) The CBED pattern for calculating the foil thickness. (b) The linear fit graph of the relationship between s_i^2 / n_k^2 and $1/n_k^2$. (c) HAADF-STEM image for calculating the number and diameter of the Ω phase. (d) HRTEM image for calculating the thickness of the Ω phase

The characterization results of mechanical properties and microstructure indicate that, compared to simply increasing the Ag element content, simultaneously increasing the Cu and Mg elements can significantly refine the size of precipitates, enhance the density of Ω phase, thereby markedly improving the mechanical properties of the alloy. To analyze whether the strengthening effect mainly comes from the Cu element or the Mg element, the isothermal section of the Al-xCu-yMg-0.6Ag alloy at 520 ℃ were calculated using the Pandat software, as shown

in Fig. 3-8. When the Cu content is higher than 4.2 wt.%, the excess Cu will be consumed in the formation of the equilibrium θ-Al_2Cu. Therefore, the dissolved Cu content in the aluminum matrix of different alloys may be at the same level, namely the differences in the size and number density of Ω phase in the different alloys are mainly due to the content of Mg and Ag. Bai et al.[82, 84] demonstrated that increasing the content of Mg and Ag can both elevate the number density of Mg-Ag co-clusters and inhibit the formation of GP zones. Therefore, increasing the content of Mg and Ag can promotes the precipitation of Ω phase, while inhibiting the formation of θ′-Al_2Cu phase. In addition, the thermal stability of Ω phase is higher than that of θ′-Al_2Cu due to the existence of AgMg segregation layer, implying that increasing the content of Ag and Mg element could improve both the strength and heat resistance of the alloy by promoting the precipitation of the Ω phase.

Comparing 1# and 2# alloys, increasing the content of Ag enhanced the number of Mg-Ag clusters, thus increasing the number density of Ω phase after artificial ageing. However, the low Mg content restricts the formation of Mg-Ag atomic clusters, resulting in the slight enhancements in the strength and heat resistance of 2# alloy. As for the 3# alloy, simultaneous increments in Mg and Ag content result in a significant augmentation of Mg-Ag co-clusters, consequently enhancing the nucleation sites of Ω phase, thereby refining the size of Ω phase, and significantly improving the strength and heat resistance of the 3# alloy. In addition, Liu et al. [83] reported that increasing Mg content could accelerate the ageing process and refine the Ω phase at the same time, thereby increasing the number density of Ω phase. As depicted in Figs. 3-1 and 3-5, the ageing process was significantly accelerated, while the size of Ω phase was greatly refined in the 3# alloy, in comparison to alloys 1# and

2#. A formula to describe the strengthening contribution by nanoprecipitates was established by Nie et al. [152]:

$$\Delta\tau = \frac{Gb}{2\pi\sqrt{1-\nu}}\left(\frac{1}{\frac{0.959}{\sqrt{nd}} - \frac{\pi d}{8} - 0.919t}\right)\ln\frac{1.061t}{b} \qquad (3\text{-}4)$$

where $\Delta\tau$ represents the increment in critical resolved shear stress (CRSS), G is the shear modulus of the aluminum matrix, b is the magnitude of the Burgers vector of the slip dislocations and ν is Poisson's ratio. According to this formula, the contribution of the shearable precipitates formed along {111} plane to the CRSS was relevant to the size and number density of the precipitates. In this study, G, b and ν were set as 25 GPa, 0.286 nm and 1/3, respectively [151, 152]. Based on the number density, diameter, and thickness of Ω shown in Tab. 3-1, the $\Delta\tau$ in 1#, 2# and 3# alloys are 41, 43 and 61 MPa, respectively. Therefore, the yield strength of 3# alloy with the highest density of Ω phase is much higher than that of the other alloys under peak ageing.

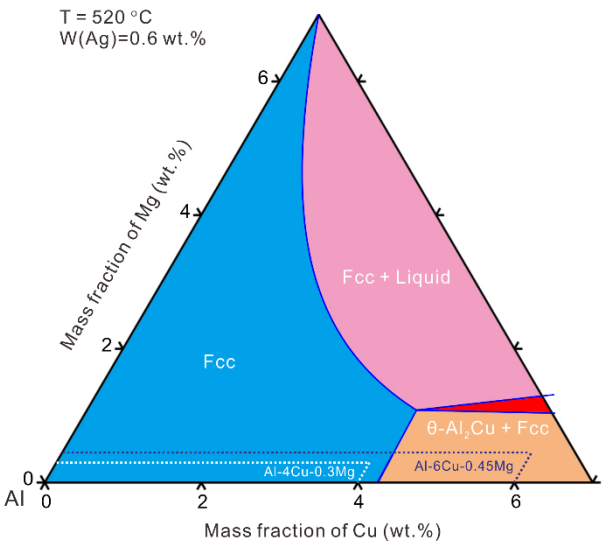

Figure 3-8 Isothermal section of Al-Cu-Mg-0.6Ag alloy at 520°C

3.4 Size change of precipitate in the different alloy under different ageing condition before and after thermal exposure

Figs. 3-9 and 3-10 are HAADF-STEM and HRTEM images of 3# alloy under different heat treatment conditions. The characterization results reveal that the main precipitate in the 3# alloy is still Ω phase, accompanied by a small amount of the equilibrium phase θ-Al_2Cu. The main precipitates of 1# and 2# alloys before and after thermal exposure are consistent with those of 3# alloy, which are all Ω phase. Therefore, the main strengthening phase in the three groups of alloys after thermal exposure is still the Ω phase. In order to analyze the effect of the over-aging state on the size change of the Ω phase, based on the HAADF-STEM and HRTEM images of the Ω phase under different heat treatment states, the diameter and thickness of the Ω phase of the three groups of alloys in the peak aging and over-aging states before and after thermal exposure were statistically analyzed, and the diameter and thickness distribution results are shown in Figs. 3-11 and 3-12. The statistical results show that the larger-sized Ω phase in the over-aged state exhibited a slower coarsening rate during thermal exposure, resulting in final sizes smaller than those in the peak-aged state in the 1# and 2# alloys. As for the 3# alloy, the statistical results manifest that the extent of over ageing also influences the final sizes of Ω phase, that is, the size of Ω in slightly over-aged (aged at 200℃ for 0.5 h) state is smaller than those in peak-aged (aged at 200℃ for 2 h) and seriously over-aged (aged at 200℃ for 5 h) conditions after thermal exposure.

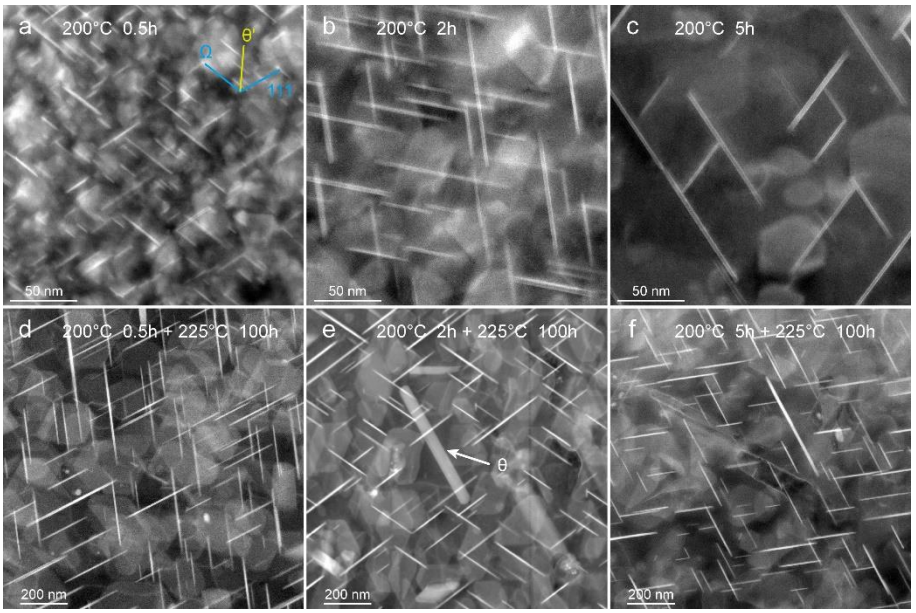

Figure 3-9 HAADF-STEM images of 3# alloys under different ageing states, taken along $[110]_{Al}$ zone axis.

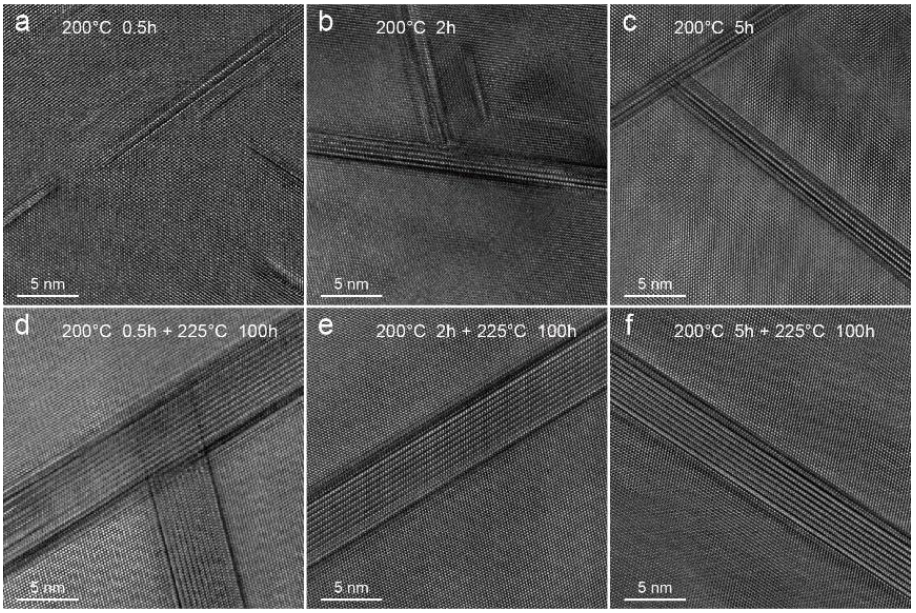

Figure 3-10 HRTEM images of 3# alloys under different ageing states

The relationship between the diameter and thickness of Ω and the mechanical properties of different alloys under different ageing states is shown in Fig. 3-13. The results reveal that the 3# alloy, with higher solute element contents, exhibits higher mechanical properties than 1# and 2# alloys, even when the sizes of Ω are similar. This is attributed to the higher number density of Ω phase facilitated by the elevated solute element content, thereby enhancing the alloy's mechanical properties. Additionally, the size of precipitates determines the mechanical properties of the alloy within the same alloy. Specifically, the smaller the sizes of Ω, the higher the number density of Ω, resulting in higher mechanical properties of the alloy.

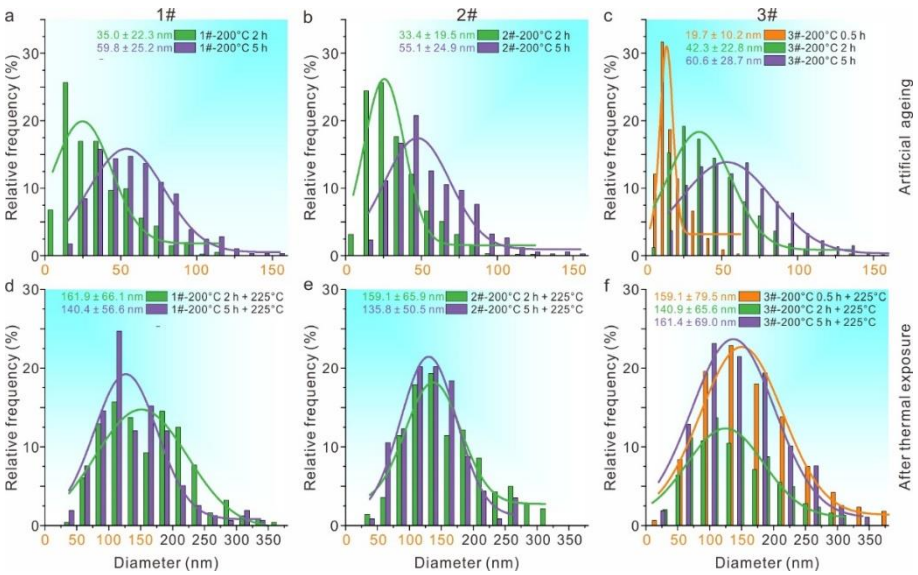

Figure 3-11 Diameter change of Ω phase in the different alloys under different aged state before and after thermal exposure. (a-c) The diameter distribution of Ω phase in the 1#, 2# and 3# alloys under artificial ageing condition, respectively. (d-e) The diameter distribution of Ω phase in the 1#, 2# and 3# alloys after thermal exposure, respectively.

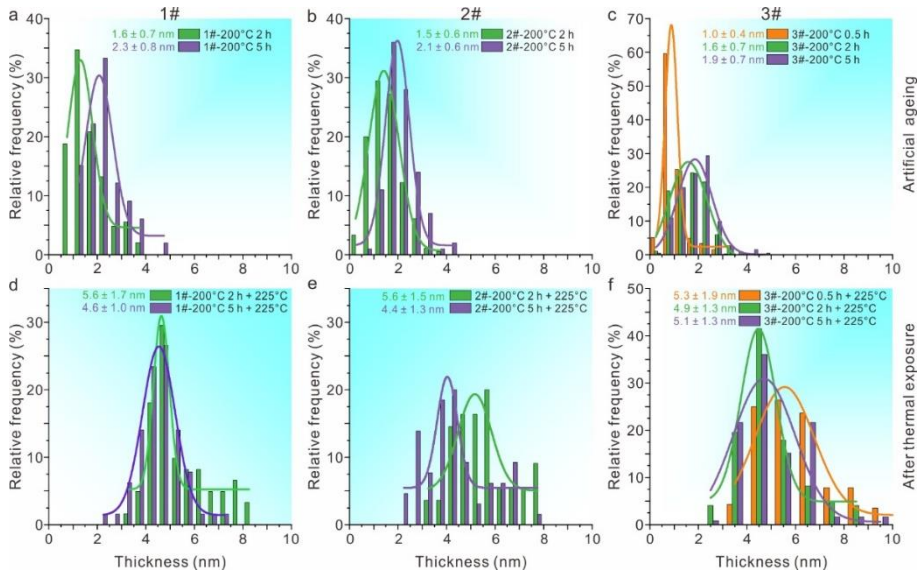

Figure 3-12 Thickness change of Ω phase in the different alloys under different aged state before and after thermal exposure. (a-c) The thickness distribution of Ω phase in the 1#, 2# and 3# alloys under artificial ageing condition, respectively. (d-e) The thickness distribution of Ω phase in the 1#, 2# and 3# alloys after thermal exposure, respectively.

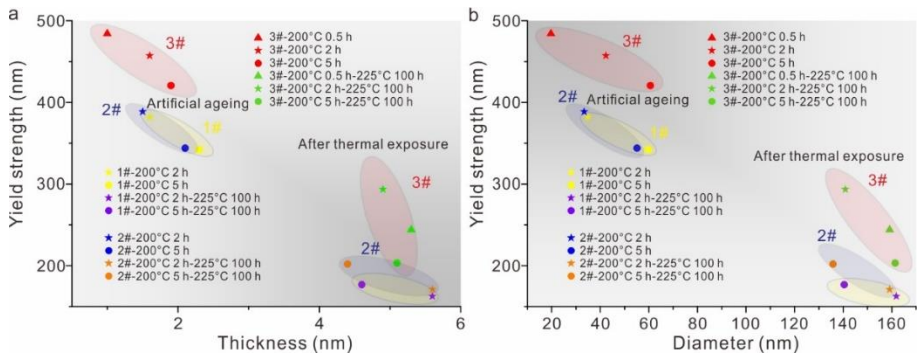

Figure 3-13 The relationship between Ω phase size and mechanical properties in different alloys. (a) thickness. (b) diameter.

To analyze the effect of over ageing extent on the heat resistance of the alloy, the diameter, thickness, and corresponding aspect ratio of Ω

phase before and after thermal exposure were measured, as shown in Tab. 3-2. Yu et al.[148] deemed that the larger aspect ratio of Ω in the over-aged sample (compared to that in peak-aged sample) contributed to the slower growth of Ω phase. The work of Hutchinson et al.[9] showed the thickening rate of Ω phase was very slow when ageing temperature was under 200℃, suggesting a gradual increase in the aspect ratio of Ω during the artificial ageing process. In this work, the aspect ratio of Ω phase in the 3# alloy increased gradually with ageing time, while the yield strength of thermally exposed 3# alloy increased with ageing time first and then decreased. That is, the seriously over-aged alloy with larger aspect ratio exhibits poorer heat resistance than the slightly over-aged alloy, which cannot be explained by the conclusion drawn by Yu et al.[148]. The critical size of a precipitate, which neither grows nor dissolves during the artificial ageing process, can be calculated by the following equation proposed by Grong et al.[153] based on Gibbs-Thomson relationship [154]:

$$r^* = \frac{2\gamma V_{at}}{R_B T} \cdot \left[\ln \frac{C_m}{C_e} \right]^{-1} \tag{3-5}$$

where r^* is critical size (in this work, it mainly represents the diameter of Ω phase), γ is the interface energy of the precipitate, V_{at} is the mean atomic or molar volume of the precipitate. R_B is the universal gas constant and T is the temperature. C_m is the average solute concentration in matrix and C_e is the solute concentration at a planar interface in the matrix in equilibrium with the precipitate of infinite radius. According to the equation, r^* depends on the C_e which is related to temperature, namely the stability of the precipitates is sensitive to the changes of temperature during ageing process. Therefore, the coarsening rate of Ω phase with different mean size in thermal exposure heat treatment may be related to the critical size of Ω phase at thermal exposure temperature ($r^*_{thermal}$).

Table 3-2 The size parameters of Ω phase in 3# alloy under different ageing conditions

	Aged 0.5 h	Aged 2 h	Aged 5 h
d (nm)	19.7 ± 10.2	42.3 ± 22.8	60.6 ± 28.7
t (nm)	1.0 ± 0.4	1.6 ± 0.7	1.9 ± 0.7
Aspect ratio	20 ± 13	26 ± 18	32 ± 19

3.5 Effect of precipitates size on the heat resistance of alloys

As mentioned above, the stability of the Ω is sensitive to the temperature during ageing process, and the coarsening rate of Ω phase in thermal exposure heat treatment may be related to the critical size of Ω phase at thermal exposure temperature ($r^*_{thermal}$). The 1# and 2# alloys achieved the peak-aged state following aging at 200℃ for 2 h, while the 3# alloy reached the peak-aged state after aging at 200℃ for 0.5 h. Additionally, considering the accelerating effect of elevated aging temperature on the aging process[155], the 1#, 2# and 3# alloys have reached peak-aged state (or slightly over-aged) after ageing at 225℃ (thermal exposure temperature) for 2 h, 2 h and 0.5 h, respectively. In this study, $r^*_{thermal}$ is close to the size of the precipitate in the peak-aged state at thermal exposure temperature. Therefore, the size of Ω phase aged at 225℃ for 2 h, 2 h and 0.5 h can be seen as the $r^*_{thermal}$ in the 1#, 2# and 3# alloy, respectively. The statistic results in Fig. 3-14 indicate that the size of Ω phase aged at 200℃ for 5 h is close to the $r^*_{thermal}$ in the 1# and 2# alloys, while the size of Ω phase aged at 200℃ for 2 h is close to that aged at 225℃ for 0.5 h in the 3# alloy. Therefore, the size of Ω phase reach $r^*_{thermal}$ after a slight over-ageing process at lower ageing temperature.

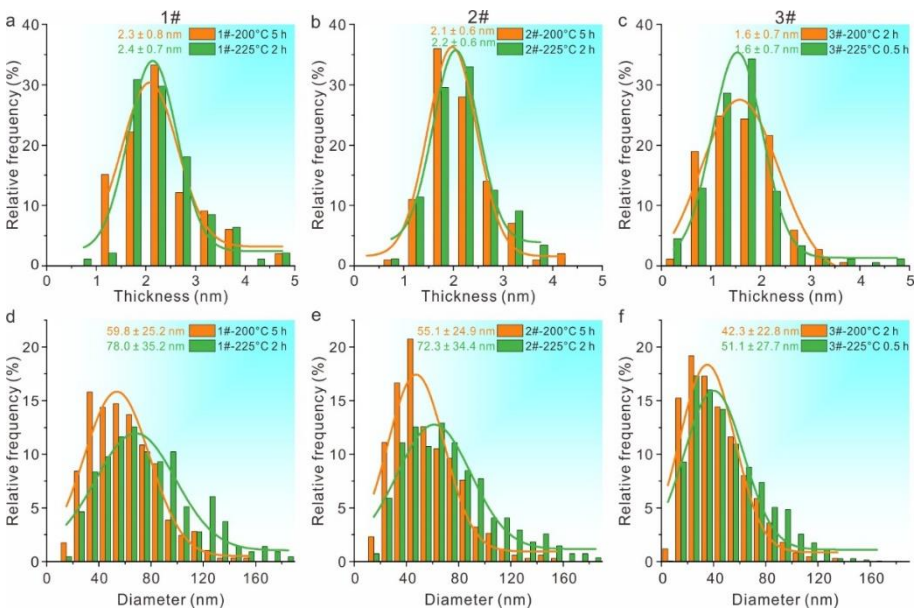

Figure 3-14 Size change of Ω phase in different alloys under different condition. (a-c) The diameter distribution of Ω phase in the 1#, 2# and 3# alloys under slightly over-aged at ageing temperature and near peak-aged at thermal exposure temperature, respectively. (d-e) The thickness distribution of Ω phase in the 1#, 2# and 3# alloys under slightly over-aged at ageing temperature and near peak-aged at thermal exposure temperature, respectively.

The schematic diagram of the size changes of precipitates in the alloy aged at different temperatures is shown in Fig. 3-15, based on Kampmann-Wagner-Numerical (KWN) modeling [156]. As peak ageing, slight over-aging and severe over-aging conditions exist simultaneously in 3# alloy, the 3# alloy is used to analyze this schematic. According to the small green and purple arrows in Fig.3-15, when the 3# alloys were aged at 200℃ for 2 h (slight over-ageing) and 5 h (sever over-ageing), the sizes of Ω phase are similar to or larger than $r^{*}_{thermal}$ before thermal exposure. According to the larger green and purple arrows, these Ω phases will coarsen very gradually at the same coarsening rate as the precipitate aged at elevated

thermal exposure temperature (along the red line). Furthermore, when the coarsening rates of Ω phase are in the same level, the larger the original size of Ω phase before thermal exposure, the larger the final size after the same thermal exposure time. According to Tab. 3-2, the size of Ω in the seriously over-aged alloy (aged at 200℃ for 5 h) is larger than that in the slightly over-aged alloy (aged at 200℃ for 2 h) during artificial ageing process. As a result, under the premise that the coarsening rates of Ω phase in the two over-aged alloys are in the same, the size of the Ω phase in the seriously over-aged alloy is still larger than that in the slightly over-aged alloy after the same period of thermal exposure heat treatment. Therefore, the larger size Ω phase in the seriously over-aged alloy leads to a lower yield strength and heat resistance than slightly over-aged alloy after thermal exposure.

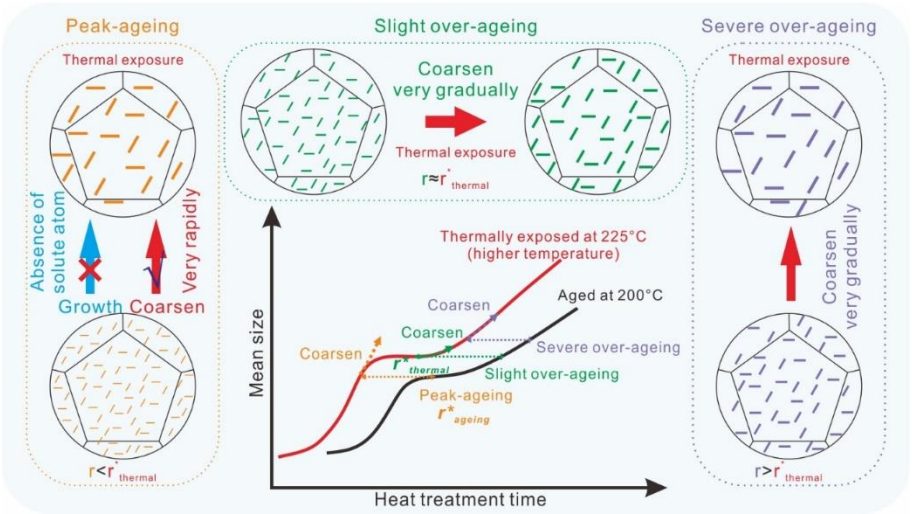

Figure 3-15 Schematic diagram of the size changes of precipitates before and after thermal exposure at an elevate temperature.

As for the 3# alloy aged at 200℃ for 0.5 h, the alloy reached peak-aged state and most of the solute elements had been used to form Ω phase ,

there were no excess solute elements in the matrix for the growing of Ω phase during thermal exposure, which resulted in the Ω phase being unable to grow to the $r^*_{thermal}$ at a normal rate. However, as indicate by the small orange arrow, the size of Ω phase in the peak-aged alloy is much smaller than $r^*_{thermal}$. To quickly reach the critical size, part of the Ω phase will dissolve and then provide solute atoms for the growth of other Ω phase. The solubility of the precipitate (C_r) with radius r can be described by Gibbs-Thomson relationship (Eq. 3-6)[154], which reveals the precipitates with smaller size are more easily dissolved into the matrix.

$$C_r = C_e\left[1+\frac{2\gamma V_{at}}{R_B T}\cdot\frac{1}{r}\right] \tag{3-6}$$

In Fig. 3-16, it is shown that the size of most Ω phases in peak-aged alloy is much smaller than the average size. Therefore, in the peak-aged alloy, most of Ω phase with small size are more likely to dissolve during the thermal exposure, resulting in the significant decrease of number density of Ω phase. Furthermore, the excess solute elements from the dissolution of the small Ω phase are then used for the coarsening of larger undissolved precipitates. As illustrated by the larger orange arrow in Fig. 3-15, the excess solute elements elevate the coarsening rate of the Ω phase, which is significantly higher than the normal coarsening rate indicated by the red line. Consequently, there is a significant coarsening of the Ω phase after thermal exposure.

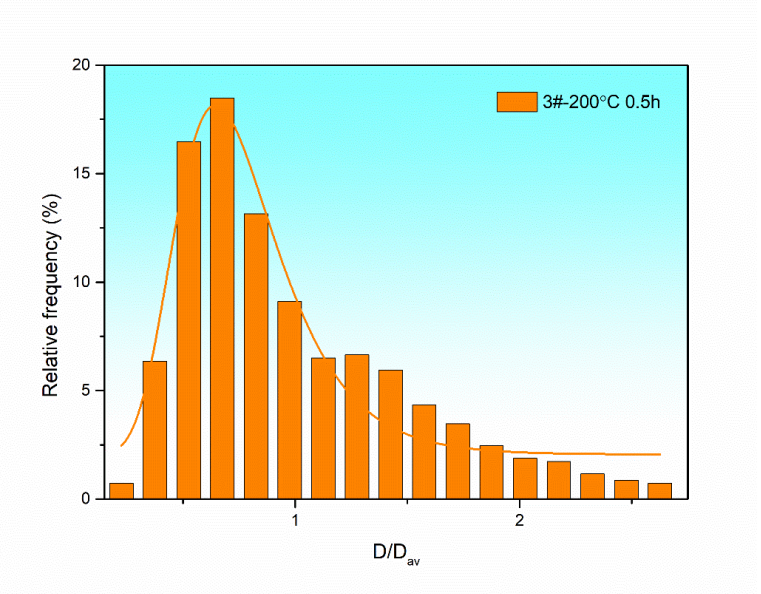

Figure 3-16 The diameter distribution of Ω phase in the different peak-aged alloy. D_{av} is the average diameter of Ω phase.

3.6. Summary of this chapter

The effect of ageing temper on the heat resistance of Al-Cu-Mg-Ag alloys with different solute elements was investigated by tensile tests, TEM and CALPHAD. The conclusions are as follows:

(1) Increasing Ag and Mg contents could simultaneously increase the yield strength and heat resistance of Al-Cu-Mg-Ag alloys due to its promoting and refinement effect on the precipitation of Ω phase.

(2) The over ageing significantly affects the heat resistance of different Al-Cu-Mg-Ag alloys even when the solute contents are significantly different. Specifically, mechanical performance testing results indicate that, compared to peak ageing, slight over ageing heat treatment improves the heat resistance of Al-Cu-Mg-Ag alloys, while server over ageing decrease it.

(3) By combining systematic statistical quantitative characterization with guidance from the KWN modeling, the critical size of Ω at high thermal exposure temperature ($r^*_{thermal}$) is clarified to be the key factor influencing the coarsening of Ω. The closer the size of Ω phase in the aging state is to $r^*_{thermal}$, the better the heat resistance of the alloy will be. Therefore, the heat resistance of the alloy can be improved by adjusting the aging process to tune the size of the Ω phase to be close to the critical size at service temperature.

Chapter 4. Synergy of multiple precipitate/matrix interface structures for a heat resistant high-strength Al alloy

4.1 Foreword

Aluminum alloys are widely used in in aerospace, automotive and other industries due to their outstanding combination of low density, high specific strength, excellent corrosion resistance and high fracture toughness[157, 158]. There exists trade-off between strength and heat resistance of various aluminum alloys. The nano-precipitates with high number densities in high-strength aluminum alloys, such as Al-Cu-based, Al-Zn-Mg-Cu-based, and also in medium-strength Al-Mg-Si-based alloys, will rapidly coarsen during service within the medium and high temperature ranges, resulting in the deterioration of the alloys' strength[42, 159-161]. On the other hand, aluminum alloys with high heat resistance, such as Al-Mn-based, Al-Si-based alloys, Al-Mg_2Si metal matrix composite (MMC) contain submicron to micron-scale dispersed phases as the main strengthening phase, leading to their relatively low strength[162, 163]. Therefore, achieving a synergistic improvement in both strength and heat resistance of aluminum alloys crucially depends on enhancing the thermal stability of precipitates in high-strength aluminum alloys.

In this study, through CALPHAD, the elements type and content in Al-Cu-Mg-Ag alloys were controlled to construct multiple interface segregation structures at θ′/Al interfaces, effectively inhibiting the coarsening of θ′-Al_2Cu. In addition, combined with multiscale characterization and first-principles calculations, it was confirmed that the

existence of multiple interface segregation structures is the main reason for the high thermal stability of the θ′-Al_2Cu phase. The designed alloy maintained a yield strength of 400 MPa after thermal exposure at 200°C for 100 h. Furthermore, the concept of constructing multiple segregation structures at the precipitate/matrix interface was proposed, providing a new strategy for the design of other heat-resistant materials.

4.2 Design of the Al-Cu-Mg-Ag-Si-Sc alloy with multiple interface segregation structures

4.2.1 Guidelines for alloy composition design

Achieving synergistic enhancement of strength and heat resistance in aluminum alloys requires high strength before service. Therefore, agehardenable aluminum alloys with high-density precipitates are the main materials for achieving synergistic enhancement of strength and heat resistance. To improve the heat resistance of agehardenable aluminum alloys, researchers[97, 99] have attempted to construct segregation layers at the precipitates/matrix interface to hinder the coarsening of precipitates under high-temperature service conditions and improve the heat resistance of the alloy. In many studies on Al-Cu-based alloys, it was found that Sc preferred to segregate at the θ′/Al interface during artificial ageing in Al-Cu-Sc alloy and improved the thermal stability of θ′-Al_2Cu precipitates[86, 97, 99, 115, 164]. In Al-Cu-Mg-Ag alloys, a AgMg segregation layer exists at the Ω/Al interface, effectively inhibiting the coarsening of Ω phase and improving the heat resistance of the alloy[165, 166]. Hutchinson et al.[9] found that the AgMg segregation layers could hinder the coarsening of the precipitates due to the retarded diffusion of solutes when the thermal exposure temperature was below 200°C, thereby improving the thermal stability of the alloy. However, when the thermal exposure temperature

was higher than 200°C, the ledges with 1/2Ω unit cell in height were more likely to form at the Ω/Al interface, which would increase the thickening kinetics of Ω phase. That is, such a single segregation structure at the precipitates/matrix interface still cannot effectively hinder the coarsening of the precipitates.

The synergistic precipitation of multiple heat-resistant structures, especially the construction of multiple interface segregation structures at the precipitate/matrix interface, is crucial for further enhancing the heat resistance of the alloy. However, research by Bai et al.[101] has shown that adding Sc to Al-Cu-Mg-Ag alloys reduces both the strength and heat resistance of the alloy. Furthermore, EDX results indicated no significant Sc segregation at Ω/Al interfaces after thermal exposure. Therefore, it is not possible to construct multiple segregation structures containing both Sc and AgMg segregation layers at Ω/Al interfaces. Gable et al.[119] and Gariboldi et al.[167] demonstrated that adding Si to Al-Cu-Mg-Ag alloys inhibits the precipitation of Ω phase and promotes the precipitation of θ′-Al_2Cu phase. At the same time, segregation layers rich in AgMg elements and the C-$AlMg_4Si_3Cu$ phase precipitated, forming a multiple interface segregation structure at θ′/Al interfaces. That is, adding Si to Al-Cu-Mg-Ag alloys promotes the formation of multiple interface segregation structures at θ′/Al interfaces and provides a possibility for further increasing the Sc segregation layer. When Si is added to Al-Cu-Mg-Ag alloy, Si can also promote the formation of C-$AlMg_4Si_3Cu$ phase or disordered L phase[112, 167]. Marioara et al.[168] reported that the disordered L-AlMgSiCu phase exhibits excellent thermal stability, and the precipitation of a high-density L phase can enhance the thermal stability of the alloy. In addition, the preferentially precipitated C/L-AlMgSiCu[169] phase can act as heterogeneous nucleation sites to promote the nucleation of θ′-Al_2Cu, thus

achieving the synergistic enhancement of heat resistance and strength in Al-Cu-Mg-Ag-Si-Sc alloys. To achieve various heat-resistant structures, especially multiple interface structures at θ′/Al interfaces, the difficulties mainly lie in two aspects: (1) selecting an appropriate amount of Sc addition to avoid formation of AlCuSc intermetallic which will consume the Cu solutes; (2) designing the exact concentrations of Mg, Si and Ag for turning Ω precipitate into θ′ and C/L phase and promoting the formation of multiple structures such as C/L phase and AgMg layers at the θ′/Al interface.

4.2.2 CALPHAD

The contents of Cu, Mg, Si, Ag and Sc were reasonably determined by CALPHAD. All the thermodynamic calculations were performed in Thermo-Calc (TC) software based on the multicomponent multiphase thermodynamic database for Al alloys (TCAL5)[141, 170]. The design principles are as follows: (1) the formation of AlCuSc phase during the homogenization should be avoided to ensure that the main alloying elements such as Cu and Sc are mostly dissolved into the matrix; (2) the generation of harmful precipitates such as S-Al_2CuMg at high temperatures should be inhibited during thermal exposure, meanwhile the Ω precipitate which is not heat resistant enough should be suppressed. (3) the formation of multiple types of structures such as C/L interface phase, AgMg-rich and Sc-rich segregation layers at the interface of θ′/Al is attempted. The specific calculation process of alloy design by CALPHAD is described as follows:

(1) Control of Cu content. As shown in Fig. 4-1a, when Cu content of an Al-*x*Cu alloy is set as 5 wt.%, the liquid phase is generated when the temperature is above 557°C while the equilibrium phase θ-Al_2Cu will be

produced when the temperature is below 532℃. Therefore, the homogenization temperature should be selected between 532-557 °C to ensure that Cu can be completely dissolved into the Al matrix. However, due to the narrow temperature range, it is easy to cause over-burning or insufficient homogenization due to the temperature deviations and fluctuations during the homogenization process. Therefore, it is necessary to reduce the Cu content to obtain a wider homogenization temperature range. When Cu content is 4 wt.%, the homogenization temperature could be selected from 507°C to 571°C, which is wider than that for Al-5Cu alloy. Hence, the Cu content is set as 4 wt.%. The specific homogenization temperature is set as 540°C, close to the average value of the temperature range.

(2) Control of Sc contents. As the homogenization temperature is 540°C, the ternary isothermal section of Al-Cu-Sc system is calculated at 540°C as shown in Fig. 4-1b. When the content of Cu is 4 wt.%, the maximum solid solubility of Sc element in the Al-Cu-Sc alloy is 0.09 wt.%. In order to suppress the formation of AlCuSc which will consume Cu during the homogenization heat treatment, the content of Sc in the currently designed alloy is set as 0.09 wt.%.

(3) Control of Ag contents. When it comes to the Ag content, although it has a high solid solubility in the aluminum matrix at 540°C, its content should be controlled at the thermal exposure temperature 210°C to avoid the formation of equilibrium phase named HCP_AlAg. According to the Fig. 4-1c, HCP_AlAg will be generated when the content of Ag is above 0.51 wt.% in the case of 4 wt.% Cu. Therefore, the content of Ag in the currently designed alloy is set as 0.5 wt.%.

(4) Control of Mg and Si contents. In order to obtain θ'-Al_2Cu precipitates with Sc and AgMg segregation layers in Al-Cu-Mg-Ag-Si-Sc

alloy, it is necessary to control the Mg/Si ratio to promote the precipitation of θ'-Al_2Cu while inhibiting the formation of Ω.

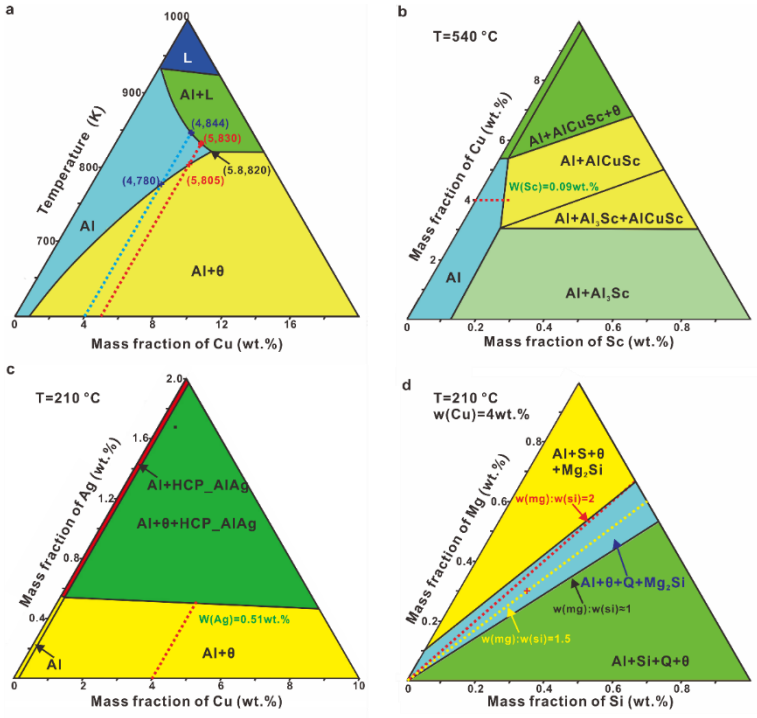

Figure 4-1 (a) Vertical section phase diagram of the Al-Cu binary alloy. (b) Ternary isothermal section of Al-Cu-Sc system at 540 °C. (c) Ternary isothermal sections of Al-Cu-Ag systems at 210 °C. (d) Isothermal sections of Al-Mg-Si-4Cu systems at 210 °C

Gable et al.[119] reported that when the Mg/Si mass ratio is below 2, the Ω precipitate in the Al-Cu-Mg-Ag alloy will be completely suppressed. Therefore, the composition should be below the red dotted line representing the Mg/Si mass ratio of 2 in Fig. 4-1d. In addition, the content of Mg should be higher than that of Si (i.e., above the phase boundary indicated by the black arrow) to ensure that there is no silicon particle. Finally, the Mg/Si mass ratio in the currently designed alloy is set as 1.5,

as shown by the yellow dotted line in Fig. 4-1d, which is in the middle of the red dotted line and the black solid line. Meanwhile, the S-Al_2CuMg phase will not be generated in this combination of temperature and composition. It should be noted that the phase equilibria of Al-Mg-Si-4Cu (in wt.%) at 175°C (ageing temperature) is very similar to those in 210°C (thermal exposure temperature).

The Mg content in the currently designed alloy will be divided into two parts. One part is used to form the C-$AlMg_4Si_3Cu$ or L phase (disordered form of C phase), which is the main heat-resistant precipitate. The other part of Mg will participate in the formation of the AgMg segregation layer at the θ′/Al interface. However, there is currently no research report on the composition of the AgMg layer at the θ′/Al interface, although it was indeed found in some conditions[167]. Therefore, the Mg/Ag atomic ratio in the AgMg layer segregated at the θ′/Al interface is based on the ratio reported for the AgMg segregation layer at the Ω/Al interface. Kang et al.[52] constructed a AgMg bi-layer model at the Ω/Al interface, in which the Ag/Mg atomic ratio is about 2:1. However, the APT results of Reich et al.[35] and Bai et al.[44, 171] show that the Ag/Mg atomic ratio in the AgMg layer is about 1:1 in the peak-aged and over-aged states. Therefore, the Ag/Mg atomic ratio is set as 1.5 in this paper, which is the intermediate value between theoretical predictions and experimental results. The AgMg segregation layers were expected, although during the design it was not known what their atomistic structures would be. According to the ratio of each element as mentioned above, the contents (in wt.%) of Mg and Si, i.e., W(Mg) and W(Si), can be calculated according to the following formulas:

$$\frac{W(Mg)_C}{Ar(Mg)} = \frac{4}{3} \times \frac{W(Si)}{Ar(Si)} \qquad (4\text{-}1)$$

$$\frac{W(Mg)_{AgMg}}{Ar(Mg)} = \frac{2}{3} \times \frac{W(Ag)}{Ar(Ag)} \quad (4\text{-}2)$$

$$W(Mg)_C + W(Mg)_{AgMg} = \frac{3}{2} \times W(Si) \quad (4\text{-}3)$$

in which $W(\mathrm{Mg})_C$ is the part of Mg used to form the C-$AlMg_4Si_3Cu$ phase, while $W(\mathrm{Mg})_{AgMg}$ is the other part used to form the AgMg segregation layer at the θ′/Al interface. The relative atomic masses of Mg, Si and Ag are represented by Ar(Mg), Ar(Si) and Ar(Ag), respectively. After calculations, the contents of Si and Mg are set as 0.21 wt.% and 0.315 wt.%, respectively. Therefore, the final alloy composition is determined as Al - 4Cu - 0.315Mg - 0.5Ag - 0.21Si - 0.09Sc (in wt.%).

4.3 Mechanical properties of the designed alloy

Microhardness curve of the designed alloy aged at 175 ℃ is shown in Fig. 4-2. In the early stages of aging, the microhardness of the alloy increased rapidly. After aging at 175 ℃ for 16 h, the microhardness reached its maximum value of 149.4 HV, indicating that the alloy was in the peak-aged state. When the alloy was further aged for 32 h, there is only a slight decrease in microhardness, indicating that the alloy exhibits high heat resistance. The peak-aged alloys were thermally exposed at 200 ℃ and 210 ℃ for 100 h, ant the mechanical properties of the alloy before and after thermal exposure are shown in Fig. 4-3. As shown in Fig. 4-3a, compared with the various aluminum alloys thermally exposed at different temperatures for 100 h [59, 149, 159, 160, 162, 172-182], the currently designed alloy shows the best combination of strength and heat resistance after thermal exposure. It reaches a strength retention ratio (the ratio between the yield strength values of an alloy after and before a thermal exposure) of 97% and the highest residual yield strength of 400 ± 5 MPa ever reported for Al alloys thermally exposed at 200°C for 100 h. This means the designed

alloy overcomes the trade-off between heat resistance and strength for different types of aluminum alloys.

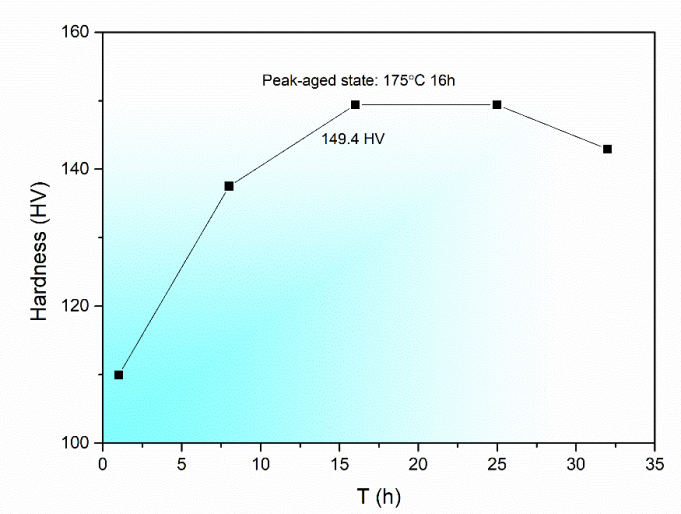

Figure 4-2 The microhardness of the designed alloy aged at 175 °C for different time

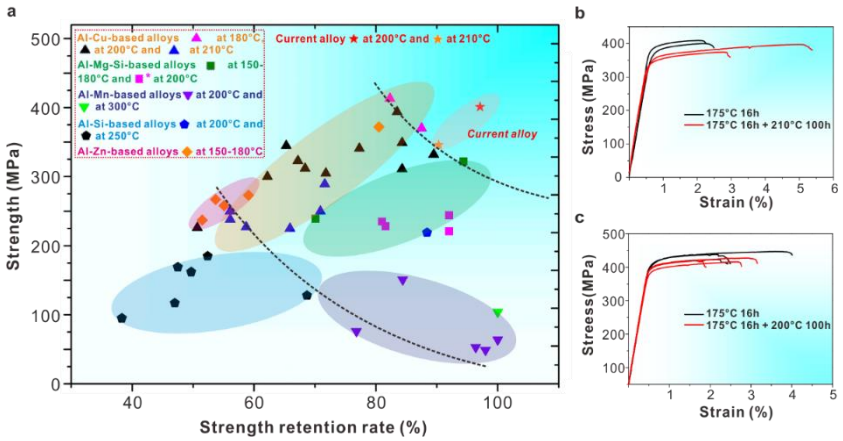

Figure 4-3 (a) The mechanical properties of the designed alloy and the alloys in literatures[149, 159, 160, 162, 172-182] before and after thermal exposure, the specific data are shown in Table 4-1. Stress-strain curves of the designed alloy before and after thermal exposure at (b) 210 °C and (c) 200 °C

Table 4-1 The mechanical properties of Al alloys used in Fig. 4-3a before and after thermal exposure

Composition	YS before (MPa)	YS after (MPa)	Retention ratio (%)	Temperature (℃)
2099-T83[178]	502	413	82.3	180
2397-T87[178]	423	370	87.5	180
AA2618[183]	369	311	84.3	200
2618-AlN[183]	371	332	89.5	200
Al-5.3Cu-0.8Mg-0.5Ag-0.3Mn-0.15Zr[177]	446	226	50.7	200
Al - 4.9Cu - 0.7Mg - 0.36Ag - 0.3Mn - 0.2Zr[149]	456	312	68.4	200
Al - 4.8Cu - 0.8Mg - 0.14Ag - 0.3Mn - 0.2Zr[149]	425	305	71.8	200
Al - 6Cu - 0.6Mg - 0.5Ag - 0.3Mn - 0.2Zr - 0.2Er[172]	441	341	77.3	200
Al - 6.6Cu - 0.6Mg - 0.5Ag - 0.3Mn - 0.14Zr[172]	472	394	83.5	200
Al - 4.72Cu - 0.45Mg - 0.54Ag - 0.17Zr[173]	414	349	84.3	200
Al-5.5Cu-1.0Mg-1.2Ag[174]	481	323	67.2	200
Al - 5.3Cu - 0.8Mg - 0.6Ag - 0.4Mn - 0.1Zr[175]	482	300	62.2	200
Al-5.3Cu-0.8Mg-0.6Ag-0.4Mn-0.1Zr-0.45Ce[175]	528	345	65.3	200
7085-T7651[178]	468	258	55.1	180
7085-T7452[178]	497	267	53.7	180
7075-T7651[178]	460	237	51.5	180
6082[159]	341	322	94.4	150
6082[159]	341	239	70.1	175
Al - Mg - Si[181]	280 (UTS)		81	200
Al - Mg - Si - 0.1La[181]	290 (UTS)		81.6	200
Al - Mg - Si - 0.22La[181]	265 (UTS)		92	200
Al - Mg - Si - 0.32La[181]	240 (UTS)		92	200
Al-12Si-4Cu-1Mg-2Ni[182]		219	88.4	200
AA3004[180]	104	104	100	300

Table 4-1 The mechanical properties of Al alloys used in Fig. 4-3a before and after thermal exposure (continued)

Composition	YS before (MPa)	YS after (MPa)	Retention ratio (%)	Temperature (°C)
Al-1.2Mn-0.75Si-0.75Cu-0.3Mg[176]	179	151	84.4	200
Al - 1.2Mn - 0.75Si - 0.3Mg[176]	99	76	76.8	200
Al - 1.2Mn - 0.75Si - 0.5Cu - 0.1Mg[176]	64	64	100	200
Al-1.2Mn-0.75Si-0.75Cu[176]	55	53	96.4	200
Al-1.2Mn-0.75Si-0.5Cu[176]	50	49	98	200
Al-6.87Si-0.61Mg-0.1Fe[179]	248	95	38.3	250
Al-6.87Si-0.61Mg-0.1Fe-0.1Zr[179]	249	117	47	250
Al-12Si-4Cu-1Mg-2Ni[182]		128	68.6	250
Al - 8.5Si - 1.76Cu - 0.55Mg - 0.32Zr[162]	323	162	49.7	250
Al - 8.4Si - 1.7Cu - 0.6Mg - 0.33Zr - 1.9Ni[162]	354	185	52.4	250
Al - 8.6Si - 1.8Cu - 0.55Mg - 0.33Zr - 0.7Mn[162]	356	169	47.5	250
Al - 4Cu - 0.5Mg - 0.5Ag - 0.19Si - 0.09Sc	405	289	71.4	210
Al - 4Cu - 0.5Mg - 0.5Ag	387	227	58.7	210
Al - 4Cu - 0.28Mg - 0.4Ag	341	225	65.9	210
Al - 4Cu - 0.28Mg - 0.6Ag	352	250	71	210
Al - 4Cu - 0.8Mg - 0.8Ag - 0.2Si - 0.1Sc	424	238	56.1	210
Al - 4Cu - 0.8Mg - 0.8Ag - 0.3Mn - 0.15Zr	446	250	56.1	210
Al - 4Cu - 0.315Mg - 0.5Ag - 0.21Si - 0.09Sc	383	346	90.3	210
Al - 4Cu - 0.315Mg - 0.5Ag - 0.21Si - 0.09Sc	413	401	97.1	200

4.4 Multi-scale microstructure of Al-Cu-Mg-Ag-Si-Sc alloy

4.4.1 Micro-scale structure of alloy before and after homogenization

To verify whether the designed alloy has avoided the excessive formation of AlCuSc intermetallic, SEM characterization was conducted on the alloy before and after homogenization. Fig. 4-4 shows the microscale constituents of the alloy before and after homogenization.

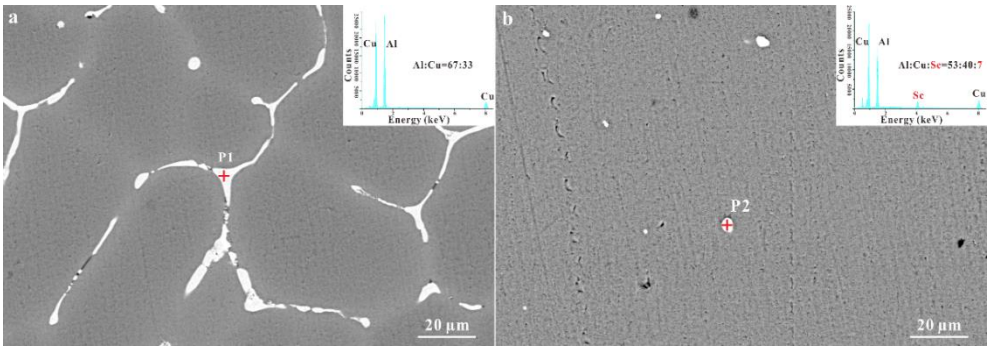

Figure 4-4 Micro-scale constituents in (a) as-cast and (b) homogenization state. The EDX of P1 and P2 are inserted in (a) and (b), respectively

According to Fig. 4-4a, the main microscale constituent is dendritic θ-Al_2Cu phase in the as-cast alloy. After homogenization at 540 ℃ for 16 h, most of dendritic constituents had dissolved into the matrix, leaving only a small amount of point-like microscale constituents in the alloy. Further combined with the EDX results, the point-like constituents is recognized as AlCuSc phase, indicating the presence of a small amount of microscale AlCuSc phases in the alloy. According to Tab. 2-1 in Chapter 2, the detected composition of the melted alloy is Al - 4.15Cu - 0.30Mg - 0.47Ag - 0.17Si - 0.10Sc. The actual Sc content is 0.1 wt.%, exceeding the

maximum solubility limit at the homogenization temperature. Excess Sc will combine with Cu during the homogenization heat treatment, resulting in the formation of a small amount of point-like AlCuSc phase.

4.4.2 Nano-scale structure of alloy in the peak aged state

The mechanical properties of the designed alloy before and after thermal exposure demonstrated that it has high heat resistance. To analyze the reasons for the improvement of heat resistance, the size distribution of the main strengthening phase θ′-Al_2Cu before and after thermal exposure of the alloy under peak aging state was statistically analyzed, and the results are shown in Fig. 4-5.

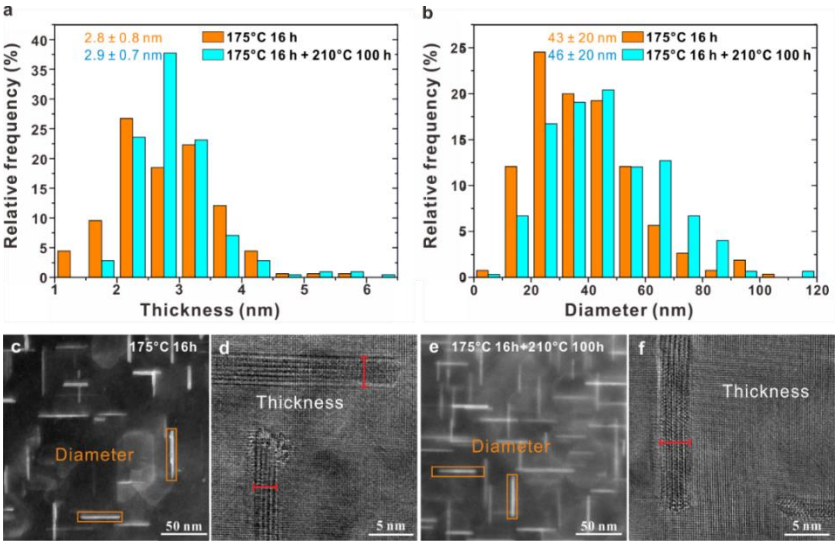

Figure 4-5 (a) Thickness distribution histogram of θ′-Al_2Cu before and after thermal exposure. (b) Diameter distribution histogram of θ′-Al_2Cu before and after thermal exposure. (c) HAADF-STEM image used to count the diameter of θ′-Al_2Cu in the peak-aged alloy. (d) HRTEM image used to count the thickness of θ′-Al_2Cu in the peak-aged alloy; (e) HAADF-STEM image used to count the diameter of θ′-Al_2Cu in the alloy after thermal exposure; (f) HRTEM image used to count the thickness of θ′-Al_2Cu in the alloy after thermal exposure

The quantitative statistical results show that the average thickness values of θ′-Al_2Cu before and after thermal exposure are 2.8 ± 0.8 nm and 2.9 ± 0.7 nm, while those values for diameter are 43 ± 20 nm and 46 ± 20 nm, respectively. The statistical results show that the main strengthening phase θ′-Al_2Cu has not been obviously coarsened after thermal exposure, explaining the alloy's high strength retention rate shown in Fig. 4-3a.

To further analyze the high thermal stability of the main strengthening phase θ′-Al_2Cu during thermal exposure, the microstructures of the peak aged alloy at the nanometer to atomic scale were characterized. Fig. 4-6 shows the APT results of the designed alloy in the peak-aged state. The iso-surface maps of different elements demonstrate that, in addition to the plate-shaped θ′-Al_2Cu phase, there are also nanoscale precipitates containing Mg, Si, and Cu elements in rod-like or plate-like shapes, as well as nanoscale precipitates containing Mg and Ag elements. Part of these precipitates containing MgSiCu and AgMg coexist with the θ′-Al_2Cu phase. In addition, in the iso-surface map of Sc, significant Sc segregation can be observed at the locations indicated by arrows.

The atomic-scale structures of various precipitates and their relationships in the peak-aged alloy are shown in Fig. 4-7. According to the atomic resolution HAADF-STEM images, the precipitates containing MgSiCu elements are plate-shaped C-$AlMg_4Si_3Cu$ phases segregated at the θ′/Al coherent interfaces, as well as the disordered L-AlMgSiCu phases present individually in the aluminum matrix or at the θ′/Al semi-coherent interfaces. The L phase is the disordered form of the C-$AlMg_4Si_3Cu$ phase and exhibits high thermal stability. The Fig.4-7c demonstrates that, in addition to the presence of the C/L-AlMgSiCu phase, there exists an interface phase containing Ag and Mg with a three-layer atomic arrangement at the θ′/Al interfaces.

This AgMg interface phase differs from the previously observed AgMg segregation layer at the Ω/Al interface and the double-layer Ag segregation layer at the θ′/Al interface. That is, the newly discovered interface phase containing Ag and Mg is named as χ-AgMg interface phase. As shown in the APT results in Fig. 4-7g, the C/L-AlMgSiCu and χ-AgMg interface phase are non-uniformly enveloped at the coherent and semi-coherent interfaces of θ′/Al. Additionally, Fig. 4-7h-i confirms that Sc has segregated at the θ′/Al interfaces. Therefore, in the designed Al-Cu-Mg-Ag-Si-Sc alloy, a multiple segregation structure containing C/L interface phase, χ-AgMg interface phase, and Sc segregation layer has been successfully constructed at the coherent and semi-coherent interfaces of θ′/Al, achieving comprehensive wrapping of θ′-Al_2Cu, consistent with the design criteria proposed during alloy design.

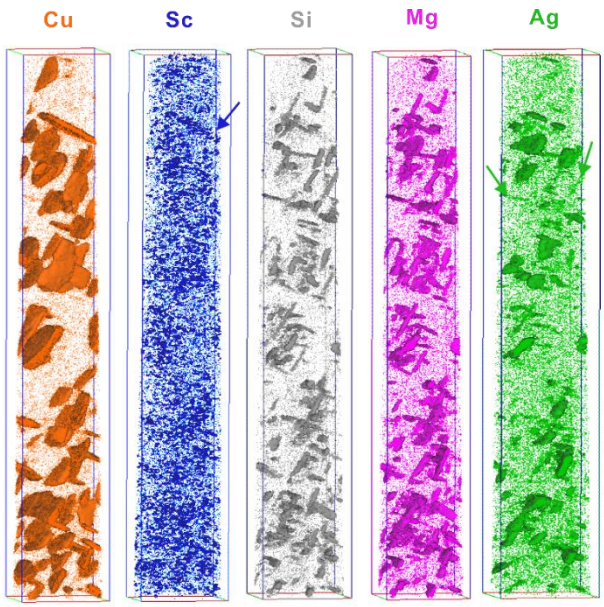

Figure 4-6 APT results of the designed alloy under peak ageing. The iso-surface of Cu, Sc, Si, Mg and Ag are set as 9.0 at.%, 0.3 at.%, 2.0 at.%, 3.0 at.% and 1.0 at.%, respectively

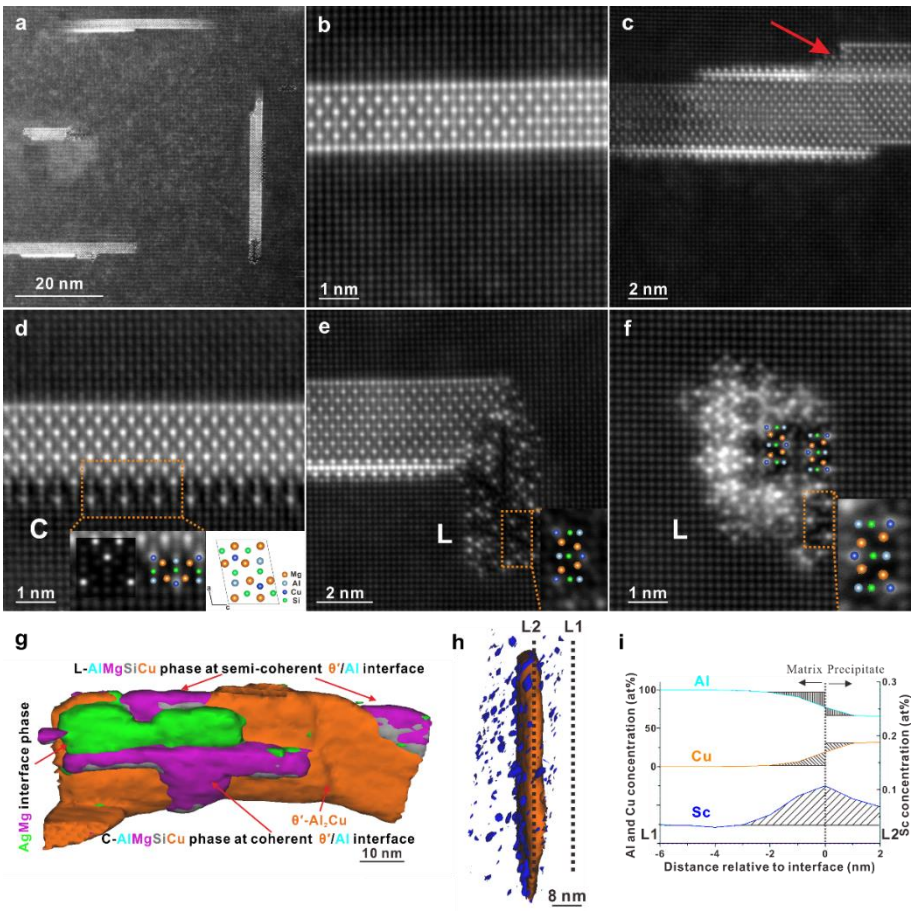

Figure 4-7 Multiple types of precipitates and interface structures of the current alloy under peak ageing. (a) Low magnification HAADF-STEM image. (b) Individual θ′-Al_2Cu. (c) χ-AgMg interface phase occurring at both upper and lower θ′/Al interfaces. (d) θ′-Al_2Cu with C-$AlMg_4Si_3Cu$ interface phase at the coherent interface. The unit cell of the C-$AlMg_4Si_3Cu$ phase and the simulated HAADF-STEM image by QSTEM have been inserted in (d). (e) θ′-Al_2Cu with a L-AlMgSiCu at the semi-coherent interface. (f) Independently precipitated L-AlMgSiCu. (g) and (h) Multiple interface phases and segregation layers at the θ′/Al interfaces detected by APT. (i) Proxigram of Sc cross the θ′/Al interface along L1 to L2 in (h)

The structure of the newly discovered χ-AgMg interface phase found in Fig. 4-7c is different from the uniformly distributed AgMg bi-layer at the Ω/Al interface[52] reported by Kang et al., or the Ag segregation layer with double atomic layers at the θ′/Al interface reported by Rosalie et al. [184]. According to Fig. 4-8a-d, the atomic arrangement of the interface phase is consistent with that of Al under different zone axes, with the light and dark atomic columns alternately arranged at sub-layers L1 and L3. These atomic columns were identified as Ag and Mg columns according to the atomic resolution energy dispersive X-ray (EDX) mapping results shown in Fig. 3e-h. As for the middle layer L2, the EDX maps show that every column contains Ag, while there is very low signal of Mg. However, the intensity line profiles of the middle layer L2, as inserted in Fig. 3a and c, show that the column intensity is in an alternative strong-weak-strong distribution, implying the atomic column with lower intensity should also contain Mg. As shown in Fig. 4-8f, Mg signals can be found at the atomic columns marked by white dotted circles in the L2 layer. Similar examples can be found in Fig. 4-9. In addition, the atomic ratio of Mg in the three layers is about 2:1:2 according to concentration line profile of Mg shown in Fig. 4-8i, further confirming that the L2 layer contains Mg atoms. According to the information mentioned above, the structure of χ-AgMg interface phase was constructed as shown in Fig. 3j, while the atomic ratio of Ag to Mg in the structure is 1.4. To validate the accuracy of the constructed interface structure, quantitative EDX results and APT results were used to verify the composition of the χ-AgMg interface phase. Fig. 4-10 shows TEM EDX results of different χ-AgMg interface phases in the peak-aged alloy, and quantitative analysis indicates that the average atomic ratio of Ag to Mg in the χ-AgMg interface phase is 1.56, which is consistent with the crystal structure model.

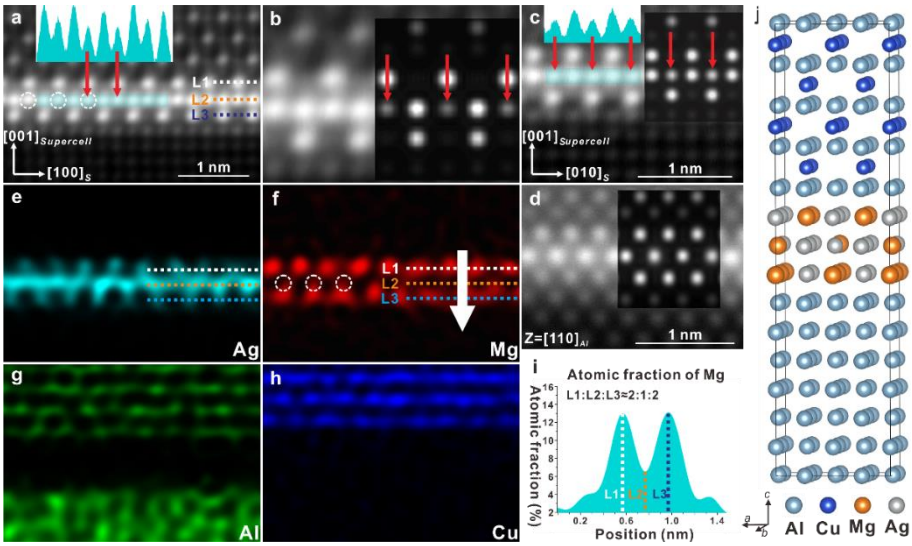

Figure 4-8 The structure of the newly discovered χ-AgMg interface phase. (a-c) Atomic resolution HAADF-STEM images of the χ-AgMg phase along $[100]_{Al}$ direction. (b) Enlargement image of (a). The intensity line profiles of the middle layer (L2) of the χ-AgMg phase are inserted in (b) and (c). (d) Atomic resolution HAADF-STEM images of the χ-AgMg phase along $[110]_{Al}$ direction. (e-h) Atomic resolution EDX elemental maps of the area shown in (a). (i) Concentration line profile of Mg in the χ-AgMg phase along the white arrow. (j) 3D model of the θ′/Al interface structure with the newly discovered χ-AgMg interface phase. It should be noted the viewing direction is parallel to [010] direction of the supercell in (j) for (a-b), [100] for (c) and [110] for (d). The atomic resolution HAADF-STEM images simulated by QSTEM using the constructed model along different directions are inserted in (a), (b) and (c). The atomic columns marked with white dotted circles in (f) correspond to those similarly marked in (a)

Fig. 4-11 displays the concentration distribution maps of all χ-AgMg interface phases obtained from APT results, showing that the average atomic ratio of Ag to Mg in the χ-AgMg interface phase is 1.44, consistent with the Ag/Mg atomic ratio in the constructed model. Therefore, both

EDX results and APT results are consistent with the constructed model, indicating its accuracy. Additionally, image simulations were conducted using QSTEM software[130]. As shown in Fig. 4-8b-d. The simulation results demonstrate that the images simulated along the [100], [010], and [110] directions of the constructed model are consistent with the experimental results, further confirming the accuracy of the constructed model.

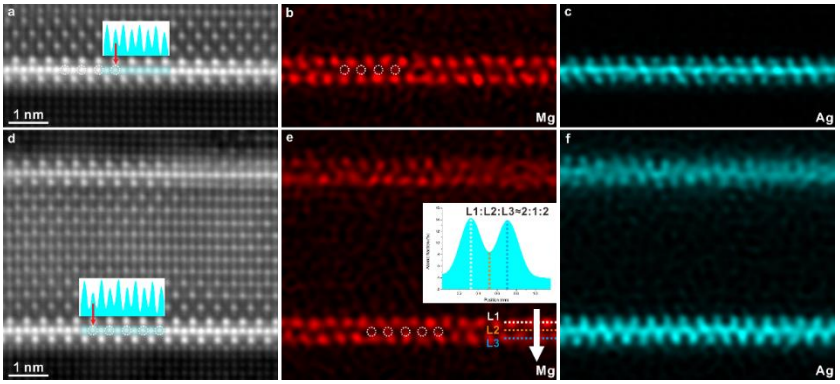

Figure 4-9 (a) and (d) Atomic resolution HAADF-STEM image with multiple χ-AgMg interface phases. (b-c) and (e-f) Atomic resolution EDX elemental maps of the area shown in (a) and (d), respectively. The atomic columns marked with white circles in (b) and (e) correspond to that in (a) and (d), respectively

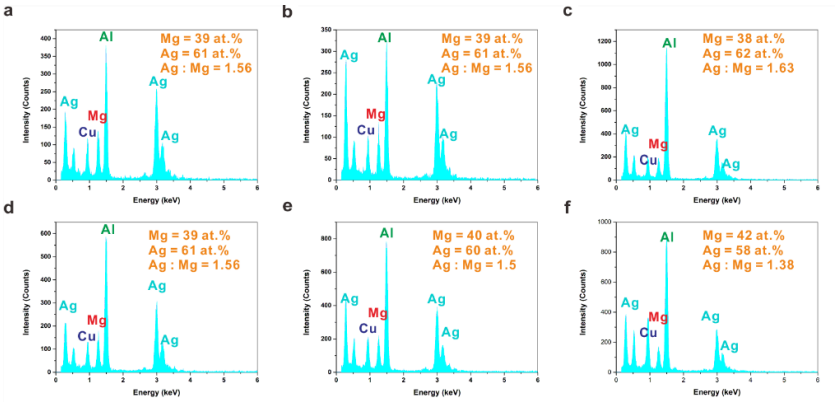

Figure 4-10 The EDX results of different χ-AgMg interface phases

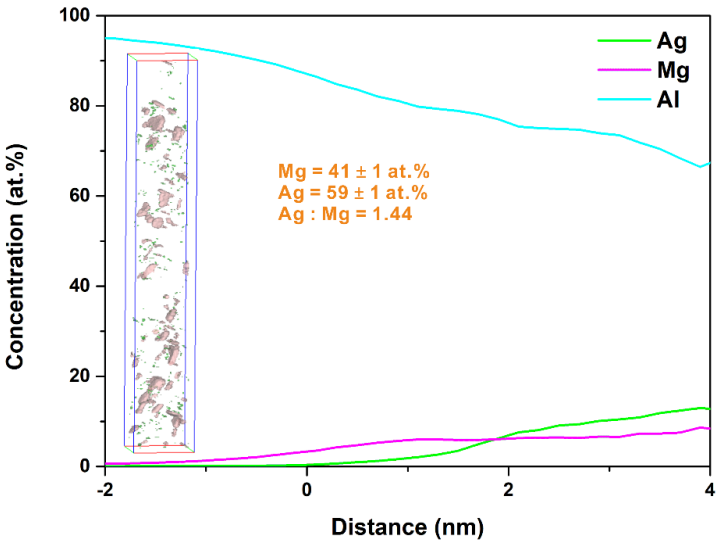

Figure 4-11 The proxigram of total χ-AgMg interface phase (marked in pink) detected by APT

4.4.3 Nano-scale structure of alloy after thermal exposure

According to Fig. 4-12a-c, the θ′-Al_2Cu, L and C phases in the current alloy were kept after a thermal exposure at 210°C for 100 h. However, there are some square σ-$Al_5Cu_6Mg_2$ (space group *P*m-3)[128] particles in the thermally exposed sample as shown in Fig. 4-13. In addition, the thin χ-AgMg interface phase in the peak-aged state disappeared after thermal exposure, while a thicker AgMgAl phase, which was discovered in this work and named ξ phase, precipitated at the σ/Al interface. Fig. 4-12d-e show the atomic resolution HAADF-STEM images and the corresponding Fast Fourier Transform (FFT) pattern, respectively. As shown in the FFT pattern, the distance g_1 is 5.17 nm^{-1}, while those of g_2 and g_3 are 4.20 and 2.99 nm^{-1}, respectively. That is, the ratios g_1/g_3 and g_2/g_3 are 1.729 and 1.404, which are all consistent with the standard electron diffraction pattern of the body-centered cubic (BCC) structure along the [011]

direction.

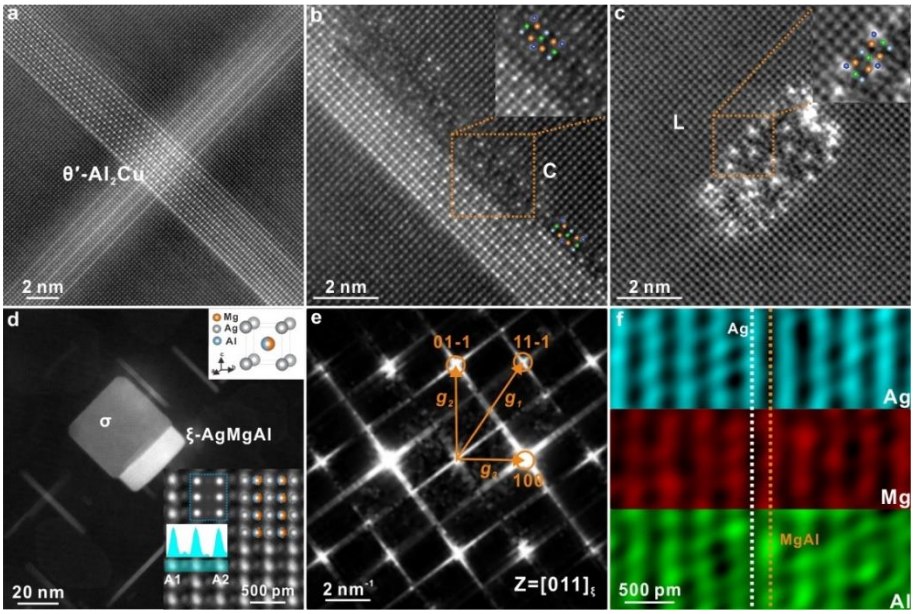

Figure 4-12. HAADF-STEM images and EDX results of precipitates after thermal exposure at 210°C for 100 h. a HAADF-STEM image of θ′-Al_2Cu. b C interface phase at the θ′/Al interface. c Independently precipitated L phase. d Low-magnification and atomic resolution HAADF-STEM images of the ξ phase. e Corresponding FFT pattern of atomic resolution HAADF-STEM image in (d). f EDX elemental maps of ξ phase. The unit cell of the ξ phase and the simulated HAADF-STEM image along $(011)_\xi$ by QSTEM have been inserted in (d). The intensity line profiles inserted in (d) shows the intensity variation from A1 to A2.

In addition, the intensity line profile inserted in Fig. 4-12d shows that the light and dark atomic columns alternately arranged along A1 to A2, which could be identified as Ag and Mg+Al atomic columns according to the EDX mapping results shown in Fig. 4-12f. It is obvious that Mg and Al atoms jointly take one site in the unit cell, most probably in a disordered way, while Ag atoms solely occupy the other site. According to the

information mentioned above, the B2 structure of ξ-$Ag_1Mg_{1-x}Al_x$ (x = 0.5) phase has been constructed as inserted in Fig. 4-12d. The space group of the ξ phase is *Pm-3m*, while the lattice parameters are determined as $a = b = c = 3.34 \pm 0.10$ Å and $\alpha = \beta = \gamma = 90°$.The atomic ratio Ag: Mg: Al in ξ phase is 2: 1: 1, which is close to the ratio of about 51: 22: 28 as obtained from the EDX data (from the very thin area shown in Fig. 4-12d). Furthermore, the HAADF-STEM image (see the blue frame in Fig. 4-12d) simulated by QSTEM software[130] along [011] direction of ξ phase is consistent with the experimental image.

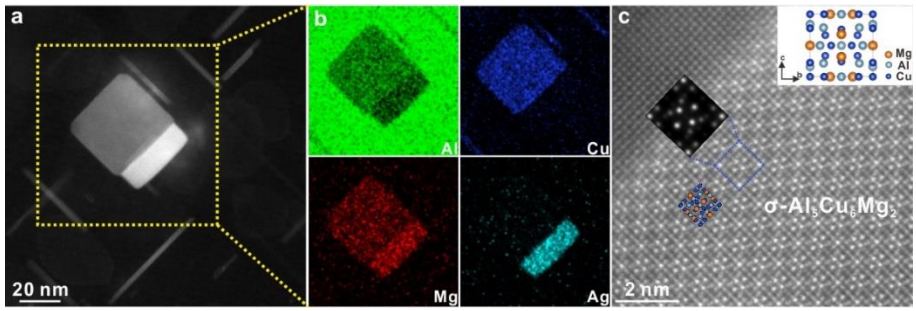

Figure 4-13. HAADF-STEM images and EDX results of precipitates after thermal exposure at 210℃ for 100 h. a Low magnification HAADF-STEM image. b EDX elemental maps of σ and the thick AgMg-rich ξ phase. c atomic resolution HAADF-STEM of σ-$Al_5Cu_6Mg_2$ precipitate. The HAADF-STEM image simulated by QSTEM is inserted in (c).

According to Fig. 4-3, The mechanical properties of the designed alloy before and after thermal exposure indicates that the exposure temperature significantly affects the heat resistance of the alloy. When the alloy is thermally exposed to 210 °C, the after thermal exposure is 90.3%, while strength retention rate reaches 97.1% when the alloy thermally exposed to 200 °C. To analyze the significant improvement in heat resistance of the alloy at 200 °C, the interface structure of precipitates in

the alloy after exposure at 200 °C for 100 h was characterized using TEM. As shown in Fig. 4-14, when the alloy was thermally exposed at 200 °C for 100 h, there is not only C-AlMgSiCu interface phase at the θ′/Al interface, but also a χ-AgMg interface phase with a larger size and a relatively complete structure. Compared to the interface structure of the alloy after thermal exposure at 210 °C for 100 h shown in Fig. 4-12, it is evident that the dissolution rate of the χ-AgMg interface phase at 200 °C is much slower than at 210 °C. Therefore, even though the structure of the χ-AgMg interface phase will gradually be destroyed and dissolve during thermal exposure heat treatment, the presence of χ-AgMg interface phase still contributes to the improvement in heat resistance, as observed from the comparison of the alloy's mechanical properties after thermal exposure at 200 °C and 210 °C.

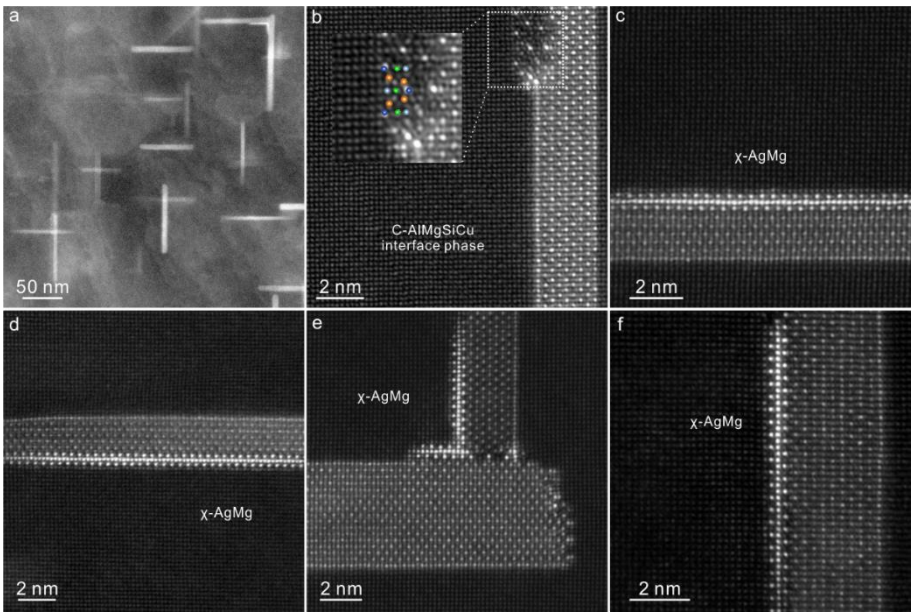

Figure 4-14 (a) Low magnification HAADF-STEM image of the alloy thermally exposed at 200 ℃ for 100 h. (b-f) HAADF-STEM images of different interface structures

The EDX result of the σ-$Al_5Cu_6Mg_2$ phase in the alloy after exposure at 200°C for 100 h shown in Fig. 4-15 indicates that even though the dissolution rate of the χ-AgMg interface phase decreases when thermally exposed at 200 °C, most of the χ-AgMg interface phase will still dissolve into the aluminum matrix due to the long thermal exposure time. Additionally, square σ-$Al_5Cu_6Mg_2$ phases and ξ-AgMgAl phases will also form in the alloy.

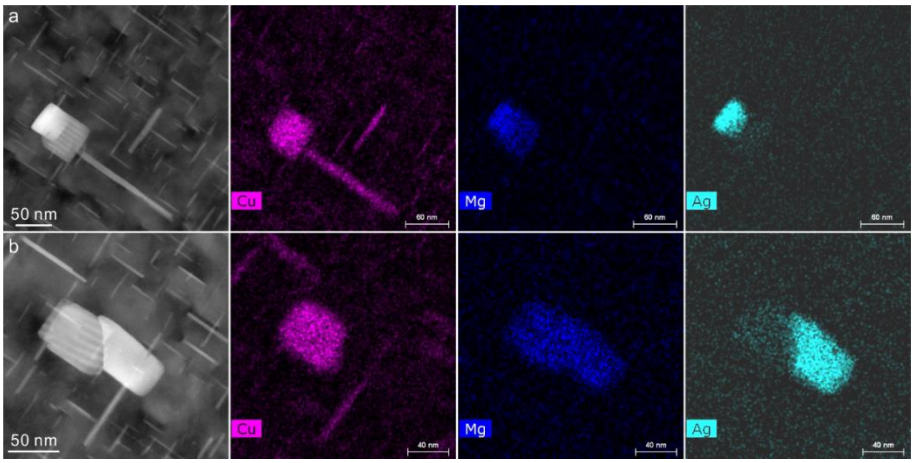

Figure 4-15 The EDX results of σ-$Al_5Cu_6Mg_2$ and ξ-AgMgAl in the designed alloy thermally exposed at 200 ℃ for 100 h

4.5 Mechanism of synergistic improvement of strength and heat resistance of Al-Cu-Mg-Ag alloy

4.5.1 Mechanism of strength improvement

In the Al-Cu-Mg-Ag alloy, the addition of Si elements alters the precipitation behavior, thereby affecting the mechanical properties of the alloy. To investigate the influence of Si on the precipitation behavior of Al-Cu-Mg-Ag-Si-Sc alloy in the early stages of aging, the composition and morphology of precipitates in the under-aged state (175°C-1h) were

detected using APT. According to Fig. 4-16, the main precipitates in the designed alloy are lath or plate-like precipitates containing Mg, Si, and Cu elements in the under-aged state. Combined with the morphology and elements distribution of the precipitates, these correspond to the disordered L-AlMgSiCu phase and the C-AlMgSiCu phase, respectively. Furthermore, part of Ag had combined with Mg to form phase rich in AgMg in the under-aged state. As for the main strengthening phase θ′-Al_2Cu in the alloy, it is smaller in size in the early stages of aging, and no obvious plate-like precipitates rich in Cu were found.

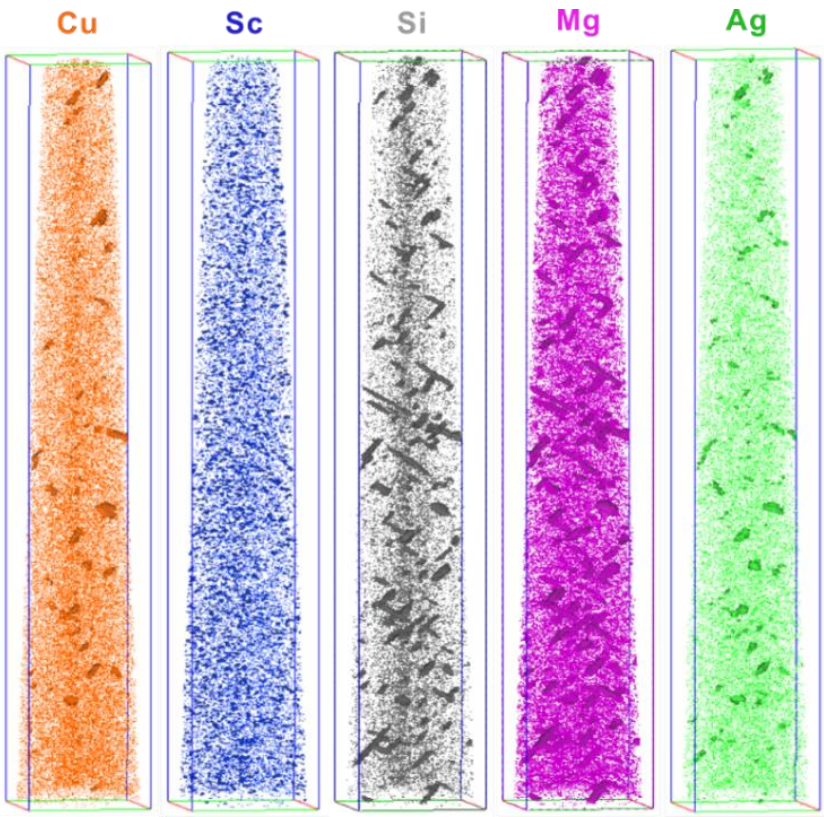

Figure 4-16 APT results of the designed alloy in the underaged state. The iso-surface of Cu, Sc, Si, Mg and Ag are set as 9.0 at%, 0.3 at%, 2.0 at%, 3.0 at% and 1.0 at%, respectively

Fig. 4-17 shows the reconstructed APT results and the elements distribution of precipitates. As shown in Fig. 4-17b-c, preferentially precipitated lath or plate-like C/L-AlMgSiCu phases can act as heterogeneous nucleation sites for the θ′-Al_2Cu phase, promoting the precipitation of the θ′-Al_2Cu phase, refining the size of the θ′-Al_2Cu phase, increasing the number density of the θ′-Al_2Cu phase, and thereby improving the mechanical properties of the alloy. The formation of C/L precipitates in the early stage of ageing consumed a substantial fraction of Mg solutes, thus there were insufficient MgAg atomic clusters to form the Ω during the subsequential stages of ageing. As a results, θ′-Al_2Cu phase was precipitated instead. Then, the remaining Mg solutes combined with Ag solutes to form the newly discovered χ-AgMg interface phase that partially covers the θ′-Al_2Cu precipitate.

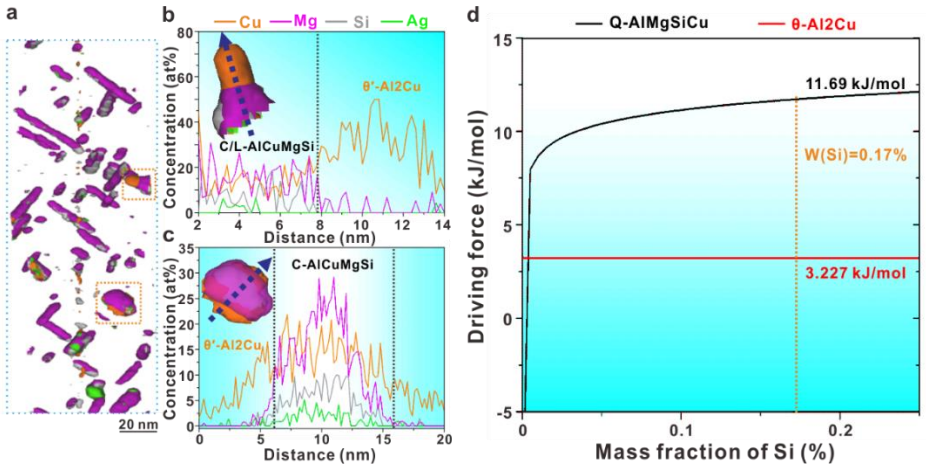

Figure 4-17 (a) APT result of the designed alloy in the under-aged state. (b) and (c) Concentration profiles of the precipitates along the blue arrows. (d) Driving force of equilibrium Q-AlMgSiCu and θ-Al_2Cu at the ageing temperature of 175 °C

The precipitation driving force of different phases is used to explain the precipitation sequence in the current alloy during the artificial ageing

heat treatment. Due to the lack of thermodynamic model of metastable C/L phase in the newest version of multi-component multi-phase thermodynamic database TCAL for Al alloys[141, 170], the precipitation driving forces of successors of C/L and θ′, i.e., the equilibrium Q-AlMgSiCu and θ-Al_2Cu phases, respectively, were calculated instead. As shown in Fig. 4-17d, the precipitation driving force of Q phase increases rapidly when Si is added to the Al-Cu-Mg-Ag alloy, while that of θ phase remains almost unchanged. The precipitation driving forces of Q and θ in the currently designed alloy are 11.69 kJ mol^{-1} and 3.227 kJ mol^{-1} (mol for atoms), respectively, which imply the C/L phases, as precursors of Q phase, will preferentially precipitate.

Ag solutes not only participate in formation of the χ-AgMg interface phases at the θ′/Al interface, but also segregate in C/L precipitates. This is revealed by the co-segregation of Mg, Si, Cu and Ag solutes in the APT results in Fig. 4-16 and the elements concentration profiles in Fig. 4-17b-c. Weng et al.[185] reported that Ag could promote the nucleation of the precipitates and increase their number density in Al-Mg-Si-Ag alloys, thereby improving the mechanical properties of the alloys. As for the current Al-Cu-Mg-Ag-Si-Sc alloy, Ag solutes probably also played an important role in increasing the number density of C/L phase, thereby increasing the number density of θ′. This accounts for the high strength of the alloy. In addition, as typically shown in Fig. 4-18, Ag was found to enrich at the interface of L precipitates to form a segregation layer, thereby further increasing the thermal stability of disordered L phase.

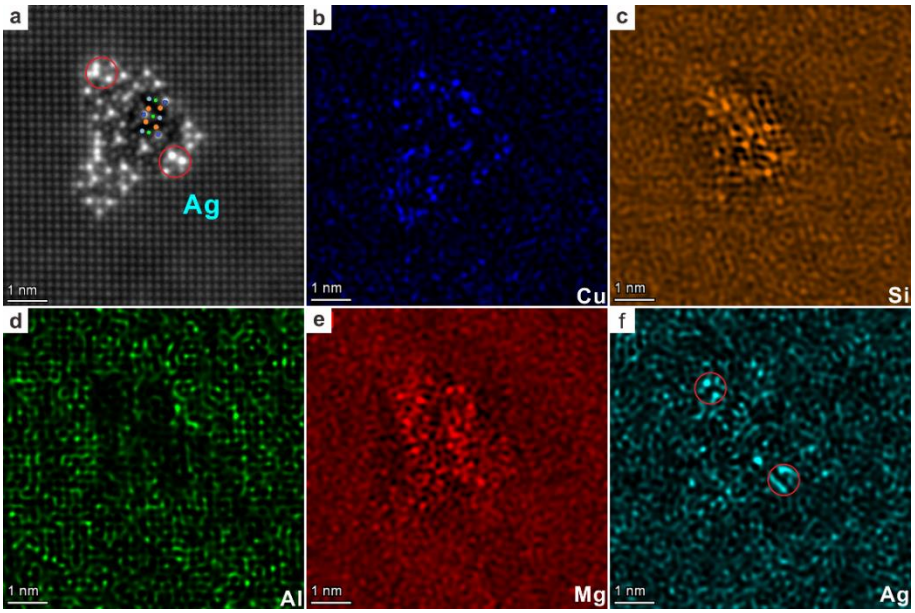

Figure 4-18 HAADF-STEM images and EDX maps of the L phase in the peak aged alloy

4.5.2 Mechanism of heat resistance improvement

The number density and size of the precipitates in the alloy are also an important factor affecting the heat resistance of the alloy. Makineni et al.[186] added Nb and Zr elements to Al-Cu alloy, increasing the number density of the θ′-Al_2Cu phase in the alloy, thereby significantly improving the heat resistance of the Al-Cu alloy. To visually analyze whether the improved heat resistance of the designed alloy in this study comes from the multiple segregation structures or the increased number density of the θ′-Al_2Cu phase, a control group of alloys without multiple segregation structures was designed. The results of previous studies showed that Ag[184], Sc[97] and Si[115, 117] elements could segregate at the θ'/Al interface, thus forming segregation structures at the precipitate/matrix interface. In addition, the addition of Mg will promote the formation of S-Al_2CuMg

precipitates, resulting in different types of precipitates in the alloy. Therefore, the alloy composition of the control alloy is set as Al-4Cu (in wt.%).

Fig. 4-19 shows the mechanical properties of the control alloy under different conditions. The microhardness results indicate that the Al-4Cu alloy reaches peak aging after aging at 175°C for 16 h. In addition, the yield strength values of the peak aged Al-4Cu alloy before and after thermal exposure are 208 ± 12 and 137 ± 3 MPa, respectively. The strength retention ratio of the Al-4Cu alloy is 65.9%, which indicates that the strength of the alloy decreases significantly after thermal exposure at 210°C for 100 h.

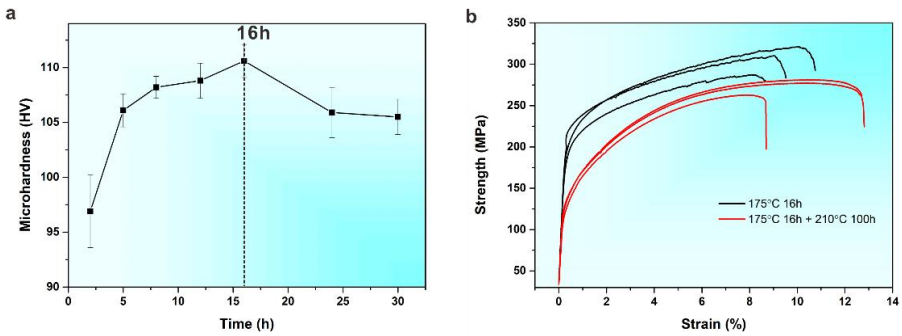

Figure 4-19 (a) Microhardness of the Al - 4Cu alloy aged for different times at 175 °C. (b) Stress-strain curves of the peak aged Al - 4Cu alloy before and after thermal exposure

Furthermore, rapid coarsening of the precipitates was observed as shown in Fig. 4-20. According to Fig. 4-20a-b, the average thickness values of θ′-Al_2Cu before and after thermal exposure are 1.1 ± 0.4 nm and 10 ± 3.5 nm, while those values for diameter are 25 ± 10 nm and 318 ± 210 nm. The statistical results show that θ′-Al_2Cu precipitates without multiple segregation structures have been obviously coarsened after thermal exposure, thereby leading to the rapid decrease in tensile

properties of the Al-4Cu alloy. That is, the presence of the multiple segregation structures at the θ′/Al interface is the main cause of effectively inhibiting the coarsening of θ′-Al_2Cu precipitates in the designed Al-4Cu-0.315Mg-0.5Ag-0.21Si-0.09Sc alloy.

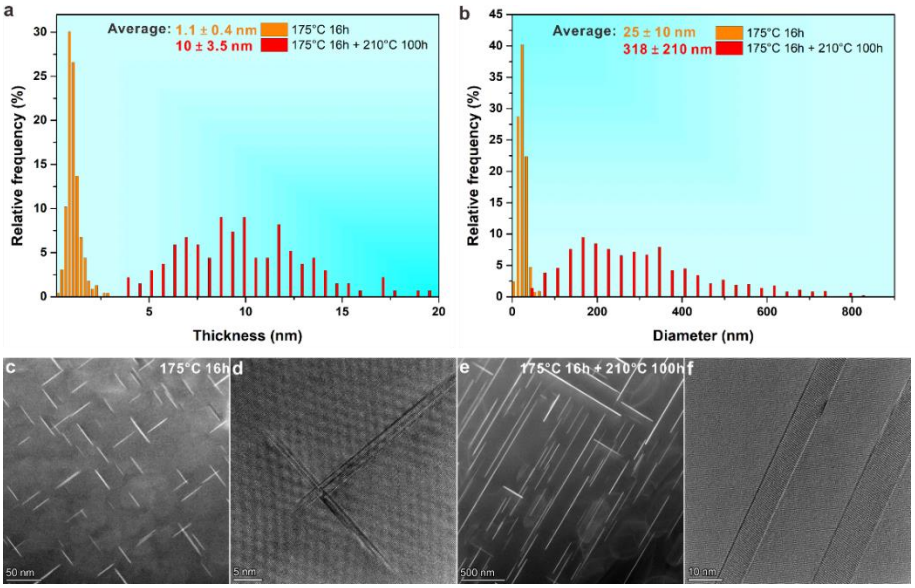

Figure 4-20 (a) and (b) Distributions of thickness and diameter of θ′-Al_2Cu phase in the peak aged Al - 4Cu alloy before and after thermal exposure. (c) and (d) Typical TEM images used to measure the diameter and thickness of θ′-Al_2Cu phase in the peak-aged alloy. (e) and (f) Typical TEM images measure the diameter and thickness of θ′-Al_2Cu phase after thermal exposure

In addition, the existence of the interface phases changed the interface structures of θ′-Al_2Cu precipitates and were found to hinder their coarsening. Bourgeois et al. [145, 187-189] reported that Cu atoms could occupy the interstitial sites at the coherent interface of θ′-Al_2Cu and reduce the energy of the system. It is concluded that the Cu interfacial segregation layer is an intermediate state beneficial for the thickening of θ′-Al_2Cu. In this study, the intensity line profile of A1-A2 in Fig. 4-21 indicate that, at

the coherent interfaces without a AgMg or C interface phase, Cu atoms can occupy the interstitial sites at the interfacial layer. In Fig. 4-7c, it is found that χ-AgMg interface phase (on the left side) effectively hinder thickening of the θ′-Al_2Cu precipitates, while in the right part with only layers containing interstitial Cu atoms there is abrupt thickening (see the red arrow in the image).

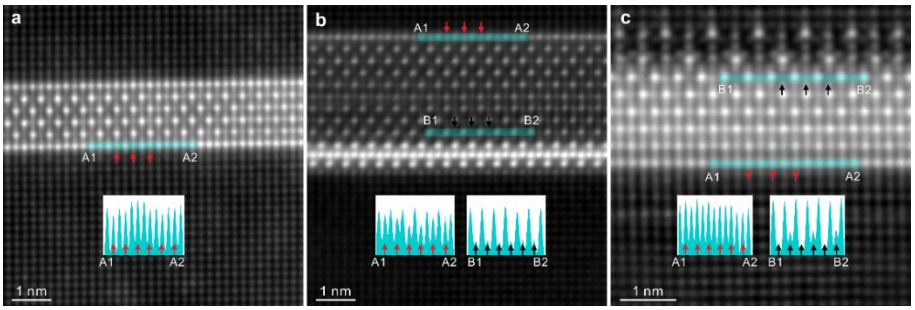

Figure 4-21 (a) Intensity distribution of the atom column in the interface of θ′-Al_2Cu and Al matrix. (b) Intensity distribution of the different atom columns in the θ′-Al_2Cu with χ-AgMg interface phase. (c) Intensity distribution of the different atom columns in the θ′-Al_2Cu with C-AlMgSiCu interface phase

To compare the effects of the various interface structures on the stability of the precipitates more accurately, the formation energies of different structures were calculated, as shown in Fig. 4-22. The formation energy of Model 3 is lower than that of Model 2, indicating that the Al-terminated θ′-Al_2Cu interface structure (with the χ-AgMg interface phase) is easier to form and more stable than Cu-terminated θ′-Al_2Cu interface structure. In addition, Model 1 shows a single χ-AgMg interface phase embedded in the matrix, with a higher formation energy than those of Model 2 and Model 3. That is, the χ-AgMg interface phases cannot precipitate alone and should exist in the coherent interface of θ′/Al. Therefore, the most energetically favorable structure containing χ-AgMg

interface phase is Model 3, which is consistent with the experimental results shown in Fig. 4-8. In addition, the formation energy of Model 6 is obviously lower than those of Models 4-5, indicating that the C interface phase layer can improve the stability of θ′-Al_2Cu more efficiently than the interstitial Cu layer. Especially, the θ′/Al interface model containing a C interface phase is most energetically favored among all the 6 models.

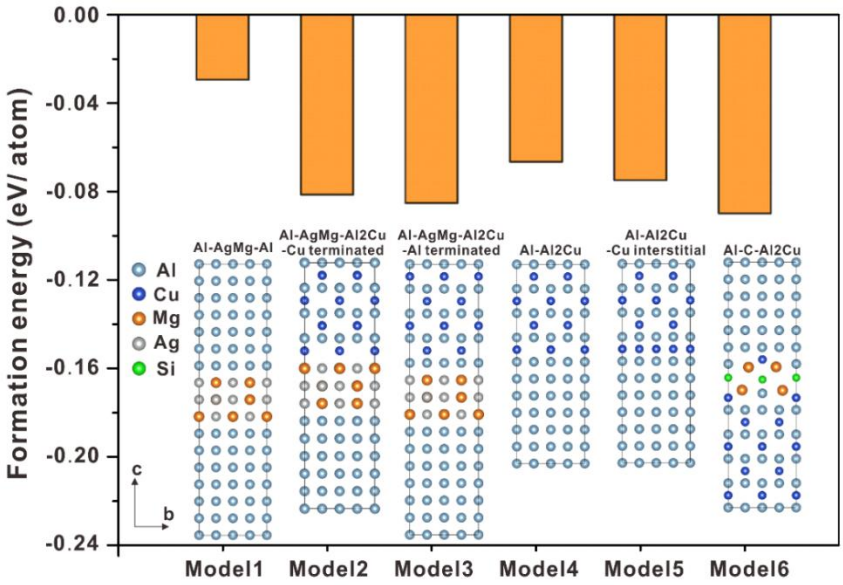

Figure 4-22 The formation energies of different interface structures

As for other θ′/Al interfacial positions without interface phases, the stability could be enhanced by the covering of Sc solutes. According to calculations by Bourgeois et al.[184], when the thickness of a θ′ precipitate is less than 4 nm, the Cu atoms tend to completely occupy the interstitial sites in the Cu-terminated interface. According to Fig. 4-5a, most θ′ plates were found to be thinner than 4 nm in the peak-aged state of the current alloy. Therefore, interstitial Cu layers were found at most coherent θ′/Al interfaces in our alloy, in addition to χ-AgMg and C interface phases.

Moreover, according to Fig. 4-7h-i, Sc segregation layers were also found at θ′/Al interfaces. Zhang et al.[190] investigated the effect of the Sc segregation layer on the stability of interface of θ′/Al by first-principles calculations. Their results showed when Sc segregated at the interface of θ′/Al, the bonding at the interface containing the Cu interstitial layer can be greatly enhanced relative to that without a Cu interstitial layer. Such strong bonding is beneficial for inhibiting the thickening of θ′. These calculations explain the high stability of θ′ precipitates partially covered with Sc segregation layers observed in our work and many other studies[97, 99, 115].

In addition to interface structures at the coherent interface of θ′, there are always disordered L precipitates at the semi-coherent interface of θ′, i.e., occurring at one end of a θ′ plate. In the early stage of artificial ageing process, the disordered L phase can serve as heterogeneous nucleation sites to promote the nucleation of the θ′-Al_2Cu [112], thereby reducing its size and increasing the number density[168]. On the other hand, broadening of θ′-Al_2Cu precipitates will also lead to the obvious decrease of the number density of θ′-Al_2Cu precipitates, leading to a decrease in the alloy properties according to the work of Nie et al.[151]. In the current alloy, due to the high thermal stability of disordered L phase[168, 191], the broadening of θ′-Al_2Cu at semi-coherent interface can be hindered during the long-time thermal exposure process. Therefore, the integration of multiple types of interface structures including χ-AgMg interface phase, C interface phase and Sc segregation layers at coherent interface and the L phase at semi-coherent interface could stabilize the interface of θ′-Al_2Cu and suppress the coarsening of the θ′-Al_2Cu precipitates, thereby improving the heat resistance of the current alloy.

4.6 Structure evolution of the χ-AgMg and C-AlMgSiCu interface phase during thermal exposure

4.6.1 Ab initio molecular dynamics simulations

The TEM results of the alloy after thermal exposure indicate that the χ-AgMg interface phase gradually dissolves and disappears during prolonged thermal exposure, while the C-AlMgSiCu interface phase remains present after long-term thermal exposure. To analyze the stability of different interface phase structures during thermal exposure, AIMD simulations had been performed to account for the stability of χ-AgMg and C interface phases during thermal exposure. As described in Chapter 2, the calculated melting temperature of pure aluminum usually differs from the actual melting temperature of bulk materials[146, 147]. Therefore, before analyzing the element diffusion behavior of interface phases using AIMD, it is necessary to determine the melting temperature of pure aluminum under the parameters used in this study and select an appropriate computational temperature based on the melting temperature. Using a 4 × 4 × 4 aluminum alloy supercell structure, AIMD simulation was performed based on the simulation parameters. The simulated Al atomic structure changes and radial distribution function (RDF) results are shown in Figs. 4-23 and 4-24.

When the simulation temperature is equal to or below 1073 K, there is no significant change in the Al supercell, and all Al atoms oscillate at their original positions. When the simulation temperature is 1173 K, the Al atoms exhibit a disordered distribution, and the RDF result changes, indicating that the Al matrix has melted. Therefore, under the parameters used in this study, the melting temperature of the aluminum alloy obtained from AIMD simulation is between 1073 K and 1173 K.

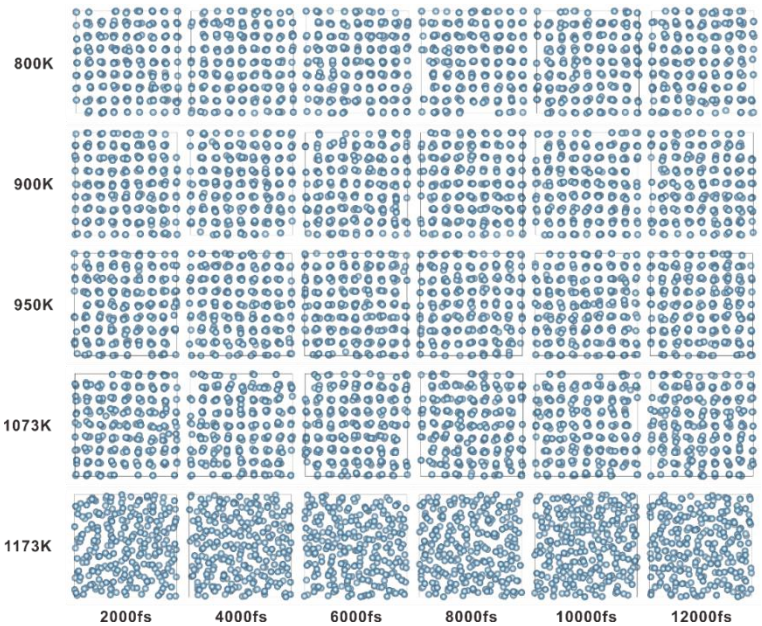

Figure 4-23 The AIMD results of pure Al calculated at different temperatures

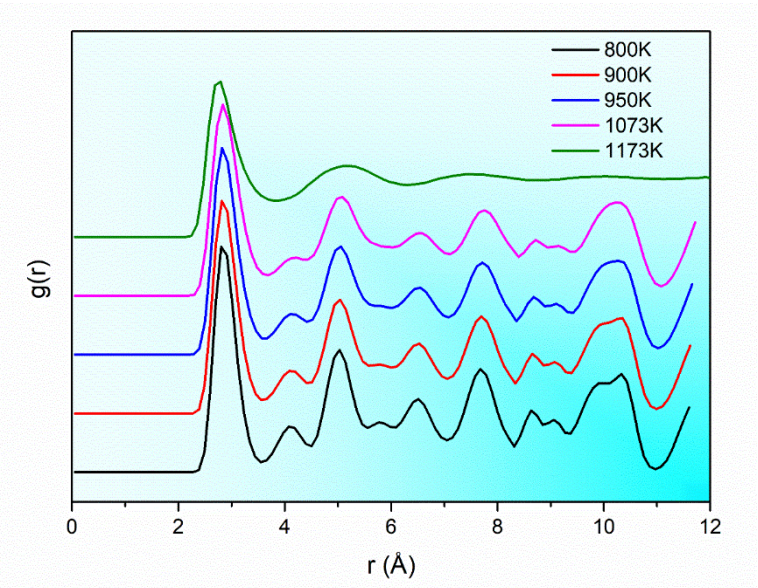

Figure 4-24 The radial distribution function (RDF) of pure aluminum at different temperatures

In the subsequent AIMD simulation process, to accelerate the rate of atomic diffusion and ensure that atoms can diffuse, the simulation temperature is set to 1073 K, which is the closest temperature to the melting point. As shown in Fig. 4-25a, Ag atoms close to the matrix gradually cross the interface and enter the aluminum matrix, while Al atoms in the interface diffuse into the χ-AgMg interface phase in turn. Therefore, the χ-AgMg interface phase gradually dissolved during thermal exposure. On the contrary, the C interface phase in Fig. 4-25b shows high stability at high temperatures and the structure can hardly be destroyed, which is consistent with the experimental results. Therefore, the C interface phase can more effectively hinder the growth of θ′ precipitates than the χ-AgMg interface phase during long term thermal exposure.

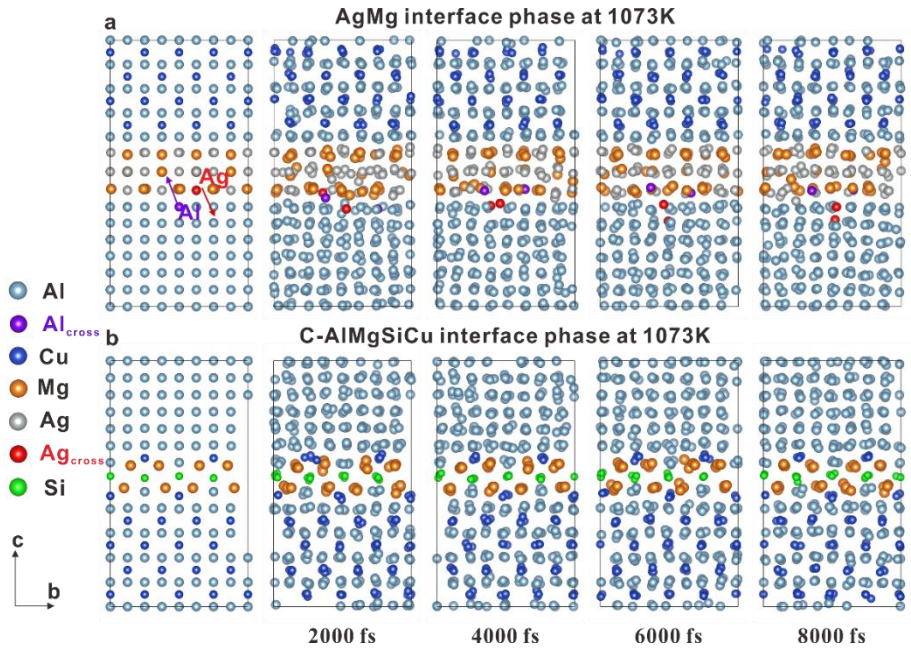

Figure 4-25 The AIMD results of χ-AgMg and C-AlMgSiCu interface phases calculated at 1073 K. The Ag and Al atoms crossing the layers are marked in red and purple, respectively

4.6.2 TEM investigation on the structure evolution of the χ-AgMg interface phase

TEM characterization and AIMD simulation results indicate that the structure of the χ-AgMg interface phase is prone to dissolve at high temperatures. The supersaturated Ag and Mg solute atoms generated after the dissolution of the χ-AgMg interface phase will form a thicker ξ-AgMgAl phase at the boundary of the σ-$Al_5Cu_6Mg_2$ phase. To observe the size and structure evolution of the χ-AgMg interface phase and the ξ-AgMgAl phase during thermal exposure, the atomic-scale microstructure of the peak-aged alloy after thermal exposure at 210 ℃ for different times was characterized.

Figs. 4-26 and 4-27 are the HAADF-STEM and EDX result of the σ-$Al_5Cu_6Mg_2$ phase in the alloy thermally exposed at 210 ℃ for 12 h, respectively. According to the atomic-resolution HAADF-STEM images, there are still many relatively large χ-AgMg interface phases at the θ′/Al interface, indicating the amount of dissolved χ-AgMg interface phases is small after thermal exposure for 12 h. The EDX result shown in Fig. 4-27 indicates that no ξ-AgMgAl phase is found at the σ/Al interface after thermal exposure for 12 h. However, the EDX mapping and line scan data show an enrichment of Ag elements in the σ-$Al_5Cu_6Mg_2$ phase, and the Ag element content is similar to the Mg element content. This result suggests that Mg solute atoms dissolved from the χ-AgMg interface phase into the aluminum matrix during thermal exposure, are used to form the σ phase. At the same time, the excess Ag solute atoms in the matrix will be enriched inside or on the surface of the σ-$Al_5Cu_6Mg_2$ phase. When the enrichment concentration reaches a certain level, the ξ-AgMgAl phase rich in Ag and Mg elements will precipitate at the σ/Al interface.

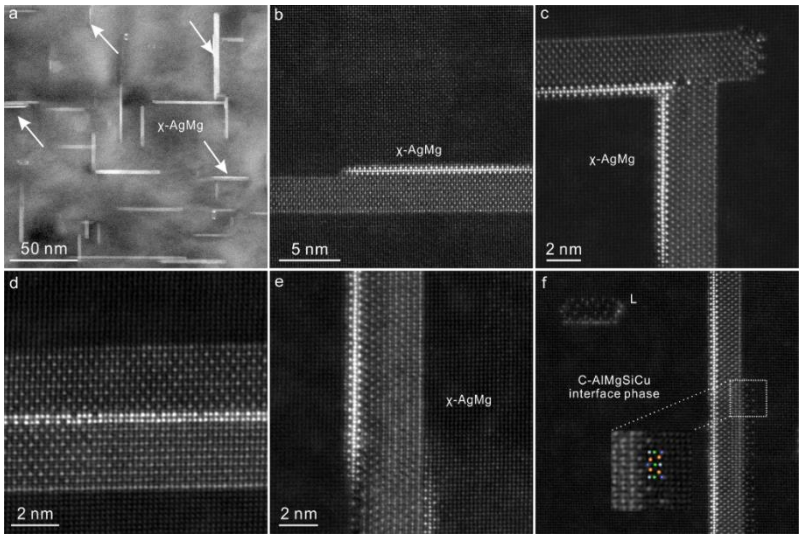

Figure 4-26 (a) Low magnification HAADF-STEM image of the alloy thermally exposed for 12 h at 210 ℃. (b-f) HAADF-STEM images of different interface structures

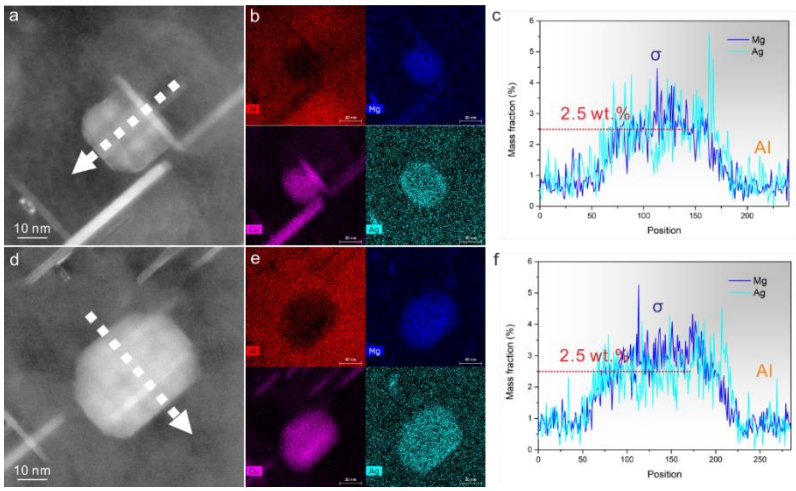

Figure 4-27 (a) and (d) are the HAADF-STEM images of the σ-$Al_5Cu_6Mg_2$ phase in the alloy thermally exposed at 210 ℃ for 12 h. (b) and (e) are the EDX mapping results of the areas shown in (a) and (d), respectively. (c) and (f) are the line scanning results for the areas indicated by arrows in the (a) and (d), respectively

Figs. 4-28 and 4-29 illustrate the HAADF-STEM and EDX results of the σ-$Al_5Cu_6Mg_2$ phase in the alloy after thermal exposure at 210 ℃ for 24 h, respectively. According to the atomic-resolution HAADF-STEM images shown in Fig. 4-28, as the thermal exposure time increases, the number of the χ-AgMg interface phase at the θ′/Al interface decreases, while its proportion within the θ′-Al_2Cu phase increases. At the same time, the size of the χ-AgMg interface phase decreases, indicating significant structural damage of the χ-AgMg interface phase during the 12 h to 24 h thermal exposure stage.

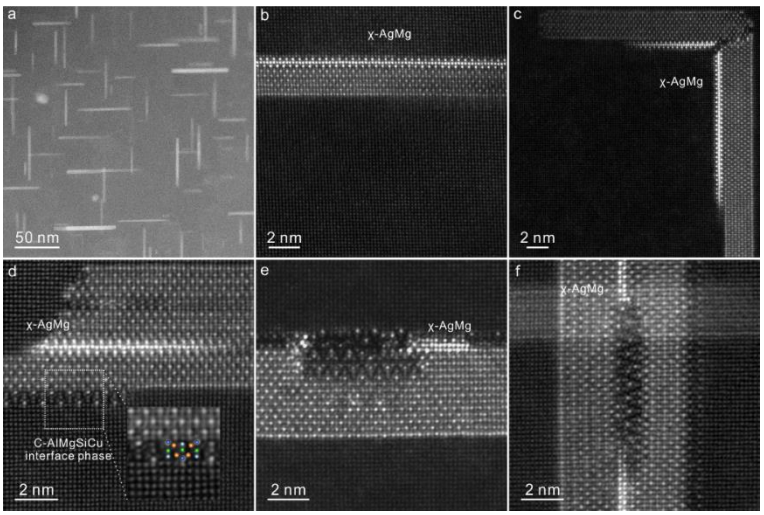

Figure 4-28 (a) Low magnification HAADF-STEM image of the alloy thermally exposed for 24 h at 210 ℃. (b-f) HAADF-STEM images of different interface structures

Combining with the EDX results of the σ-$Al_5Cu_6Mg_2$ phase in Fig. 4-29, it is evident that as the χ-AgMg interface phase gradually dissolves into the aluminum matrix, the content of Ag and Mg solute atoms in the matrix increases, resulting in an increase in the number of the σ-$Al_5Cu_6Mg_2$ phase. Additionally, Fig. 4-29a-c demonstrates the segregation of Ag in the σ-

$Al_5Cu_6Mg_2$ phase is still significant, and the content of Ag is much higher than that in the σ phase in the alloy after 12 hours of thermal exposure, further confirming that the Ag solute atoms dissolved in the aluminum matrix will segregate to the surface or interior of the σ phase during thermal exposure.

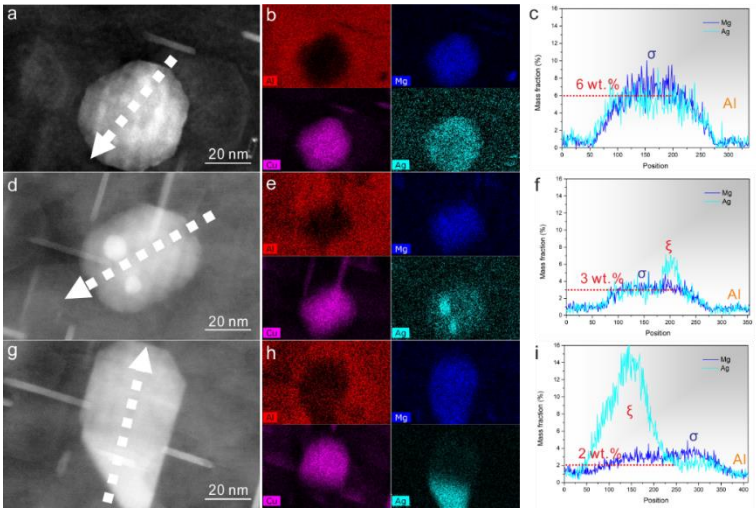

Figure 4-29 (a), (d) and (g) are the HAADF-STEM images of σ-$Al_5Cu_6Mg_2$ in the alloy thermally exposed at 210 ℃ for 24 h. (b), (e) and (h) are the EDX mapping results of the areas shown in (a), (d) and (g), respectively. (c), (f) and (i) are the line scanning results for the areas indicated by arrows in the (a), (d) and (g), respectively

Fig. 4-29d-f shows the EDX results of the σ phase with Ag-rich clusters on the surface. According to the line scan results, in the Ag-rich cluster part, the Mg also has certain fluctuations, indicating that the Ag-rich cluster is ξ -AgMgAl phase. Furthermore, in regions without Ag clusters in the σ phase, the line scan results reveal a lower Ag segregation content compared to the regions without ξ-AgMgAl in the σ phase, suggesting that once the Ag segregation content reaches a certain level on the surface or interior of the σ phase, the excess Ag atoms will combine

with Mg atoms to form new ξ-AgMgAl phases on the surface of the σ phase, thereby consuming the previously segregated Ag atoms on the surface or interior of the σ phase. The EDX result of the σ/Al interface containing ξ-AgMgAl after thermal exposure for 24 h is shown in Fig. 4-29g-i. The line scan result in Fig. 4-29i indicates that as the ξ-AgMgAl phase grows, the content of Ag atoms enriched on the surface or interior of the σ phase gradually decreases, eventually becoming lower than the Mg content in the σ phase. This indicates that as the ξ-AgMgAl phase grows, the Ag enriched on the surface or inside the σ phase is gradually consumed, resulting in a gradual decrease in the Ag enrichment content in the σ phase.

Figs. 4-30 and 4-31 are the HAADF-STEM and EDX results of the σ-$Al_5Cu_6Mg_2$ phase in the alloy after thermal exposure at 210 ℃ for 48 h, respectively. With the extension of the thermal exposure time to 48 h, the atomic resolution HAADF-STEM reveals that most of the χ-AgMg interface phases in the alloy dissolve and disappear. At the θ′/Al interface, there mainly exist the C-AlMgSiCu interface phase and smaller χ-AgMg interface phases, while larger and structurally non-uniform χ-AgMg interface phases are present inside the θ′-Al_2Cu phase or at the interface between two θ′-Al_2Cu phases. In addition, the line scan data in Fig. 4-31c demonstrates that in the alloy thermally exposed for 48 h, the Ag content enriched in the σ phase containing ξ-AgMgAl phases at the σ/Al interface is much lower than that in the σ phase in the alloy thermally exposed for 12 h and 24 h, confirming that the Ag elements enriched in the σ phase are used to generate ξ-AgMgAl interface phases. Furthermore, the Ag content enriched in the σ phase is also lower than the Mg content, indicating that with the extension of the thermal exposure time, the Ag elements enriched on the surface or interior of the σ phase gradually decrease and are used

for the growth of ξ-AgMgAl phases at the σ/Al interface. Therefore, the EDX results under different thermal exposure conditions indicate that the σ-$Al_5Cu_6Mg_2$ phase serves as the nucleation site for ξ-AgMgAl phases, which also explains why separate ξ-AgMgAl phases are not found inside the Al matrix.

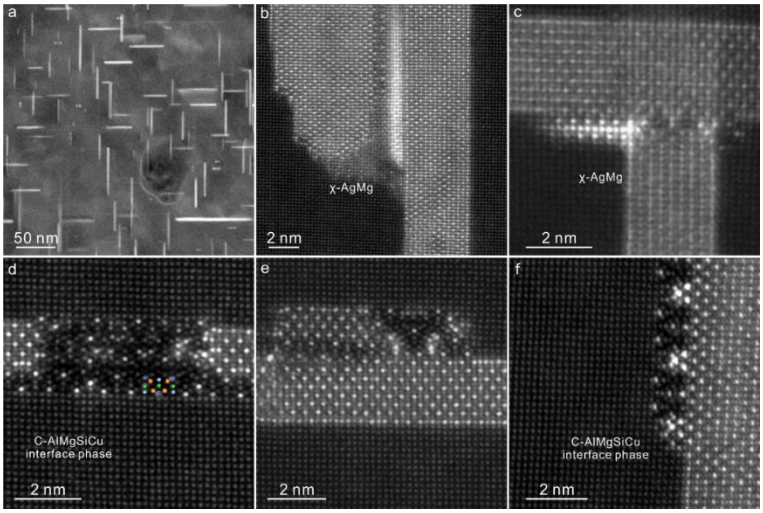

Figure 4-30 (a) Low magnification HAADF-STEM image of the alloy thermally exposed for 48 h at 210 ℃. (b-f) HAADF-STEM images of different interface structures

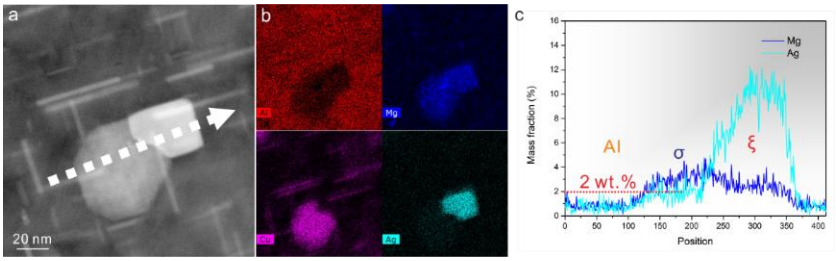

Figure 4-31 (a) is the HAADF-STEM image of σ-$Al_5Cu_6Mg_2$ in the alloy thermally exposed at 210 ℃ for 48 h. (b) is the EDX mapping result of the area shown in (a). (c) is the line scanning result for the area indicated by arrow in the (a)

In ex-situ TEM characterization, it was not observed where the structural damage of the χ-AgMg interface phase begins. To achieve an in-situ observation of the structure evolution of the χ-AgMg interface phase, in-situ TEM heating experiments were conducted using DENS Solutions equipment. The DENS Solutions sample holder cannot directly place the TEM sample prepared by electropolishing. Therefore, it is necessary to use FIB to cut the area at the edge of the sample prepared by electropolishing and place it on the in-situ heating chip. To fix the selected sample, Pt is used to connect the cut sample to the surface of the chip. During fixation process, Pt may splash, resulting in Pt particles and C deposition on the sample surface. The contaminants containing Pt and C are difficult to remove by plasma cleaning, affecting the atomic resolution TEM observation. Therefore, in the final step of sample preparation by FIB, it is necessary to clean the contaminants on the sample surface. As the Ga ion beam has strong energy, it is easy to damage the precipitate structure[192-194]. Therefore, low voltage and low beam current should be used to avoid damage to the sample during the cleaning process. Fig. 4-32 shows the atomic resolution HAADF-STEM image of the in-situ heating sample prepared using FIB.

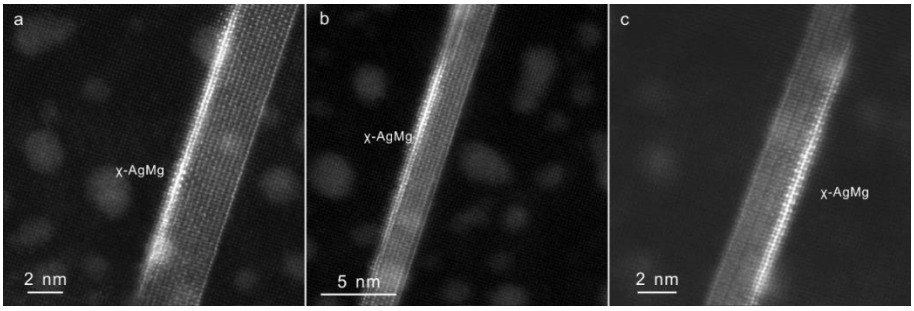

Figure 4-32 Atomic resolution HAADF-STEM images of the χ-AgMg interface phase before in-situ heating experiment

After cleaning the sample surface with a low voltage and low beam current ion beam, the χ-AgMg interface phase still has a three-layer atomic column structure, with the two layers in contact with the θ′-Al_2Cu phase and the aluminum matrix showing a bright-dark-bright alternating distribution, consistent with the structure of the χ-AgMg interface phase in the peak-aged state. That is, after cleaning with a low-current Ga ion beam, there is no significant damage in the χ-AgMg interface phase, which can be directly used for further in-situ TEM heating observation.

Fig. 4-33 shows the atomic-resolution HAADF-STEM images of the same χ-AgMg interface phase after in-situ heating at 210 ℃ for different times. According to Fig. 4-33a, as indicated by the red arrows, the atom layer in the χ-AgMg interface phase near aluminum matrix exhibits a clear bright-dark-bright alternating distribution before in-situ heating. After heating to 210 ℃ for 10 min, as shown by the red arrow in Fig. 4-33b, the interface structure of the χ-AgMg interface phase in contact with the aluminum matrix changed. There is no obvious bright atomic column at the top red arrow, that is, the Ag atoms has diffused. Upon further heating to 20 min, as shown in Fig. 4-33c, the brightness of the outermost atomic columns in contact with the aluminum matrix is significantly reduced, while the inner atomic columns in contact with the θ′-Al_2Cu phase still exhibit a bright-dark-bright alternating distribution. Therefore, during thermal exposure, the damage to the χ-AgMg interface phase is caused by the diffusion of Ag atoms in the outermost atomic columns in contact with the aluminum matrix, consistent with the results of AIMD simulations. As the in-situ heating time increases, the brightness of the outermost atomic columns in the χ-AgMg interface phase further decreases, and the brightness at the top of the χ-AgMg interface phase also gradually decreases according to Fig. 4-33d. This indicates that after the outermost

atomic columns of the χ-AgMg interface phase are damaged, its protection of the inner columns and those in contact with the θ′-Al_2Cu phase decreases, leading to gradual diffusion of the inner elements. When the in-situ heating time reaches 95 min, as shown in Fig. 4-33f, the white arrow indicates the position of Ag atomic columns in the innermost layer of the χ-AgMg interface phase in contact with the θ′-Al_2Cu phase. After heating for a long time, the brightness at this position gradually decreases and eventually becomes consistent with the Al matrix, indicating that the uppermost part of the χ-AgMg interface phase has completely dissolved into the matrix.

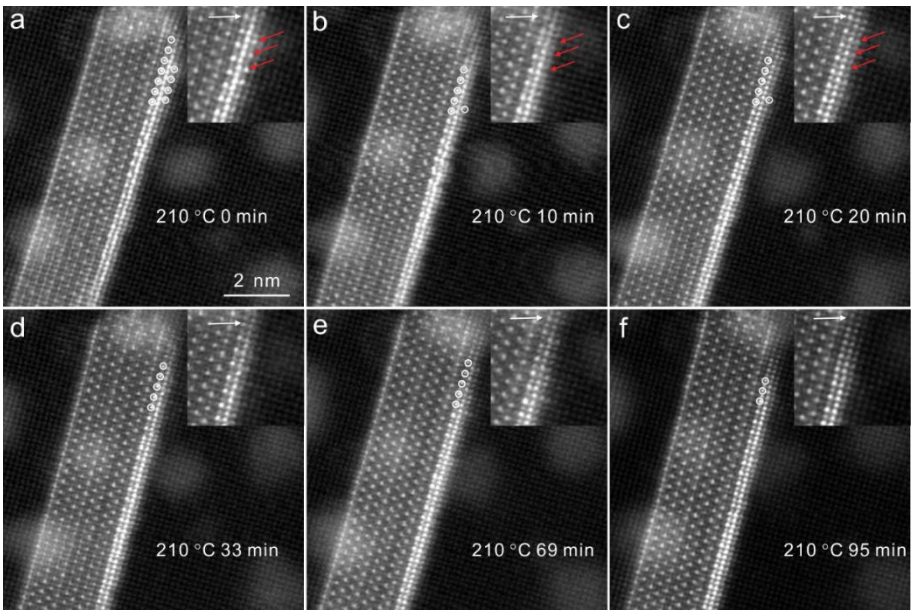

Figure 4-33 Atomic resolution HAADF-STEM images of the χ-AgMg interface phase after in-situ heating at 210 °C for different times

Combining the TEM in-situ heating experiments and the results of AIMD simulations, it is shown that in the early stages of high-temperature thermal exposure, Ag atoms in the outermost atomic column in contact

with the Al matrix gradually diffuses, leading to structural damage of the outermost atomic columns and consequently reducing their protection of the inner columns. As the thermal exposure time increases, Ag diffusion also occurs in the inner atomic columns of the χ-AgMg interface phase, leading to gradual structural damage of the χ-AgMg interface phase from the end towards the interior, ultimately dissolving into the matrix. In ex-site TEM characterizations, the χ-AgMg interface phase in samples thermally exposed at 210 ℃ for different durations all disappeared from both ends, and no structure defects leading to the dissolution of the χ-AgMg interface phase from the middle were observed, which verified the experimental results of the in-situ TEM heating.

4.6.3 TEM investigation on the structure evolution of the C-AlMgSiCu interface phase

AIMD simulations have shown that the C-AlMgSiCu interface phase exhibits higher thermal stability during thermal exposure. To verify the accuracy of the AIMD results, ex-situ TEM research was conducted on samples thermally exposed at 210 ℃ for different times to investigate the thermal stability of C-AlMgSiCu interface phase.

Fig. 4-34 shows the atomic-resolution HAADF-STEM image of the alloy after thermal exposure at 210 ℃ for 4 hours. The disordered L-AlMgSiCu interface phase at the θ′/Al interface exhibits smaller size and no significant change. However, for the C-AlMgSiCu interface phase at the θ′/Al interface, its orientation differs from that in the peak-aged state. As shown in Fig. 4-34d, at the θ′/Al coherent interface, one side exhibits the χ-AgMg interface phase, while the other side shows an interface phase with lower brightness but a different structure from the C-AlMgSiCu interface phase along the $[010]_C$ zone axis. According to its atomic

arrangement, this interface phase is still the C-AlMgSiCu interface phase, but its growth direction is different, along the $[001]_C$ zone axis. Therefore, the structure of the C-AlMgSiCu interface phase along the $[010]_C$ zone axis shows no significant change after thermal exposure at 210 ℃ for 4 h, but a C-AlMgSiCu interface phase along the $[001]_C$ zone axis is observed at the θ′/Al coherent interface.

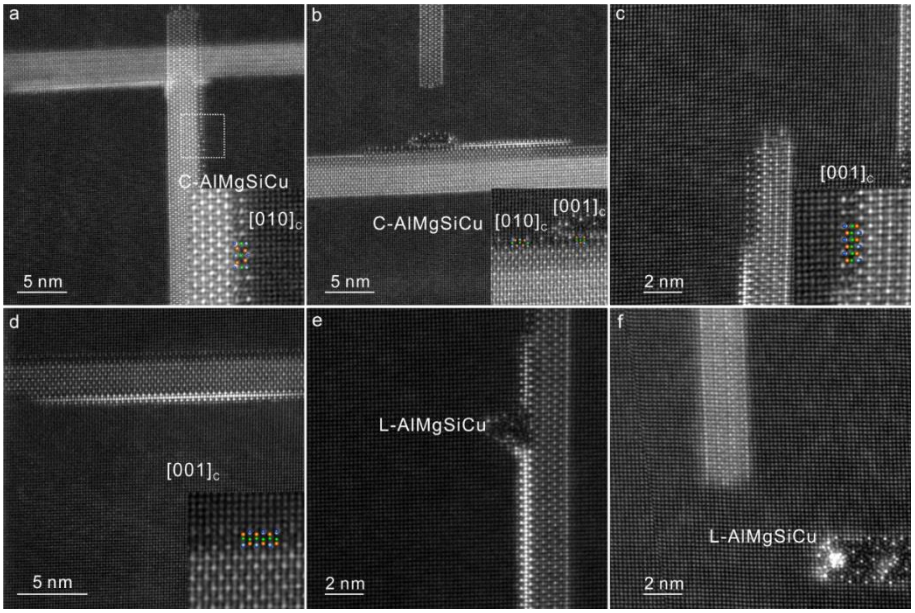

Figure 4-34 HAADF-STEM images of the C/L-AlMgSiCu phase under different directions in the alloy thermally exposed at 210 ℃ for 4 h

The atomic-resolution HAADF-STEM image of the alloy after thermal exposure at 210 ℃ for 12 h is shown in Fig. 4-35. With the increase in thermal exposure time, the size of the disordered L-AlMgSiCu interface phase at the θ′/Al interface gradually increases. That is, the thermal stability of the disordered L-AlMgSiCu phase decreases at 210 ℃. As for the C-AlMgSiCu interface phase at the θ′/Al coherent interface, the C-AlMgSiCu interface phases along both the $[001]_C$ and $[010]_C$ zone axes

are observed. However, the C-AlMgSiCu interface phase along the $[010]_C$ zone axis, which is the same as that in the peak aged state, is still the main type.

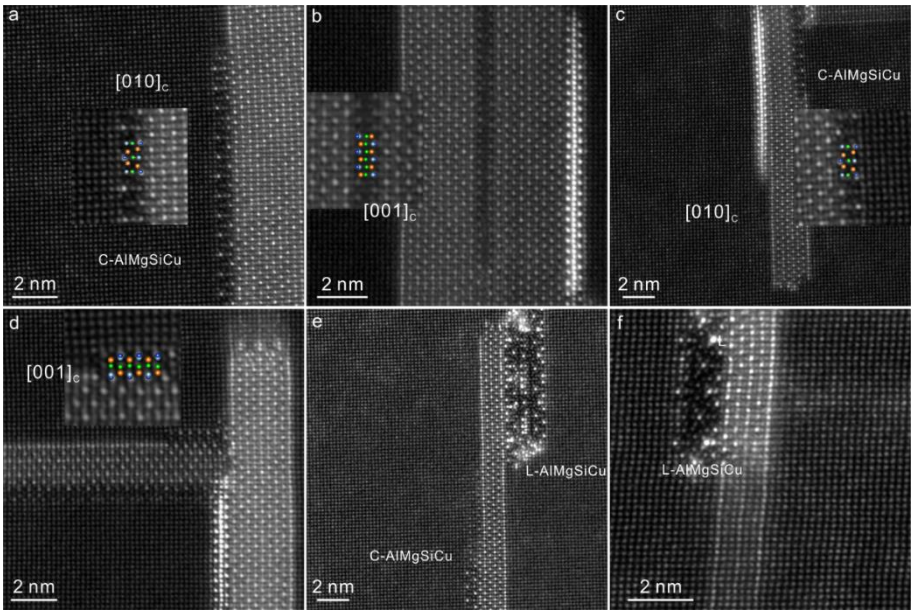

Figure 4-35 HAADF-STEM images of the C/L-AlMgSiCu phase under different directions in the alloy thermally exposed at 210 ℃ for 12 h

Fig. 4-36 shows the atomic-resolution HAADF-STEM image of the alloy after thermal exposure at 210 ℃ for 24 h. As the thermal exposure time continues to increase, there is no significant change in the type of C-AlMgSiCu interface phase at the θ′/Al coherent interface compared to the alloy under short-term thermal exposure conditions. However, Fig. 4-36d indicates a trend of coarsening in the C-AlMgSiCu interface phase after thermal exposure for 24 h. As indicated by the white arrow, regular arrays of Cu atoms appear at the interface between the C-AlMgSiCu interface phase and the aluminum matrix, and the continuous aggregation of Cu atoms can promote the coarsening of the C-AlMgSiCu interface phase.

When the thermal exposure time is extended to 48 hours, the atomic-resolution HAADF-STEM image, as shown in Fig. 4-37, reveals the appearance of a complete lattice structure of the C-AlMgSiCu phase at the lower end of the C-AlMgSiCu interface phase. This indicates a trend of growth in the C-AlMgSiCu interface phase during long-term exposure to 210 ℃. In addition, after the alloy was thermally exposed at 210 °C for 24 h and 48 h, C-AlMgSiCu interface phases growing in different directions were still present in the alloy.

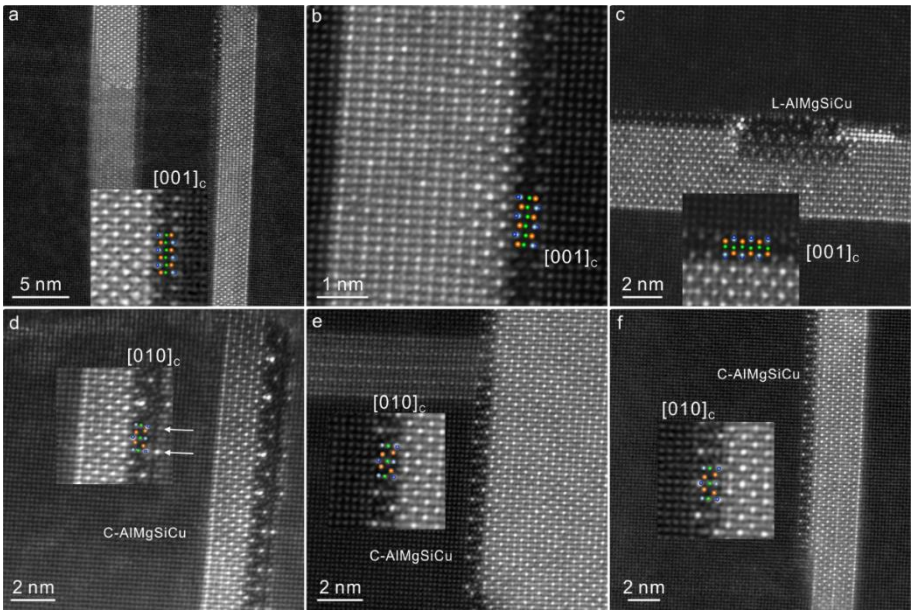

Figure 4-36 HAADF-STEM images of the C/L-AlMgSiCu phase under different directions in the alloy thermally exposed at 210 ℃ for 24 h

The ex-situ TEM research of alloys under different thermal exposure conditions indicates that the growth direction of the C-AlMgSiCu interface phase changes during thermal exposure, transitioning from mainly along the $[010]_C$ zone axis in the peak-aged state to coexistence along both the $[001]_C$ and $[010]_C$ zone axes. However, the types are all C-AlMgSiCu

interface phases, further confirming the higher thermal stability of the C-AlMgSiCu interface phase during thermal exposure. That is, the C-AlMgSiCu interface can effectively inhibit the diffusion of elements, thereby suppressing the coarsening of the θ′-Al_2Cu.

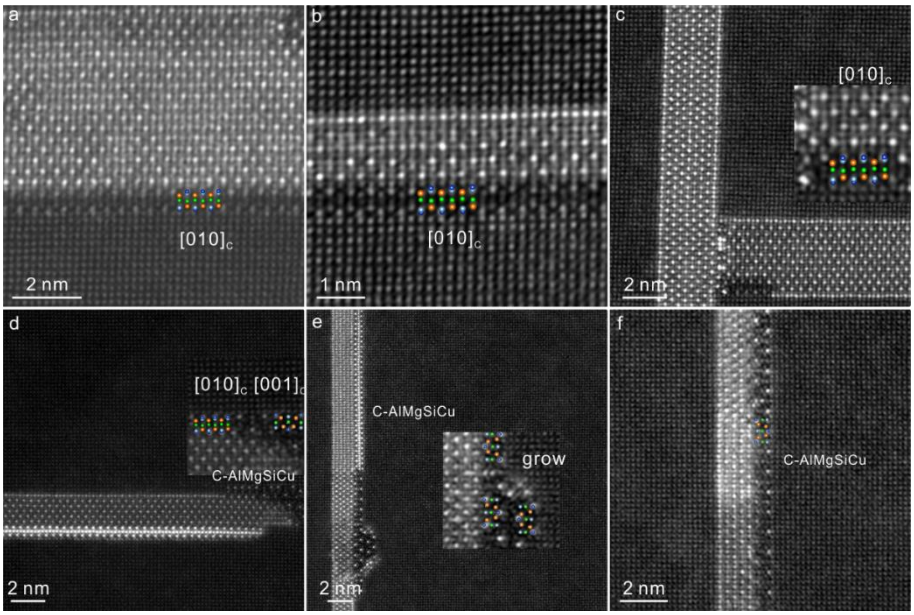

Figure 4-37 HAADF-STEM images of the C/L-AlMgSiCu phase under different directions in the alloy thermally exposed at 210 ℃ for 48 h

As for the C-AlMgSiCu interface phase growing along the $[001]_C$ zone axis, the structures shown in Figs. 4-34c and 4-37c show that it may be based on Cu atomic columns in the θ′-Al_2Cu phase, and the growth direction change may be achieved through the diffusion of Mg/Si elements, but the specific growth mechanism still requires further investigation. Furthermore, even though the C-AlMgSiCu and disordered L-AlMgSiCu interface phases have high thermal stability, both interface phases exhibit a trend of coarsening after thermal exposure at 210 °C for 24 h. The coarsening of both interface phases requires the consumption of solute

atoms such as Cu, Mg, and Si, leading to the dissolution of smaller C/L-AlMgSiCu interface phases, thereby reducing the number density and volume fraction of precipitates containing MgSiCu elements in the alloy. Therefore, the mechanical properties of the alloy still decreases after long-term thermal exposure.

Fig. 4-38 shows the EDX mapping and line scan results of the C-AlMgSiCu interface phase along the $[001]_C$ zone axis after thermal exposure at 210 ℃ for 24 h. The results indicate that, consistent with the peak-aged state, the main elements are Mg and Si, with no significant enrichment of Ag elements.

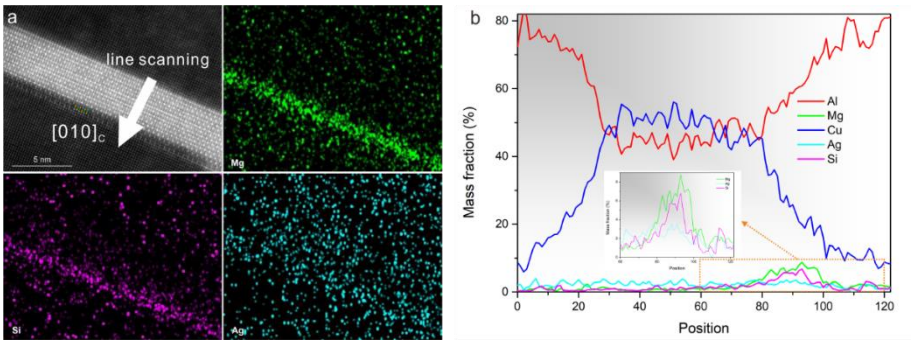

Figure 4-38 The EDX results of the C-AlMgSiCu interface structure under $[001]_C$ direction in the alloy thermally exposed at 210 ℃ for 24 h. (b) is the line scanning result for the area indicated by arrow in the (a). The small picture in (b) is a partial enlargement of the orange area

The EDX result of different precipitates in the alloy after thermal exposure at 210 ℃for 24 h are shown in Fig. 4-39. The EDX results indicate that there is Ag segregation at the interface disordered L and Al matrix. The research of Weng et al.[185, 195, 196] showed that the Ag tends to segregate at the interface between the precipitates such as L/QP1/Q′-AlMgSiCu and the aluminum matrix in the over-aged state. Therefore,

during the thermal exposure process, the dissolution of the χ-AgMg interface phase leads to the presence of supersaturated Ag solute atoms in the aluminum matrix. Part of the supersaturated Ag solute atoms precipitates as the ξ-AgMgAl phase, while the other part enriches at the boundaries of the disordered L phase. As for the C-AlMgSiCu interface phase along the $[010]_C$ at the θ′/Al coherent interface, consistent with the results of the C-AlMgSiCu interface phase along the $[001]_C$ in Fig. 4-38, there is no significant Ag segregation at its interface.

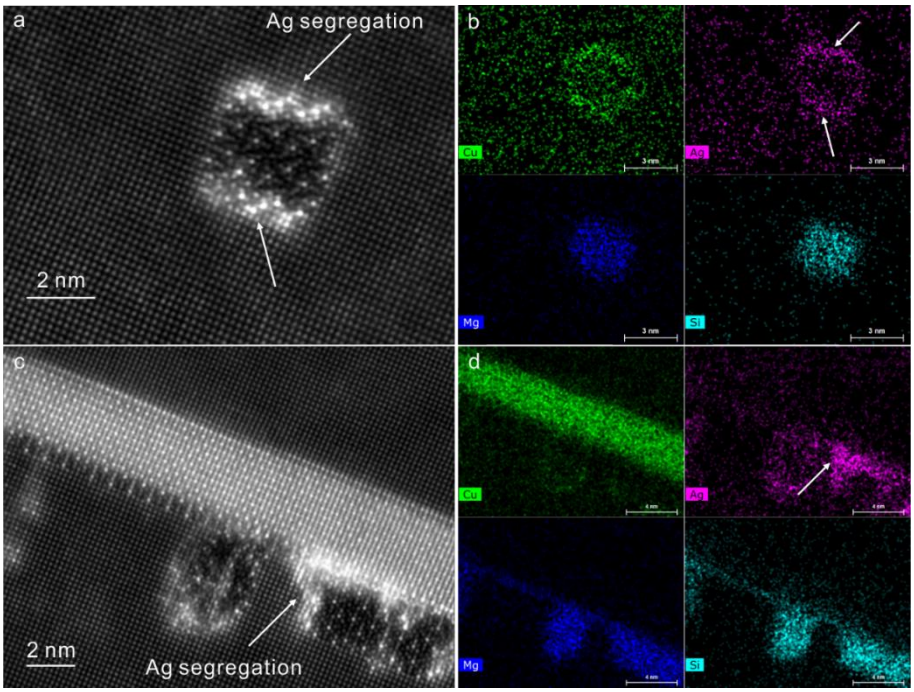

Figure 4-39 (a-b) Atomic-resolution HAADF-STEM image and EDX maps of the disordered L-AlMgSiCu phase in the matrix of the alloy thermally exposed at 210 ℃ for 24 h. (c-d) Atomic-resolution HAADF-STEM image and EDX maps of the C/L-AlMgSiCu interface phases at the θ′/Al interface in the alloy thermally exposed at 210 ℃ for 24 h

4.7. Summary of this chapter

In this chapter, based on CALPHAD, the content of each element in the Al-Cu-Mg-Ag-Si-Sc alloy was reasonably controlled, achieving a synergistic enhancement of strength and heat resistance in the Al-Cu-Mg-Ag alloy. Furthermore, combined with multiscale characterization and first-principles calculations, the effects of different precipitate structures on mechanical properties and heat resistance were analyzed. The main conclusions are as follows:

(1) The concept of constructing multiple interface segregation structure containing interface phases and segregation layers at the precipitate/matrix interface was proposed. Combined with CALPHAD, the alloy designed based on this concept achieved a yield strength of 400 MPa after thermal exposure at 200 ℃ for 100 h, with a strength retention rate of 97%. This sets a new record for the synergistic enhancement of strength and heat resistance in aluminum alloys. At the same time, the concept of constructing multiple segregation structure at the precipitate/matrix interface can provide references for the design of other heat-resistant materials.

(2) A multiple interface segregation structure containing C/L-AlMgSiCu interface phase, χ-AgMg interface phase, and Sc segregation layer was constructed at the θ′/Al coherent and semi-coherent interfaces in the designed alloy under peak-aged state. This multiple interface segregation structure effectively hindered the coarsening of θ′-Al_2Cu phase during thermal exposure, thereby improving the heat resistance of the alloy. Moreover, the added Si promoted the formation of C/L-AlMgSiCu phase in the early ageing stage, which further served as heterogeneous nucleation sites for θ′-Al_2Cu phase, promoting the precipitation of θ′-Al_2Cu phase and enhancing the room temperature

mechanical properties of the alloy, ultimately achieving a synergistic enhancement of strength and heat resistance.

(3) The χ-AgMg interface phase is a newly discovered three-layer atomic interface phase. Based on atomic resolution HAADF-STEM and EDX data, a crystal model of this structure was successfully constructed. Ex-situ/in-situ TEM characterization and AIMD calculations showed that Ag atoms near the aluminum matrix in the χ-AgMg interface phase were prone to diffuse into the matrix at high temperatures, causing the structure to gradually be destroyed and eventually dissolve into the matrix. However, the presence of the χ-AgMg interface phase can still inhibited the coarsening of θ′-Al_2Cu phase to a certain extent. In contrast, the C-AlMgSiCu phase has higher thermal stability can better hinder the coarsening of the θ′-Al_2Cu phase during long-term thermal exposure.

(4) After the χ-AgMg interface phase dissolves into the matrix, larger σ-$Al_5Cu_6Mg_2$ and ξ-AgMgAl phases were formed. Combined with multiscale ex-situ TEM characterization, σ phase can act as nucleation sites, promoting the precipitation of ξ-AgMgAl phase.

Chapter 5. Revisiting the effect of Ag additions on Ω precipitation and heat resistance of Al-Cu-Mg-Si-Ag alloys

5.1 Foreword

In Chapter 4, the design process of heat-resistant aluminum alloy referenced the research of Gable et al.[119, 197] on the effect of Mg/Si mass ratio on the precipitation behavior of Ω phase in Al-Cu-Mg-Ag-Si alloy. The results showed that when the Mg/Si mass ratio is less than 2, the precipitation of Ω phase will be completely inhibited. However, studies by Bai et al.[81, 171] and Zhou et al.[149] indicated that increasing the content of Ag can inhibit the formation of θ′-Al_2Cu phase and promote the precipitation of Ω phase in Al-Cu-Mg-Ag alloy. Therefore, the increase of Ag content can inhibit the formation of θ′-Al_2Cu phase and promote the precipitation of Ω phase[198-200], while the addition of Si will inhibit the precipitation of Ω phase and promote the formation of θ′-Al_2Cu phase. When Si and Ag are added to the alloy at the same time, their inhibition and promotion effects on the precipitation of Ω phase will compete. In addition, in the study of Gable et al.[119, 197], the Ag content in the alloy was only 0.3 wt.%, which is relatively low. Therefore, it remains questionable whether simply increasing the Ag content in low Mg/Si mass ratio Al-Cu-Mg-Ag-Si alloys can promote the precipitation of the Ω phase.

In this study, two groups of Al-Cu-Mg-Ag-Si alloys with different Ag contents, namely Al-4Cu-0.4Mg-0.2Si-0.5Ag and Al-4Cu-0.4Mg-0.2Si-0.8Ag, were used to investigate the effect of Ag content in low Mg/Si mass ratio alloys on the precipitation behavior of the Ω phase and alloy properties. Quantitative results such as SEM, TEM, EBSD and mechanical

properties show that when the Mg/Si mass ratio in the alloy is less than 2, increasing the Ag content can promote the precipitation of Ω phase. Based on the above results, the critical conditions for the precipitation of Ω phase in Al-Cu-Mg-Ag-Si alloys are proposed, which helps us design a new heat-resistant aluminum alloy system with different Ω/θ′ phase ratios according to service conditions.

5.2 Mechanical properties of Al-Cu-Mg-Ag-Si alloys with low Mg/Si ratio

As shown in Fig. 5-1a, in the early stage of ageing, the microhardness of the alloys increased rapidly, and the alloys with different Ag content both reached the peak aged state after 4 hours of ageing. The microhardness of 0.8Ag and 0.5Ag alloys under peak aged state are 165.79 ± 3.10 HV and 165.6 ± 3.83 HV, respectively. After reaching the peak ageing, the microhardness of both alloys gradually decreased with the extension of ageing time, while the 0.8Ag alloy showed a more significant decrease in the microhardness.

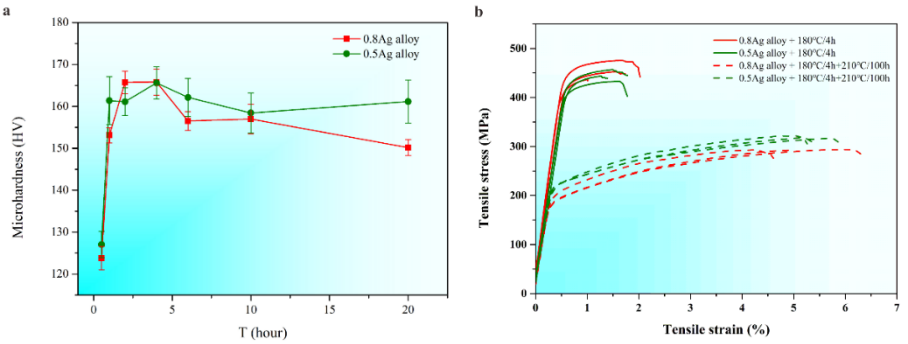

Figure 5-1 Mechanical properties of different alloys. (a) is the microhardness of different alloys under different ageing conditions, and (b) shows the stress-strain curves of the peak aged alloys before and after thermal exposure

The stress strain curves of different alloys under different ageing conditions are shown in Fig. 5-1b. The yield strength of 0.8Ag and 0.5Ag alloys under peak aged state are 437 ± 13 MPa and 428 ± 9 MPa, respectively. When the peak aged alloys were thermally exposed at 210℃ for 100 h, the yield strength of 0.8Ag and 0.5Ag alloys drop to 199 ± 7 MPa and 225 ± 1 MPa, respectively. That is, increasing the content of Ag could slightly improve the strength of the alloys under the peak ageing condition but reduces heat resistance of Al-Cu-Mg-Ag-Si alloys. As for the elongation of the alloys, Liang et al.[201] and Li et al.[20] reported that Si addition to the Al-Cu-Mg alloys would reduce the elongation of the alloys. Thus, the elongation of the 0.8Ag and 0.5Ag alloys under the peak ageing condition is relatively low, which is around 2%. After thermal exposure, the elongation of both alloys is increased as the tensile properties decrease.

5.3 Multi-scale microstructure of Al-Cu-Mg-Ag-Si alloys with low Mg/Si ratio

5.3.1 Micro scale structures of the alloys after solid solution treatment

The micro scale constitutes and corresponding EDX spectra of the 0.8Ag and 0.5Ag alloys are shown in Fig. 5-2a and Fig. 5-2b, respectively. After the homogenization heat treatment, most of the micro scale constituents had been dissolved to the Al matrix, thus there is a small number of dot-like micro-scale constituents in both alloys. According to the calculated vertical section of the Al-Cu-Mg-Si-Ag quinary phase diagram in Fig. 5-3, ideally there should be no constituents in both alloys after homogenization heat treatment at 530 °C. The existence of the dot-like constituents may be caused by the incomplete dissolution of the micro-scale constituents in the alloy due to the insufficient homogenization time.

The EDX spectra shown in Fig. 5-2 show that the dot-like constituents contain Al, Cu and Ag. However, due to the small size of the constituents, the EDX results may be influenced by matrix composition. The detected content of Ag in the matrix is about 2.3 at. %, which is higher than that in the dot-like constituents. Therefore, the Ag was dissolved in the matrix almost completely in both alloys after homogenization, and the constituents might be the Al_2Cu phase [101].

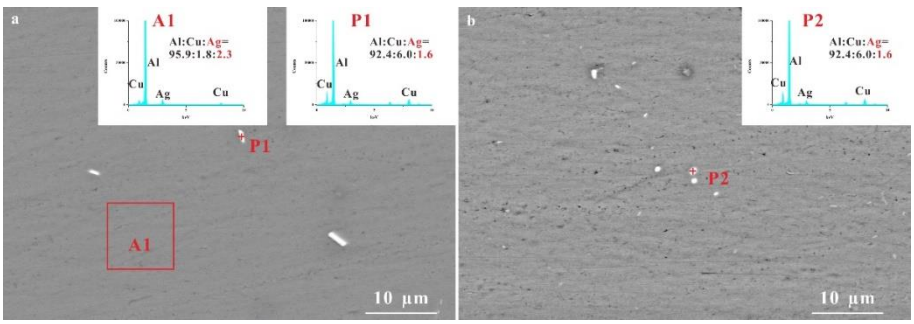

Figure 5-2 Microstructure of (a) 0.8Ag alloy and (b) 0.5Ag alloy after homogenization heat treatment

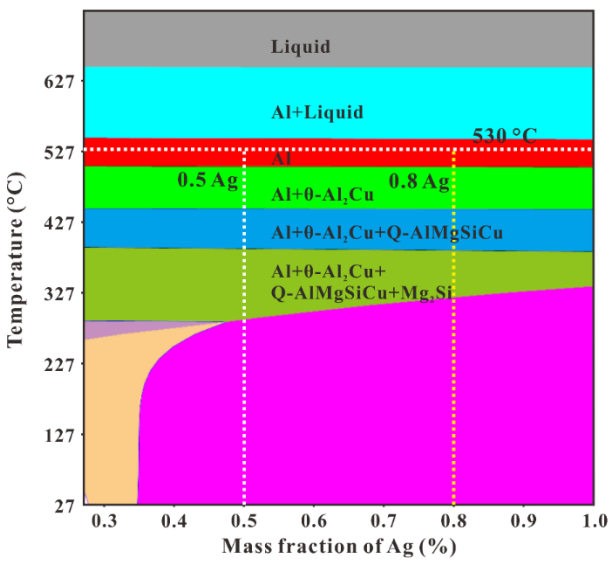

Figure 5-3 Vertical section at the composition Al-4Cu-0.4Mg-0.2Si-*x*Ag (wt.%)

5.3.2 Nano scale precipitates under peak ageing

According to the HAADF-STEM images and HRTEM images shown in Fig. 5-4, there are Ω, θ′-Al_2Cu and L-AlMgSiCu (the disordered version of C-$AlMg_4Si_3Cu$ phase, also named QP2 or Q″)[112, 191, 202] precipitates in the 0.8Ag alloy, while no Ω phase has been found in the 0.5Ag alloy under different zone axes.

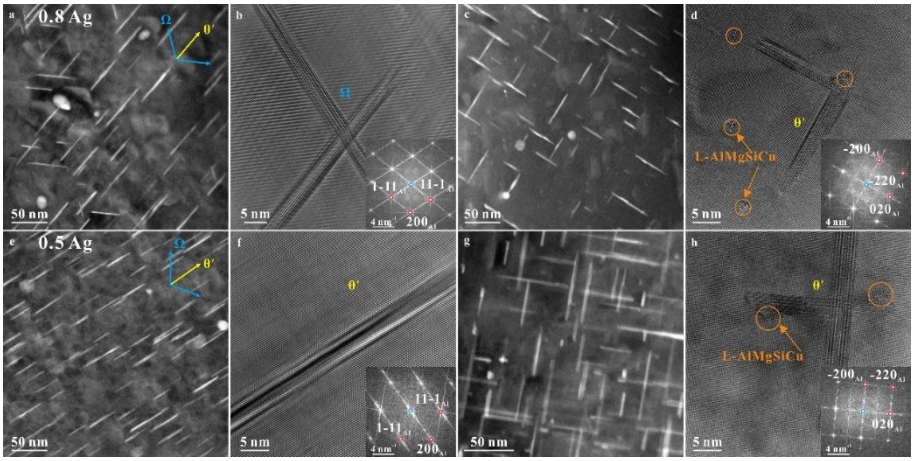

Figure 5-4 The nano-scale precipitates in the different alloys under peak aged state. (a) and (c) are the HAADF-STEM images of 0.8Ag alloy along $[110]_{Al}$ and $[001]_{Al}$ zone axes, respectively. (b) and (d) are the HRTEM images of Ω phase and θ′-Al_2Cu in 0.8Ag alloy along the two axes, respectively. (e) and (g) show the HAADF-STEM images of 0.5Ag alloy along these two axes, and the HRTEM images of θ′-Al_2Cu are shown in (f) and (h), respectively. The corresponding fast Fourier transform (FFT) patterns are inserted in the HRTEM images.

Therefore, it has been concluded that not only Mg/Si but also Ag content can affect the precipitation of Ω phase in Al-Cu-Mg-Ag-Si alloys. According to the statistical results measured using HAADF-STEM images of 0.8Ag alloy under peak aged state, the numbers of Ω and θ′-Al_2Cu precipitates in the same area are 83 and 289, respectively. The Ω and θ′-

Al_2Cu precipitate on the $\{100\}_{Al}$ and $\{111\}_{Al}$ habit planes, respectively. When the zone axis of the observed areas is $[011]_{Al}$, the θ′-Al_2Cu precipitates grown on the (100) plane and the Ω precipitates grown on the $(11\bar{1})$ and $(\bar{1}1\bar{1})$ planes can be observed. Therefore, when the thickness is not considered, the numbers of observed θ′-Al_2Cu and Ω precipitates are 1/3 and 1/2 of total numbers of θ′-Al_2Cu and Ω precipitates, respectively. Thus, the actual number of θ′ phases is 867, and that of Ω phases is 166 (see Tab. 5-1).

Table 5-1 The number of different precipitates in the same large region in 0.8Ag alloy under peak ageing

	θ′	Ω	θ′ + Ω
Observed	289	83	
Actual	867	166	1033
Percentage	83.9%	16.1%	100%

Ag and Mg elements will not only segregate at the Ω/Al interface, but also at the θ′/Al interface. Fig. 5-5 shows the EDX elemental maps of precipitates in different alloys. In addition to evenly distributed AgMg segregation layers at the Ω/Al interface, the unevenly distributed AgMg segregation layers were also found in the 0.8Ag alloy, while there were only unevenly distributed AgMg segregation layers in the 0.5Ag alloy. The atomic structure of the unevenly distributed AgMg segregation layers observed in 0.8Ag alloy was shown in Fig. 5-6. There are three atom layers in the newly discovered AgMg interface phase. The Ag (bight) and Mg (dark) atomic columns alternately arrange in each of the 1st and 3rd layers while the 2nd layer is comprised of alternative Ag (bight) and Ag+Mg (less bight) columns. That is, the unevenly distributed AgMg segregation layers in 0.8Ag and 0.5Ag alloys are also the recently discovered χ-AgMg interface phase.

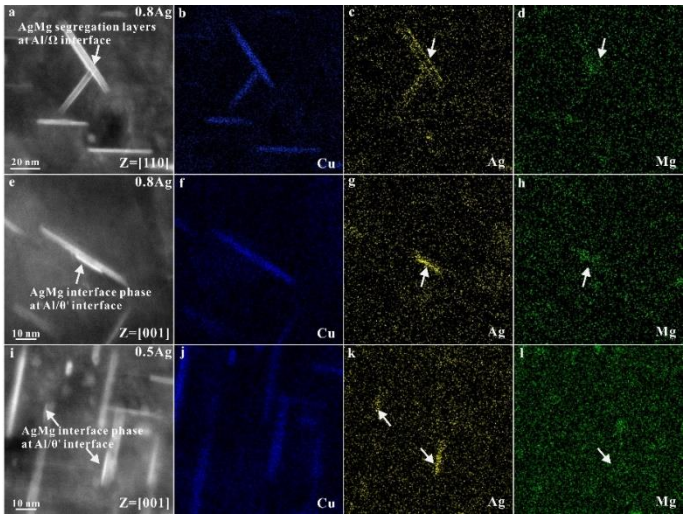

Figure 5-5 The HAADF images and EDX elemental maps of nano-scale precipitates in different alloys. (a) and (e) show the HAADF-STEM images in 0.8Ag alloy along [110] and [001] zone axes, while (b-d) and (f-h) show the corresponding EDX elemental maps, respectively. The precipitates in 0.5Ag alloy along [001] zone axis is shown in (i), while the corresponding EDX elemental maps are shown in (j-l).

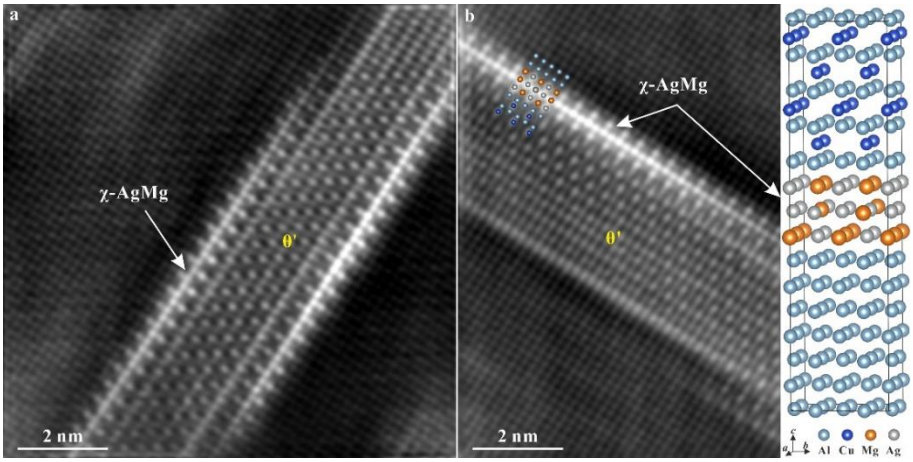

Figure 5-6 The atomic resolution HAADF-STEM images of the χ-AgMg interface phase at the θ′/Al interface in peak aged 0.8Ag alloy. The crystal information of interface structure containing χ-AgMg is inserted in (b).

In addition to the χ-AgMg interface phase at the θ′/Al interface, there are C/L-AlMgSiCu interface phases. As shown in Fig. 5-7, the C-AlMgSiCu interface phase exists at the coherence θ′/Al interface, while the disordered L-AlMgSiCu phase with interrupted C unit cells precipitates at the edge of the θ′-Al_2Cu. Marioara et al.[168] reported that the disordered L-AlMgSiCu had high thermal stability, thereby improving the heat resistance of alloys. Therefore, there are multiple interface structures including χ-AgMg and C/L-AlMgSiCu at the coherence/semi-coherence θ′/Al interface in both alloys. Based on the work in Chapter 4, the multiple interface structures had been proven to be effective in inhibiting the coarsening of θ′-Al_2Cu, thereby improving the heat resistance of the alloys. It was also found the C interface phase is quite tough during thermal exposure.

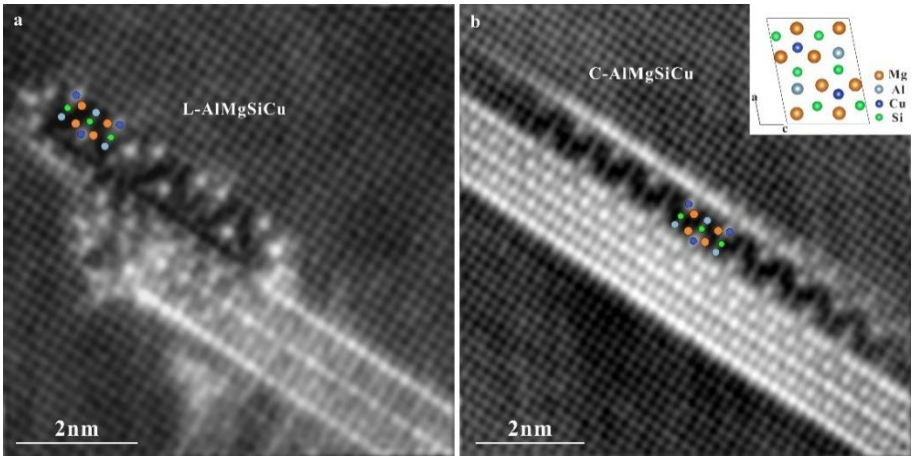

Figure 5-7 The atomic resolution HAADF-STEM images of the θ′-Al_2Cu with C-AlMgSiCu interface phase in peak aged 0.8Ag alloy. The crystal information of C phase is inserted in (b).

5.3.3 Nano scale precipitates after thermal exposure

Similar to the alloys in peak-aged state, as shown in Fig. 5-8, Ω still

only exists in the 0.8Ag alloy, while there are θ′-Al_2Cu phases in both alloys after thermal exposure.

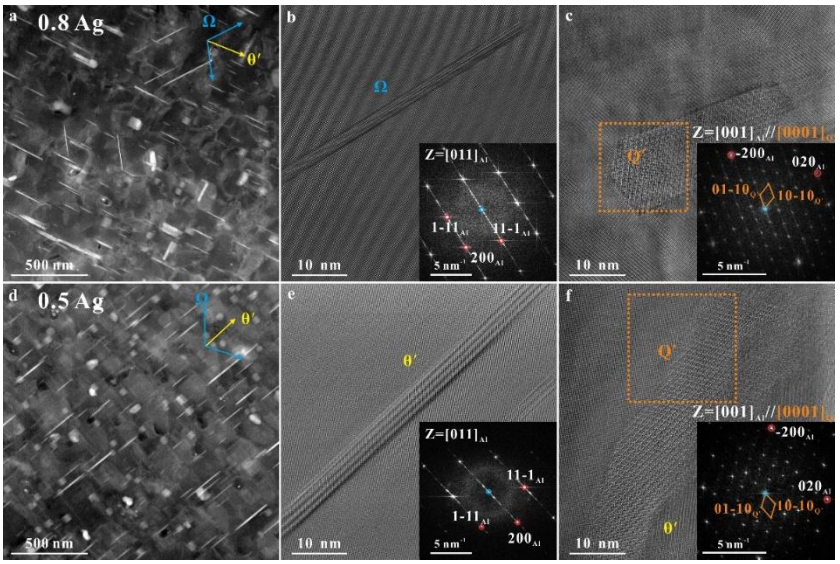

Figure 5-8 The nano-scale precipitates in the different alloys after thermal exposure. (a) is the HAADF-STEM image of 0.8Ag alloy along $[011]_{Al}$. (b) and (c) are the HRTEM images in 0.8Ag alloy along $[011]_{Al}$ and $[001]_{Al}$, respectively. (d) shows the HAADF-STEM image of 0.5Ag alloy along $[011]_{Al}$, and the HRTEM images along $[011]_{Al}$ and $[001]_{Al}$ are shown in (e) and (f), respectively. The corresponding Fast Fourier Transform (FFT) patterns are inserted in the HRTEM images.

However, the statistic results for 0.8Ag alloy, as given in Tab. 5-2, shows that the percentage of Ω phase drop significantly from 16.1% to 2.4% after thermal exposure heat treatment. According to Figs. 5-8, 5-9 and 5-10, in addition to θ′-Al_2Cu, the square σ-$Al_5Cu_6Mg_2$ [109], ξ-AgMgAl, irregularly shaped AgMg phase and lath-like Q′-$Al_3Cu_2Mg_9Si_7$ [191] precipitated in both alloys during thermal exposure heat treatment. That is, the thin χ-AgMg interface phase also disappeared and the thick ξ-AgMgAl

interface phase (shown in the white dashed box in Fig. 5-10a) precipitated at the σ/Al interface after thermal exposure.

Table 5-2 The number of different precipitates in the same large region in 0.8Ag alloy after thermal exposure

	θ′	Ω	θ′ + Ω
Observed	1714	62	
Actual	5142	124	5266
Percentage	97.6%	2.4%	100%

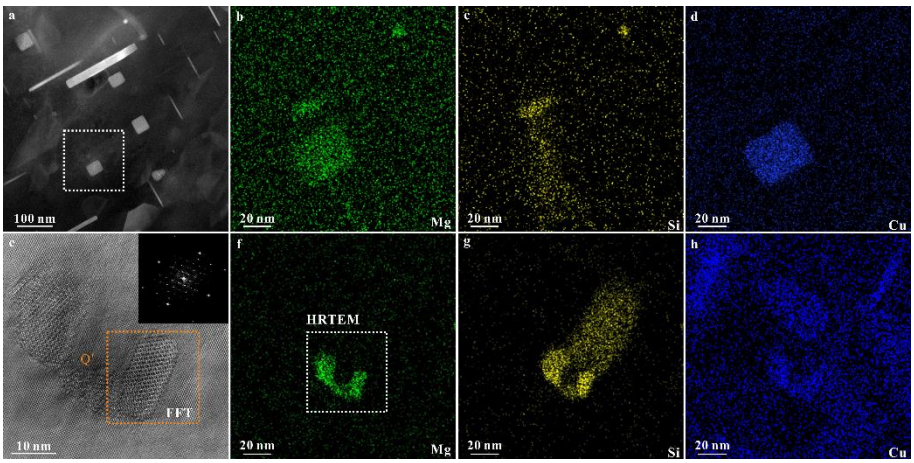

Figure 5-9 TEM images and EDX elemental maps of precipitates in 0.8Ag alloy after thermal exposure. (a) is the HAADF STEM image. (b-d) are the corresponding EDX elemental maps of the area marked by the white dashed box. (e) shows the HRTEM image along $[001]_{Al}$, while the corresponding EDX elemental maps of e are shown in (f-h), which is marked by the white dashed box. The corresponding Fast Fourier Transform (FFT) pattern of Q′ marked by orange dashed box is inserted in (e).

In addition, Ding et al.[191] reported that the L-AlMgSiCu (or termed QP2) phase is the precursor phase of Q′-$Al_3Cu_2Mg_9Si_7$. That is, the independently L-AlMgSiCu and C/L-AlMgSiCu interface phase

precipitated during the artificial ageing heat treatment gradually grew and transformed to Q′-$Al_3Mg_9Si_7Cu_2$. Furthermore, the size of Q′-$Al_3Mg_9Si_7Cu_2$ is larger than that of L-AlMgSiCu by comparing Fig. 5-8 with Fig. 5-4. Therefore, the phase transition during the thermal exposure heat treatment gradually led to a decrease in the number density of L-AlMgSiCu at semi-coherence θ′/Al interface and partly destroyed the multiple interface structures. As a result, the corresponding inhibiting effect on coarsening of θ′-Al_2Cu is reduced, resulting the significantly decline in the mechanical properties of both alloys after thermal exposure.

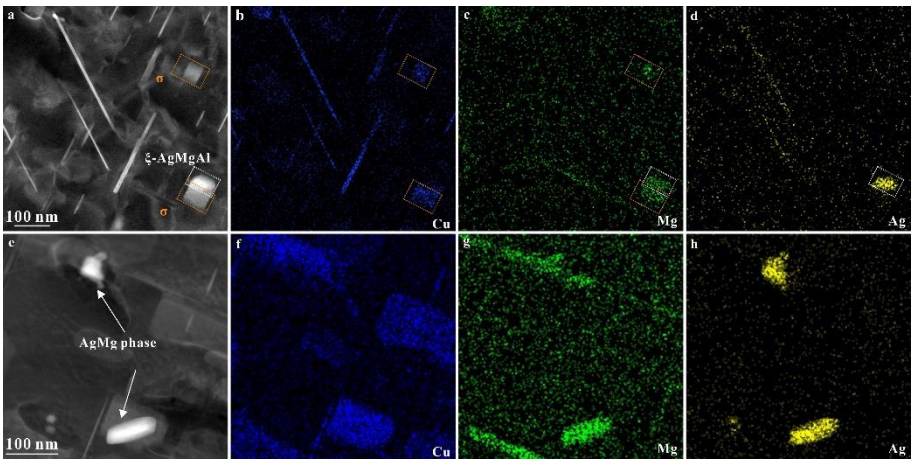

Figure 5-10 HAADF-STEM images and EDX elemental maps of precipitates in 0.8Ag alloy after thermal exposure. (a) and (e) are the HAADF STEM images, (b-d) and (f-g) show the corresponding EDX elemental maps.

5.4 Anomalous decrease in heat resistance due to increase of Ag content

The tensile test results show that increasing the content of Ag in Al-Cu-Mg-Ag-Si alloys improves the yield strength of the alloys, but reduces the heat resistance of the alloys. As for the age hardenable aluminum alloys, the yield strength of the alloys at room temperature could be calculated by

the following equation[203-208]:

$$\sigma_y = \sigma_{ss} + \sigma_g + \sigma_{ppt} \tag{5-1}$$

where the σ_y is the total strength of the age hardenable aluminum alloy, σ_{ss} and σ_g represent the solid solution strengthening effect and the grain size strengthening effect, respectively. σ_{ppt} is the contribution of precipitation strengthening to the overall strength.

According to the Tab. 2-1, the contents of main solute elements except Ag are similar in different alloys. In addition, under peak aged state, the supersaturated solute elements basically form different types of precipitates or AgMg segregation layers. Therefore, the remaining contents of solute elements in the matrix of both alloys are similar and the contribution of solid solution strengthening (σ_{ss}) is almost the same in both 0.8Ag and 0.5Ag alloys. Meanwhile, the grain size of different alloys is shown in Fig. 5-11. After rolling process and artificial ageing heat treatment, the grain size of the 0.8Ag alloy is consistent with that of 0.5Ag alloy. That is, the contribution of grain size strengthening (σ_g) is similar in both 0.8Ag and 0.5Ag alloys. Therefore, the superior strength of the 0.8Ag alloy over the 0.5Ag alloy under the peak aged state is mainly due to the difference in precipitation strengthening.

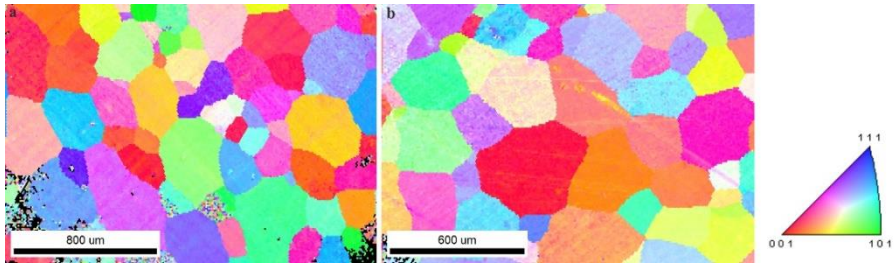

Figure 5-11 The EBSD inverse pole images of 0.8Ag and 0.5Ag alloys under peak aged condition. The average grain diameter of (a) 0.8Ag and (b) 0.5Ag alloys are 201 ± 111 and 180 ± 99 μm, respectively.

As shown in Fig. 5-4, θ′-Al_2Cu and L-AlMgSiCu phases are present in both 0.8Ag and 0.5Ag alloys, while Ω phase is present only in the 0.8Ag alloy. In addition, the content of Si in 0.8Ag alloy is consistent with that in 0.5Ag alloy. Therefore, the volume fraction of L-AlMgSiCu phase is similar in both 0.8Ag and 0.5Ag alloys as only L-AlMgSiCu phase consume Si content during artificial ageing heat treatment. Fig. 5-12 shows the diameter distribution of θ′-Al2Cu and Ω phase in both alloys under peak aged state.

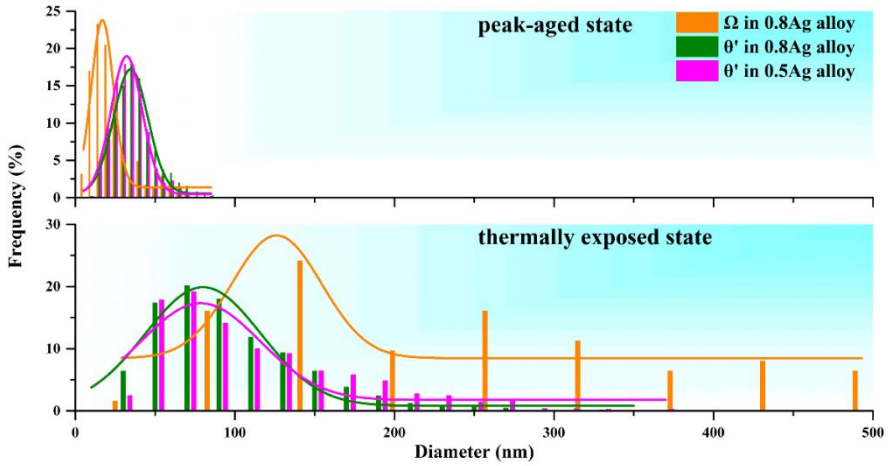

Figure 5-12 The diameter distribution of θ′-Al_2Cu and Ω phase in different alloys, under peak aged state and thermally exposed state.

The average diameter of Ω phase is 22.7 ± 13.2 nm, while the average diameters of θ′-Al_2Cu in 0.8Ag and 0.5Ag alloys are 36.6 ± 12.7 nm and 34.8 ± 12.8 nm, respectively. As mentioned above, the main body (i.e., core) of Ω phase is an orthorhombic Al_2Cu [48] (space group: *Fmmm*， a = 0.496 nm, b = 0.859 nm and c = 0.848 nm), while the θ′ is an Al_2Cu phase with tetragonal structure [209, 210] (space group *I4/mmm*, a = 0.404 nm, c = 0.580 nm). Therefore, the Ω core has the same composition as the θ′ phase.

In addition, the diameter of Ω phase is smaller than that of θ′ phase in the 0.8Ag alloy. As a result, it is speculated that a larger number of fine Ω precipitates and coarse θ′ precipitates can be generated in the 0.8Ag alloy, than the coarsen θ′ precipitates in the 0.5Ag alloy, as the two alloys have highly similar amounts of solutes (except for Ag) in the supersaturated solid solution and almost the same size for θ′ precipitates. Thus, the total number density of precipitates is higher in the 0.8Ag alloy, improving its yield strength.

After heat exposure treatment at 210 ℃ for 100 h, the yield strength of the 0.8Ag alloy turned to be lower than those of the 0.5Ag alloy. Before the thermal exposure process, both alloys were in the peak aged state, i.e., almost all solutes in the initial SSSS aggregated to form precipitates. Therefore, the subsequent thermal exposure process is the coarsening period of the precipitates. Hutchinson et al.[9] reported that the thickening kinetics of Ω phase increased when the temperature was above 200 ℃. The statistic results in Tabs. 5-1 and 5-2 support that Ω phase is prone to coarsening under 210 °C thermal exposure heat treatment, leading to a rapid decrease in the number density of Ω phase. Therefore, the more obvious decrease in the number density of precipitates in 0.8Ag alloy than that in 0.5Ag alloy leads to the more obvious decline in strength of 0.8Ag alloy.

5.5 Facilitating effect of Ag on Ω phase precipitation in Al-Cu-Mg-Ag-Si alloys

The current work reveals that increasing the content of Ag will promote the precipitation of Ω phase in Al-Cu-Mg-Ag-Si alloys even with a low mass ratio of Mg/Si. According to TEM characterization results, the addition of Si to Al-Cu-Mg-Ag-Si alloys will promote the precipitation of

C/L-AlMgSiCu phase at the very early stage of ageing, which will consume Mg atoms (labeled as Mg_C) in the supersaturated solid solution. Then, the remaining Mg atoms (labeled as Mg_{excess}) in the supersaturated solid solution will combine with Ag to form AgMg interface phase at θ'/Al interface or/and AgMg segregation layers at Ω/Al interface. C phase has a monoclinic structure with the atomic composition of $AlMg_4Si_3Cu$ [169] (space group $P2_1/m$, a = 1.032 nm, b = 0.405 nm, c = 0.810 nm, β = 100.9°). However, as shown in Fig. 5-7a, the L-AlMgSiCu is disordered, which means the actual atomic Mg/Si ratio of L-AlMgSiCu is deviating from that of C-AlMgSiCu. Using atom probe tomography (APT), Ding et al. [191] and Torsæter et al. [211] detected that the atomic Mg/Si ratio in L-AlMgSiCu is about 1. In addition to the L-AlMgSiCu phase, there are C-AlMgSiCu interface phases with regular lattice in the alloys. Therefore, the atomic ratio of Mg to Si in C/L phase is set as 1.2 and the parameters in Tab. 5-3 can be calculated according to the following Equations:

$$W(Mg)_C = 1.2 * \frac{W(Si)}{Ar(Si)} * Ar(Mg) \tag{5-2}$$

$$W(Mg)_{excess} = W(Mg) - W(Mg)_C \tag{5-3}$$

in which $W(Mg)_C$ is the part of Mg used to form the C/L phase, while $W(Mg)_{excess}$ is the remaining Mg in the supersaturated solid solution used to form the AgMg interface structure. The relative atomic masses of Mg, Si and Ag are represented by Ar(Mg), Ar(Si) and Ar(Ag), respectively. The actual content of Mg and Si elements in the supersaturated solid solution after solution heat treatment are marked using W(Mg) and W(Si), respectively.

The contents of Mg_C, Mg_{excess} and corresponding Ag/Mg_{excess} atomic ratios of different Al-Cu-Mg-Ag-Si alloys, as well as their correlation to

the presence or absence of Ω phase in the aged alloys, are summarized in Tab. 5-3. When the mass ratio of Mg to Si in alloys is around 1.7, Ω phase only precipitates when the content of Ag is 0.8 with an Ag/Mg_{excess} atomic ratio of 1.12, while there is no Ω phase when the atomic ratio of Ag to Mg_{excess} in the alloys are 0.33, 0.73 and 0.80.

Table 5-3 Summary of Ω precipitation in Al–Cu–Mg–Ag–Si alloys with a low Mg/Si ratio

Composition (wt.%)	W(Mg)/W(Si)	Mg_C (wt.%)	Mg_{excess} (wt.%)	Ag/Mg_{excess} (atomic ratio)	Ω
Al-4.0Cu-0.4Mg-0.2Si-0.3Ag[119]	2	0.20	0.20	0.33	No
Al-3.89Cu-0.4Mg-0.24Si-0.49Ag	1.67	0.25	0.15	0.73	No
Al-4.15Cu-0.3Mg-0.17Si-0.47Ag-0.1Sc	1.76	0.17	0.13	0.80	No
Al-3.66Cu-0.38Mg-0.22Si-0.76Ag	1.72	0.23	0.15	1.12	Yes
Al-4.4Cu-0.3Mg-0.7Ag-0.3Mn-0.2Ti-0.50Si[120]	0.73*	0.43	0	∞	No

* Represent the actual mass fraction of Mg to Si in the supersaturated solid solution after solution heat treatment. After calculation using CALPHAD, the actual composition of the supersaturated solid solution is Al-4.43Cu-0.30Mg-0.71Ag-0.13Mn-0.12Ti-0.41Si (in wt.%)

According to the APT results [35], the atomic ratio of Ag and Mg atoms in the co-AgMg clusters, which are the precursors of Ω-phase, is close to 1. Therefore, it is inferred that only when the atomic ratio of Ag to Mg_{excess} in the supersaturated solid solution is greater than 1, it is possible to form

precursor co-AgMg clusters that can continue to convert to the Ω phase. When it comes to the Al-4.4Cu-0.3Mg-0.7Ag-0.3Mn-0.2Ti-0.50Si alloy, although the atomic ratio of Ag to Mg_{excess} is close to infinity, much higher than 1, there are still no Ω phases precipitated during artificial ageing. This is because all the content of Mg was consumed by the formation of C/L phase, there is no Mg_{excess} available to combine with Ag in the supersaturated solid solution. Therefore, another criterion that the Ω phase can precipitate is the presence of an appropriate amount of Mg_{excess} in the supersaturated solid solution. As mentioned above, the atomic ratio of Mg to Si in C/L phase is about 4:3, there will be Mg_{excess} in the supersaturated solid solution when the mass fraction of Mg to Si in the supersaturated solid solution is higher than 1.2. To ensure sufficient Mg_{excess} for the formation of co-AgMg clusters, the criterion of Mg/Si mass fraction in supersaturated solid solution is set as higher than 1.4. Therefore, only when the two criteria are met at the same time in alloys, W(Mg)/W(Si) > 1.4 and $X(Ag)/X(Mg_{excess}) > 1$, can the Ω phases precipitate.

5.6 Summary of this chapter

The influence of Ag content on Ω precipitation and heat resistance of the Al-Cu-Mg-Si-Ag alloys, with Mg/Si mass ratio lower than 2, has been investigated by SEM, EBSD, TEM and CALPHAD. The conclusions are as follows:

(1) When the Mg/Si mass ratio in Al-Cu-Mg-Ag-Si alloys is lower than 2, increasing the content of Ag could still promote the precipitation of Ω phase during artificial ageing state. This is contrary to previous findings. However, the predominant precipitate is still the θ′-Al_2Cu phase, in both alloys with 0.8 and 0.5 wt.% Ag.

(2) For such alloys, new criterions of W(Mg)/W(Si) > 1.4 and

$X(Ag)/X(Mg_{excess}) > 1$ correspond to the formation of Ω phase, where Mg_{excess} denotes the remaining Mg solutes after the formation of precursory C/L phase.

(3) After artificial ageing of the alloy with 0.8 wt.% Ag at 180℃, the Ω precipitates are smaller than θ′-Al_2Cu precipitates in both alloys. Ω phase, excluding its interfacial Ag-Mg layers, has the same composition as θ′-Al_2Cu. Therefore, the formation of fine Ω precipitates increases the number density of the precipitates, improving the yield strength.

(4) The Ω precipitates are more likely to coarsen than the θ′ with multiple interface structures during the thermal exposure treatment at 210℃. This significantly reduces the number density of precipitates in the 0.8Ag alloy and thus causes the abrupt deterioration of residual strength.

Chapter 6. Precipitation behavior of σ/Ω/θ′ phase in Al-Cu-Mg-Ag-Si Alloy

6.1 Foreword

The results of Chapter 5 indicate that increasing the Ag content in low Mg/Si mass ratio Al-Cu-Mg-Ag-Si alloys can promote the precipitation of the Ω phase. That is, there exists a mutual restriction relationship between Ag and Si on the precipitation of the Ω phase in Al-Cu-Mg-Ag-Si alloys.

Liu et al.[112] and Barlow et al.[109] have reported that increasing the Mg content in Al-Cu-Mg-Si alloys can promote the formation of the σ-$Al_5Cu_6Mg_2$ phase. Gable et al.[119] demonstrated that increasing Mg content in Al-Cu-Mg-Ag-Si alloys can promote the formation of the Ω phase, but the influence of Mg content on the precipitation of the σ-$Al_5Cu_6Mg_2$ phase was not investigated. Therefore, further research is needed to determine whether increasing the Mg and Ag content simultaneously in Al-Cu-Mg-Ag-Si alloys would lead to competition between the σ- $Al_5Cu_6Mg_2$ and Ω phases. Moreover, the influence of different precipitates on the mechanical properties and heat resistance of the alloy is not yet clear and requires further investigation. Clarifying the relationship between the content of each element in Al-Cu-Mg-Ag-Si alloy and the precipitation behavior, mechanical properties and heat resistance of the alloy is helpful to deeply understand the influence of different types of precipitation on the strength and heat resistance of the alloy.

In this study, the influence of Mg/Ag content on the precipitation behavior of the Ω, σ, and θ′ phases in Al-Cu-Mg-Ag-Si alloys and their heat resistance properties were investigated using four groups of alloys

with different Mg and Ag content. Mechanical properties and multiscale microstructure characterization results indicate that increasing Mg content can simultaneously promote the precipitation of the Ω and σ phases while inhibiting the precipitation of the θ′ phase. Moreover, simultaneous increase in Mg/Ag content can promote the precipitation of the Ω phase while inhibiting the precipitation of the σ and θ′ phases. Regarding the mechanical properties of the alloy, alloys mainly strengthened by the Ω phase exhibit excellent room temperature mechanical properties but poor performance under long-term high-temperature service conditions. On the other hand, alloys primarily strengthened by the θ′ phase with a multiple-precipitate structure show lower room temperature mechanical properties but better performance under long-term high-temperature service conditions. Additionally, based on these results, critical conditions for the precipitation of σ/Ω/θ′ phases in Al-Cu-Mg-Ag-Si alloys are proposed, which helps us to select the appropriate alloy composition range based on different service conditions.

6.2 Effect of Mg/Ag content on mechanical properties and heat resistance of alloys

In this study, four groups of Al-Cu-Mg-Ag-Si alloys with different Mg/Ag elemental contents were utilized to investigate the influence of alloy composition on the precipitation sequence of the Ω phase, σ-$Al_5Cu_6Mg_2$ phase, and θ′-Al_2Cu phase in the alloy. The specific alloy compositions are listed in Tab. 2-1. Based on the Mg and Ag contents in the alloys, the alloys were named 3M5A, 5M5A, 8M5A, and 8M8A, where "M" represents the Mg content and "A" represents the Ag content. For example, 3M5A denotes Mg and Ag elemental contents of 0.3 wt.% and 0.5 wt.%, respectively. Fig. 6-1a illustrates the microhardness of different

alloys aged at 180 ℃ for different ageing times. According to the microhardness results, it can be observed that when the Ag content is constant, increasing the Mg content enhances the room temperature mechanical properties of the alloy. Moreover, further increasing the Ag content can enhance the strength of the alloys with high Mg content, indicating that increasing both Mg and Ag contents improves the room temperature mechanical properties of the alloy. Fig. 6-1b shows the microhardness results of peak-aged alloys after thermal exposure at 210 ℃ for different times. Increasing the Mg content enhances the room temperature mechanical properties of the alloy but leads to a rapid decline in strength during thermal exposure at 210 ℃. As for the high Ag content alloy 8M8A, although its strength decreases, its final strength after thermal exposure at 210 ℃ for 100 h still exceeds that of the low Ag content 8M5A alloy. That is, increasing the Mg content enhances the room temperature mechanical properties of the alloy but reduces its long-term service performance at high temperatures. Conversely, increasing the Ag content can simultaneously enhance the room temperature mechanical properties and heat resistance of the alloy.

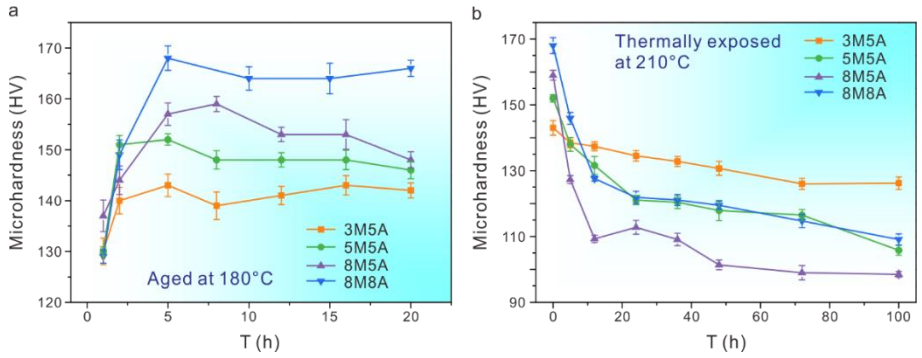

Figure 6-1 (a) The microhardness of different alloys under different ageing conditions. (b) The microhardness of different alloys after different durations of thermal exposure

In addition to long-term service at high temperatures, heat-resistant aluminum alloys also need to exhibit good tensile properties at high temperatures. Fig. 6-2 shows the tensile results of the four alloy groups tested at 210 ℃. According to the high-temperature tensile strength, the yield strengths of the 3M5A, 5M5A, 8M5A, and 8M8A alloy groups at 210 ℃ are 289 ± 14 MPa, 292 ± 13 MPa, 296 ± 6 MPa, and 325 ± 7 MPa, respectively. That is, increasing the Mg content can improve the tensile properties of the alloy at 210 ℃ to a certain extent, but the 8M8A alloy with a higher Ag content has the most obvious improvement in tensile properties at 210 ℃. This may be attributed to the fact that in the peak-aged state, alloys with high Mg/Ag content exhibit higher initial strength, and their strength decrease trend at high temperatures is lower than that of alloys with lower Ag content, ensuring that the 8M8A alloy maintains good high-temperature mechanical properties at 210 ℃.

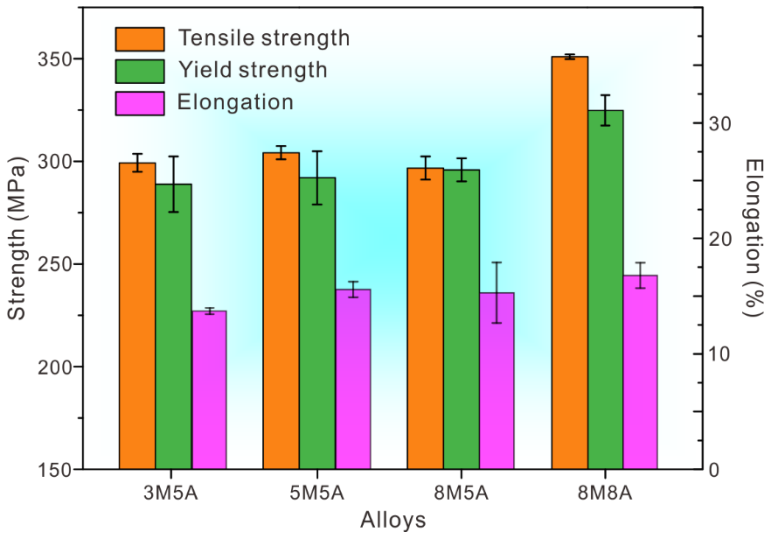

Figure 6-2 High temperature mechanical properties of different alloys tested at 210 ℃

6.3 Multi-scale microstructure characterization of Al-Cu-Mg-Ag-Si alloy

6.3.1 Micrometer scale microstructure

8M8A alloy, with the highest content of alloying elements, was chosen as the sample to investigate the micron scale constituents during homogenization heat treatment. The as-cast microstructure in Fig. 6-3a-b reveals that the micron scale constituent is mainly dendritic AlCu-rich phase. After homogenization at 520 ℃ for 24 h, most of the dendritic micron scale constituents have dissolved into the matrix, leaving behind some scattered point-like constituents.

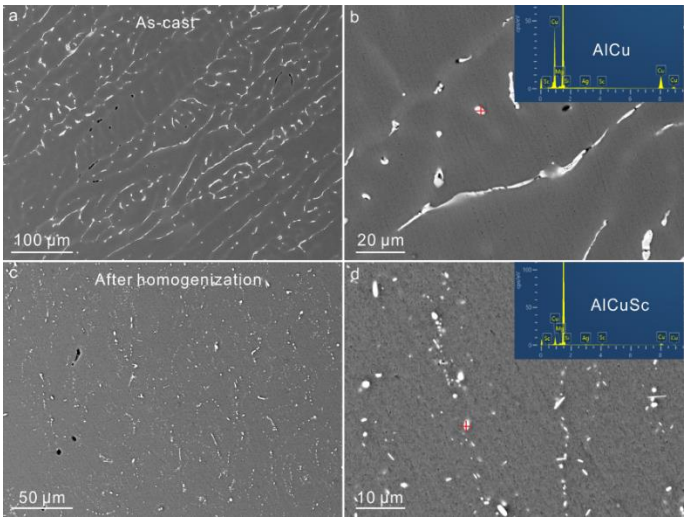

Figure 6-3 (a-b) SEM images of the 8M8A alloy under as-cast state at different magnification. (c-d) SEM images of the 8M8A alloy after homogenization at different magnification. The EDX spectrum results are inserted in (b) and (d)

Combining with the EDX results, these point-like micron scale constituents were identified as AlCuSc phase. According to the Tab. 2-1, the alloy used in this study contains a small amount of Sc, leading to the

formation of AlCuSc phases during homogenization. In addition, referring to the vertical cross-section phase diagram of Al - 4Cu - 0.5Ag - 0.2Si - 0.1Sc – xMg alloys shown in Fig. 6-4, the melting temperature of the alloy gradually decreases with the increase in Mg content. When the Mg content reaches 0.8 wt.%, the melting point of the alloy is around 533 ℃. Considering the temperature fluctuation phenomenon during the actual heat treatment process, a homogenization and solution temperature of 520 ℃ was chosen. Therefore, the excessive presence of micro scale point-like constituents in the homogenized alloy might also be attributed to insufficient homogenization temperature or time, resulting in incomplete dissolution of the dendritic AlCu-rich constituents.

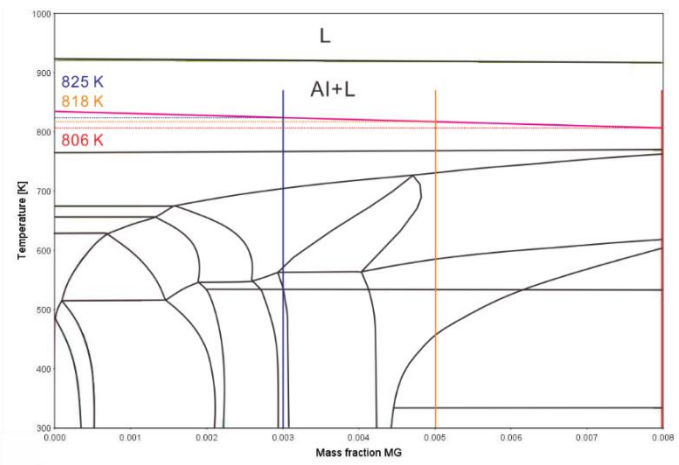

Figure 6-4 Vertical cross-section phase diagram of Al - 4Cu - 0.5Ag - 0.2Si - 0.1Sc - xMg alloy

Fig. 6-5 shows the EBSD results of the 3M5A and 8M8A alloys after solution heat treatment. The average grain sizes of the 3M5A and 8M8A alloys are 45 ± 30 μm and 39 ± 25 μm, respectively, indicating that the grain sizes of the alloy plates are similar after rolling and solution heat

treatment. Therefore, grain boundary strengthening contributes similarly to the overall strength of the alloys used in this study. After aging heat treatment, the difference in strength between the alloys is mainly attributed to the differences in the types, number densities, and volume fractions of nano-precipitates in different alloys.

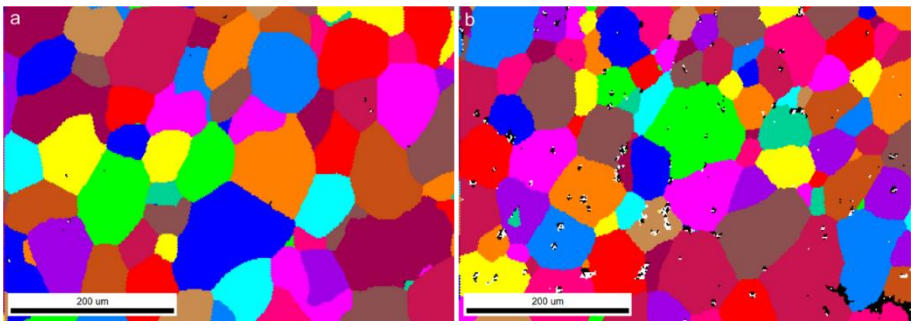

Figure 6-5 EBSD results of the (a) 3M5A and (b) 8M8A alloys after solid solution treatment

6.3.2 Nanoscale microstructure of alloy in peak aging state

The variation in solute element content significantly alters the precipitation behavior of Al-Cu-Mg-Ag-Si alloys. Fig. 6-6 shows the HAADF-STEM images obtained along different zone axes of the four alloys in the peak-aged state. In the 3M5A alloy with low Mg content, the main strengthening phase is the plate-like θ′-Al_2Cu phase. As the Mg content increases, the Ω phase and the σ-$Al_5Cu_6Mg_2$ phase gradually precipitate. In the 8M5A alloy with higher Mg but lower Ag content, the precipitation of θ′-Al_2Cu phase is suppressed, and the main strengthening phases is transformed into plate-like Ω phase and square-shaped σ-$Al_5Cu_6Mg_2$ phase. When the Ag content is further increased in the high Mg alloy, the precipitation of the σ-$Al_5Cu_6Mg_2$ phase and the θ′-Al_2Cu phase is completely suppressed, and the generation of the Ω phase is

promoted. Similar to the findings of Gable et al.[119], it is demonstrated that increasing the Mg/Si mass ratio in Al-Cu-Mg-Ag-Si alloys enhances the precipitation rate of Ω phase.

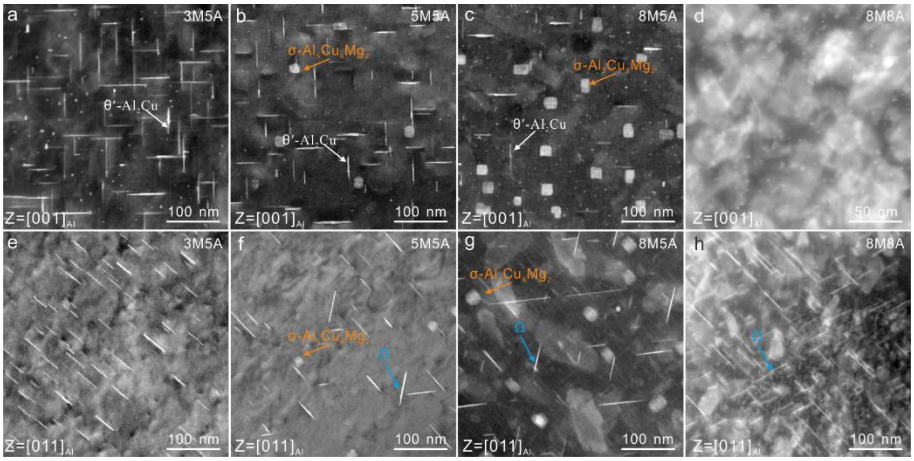

Figure 6-6 (a-d) HAADF-STEM images of 3M5A, 5M5A, 8M5A, and 8M8A alloys along $[001]_{Al}$ zone axis in peak aging states. (e-h) HAADF-STEM images of 3M5A, 5M5A, 8M5A, and 8M8A alloys along $[011]_{Al}$ zone axis in peak aging states

Therefore, altering the solute element content in Al-Cu-Mg-Ag-Si alloys can control the types of precipitates during the artificial ageing heat treatment. Increasing Mg content can suppress the formation of θ′-Al_2Cu phase while promoting the precipitation of Ω phase and σ-$Al_5Cu_6Mg_2$ phase. Elevating Ag content can simultaneously inhibit the precipitation of σ-$Al_5Cu_6Mg_2$ and θ′-Al_2Cu phases while promoting the formation of Ω phase. The results from Chapters 4 and 5 of this study indicate that when the precipitation of Ω phase is suppressed in Al-Cu-Mg-Ag-Si alloys, Ag elements in the alloy form χ-AgMg interface phase at the θ′/Al coherent interface. Figs. 6-7 and 6-8 show the EDX mapping results at the θ′/Al interface and Ω/Al interface for different alloys.

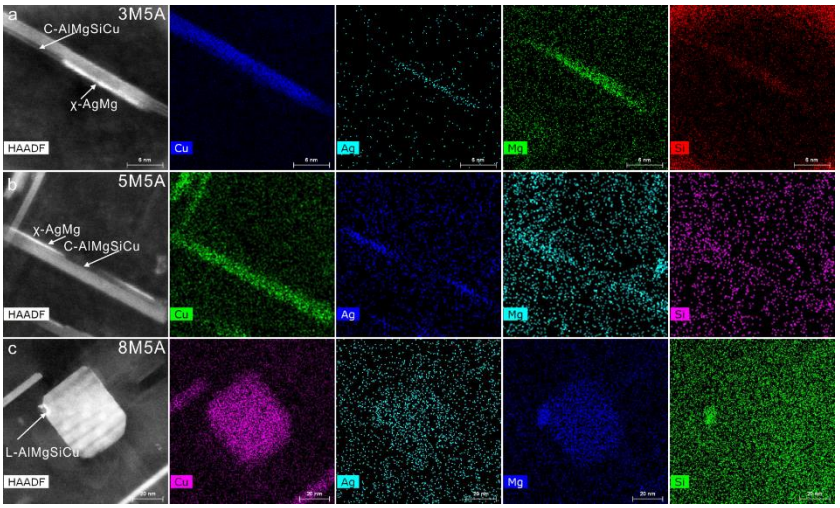

Figure 6-7 (a) EDX maps of 3M5A alloy in peak-aged state. (b) EDX maps of 5M5A alloy in peak-aged state. (c) EDX maps of 8M5A alloy in peak-aged state

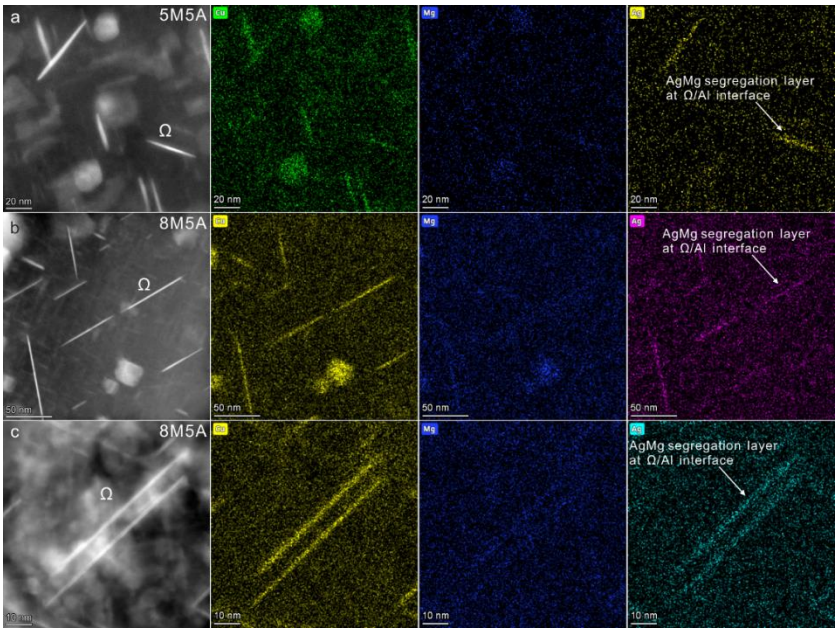

Figure 6-8 (a) EDX maps of 5M5A alloy in peak-aged state. (b) EDX maps of 8M5A alloy in peak-aged state. (c) EDX maps of 8M8A alloy in peak-aged state

According to the EDX results, χ-AgMg and C-AlMgSiCu interface phases exist at the θ′/Al coherent interface in the 3M5A and 5M5A alloys with low Mg content. However, due to the small size and low number density of θ′-Al_2Cu phases in the 8M5A alloy with higher Mg content, χ-AgMg interface phase is not observed at the θ′/Al coherent interface. As shown in Fig. 6-8, increasing Ag content suppresses the precipitation of θ′-Al_2Cu phase in the 8M8A alloy, resulting in the formation of an AgMg segregation layer with a double atomic layer structure at the Ω/Al interface.

Fig. 6-9 shows the atomic-resolution HAADF-STEM images of the θ′-Al_2Cu phase interface structure in different alloys. The interface phase structure at the θ′/Al coherent interface is characterized as χ-AgMg and C-AlMgSiCu interface phases. Thus, in the low Mg content 3M5A and 5M5A alloys, the presence of multiple segregation structures at the θ′/Al interface effectively inhibits the coarsening of θ′-Al_2Cu, enhancing the heat resistance of the alloy. As for the phases precipitated at the semi-coherent interface, with the increase in Mg content, they gradually transition from the disordered L-AlMgSiCu phase to the disordered QP-AlMgSiCu phase and GPB zone.

Fig. 6-10 is atomic-resolution HAADF-STEM images of precipitates containing MgSiCu, where blue triangles represent the C-AlMgSiCu unit cell structure, orange hexagons represent the Q′-AlMgSiCu unit cell structure, and green triangles represent the unit cell structure of the GPB zone. According to the Fig. 6-10, the nanoscale precipitates in the 3M5A alloy along the $[001]_{Al}$ direction mainly consist of the disordered L-AlMgSiCu phase with excellent heat resistance, containing a small amount of the disordered QP1 phase with the Q′ unit cell structure. As for the 5M5A alloy, the nanoscale precipitates along the $[001]_{Al}$ direction mainly consist of a composite disordered phase containing both L-AlMgSiCu and

QP1, indicating the coexistence of C and Q′ unit cells. The large amount of the QP1 phase makes it prone to phase transformation during subsequent high-temperature exposures, thereby reducing the heat resistance of the alloy. In the 8M5A alloy, besides the coexistence of L and QP1 disordered phases, there are also S-Al_2CuMg phases and GPB zones. The presence of the S phase can effectively enhance the room-temperature mechanical properties of the alloy, but it tends to coarsen after temperatures exceed 150 ℃[212], leading to a significant decrease in heat resistance. In the 8M8A alloy, the main nanoscale precipitates transform into a composite precipitate structure containing both C-AlMgSiCu unit cell and GPB zone. The larger S-Al_2CuMg phase is less, which may be mainly due to the precipitation of the Ω phase, resulting in a large amount of Mg element being consumed.

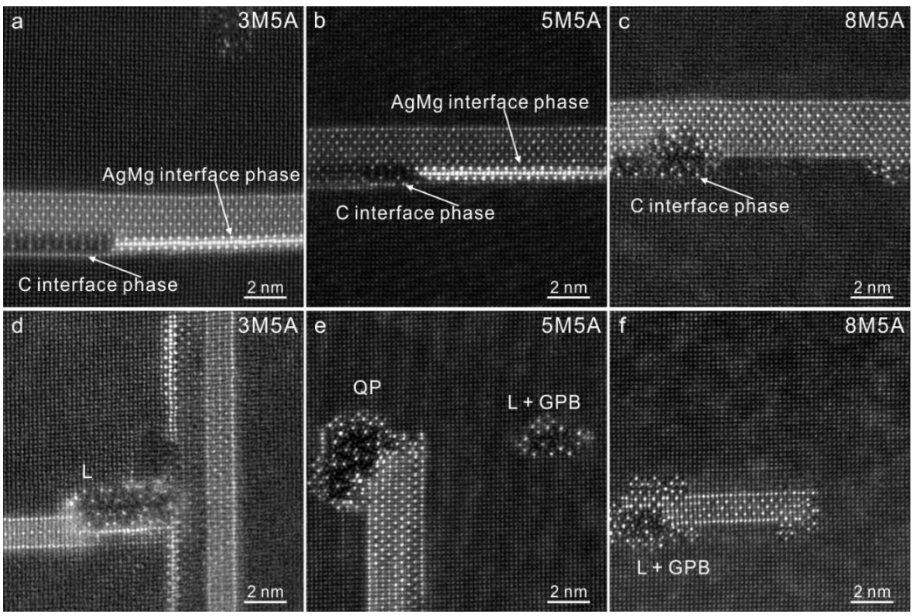

Figure 6-9 Atomic-resolution HAADF-STEM images of θ′/Al interface structures in the different alloys under peak-aged state. (a) and (d) 3M5A alloy. (b) and (e) 5M5A alloy. (c) and (f) 8M5A alloy

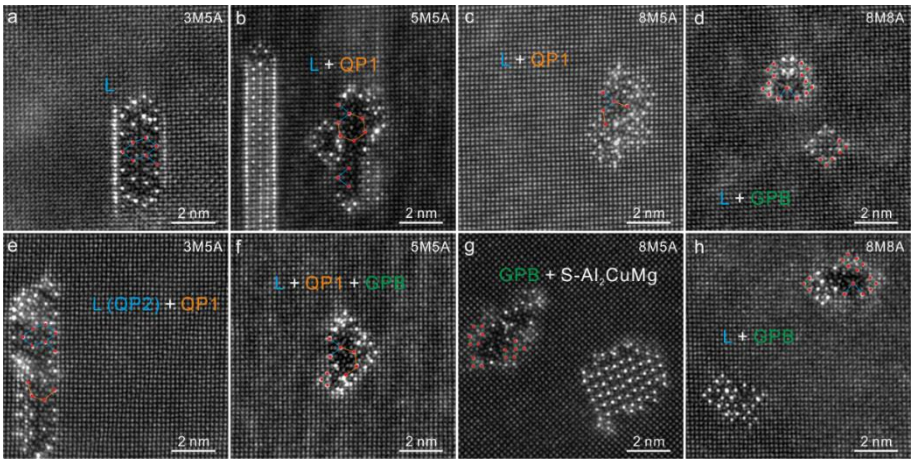

Figure 6-10 Atomic resolution HAADF-STEM images along the $[001]_{Al}$ zone axis of different alloys under peak-aged state. (a) and (e) 3M5A alloy. (b) and (f) 5M5A alloy. (c) and (g) 8M5A alloy. (d) and (h) 3M5A alloy

To quantitatively analyze the content of different types of precipitates in the alloy, the number density and volume fraction of θ′-Al_2Cu, Ω, and σ-$Al_5Cu_6Mg_2$ phases in the different alloys were calculated based on the method shown in Fig. 6-11. As for the θ′-Al_2Cu phase, the formula established by Nie et al.[151] was used, which considers the difference in sample thickness (T) and the observed area (A_{fov}) to correct the number of precipitates in the actual observation area. The specific formula is as follows:

$$N1 = \frac{N}{2}\left(\frac{T+d}{\sqrt{A_{fov}}}\right) \tag{6-1}$$

$$n = \frac{N+N1}{A_{fov}(T+d)} = \frac{N\left(1+\frac{T+d}{2\sqrt{A_{fov}}}\right)}{A_{fov}(T+d)} \tag{6-2}$$

$$f_v = nt\frac{\pi d^2}{4} \tag{6-3}$$

Where N is the number of θ′-Al_2Cu phases directly counted in the observed

area, $N1$ is the number of θ′-Al_2Cu phases that cannot be directly observed, n and f_v are the number density and volume fraction of the θ′-Al_2Cu phase, d represents the average diameter of the θ′-Al_2Cu phase, and A_{fov} represents the area of the observed area. t is the thickness of the θ′-Al_2Cu phase, and T is the thickness of the observed area in the TEM sample, which is calculated based on CBED.

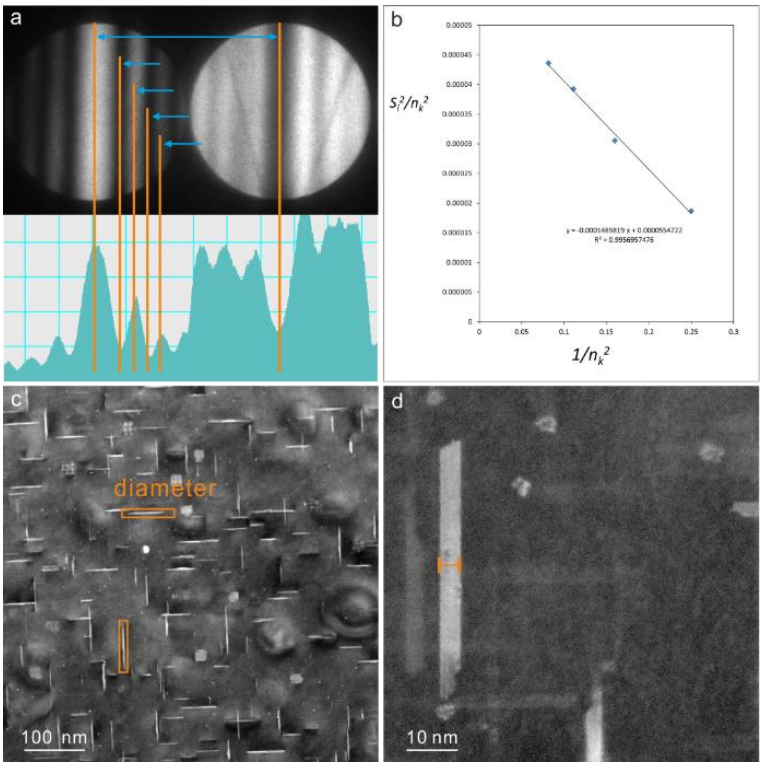

Figure 6-11 (a) The CBED pattern for calculating the foil thickness. (b) The linear fit graph of the relationship between s_i^2 / n_k^2 and $1/n_k^2$. (c) HAADF-STEM image for calculating the number and diameter of Ω phase. (d) HRTEM image for calculating the thickness of Ω phase

After calculation, the number density and volume fraction of the θ′-Al_2Cu phase in different alloys are shown in Tab. 6-1. For the calculation

of the number density and volume fraction of the Ω phase, the relevant formulas have been established in the Chapter 3 of this work. Therefore, the number density and volume fraction of the Ω phase in different alloys can be directly calculated using formulas 3-1, 3-2, and 3-3. The calculation results are shown in Tab. 6-2.

Table 6-1 The number density, volume fraction and corresponding parameters of θ′-Al_2Cu phase in peak-aged state

	3M5A	5M5A	8M5A	8M8A
d (nm)	37.2 ± 14.8	38.2 ± 15.0	26.4 ± 12.0	\
t (nm)	2.3 ± 0.6	2.5 ± 0.7	3.07 ± 0.7	\
T (nm)	130 ± 3.9	133 ± 4.0	118 ± 3.54	\
n (nm^{-3})	$3.08 \pm 0.3 \times 10^{-6}$	$2.81 \pm 0.2 \times 10^{-6}$	$0.58 \pm 0.1 \times 10^{-6}$	\
f_v (%)	0.77 ± 0.06	0.79 ± 0.06	0.10 ± 0.01	\

Table 6-2 The number density, volume fraction and corresponding parameters of Ω phase in peak-aged state

	3M5A	5M5A	8M5A	8M8A
d (nm)	\	36.9 ± 19.2	47.5 ± 29.6	28.0 ± 17.7
t (nm)	\	1.57 ± 0.31	1.5 ± 0.2	1.51 ± 0.33
T (nm)	\	110 ± 3.3	56.1 ± 1.7	67 ± 2.01
n (nm^{-3})	\	$0.3 \pm 0.1 \times 10^{-6}$	$1.8 \pm 0.4 \times 10^{-6}$	$8.5 \pm 1.3 \times 10^{-6}$
f_v (%)	\	0.05 ± 0.01	0.48 ± 0.11	0.81 ± 0.12

As for the σ-$Al_5Cu_6Mg_2$ phase, it has a cubic structure, and its orientation relationship with the aluminum matrix conforms to $[100]_\sigma$ // $[100]_{Al}$ and $(100)_\sigma$ // $(100)_{Al}$. When observed from the $[100]_{Al}$ zone axis, due to the nanoscale size of this precipitate phase and its thickness being much smaller than the actual thickness of the observed region, σ-$Al_5Cu_6Mg_2$ phases growing along the $[100]_{Al}$, $[010]_{Al}$, and $[001]_{Al}$ directions can all be observed. Therefore, the total number of σ-$Al_5Cu_6Mg_2$ phases counted using TEM images is the actual total number of σ-

$Al_5Cu_6Mg_2$ phases in the observed region, without the need for further correction of the actual quantity. Thus, based on the formula established by Nie et al.[151] and optimized according to the actual orientation relationship, the formula for calculating the number density and volume fraction of the σ-$Al_5Cu_6Mg_2$ phase is as follows:

$$d = \sqrt{d_1 \times d_2} \tag{6-4}$$

$$n = \frac{N}{A_{fov}(T + d)} \tag{6-5}$$

$$f_v = nt\frac{\pi d^2}{4} \tag{6-6}$$

where d is the equivalent diameter of the σ-$Al_5Cu_6Mg_2$ phase, and d_1 and d_2 are the lengths of the two sides of the same σ-$Al_5Cu_6Mg_2$ phase. N is the number of σ-$Al_5Cu_6Mg_2$ phases directly counted in the observation area, and T and A_{fov} are the thickness and area of the observation area of the transmission electron microscope sample, respectively. n and f_v represent the number density and volume fraction of the σ-$Al_5Cu_6Mg_2$ phase, respectively. The calculation results are shown in Tab. 6-3.

Table 6-3 The number density, volume fraction and corresponding parameters of σ phase in peak-aged state

	3M5A	5M5A	8M5A	8M8A
d (nm)	\	17.2 ± 2.1	19.9 ± 2.2	\
T (nm)	\	133 ± 4.0	118 ± 3.54	\
n (nm^{-3})	\	$0.11 \pm 0.01 \times 10^{-6}$	$0.92 \pm 0.01 \times 10^{-6}$	\
f_v (%)	\	0.06 ± 0.01	0.72 ± 0.01	\

The statistical results presented in Tabs. 6-1, 6-2, and 6-3 indicate that with the increase in Mg content, the number density of θ′-Al_2Cu phases in the alloy gradually decreases, and the thickness of the θ′-Al_2Cu phase gradually increases, while the number density of Ω phase and σ phase

gradually increases. When the Ag content is increased, the size of the Ω phase can be refined, while the growth of the σ phase will be inhibited.

6.3.3 Nanoscale microstructure of alloy after thermal exposure

Fig. 6-12 shows low-magnification HAADF-STEM images of the four peak-aged alloys after thermal exposure at 210°C for 100 h, which are used to analyze the size changes of the θ′-Al_2Cu phase, Ω phase, and σ-$Al_5Cu_6Mg_2$ phase before and after thermal exposure. The main strengthening phase remains unchanged before and after thermal exposure in the 3M5A alloy, which is still the θ′-Al_2Cu phase. When the increase of Mg content, as indicated by the EDX mapping results shown in Fig. 6-13, the 5M5A alloy still contains the θ′-Al_2Cu phase, Ω phase, and σ-$Al_5Cu_6Mg_2$ phase after thermal exposure, but the number of the Ω phase notably decreases. As for the 8M5A alloy, the main precipitate remains the σ-$Al_5Cu_6Mg_2$ phase, with minor amounts of the θ′-Al_2Cu phase and Ω phase. Similarly, the amount of Ω phase also decreases significantly. In the high Mg and high Ag 8M8A alloy, the precipitate significantly changes before and after thermal exposure. At the peak-aged state, the main precipitate in the 8M8A alloy is the Ω phase and the GPB zone containing the C-AlMgSiCu unit cell along the $[001]_{Al}$ direction. With the increase of thermal exposure time, the Ω phase still exists in the alloy, but its number density decreases significantly, while larger precipitates of the S-Al_2CuMg and σ-$Al_5Cu_6Mg_2$ phases are precipitated along the $[001]_{Al}$ direction.

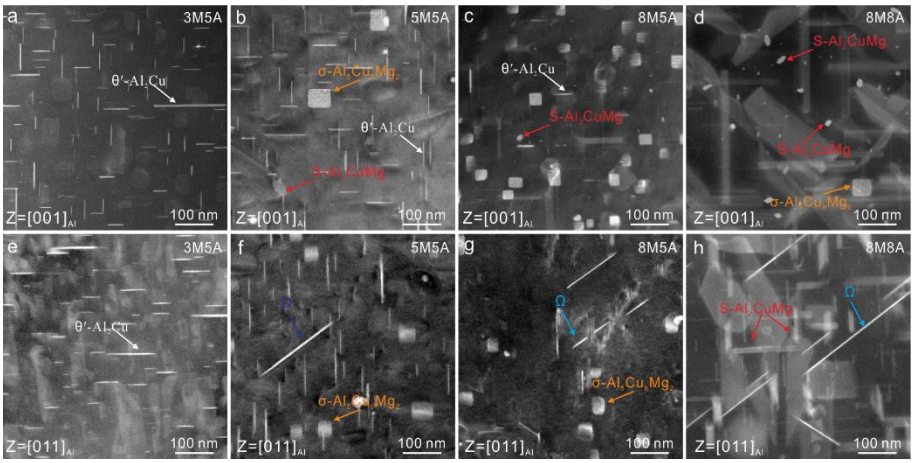

Figure 6-12 (a-d) HAADF-STEM images of 3M5A, 5M5A, 8M5A, and 8M8A alloys along $[001]_{Al}$ zone axis after thermal exposure. (e-h) HAADF-STEM images of 3M5A, 5M5A, 8M5A, and 8M8A alloys along $[011]_{Al}$ zone axis after thermal exposure

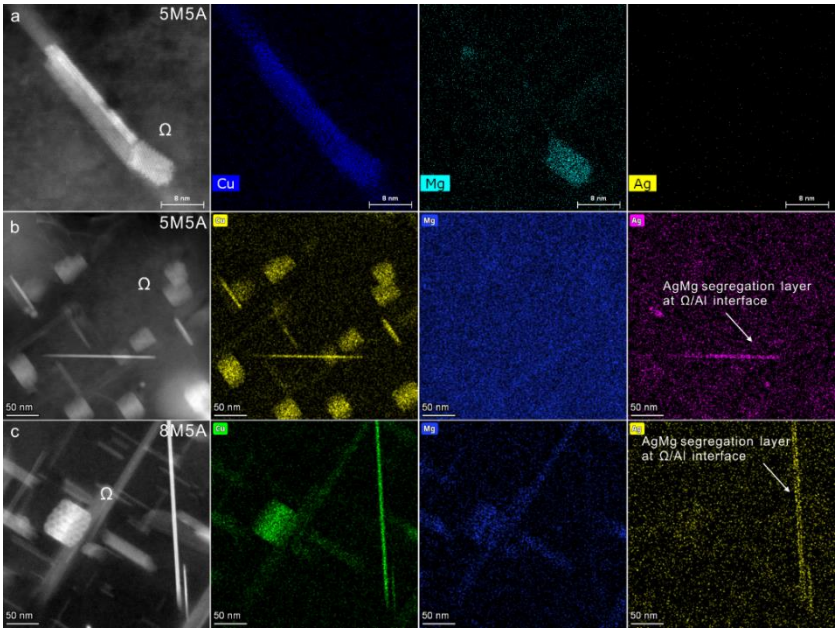

Figure 6-13 EDX maps of (a)5M5A alloy, (b) 8M5A alloy and (c) 8M8A alloy after thermal exposure, respectively.

Fig. 6-14 is atomic resolution HAADF-STEM images of the precipitates in the different alloys grown along the $[001]_{Al}$ direction after thermal exposure. As for the low Mg content 3M5A alloy, similar to the peak-aged state, the main precipitate after thermal exposure is still the disordered L-AlMgSiCu phase, with only a small number of the combined L+QP1 disordered phase containing both C-AlMgSiCu and Q′-AlMgSiCu unite cell. In addition, the main precipitate consists of a combined disordered phase of L+QP1 and GPB zones in the peak-aged 5M5A alloy. After thermal exposure, both the L+QP1 disordered phase and the the GPB zone continue to grow and transform into larger Q′-AlMgSiCu and S-Al_2CuMg phases.

Fig. 6-14c and 6-14g reveals that the 8M5A alloy is similar to the 5M5A alloy, where the main precipitates at the peak-aged state are the L+QP1 disordered phase and the S-Al_2CuMg/GPB composite precipitate. After thermal exposure, the precipitates gradually transform into the Q′-AlMgSiCu and S-Al_2CuMg phases. As for the 8M8A alloy, the main precipitates at the peak-aged state are the small-sized composite precipitates containing the C-AlMgSiCu unite cell and the GPB zone. These composite precipitates grow during thermal exposure, transforming into larger Q′-AlMgSiCu and S-Al_2CuMg phases. Considering the low-magnification HAADF-STEM images shown in Fig. 6-12, although the 5M5A, 8M5A, and 8M8A alloys all contain larger precipitates of Q′-AlMgSiCu and S-Al_2CuMg phases after long term thermal exposure, there are significant differences in their number densities. As the Mg content increases, the number of the S-Al2CuMg phase with a coarser cross-sectional area gradually increases. Therefore, in the three groups of 5M5A, 8M5A and 8M8A alloys with lower thermal exposure performance, the rapid decrease in the number density of the Ω phase before and after

thermal exposure and the rapid coarsening of the precipitated phase along the $[001]_{Al}$ direction are the reasons for the significant decrease in the heat resistance of the alloy.

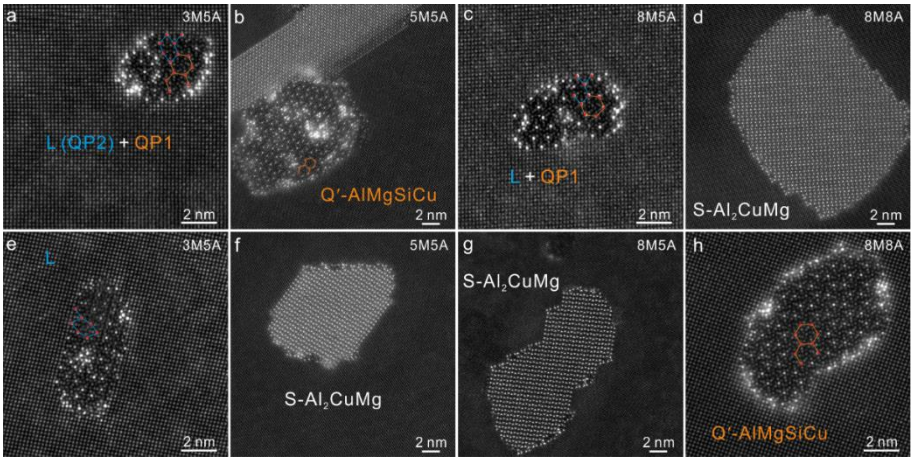

Figure 6-14 Atomic resolution HAADF-STEM images along the $[001]_{Al}$ zone axis of different alloys after thermal exposure. (a) and (e) 3M5A alloy. (b) and (f) 5M5A alloy. (c) and (g) 8M5A alloy. (d) and (h) 3M5A alloy. The blue triangle is the C-AlMgSiCu unit cell structure, and the orange regular hexagon is the Q′-AlMgSiCu unit cell structure

6.4 Effect of precipitation phase type on strength and heat resistance of Al-Cu-Mg-Ag-Si alloy

To analyze the influence of different types of precipitates on the strength and heat resistance of the alloy, it is necessary to quantitatively analyze the size changes of the θ′-Al_2Cu phase, Ω phase and σ-$Al_5Cu_6Mg_2$ phase before and after thermal exposure. Low-magnification HAADF-STEM images were used to statistically count the diameter or side length changes of the precipitates. The results are shown in Figs. 6-15, 6-16, and 6-17.

As shown in Fig. 6-15, under the peak-aged state, there is no

significant change in the size of the θ′-Al_2Cu phase in the 3M5A and 5M5A alloys, while the size of the θ′-Al_2Cu phase in the 8M5A alloy changes significantly. This is mainly attributed to the increase in Mg content, which promotes the precipitation of the Ω phase and σ-$Al_5Cu_6Mg_2$ phase while inhibiting the precipitation of the θ′-Al_2Cu phase. Consequently, a large amount of Cu solute atoms in the alloy are used for the precipitation of the Ω phase and σ-$Al_5Cu_6Mg_2$ phase, leading to a decrease in the size of the θ′-Al_2Cu phase. After thermal exposure, significant coarsening of the θ′-Al_2Cu phase is observed in the high-Mg 5M5A and 8M5A alloys, while no significant size change is observed in the low-Mg 3M5A alloy. The high thermal stability of the main strengthening phase, θ′-Al_2Cu, ensures that the 3M5A alloy maintains high mechanical performance even after long term thermal exposure.

Regarding the Ω phase, since the Ω phase in the 5M5A alloy is almost completely dissolved after thermal exposure at 210°C for 100 h, the size change of the Ω phase before and after thermal exposure in the 5M5A alloy was not statistically analyzed. As shown in Fig. 6-16, simultaneously increasing the Mg/Ag element content effectively refines the size of the Ω phase and increases its number density. After long term thermal exposure, significant coarsening of the Ω phase is observed in both alloys, but it is more pronounced in the high-Ag 8M8A alloy. This indicates that in high-Mg alloys, the Ω phase is prone to coarsening during long term thermal exposure, leading to a rapid decline in alloy mechanical properties. For the σ-$Al_5Cu_6Mg_2$ phase, the size statistical results show that it also coarsens to a certain extent before and after thermal exposure.

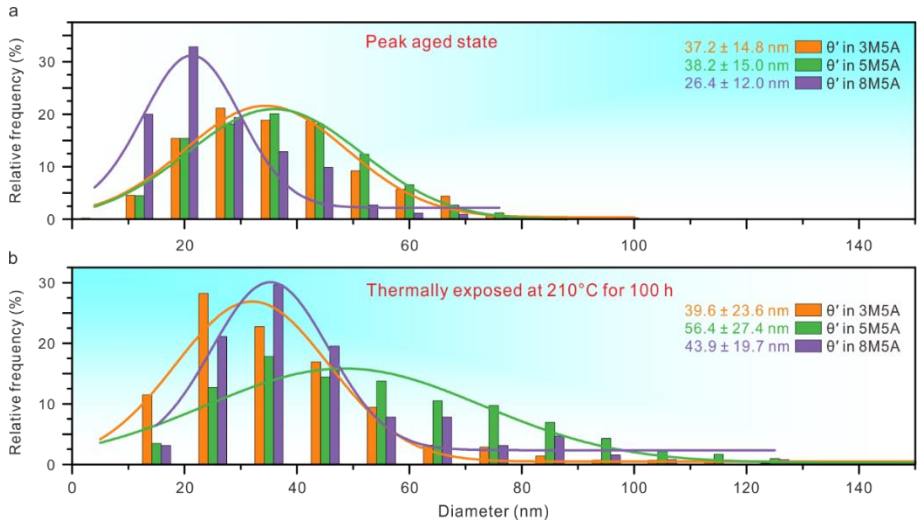

Figure 6-15 The diameter distribution of θ′-Al_2Cu phase in different alloys before and after thermal exposure. The average diameter of the θ′-Al_2Cu phase of different alloys under different heat treatment states is inserted

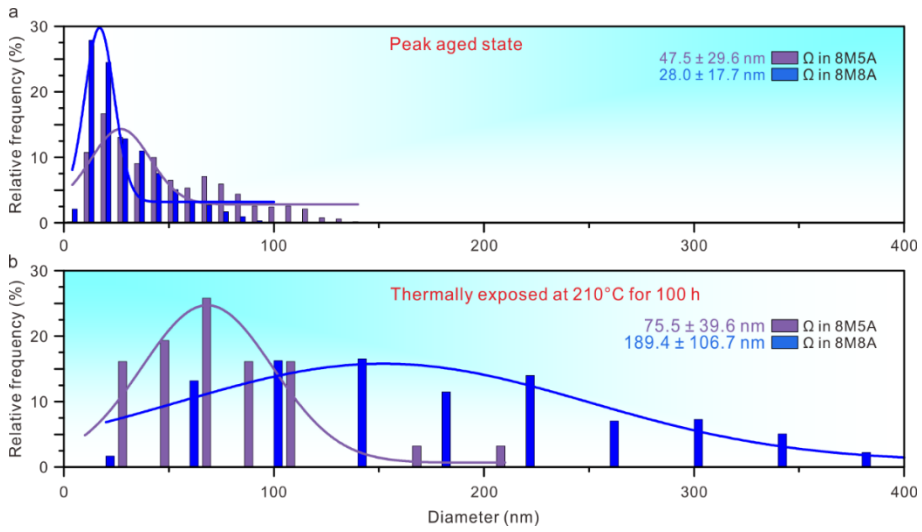

Figure 6-16 The diameter distribution of Ω phase in different alloys before and after thermal exposure. The average diameter of the Ω phase of different alloys under different heat treatment states is inserted

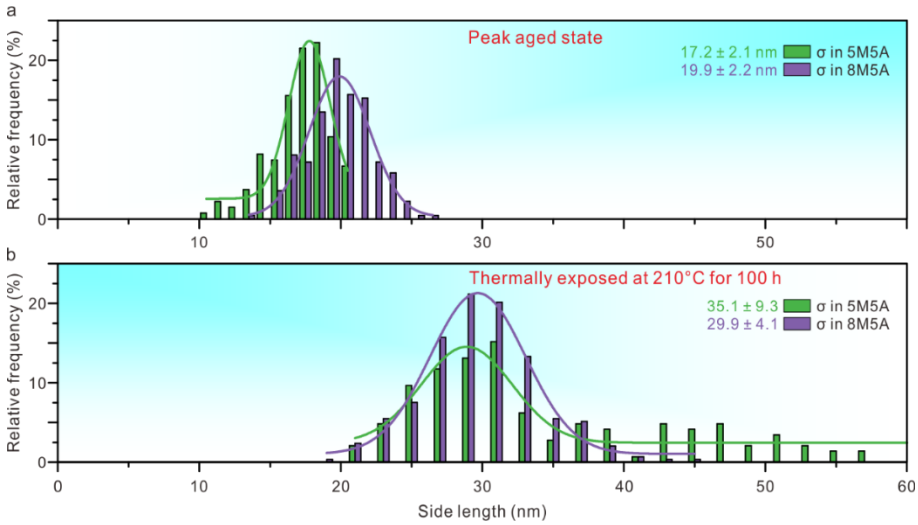

Figure 6-17 The side length distribution of σ-$Al_5Cu_6Mg_2$ phase in different alloys before and after thermal exposure. The average side length of the σ-$Al_5Cu_6Mg_2$ phase of different alloys under different heat treatment states is inserted

Fig. 6-18 shows the isothermal section of the Al-Cu-Mg-0.5Ag-0.2Si-0.1Sc alloy at 210°C. When the Cu content is 4 wt.%, the equilibrium phase containing MgSi gradually transitions from the Q-AlMgSiCu phase to the S-Al_2CuMg phase in the alloy with increasing Mg content. In the 3M5A alloy, the precipitates containing MgSi elements in the alloy are mainly the disordered L-AlMgSiCu phases and the C-AlMgSiCu interface phase at θ′/Al interface before thermal exposure. Both the L-AlMgSiCu phase and the C-AlMgSiCu interface phase exhibit high thermal stability, and their phase transformation rates are relatively slow. Therefore, there is no significant change in the size of the C/L-AlMgSiCu phase after thermal exposure. Consequently, the C/L-AlMgSiCu interphase phase existing at the θ′/Al interface in the 3M5A alloy can effectively inhibit the coarsening of the θ′-Al_2Cu phase, thereby improving the heat resistance of the 3M5A alloy.

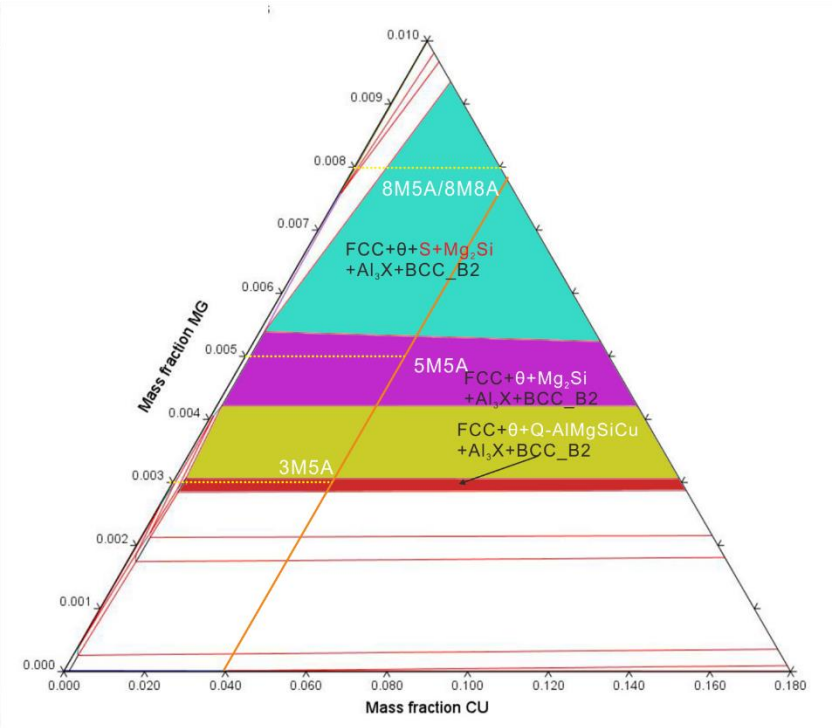

Figure 6-18 Isothermal section of Al-Cu-Mg-0.5Ag-0.2Si-0.1Sc alloy at 210 °C

When the Mg content is increased to 0.5 wt.%, the main precipitate in the peak aged alloy is the L-QP1-GPB composite disordered precipitate phase. QP1 and GPB zone are easy to coarsen and grow during subsequent thermal exposure, transforming into larger Q′-AlMgSiCu phase and S-Al_2CuMg phase. The growth of precipitates leads to a reduction in the number density of the C/L-AlMgSiCu interface phase at the θ′/Al interface, weakening its inhibitory effect on the coarsening of the θ′-Al_2Cu phase, resulting in an increase in the size of the θ′-Al_2Cu phase. In addition, the growth of the L-QP1-GPB composite precipitate requires a higher number of solute atoms such as Mg and Cu, leading to the dissolution of the Ω phase in the alloy, further reducing the number density and volume fraction of precipitates in the alloy, thereby causing a rapid decrease in mechanical properties after long term high-temperature thermal exposure.

When the Mg content is increased to 0.8 wt.%, due to the consumption of Mg elements by the abundant σ-$Al_5Cu_6Mg_2$ phase precipitated in the 8M5A alloy, the main precipitates at peak aging are still the L-QP1-GPB composite disordered precipitates. This composite precipitate phase coarsens during subsequent thermal exposure, transforming into larger-sized Q'-AlMgSiCu and S-Al_2CuMg phases. In contrast, in the 8M8A alloy with high Ag content, the main precipitate at peak aging is the GPB zone, the precursor of the S-Al_2CuMg phase, which is easy to grow further and transform into the S-Al_2CuMg phase during the thermal exposure process. The growth of both the L-QP1-GPB composite disordered precipitate and the GPB zone in the two alloys requires a higher content of Mg/Cu elements, leading to the dissolution of the Ω phase in the alloy, reducing the number density of precipitates in the alloy, and consequently reducing the mechanical properties of the alloy after long term high-temperature thermal exposure.

Moreover, for the 8M5A and 8M8A alloys, the σ-$Al_5Cu_6Mg_2$ phase present in low Ag content alloys exhibits high thermal stability at elevated temperatures[22]. However, the σ-$Al_5Cu_6Mg_2$ phase is a cubic particle. When it is dispersed in the matrix, the probability of hindering dislocation movement is less than that of the lath-shaped C/L/Q′-AlMgSiCu phase, the rod-shaped S-Al_2CuMg phase, the disc-shaped θ′-Al_2Cu phase and the Ω phase, resulting in a low contribution value of the σ phase to the mechanical properties. In the 8M5A alloy, the significant reduction in the density of Ω phase after long term thermal exposure leads to the predominant presence of the σ-$Al_5Cu_6Mg_2$ phase. In contrast, in the 8M8A alloy, although the number density of the Ω phase also significantly decreases, the number of the rod-like S-Al_2CuMg phase in the alloy increases significantly after long term thermal exposure. The strengthening

effect of S-Al_2CuMg phase is superior to that of the cubic σ-$Al_5Cu_6Mg_2$ phase. Therefore, after long term thermal exposure, the strength of the 8M8A alloy is higher than that of the 8M5A alloy. This indicates that although the σ-$Al_5Cu_6Mg_2$ phase exhibits high thermal stability, its cubic shape has a poorer effect on dislocation hindrance, and it cannot serve as a beneficial precipitate phase in high-strength heat-resistant aluminum alloys.

Furthermore, considering the mechanical properties of alloys under different heat treatment conditions and temperatures as shown in Figs. 6-1 and 6-2, the low-Mg 3M5A alloy exhibits lower mechanical properties at room temperature in the peak-aged state. However, its performance does not show a significant decrease after long term thermal exposure at high temperature, allowing it to serve for extended periods at high temperatures. This is mainly attributed to the multiple interface structures containing χ-AgMg interface phase, C/L-AlMgSiCu interface phase, and Sc segregation layer at the θ′/Al interface, which inhibits the coarsening of θ′ during high-temperature thermal exposure. When the Mg content is increased, the rapid precipitation of the Ω phase improves the mechanical properties of the alloy at room temperature. However, the increase in Mg content promotes the precipitation of QP1, GPB, and S-Al_2CuMg phases, which are prone to coarsening or phase transformation during aging, leading to rapid coarsening of precipitates in the alloy during thermal exposure. Moreover, to provide the solute atoms required for the growth of precipitates such as S-Al_2CuMg, the Ω phase, which has low stability at 210°C, tends to dissolve. Therefore, high-Mg alloys have higher mechanical properties at room temperature but lower heat resistance after long term thermal exposure. Currently, in the Al-Cu-Mg-Ag system, increasing the Mg content is an important factor in improving the alloy's mechanical

properties at room temperature[38]. However, in high-Mg alloys, the phase transformation during long term thermal exposure leads to a rapid decline in performance, which is detrimental to the stability of components requiring long-term service. The results in Fig. 6-2 indicate that high-Mg alloys with a high content of the Ω phase still exhibit significant advantages in mechanical properties under short-term high-temperature service conditions. Therefore, high-Mg/Ag Al-Cu-Mg-Ag-(Si) alloys mainly strengthened by the Ω phase are more suitable for fabricating components that require short-term service but operate at high temperatures. Conversely, low-Mg Al-Cu-Mg-Ag-Si alloys containing multiple interfacial segregation structures are more suitable for components requiring long-term service at medium to high temperatures.

6.5 Precipitation mechanism of σ/Ω/θ′ phase in Al-Cu-Mg-Ag-Si alloy

6.5.1 Precipitation mechanism of σ phase in Al-Cu-Mg-Ag-Si alloy

The presence of Si is crucial for the precipitation of the cubic σ-$Al_5Cu_6Mg_2$ phase in Al-Cu-Mg-Ag alloys[109]. However, there is no Si in the σ-$Al_5Cu_6Mg_2$ phase. Currently, the mechanism by which Si promotes the precipitation of the σ-$Al_5Cu_6Mg_2$ phase in Al-Cu-Mg-Ag alloys remains unclear. To analyze the effect of Si addition on the precipitation behavior of the σ-$Al_5Cu_6Mg_2$ phase, the relationship between the equilibrium phase type and σ-$Al_5Cu_6Mg_2$ phase in different Al-Cu-Mg-(Ag)-Si alloys under heat treatment in the existing literature was calculated using Pandat software. The results are shown in Fig. 6-19, and the corresponding data used for Fig. 6-19 are presented in Tab. 6-4.

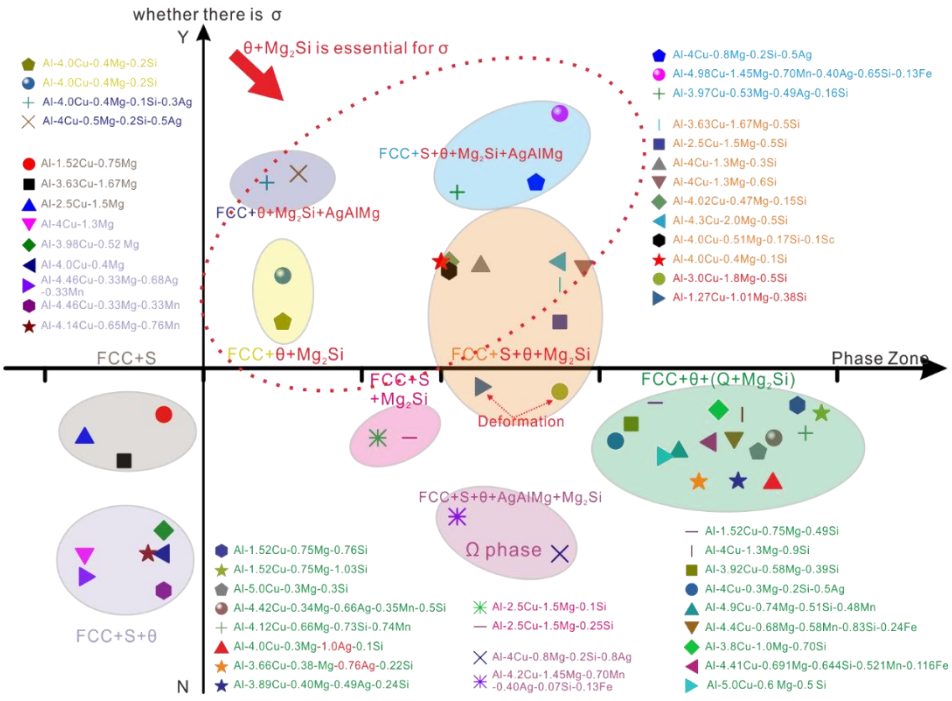

Figure 6-19 A schematic diagram illustrating the relationship between equilibrium phases and σ-$Al_5Cu_6Mg_2$ at different aging temperatures for various alloys[19, 20, 27, 109, 113, 119, 120, 122, 166, 201, 213-222]. All equilibrium phases for the alloys are based on heat treatment processes and alloy compositions obtained using Pandat software, as described in the referenced literatures

As shown in Fig. 6-19, there is no presence of the σ-$Al_5Cu_6Mg_2$ phase after aging heat treatment in Al-Cu-Mg alloys without Si. After adding Si elements to the alloy, not all Si-containing alloys exhibit the σ-$Al_5Cu_6Mg_2$ phase. When the equilibrium phases of the alloy after heat treatment is FCC + S + Mg2Si or FCC + θ + Q + (Mg2Si + Si), there is no σ-$Al_5Cu_6Mg_2$ phase present in the alloy. However, when the equilibrium phase composition is FCC + θ + Mg2Si or FCC + θ + Mg2Si + S, the σ-$Al_5Cu_6Mg_2$ phase is present in the alloy.

Table 6-4 The equilibrium phase parameters corresponding to each alloy shown in Fig.6-19

composition	Ageing temperature	Equilibrium phase	σ
Al - 3.63Cu - 1.67Mg[109]	200/265 ℃	FCC + S	N
Al - 1.52Cu - 0.75Mg[213]	190 ℃	FCC + S	N
Al - 2.5Cu - 1.5Mg[19]	200 ℃	FCC + S	N
Al - 4Cu - 1.3Mg[214]	190 ℃	FCC + S + θ	N
Al - 3.98Cu - 0.52 Mg[201]	175/225 ℃	FCC + S + θ	N
Al - 4.0Cu - 0.4Mg[119]	250 ℃	FCC + S + θ	N
Al-4.46Cu-0.33Mg-0.68Ag-0.33Mn[120]	190 ℃	FCC + θ + $Al_{12}Mn$ + AgAlMg + S	N
Al-4.46Cu - 0.33Mg - 0.33Mn[120]	190 ℃	FCC+θ+$Al_{12}Mn$+S	N
Al- 4.14Cu - 0.65Mg - 0.76Mn[20]	160 ℃	FCC+$Al_{12}Mn$+θ+S	N
Al - 4.0Cu - 0.4Mg - 0.2Si[119]	250 ℃	FCC + θ + Mg_2Si	Y
Al-4.0Cu-0.4Mg-0.2Si-0.3Ag[119]	250 ℃	FCC + θ + Mg_2Si	Y
Al-4.0Cu-0.4Mg-0.1Si-0.3Ag[119]	250 ℃	FCC + θ + Mg_2Si + AgAlMg	Y
Al - 4Cu - 0.5Mg - 0.2Si - 0.5Ag	180 ℃	FCC+θ+Mg_2Si+ AgAlMg	Y
Al - 2.5Cu - 1.5Mg - 0.1Si[19]	200 ℃	FCC + S + Mg_2Si	N
Al - 2.5Cu - 1.5Mg - 0.25Si[19]	200 ℃	FCC + S + Mg_2Si	N
Al - 3.63Cu - 1.67Mg – 0.5Si[109]	200/265 ℃	FCC+S+θ+Mg2Si	Y
Al - 2.5Cu - 1.5Mg - 0.5Si[19]	200 ℃	FCC+S+Mg_2Si+θ	Y
Al - 3.0Cu - 1.8Mg - 0.5Si[27]	180 ℃	FCC+S+Mg_2Si+θ	N
Al - 4Cu - 1.3Mg - 0.3Si[214]	190 ℃	FCC+S+θ+Mg_2Si	Y
Al - 4Cu - 1.3Mg - 0.6Si[214]	190 ℃	FCC+S+Mg_2Si+θ	Y
Al- 4.02Cu - 0.47Mg - 0.15Si[201]	175/225 ℃	FCC+θ+Mg_2Si+S	Y
Al-1.52Cu- 0.75Mg-1.03Si[213]	190 ℃	FCC + Q + θ + Si	N
Al - 4.3Cu - 2.0Mg - 0.5Si[216]	190 ℃	FCC+S+θ+Mg_2Si	Y

Table 6-4 The equilibrium phase parameters corresponding to each alloy shown in Fig.6-19 (continued)

composition	Ageing temperature	Equilibrium phase	σ
Al- 1.27Cu - 1.01Mg - 0.38Si[217]	170 ℃	FCC+S+Mg2Si+θ	N
Al - 4.0Cu - 0.51Mg - 0.17Si - 0.1Sc[215]	175/225 ℃	FCC + θ + S + Mg_2Si + $ScSi_x$	Y
Al - 4.0Cu - 0.4Mg - 0.1Si[119]	250 ℃	FCC+θ+Mg_2Si+S	Y
Al - 4Cu - 0.8Mg - 0.2Si - 0.5Ag	180 ℃	FCC+θ+S+Mg2Si+ AgAlMg	Y
Al - 4.98Cu - 1.45Mg - 0.70Mn - 0.40Ag - 0.65Si - 0.13Fe[218]	180 ℃	FCC + θ+ Mg_2Si + S + AgAlMg	Y
Al - 4Cu - 0.8Mg - 0.2Si - 0.8Ag	180 ℃	FCC+θ+S+AgAlMg+ Mg_2Si	N
Al - 4.2Cu - 1.45Mg - 0.70Mn - 0.40Ag - 0.07Si - 0.13Fe[218]	180 ℃	FCC + θ + S + AgAlMg + Mg_2Si	N
Al - 1.52Cu - 0.75Mg - 0.49Si[213]	190 ℃	FCC + θ + Mg_2Si + Q	N
Al - 4Cu - 1.3Mg - 0.9Si[214]	190 ℃	FCC+θ+Q+Mg_2Si	N
Al - 3.92Cu - 0.58Mg - 0.39Si[23]	175 ℃	FCC+θ+Q+Mg_2Si	N
Al - 4Cu - 0.3Mg - 0.2Si - 0.5Ag	180 ℃	FCC+θ+Q+Mg_2Si	N
Al - 4.9Cu - 0.74Mg - 0.51Si - 0.48Mn[113]	170 ℃	FCC + θ + $Al_{12}Mn$ + Q + Mg_2Si	N
Al - 3.8Cu - 1.0Mg - 0.70Si[220]	160 ℃	FCC+θ+Q+Mg_2Si	N
Al - 4.4Cu - 0.68Mg - 0.58Mn - 0.83Si - 0.24Fe[219]	190 ℃	FCC+θ+Q+Mg_2Si	N
Al - 4.41Cu - 0.69Mg - 0.64Si - 0.52Mn - 0.12Fe[221]	170 ℃	FCC+θ+Q+Mg_2Si	N
Al - 5.0Cu - 0.6Mg - 0.5Si[222]	160 ℃	FCC+θ+Q+Mg_2Si	N
Al - 5.0Cu - 0.3Mg - 0.3Si[112]	180 ℃	FCC + θ + Q + Si	N
Al - 4.42Cu - 0.34Mg - 0.66Ag - 0.35Mn - 0.5Si[120]	190 ℃	FCC + θ + S + Q + Si	N
Al-4Cu-0.7Mg-0.7Si- 0.74Mn[20]	160 ℃	FCC+θ+$Al_{12}Mn$ + Q	N
Al-1.52Cu-0.75Mg-0.76Si[213]	190 ℃	FCC + Q + θ + Si	N

Comparing the equilibrium phases of several alloys with and without the presence of the σ-$Al_5Cu_6Mg_2$ phase, it can be concluded that θ-Al_2Cu and Mg2Si phases are key equilibrium phases for the precipitation of the σ-$Al_5Cu_6Mg_2$ phase. Therefore, the presence of the σ-$Al_5Cu_6Mg_2$ phase in the alloy is possible only when the equilibrium phases at the aging heat treatment temperature include θ-Al_2Cu and Mg2Si phases. When the equilibrium phases lack θ-Al_2Cu, indicating lower Cu content and higher Mg content in the alloy. The σ-$Al_5Cu_6Mg_2$ phase, with a higher Cu/Mg atomic ratio compared to the S-Al_2CuMg phase, requires more Cu. Therefore, in low-Cu alloys, the S-Al_2CuMg phase is more likely to precipitate. When there is no Mg2Si in the equilibrium phase, it indicates either the absence of Si or relatively high Si content in the alloy, favoring the formation of the Q-Al4Cu2Mg8Si7 phase, which consumes more Cu/Mg elements, resulting in insufficient Cu/Mg elements in the alloy to precipitate the σ-$Al_5Cu_6Mg_2$ phase.

In alloys with equilibrium phases of FCC + θ + Mg2Si + S, two groups of deformed alloys did not produce the σ-$Al_5Cu_6Mg_2$ phase before artificial ageing heat treatment. Niu et al.[27] demonstrated that pre-strain-induced dislocations promoted the nucleation of GPB zone, facilitating the precipitation of the S-Al_2CuMg phase. The precipitation of the S-Al_2CuMg phase consumes Cu/Mg elements, thereby inhibiting the precipitation of the σ-$Al_5Cu_6Mg_2$ phase, indicating a competitive relationship between the σ-$Al_5Cu_6Mg_2$ and S-Al_2CuMg phases. The HAADF-STEM images of different alloys after aging heat treatment in Fig. 6-12 show that in the 8M5A alloy with a higher density of σ-$Al_5Cu_6Mg_2$ phase, there is a lower number of S-Al_2CuMg phase after long term heat exposure. Conversely, in the 8M8A alloy with a lower density of σ-$Al_5Cu_6Mg_2$ phase, there is a higher number of S-Al_2CuMg phase after thermal exposure, further

confirming the competitive relationship between the σ-$Al_5Cu_6Mg_2$ and S-Al_2CuMg phases.

Fig. 6-20 shows the isothermal sections of Al-Cu-Mg-xSi alloys with different Si contents at 180 ℃. With the increase of Mg content, the phase boundary for the precipitation of the σ-$Al_5Cu_6Mg_2$ phase shifts parallel to the right, while its slope remains constant. That is, the relationship between Mg, Si, and Cu elements at the phase boundary can be correlated by a single expression, aiding in directly determining the possible types of precipitates during artificial aging processes based on alloy composition, and subsequently enabling efficient alloy composition selection for service environments.

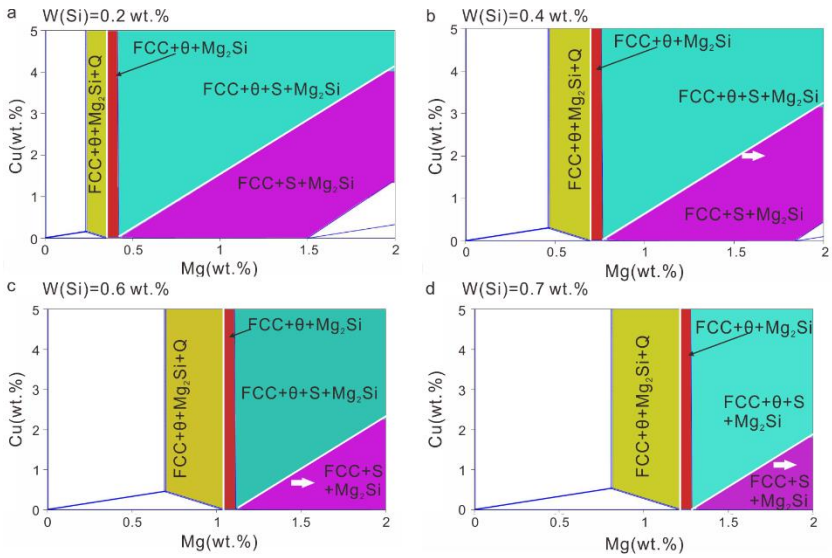

Figure 6-20 Isothermal section of Al-Cu-Mg-xSi alloys with different Si element contents at 180 ℃. (a) 0.2 wt.% . (b) 0.4 wt.%. (c) 0.6 wt.%. (d) 0.7 wt.%

Based on the isothermal sections shown in Fig. 6-20 for different compositions, the critical conditions for the FCC + θ + Mg2Si and FCC + θ + Mg2Si + Q phase regions are W(Mg)/W(Si) ≈ 1.8, and for the FCC +

θ + Mg2Si + S and FCC + Mg2Si + S phase regions, the critical condition is W(Cu) = 2.7 × W(Mg) – 5 × W(Si). Therefore, when the alloy undergoes artificial ageing heat treatment at 180 ℃, the conditions for the precipitation of theσ-$Al_5Cu_6Mg_2$ phase in the alloy are (1) W(Mg)/W(Si) > 1.8 and (2) W(Cu) > 2.7 × W(Mg) – 5 × W(Si). In Al-Cu-Mg-Ag-Si alloys, when the alloy content satisfies these criteria, the σ-$Al_5Cu_6Mg_2$ phase will precipitate. Conversely, when W(Mg)/W(Si) < 1.8, the alloy falls into the FCC + θ + Mg2Si + Q phase region, where the alloy mainly consists of the Q-phase precursor C/L/Q′-AlMgSiCu. Similarly, when W(Cu) < 2.7 × W(Mg) – 5 × W(Si), the alloy falls into the FCC + Mg2Si + S region, where Mg mainly combines with Cu to form the S-Al_2CuMg phase.

From the atomic resolution HAADF-STEM image of the σ-$Al_5Cu_6Mg_2$ phase in the peak-aged 8M5A alloy shown in Fig. 6-21, the C/L-AlMgSiCu phase exists at the σ/Al interface. The APT results in Chapter 4 indicate that the Si can promote the rapid precipitation of the C/L-AlMgSiCu phase. The preferentially precipitated C/L-AlMgSiCu phase not only serves as heterogeneous nucleation sites for the θ′-Al_2Cu phase but also for the σ-$Al_5Cu_6Mg_2$ phase, thereby facilitating the rapid precipitation of the σ-$Al_5Cu_6Mg_2$ phase.

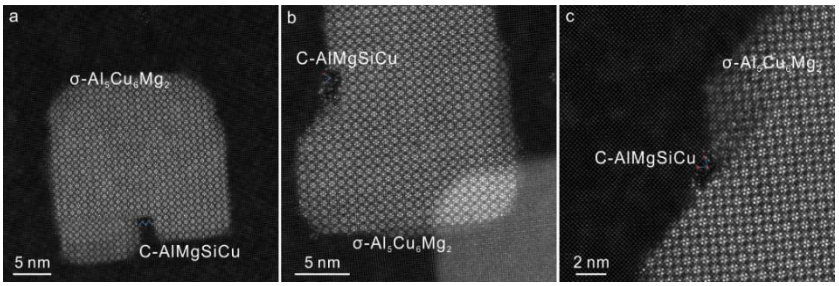

Figure 6-21 Atomic resolution HAADF-STEM images of the σ-$Al_5Cu_6Mg_2$ phase in the 8M5A alloy under peak-aged state. The C-AlMgSiCu phase unit cell structure exists at the σ/Al interface

Figs. 6-22 and 6-23 show the HAADF-STEM and EDX electron tomography reconstruction results of the peak-aged 8M5A alloy, respectively. Combining the Cu/Mg/Si element segregation positions in the EDX results with the contrast and position information in the HAADF-STEM images at different angles, the lath-like L-AlMgSiCu phase, plate-like θ′-Al_2Cu phase, and cubic σ-$Al_5Cu_6Mg_2$ phase coexist in the rod-shaped samples prepared. The EDX and HAADF-STEM electron tomography reconstruction results indicate that the L-AlMgSiCu phase is in contact with the edge of the σ-$Al_5Cu_6Mg_2$ phase. Therefore, the L-AlMgSiCu phase precipitated in the early stages of artificial ageing can serve as heterogeneous nucleation sites to promote the precipitation of the σ-$Al_5Cu_6Mg_2$ phase.

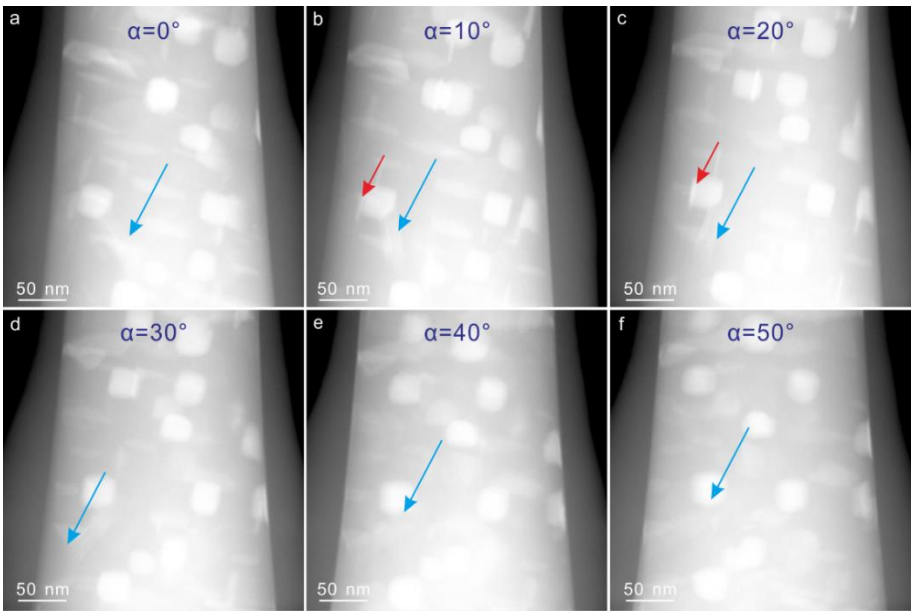

Figure 6-22 The electron tomography characterization results of the 8M5A alloy under peak-aged state

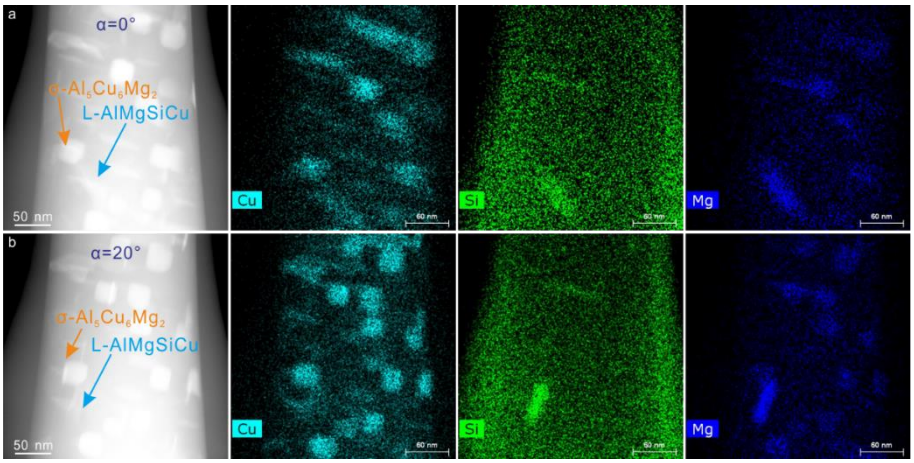

Figure 6-23 The EDX electron tomography characterization results of the 8M5A alloy under peak-aged state

6.5.2 Precipitation mechanism of Ω phase in Al-Cu-Mg-Ag-Si alloy

The content of Ag significantly influences the number density of the Ω phase in Al-Cu-Mg-Ag-Si alloys. For the 8M5A and 8M8A alloys with consistent Mg content, higher Ag content promotes the precipitation of the Ω phase, ensuring its role as the main strengthening phase. Fig. 6-19 summarizes the relationship between the precipitation of the σ-$Al_5Cu_6Mg_2$ phase and the equilibrium phase composition in Al-Cu-Mg-Ag-Si alloys, where the equilibrium phases are ordered based on their phase fractions. In Fig 6-19, when the equilibrium phase of the alloy at the ageing temperature is FCC + S + θ + AgMgAl + Mg2Si, no σ-$Al_5Cu_6Mg_2$ phase precipitates, and the main precipitate is the Ω phase. However, when the equilibrium phase of the alloy at the ageing temperature is FCC + θ + Mg2Si + AgMgAl, σ-$Al_5Cu_6Mg_2$ phase will precipitate. That is, the relative fractions of AgMgAl and Mg2Si in the equilibrium phase are crucial for whether the Ω phase dominates in the alloy. The equilibrium phase AgMgAl contains both Ag and Mg elements, similar to the AgMg

segregation layer. Therefore, the equilibrium phase AgMgAl can be considered as a phase related to the Ω phase. Fig. 6-24 calculates the phase fractions of AgMgAl and Mg2Si in equilibrium in Al-Cu-Mg-Ag-Si alloys with different Si contents. When the Si content is consistent, changing the Ag element content results in no significant change in the phase fraction of Mg2Si, but the phase fraction of AgMgAl undergoes a significant change. According to the calculated results, when W(Ag)/W(Si) > 4, the phase fraction of AgMgAl at the ageing temperature exceeds that of Mg2Si in Al-Cu-Mg-Ag-Si alloys. Thus, W(Ag)/W(Si) > 4 is the critical condition for obtaining the Ω phase as the main precipitate in Al-Cu-Mg-Ag-Si alloys. Under the premise of meeting this critical condition, selecting an appropriate Mg content can result in Al-Cu-Mg-Ag-Si alloys with the Ω phase as the primary precipitate.

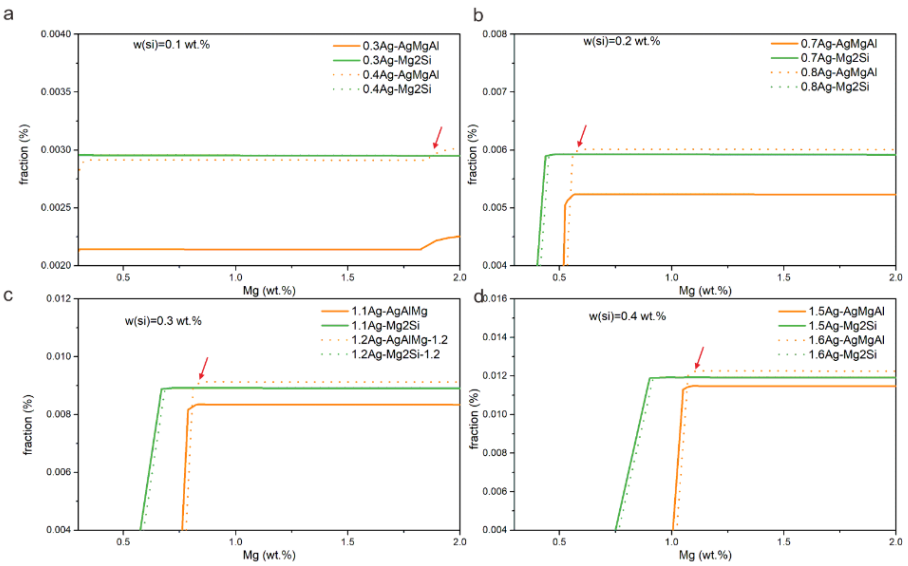

Figure 6-24 The phase fraction for equilibrium phases AgMgAl and Mg_2Si in Al-Cu-Mg-Ag-Si alloys with different Si contents

6.6 Summary of this chapter

In this chapter, four groups of Al-Cu-Mg-Ag-Si alloys were characterized using multiple scale structure analysis and mechanical properties. Combined with literature data and thermodynamic calculations by CALPHAD, the effects of Cu/Mg/Si/Ag elements on the precipitation behavior of the σ-$Al_5Cu_6Mg_2$ phase and Ω phase in Al-Cu-Mg-Ag-Si alloys were analyzed. The effects of different precipitates on the strength and heat resistance of the alloys were summarized. The main conclusions are as follows:

(1) Increasing the Mg content promotes the precipitation of the Ω phase and σ-$Al_5Cu_6Mg_2$ phase while suppressing the precipitation of the θ′-Al_2Cu phase in Al-Cu-Mg-Ag-Si alloys. Increasing Ag content will promote the precipitation of the Ω phase and inhibits the precipitation of the θ′-Al_2Cu phase and σ-$Al_5Cu_6Mg_2$ phase.

(2) Comparing the effects of different precipitates on the long-term thermal exposure performance and high-temperature mechanical properties of the alloys, Al-Cu-Mg-Ag-(Si) alloys with Ω phase as the main strengthening phase are more suitable for the preparation of structural parts with short service life but high service temperature. Conversely, Al-Cu-Mg-Ag-Si alloys with low Mg content containing multiple interface segregation structures at θ′/Al interface are better suited for components requiring long-term service at intermediate to high temperatures.

(3) Based on CALPHAD results and literature data, the critical conditions for the precipitation of the σ-$Al_5Cu_6Mg_2$ phase in Al-Cu-Mg-Ag-Si alloys were summarized as follows: (1) W(Mg)/W(Si) > 1.8; (2) W(Cu) > 2.7 × W(Mg) – 5 × W(Si). When W(Mg)/W(Si) < 1.8, the main precipitate phase in the alloy will be the C/L/Q′-AlMgSiCu phase, which is precursor of equilibrium Q phase. When W(Cu) < 2.7 × W(Mg) – 5 ×

W(Si), the alloy will generate precursors such as the GPB zone for the S-Al_2CuMg phase. Within the commonly used aging temperature range, there are no significant differences in the equilibrium phases of the alloy, making this criterion universally applicable.

(4) Based on CALPHAD results and literature data, the critical conditions for promoting the precipitation of the Ω phase while inhibiting the σ-$Al_5Cu_6Mg_2$ phase and θ′-Al_2Cu phase in Al-Cu-Mg-Ag-Si alloys were summarized. When W(Ag)/W(Si) > 4, selecting an appropriate Mg content can result in Al-Cu-Mg-Ag-Si alloys with the Ω phase as the main precipitates.

Chapter 7. Summary

In this work, the effects of aging heat treatment processes and alloy element compositions on the precipitation behavior, mechanical properties, and heat resistance of Al-Cu-Mg-Ag-(Si) alloys were investigated by combining the SEM, TEM, APT, microhardness test and tensile test and other characterization test methods with CALPHAD, first principle calculation and AIMD simulations. In addition, the critical conditions for the precipitation of the σ-$Al_5Cu_6Mg_2$ phase, θ′-Al_2Cu phase, and Ω phase in Al-Cu-Mg-Ag-Si were established. Moreover, A multiple interface segregation structure was constructed at the θ′/Al interface, achieving a synergistic improvement in the strength and heat resistance of the aluminum alloy. The main conclusions are as follows:

(1) Based on the Kampmann-Wagner-Numerical theory, it is revealed that the relationship between the size of the Ω phase and the critical size ($r^*_{thermal}$) of the Ω phaseat thermal exposure temperature is a key factor influencing the coarsening of Ω phase during thermal exposure. After artificial ageing heat treatment, when the size of the Ω phase in the alloy is smaller than the critical size $r^*_{thermal}$, the rapid dissolution of smaller Ω phases leads to a significant decrease in the number density of Ω phases in the alloy, resulting in a notable reduction in heat resistance. However, when the size of the Ω phase is greater than or equal to the critical size $r^*_{thermal}$, the coarsening rate of the Ω phase is consistent with the normal coarsening rate under thermal exposure temperature, but a larger initial size results in a larger final size after long-term thermal exposure. Therefore, the closer the size of the Ω phase in the alloy after artificial ageing is to the critical size at thermal exposure temperature, the better the heat resistance of the alloy. This discovery contributes to optimizing heat

treatment parameters in industrial production to achieve maximum heat resistance of the alloy while ensuring ageing strength.

(2) The concept of constructing a multiple interface segregation structure at the precipitate/matrix interface is proposed. Alloys designed based on this concept exhibit a yield strength of 400 MPa after thermal exposure at 200 ℃ for 100 h, with a strength retention rate of 97%, setting a new record for the synergistic improvement of strength and heat resistance in aluminum alloys. A multiple interface segregation structure containing C/L-AlMgSiCu interface phase, χ-AgMg interface phase, and Sc segregation layer was constructed at the θ′/Al coherent and semi-coherent interfaces in the designed alloy under peak-aged state. First-principles calculations show that the C -AlMgSiC interface phase and χ-AgMg interface phase can significantly reduce the formation energy of the θ′-Al_2Cu phase and improve the stability of the θ′-Al_2Cu phase. The addition of Si promotes the rapid precipitation of the C/L-AlMgSiCu phase in the early stages of artificial ageing, further acting as a heterogeneous nucleation site for the precipitation of the θ′-Al_2Cu phase, increasing the density and volume fraction of the θ′-Al_2Cu phase, and ultimately achieving a synergistic improvement in alloy strength and heat resistance.

(3) The χ-AgMg interface phase is identified as a new interface structure. Based on atomic resolution HAADF-STEM and EDX data, a crystal model of this structure was successfully constructed. Combined with TEM characterization and first-principles calculations, it is revealed that the dissolution of the χ-AgMg interface phase during high-temperature exposure is caused by the diffusion of Ag elements in contact with the aluminum matrix. Furthermore, TEM results at different thermal exposure temperatures demonstrate that although the χ-AgMg interface phase gradually dissolves at high temperatures, it still partially inhibits the

coarsening of the θ′-Al_2Cu phase, thereby improving the heat resistance of the alloy to some extent.

(4) Using two groups of low Mg/Si ratio Al-Cu-Mg-Ag-Si alloys with different Ag contents, based on CALPHAD, multiple scale structure characterization and mechanical property tests, the critical conditions for the precipitation of the Ω phase in low Mg/Si ratio Al-Cu-Mg-Ag-Si alloys were updated as: W(Mg)/W(Si) > 1.4 and X(Ag)/X(Mg_{excess}) > 1. Here, X(Mg_{excess}) represents the atomic percentage of Mg remaining after the formation of the C/L-AlMgSiCu in supersaturated solid solution. This update enhances the understanding of the precipitation sequence and heat resistance performance of Al-Cu-Mg-Ag-Si alloys, facilitating the design of new heat-resistant aluminum alloy systems with different proportions of Ω/θ′ precipitate phases based on different service conditions.

(5) Increasing the Mg and Ag contents promotes the rapid precipitation of the Ω phase and improves the room temperature mechanical properties of Al-Cu-Mg-Ag-Si alloys. However, in high Mg/Ag alloys, the Ω phase and the QP1/S phase coarsen rapidly during prolonged exposure at 210 ℃, leading to a rapid decline in alloy mechanical properties. Comparing the effects of different precipitates on the long-term thermal exposure performance and high-temperature mechanical properties of the alloys, Al-Cu-Mg-Ag-(Si) alloys with Ω phase as the main strengthening phase are more suitable for the preparation of structural parts with short service life but high service temperature. Conversely, Al-Cu-Mg-Ag-Si alloys with low Mg content containing multiple interface segregation structures at θ′/Al interface are better suited for components requiring long-term service at intermediate to high temperatures.

(6) Based on CALPHAD results and literature data, the critical

conditions for the precipitation of the σ-$Al_5Cu_6Mg_2$ phase in Al-Cu-Mg-Ag-Si alloys were summarized as follows: (1) W(Mg)/W(Si) > 1.8; (2) W(Cu) > 2.7 × W(Mg) – 5 × W(Si). When W(Mg)/W(Si) < 1.8, the main precipitate phase in the alloy will be the C/L/Q′-AlMgSiCu phase, which is precursor of equilibrium Q phase. When W(Cu) < 2.7 × W(Mg) – 5 × W(Si), the alloy will generate precursors such as the GPB zone for the S-Al_2CuMg phase. In addition, the critical conditions for promoting the precipitation of the Ω phase while inhibiting the σ-$Al_5Cu_6Mg_2$ phase and θ′-Al_2Cu phase in Al-Cu-Mg-Ag-Si alloys were summarized. When W(Ag)/W(Si) > 4, selecting an appropriate Mg content can result in Al-Cu-Mg-Ag-Si alloys with the Ω phase as the main precipitates.

References

1. Nakai, M.&Eto, T. New aspect of development of high strength aluminum alloys for aerospace applications. *Materials Science and Engineering: A* **285**, 62-68 (2000).
2. Guan, R. et al. Development of aluminum alloy materials: Current status, trend, and prospects. *Strategic Study of Chinese Academy of Engineering* **22**, 68-75 (2020).
3. Lan, X., Li, K., Wang, J., Yang, M., Lu, Q.&Du, Y. Developing Al-Fe-Si alloys with high thermal stability through tuning Fe, Si contents and cooling rates. *Intermetallics* **144**, 107505 (2022).
4. Ma, Y. et al. Atomic-scale investigation of the interface precipitation in a TiB_2 nanoparticles reinforced Al-Zn-Mg-Cu matrix composite. *Acta Materialia* **185**, 287-299 (2020).
5. Polmear, I. J.&Couper, M. J. Design and development of an experimental wrought aluminum alloy for use at elevated temperatures. *Metallurgical Transactions A* **19**, 1027-1035 (1988).
6. Bahl, S. et al. Aging behavior and strengthening mechanisms of coarsening resistant metastable θ' precipitates in an Al-Cu alloy. *Materials & Design* **198**, 109378 (2021).
7. Ringer, S. P., Sakurai, T.&Polmear, I. J. Origins of hardening in aged Al-Cu-Mg-(Ag) alloys. *Acta Materialia* **45**, 3731-3744 (1997).
8. Gazizov, M. R. et al. The deformation behavior of the $\{111\}_{Al}$ plates in an Al-Cu-Mg-Ag alloy. *Acta Materialia* **243**, 118534 (2023).
9. Hutchinson, C. R., Fan, X., Pennycook, S. J.&Shiflet, G. J. On the origin of the high coarsening resistance of Ω plates in Al-Cu-Mg-Ag Alloys. *Acta Materialia* **49**, 2827-2841 (2001).
10. Ryen, Ø., Holmedal, B., Nijs, O., Nes, E., Sjölander, E.&Ekström, H.-

E. Strengthening mechanisms in solid solution aluminum alloys. *Metallurgical and Materials Transactions A* **37**, 1999-2006 (2006).

11. Hansen, N. Hall–Petch relation and boundary strengthening. *Scripta Materialia* **51**, 801-806 (2004).
12. Hu, J., Shi, Y. N., Sauvage, X., Sha, G.&Lu, K. Grain boundary stability governs hardening and softening in extremely fine nanograined metals. *Science* **355**, 1292-1296 (2017).
13. Yao, X.&Zajac, S. The strain-rate dependence of flow stress and work-hardening rate in three Al-Mg alloys. *Scandinavian Journal of Metallurgy* **29**, 101-107 (2000).
14. Werinos, M., Antrekowitsch, H., Ebner, T., Prillhofer, R., Uggowitzer, P. J.&Pogatscher, S. Hardening of Al-Mg-Si alloys: Effect of trace elements and prolonged natural aging. *Materials & Design* **107**, 257-268 (2016).
15. Liu, G., Zhang, G. J., Ding, X. D., Sun, J.&Chen, K. H. The influences of multiscale-sized second-phase particles on ductility of aged aluminum alloys. *Metallurgical and Materials Transactions A* **35**, 1725-1734 (2004).
16. Yuan, S. P. et al. Effect of precipitate morphology evolution on the strength–toughness relationship in Al-Mg-Si alloys. *Scripta Materialia* **60**, 1109-1112 (2009).
17. Ber, L. B., Teleshov, V. V.&Ukolova, O. G. Phase composition and mechanical properties of wrought aluminum alloys of the system Al-Cu-Mg-Ag-X_i. *Metal Science and Heat Treatment* **50**, 220-227 (2008).
18. Lan, J., Shen, X., Liu, J.&Hua, L. Strengthening mechanisms of 2A14 aluminum alloy with cold deformation prior to artificial aging. *Materials Science and Engineering: A* **745**, 517-535 (2019).
19. Hutchinson, C. R.&Ringer, S. P. Precipitation processes in Al-Cu-Mg

alloys microalloyed with Si. *Metallurgical and Materials Transactions A* **31**, 2721-2733 (2000).

20. Li, J., Chen, S., Li, F., Chen, K.&Huang, L. Synergy effect of Si addition and pre-straining on microstructure and properties of Al-Cu-Mg alloys with a medium Cu/Mg ratio. *Materials Science and Engineering: A* **767**, 138429 (2019).
21. Yang, H. et al. Influence of Cu/Mg ratio and content on heat-resistance of Al-Cu-Mg alloys. *Journal of Materials Research and Technology* **29**, 1040-1051 (2024).
22. Schueller, R. D., Wawner, F. E.&Sachdev, A. K. Strengthening potential of the cubic σ precipitate in Al-Cu-Mg-Si alloys. *Journal of Materials Science* **29**, 239-249 (1994).
23. Liang, S. S., Wen, S. P., Wu, X. L., Huang, H., Gao, K. Y.&Nie, Z. R. The synergetic effect of Si and Sc on the thermal stability of the precipitates in AlCuMg alloy. *Materials Science and Engineering: A* **783**, 139319 (2020).
24. Li, Z. Q., Ren, W. R., Chen, H. W.&Nie, J. F. θ‴ precipitate phase, GP zone clusters and their origin in Al-Cu alloys. *Journal of Alloys and Compounds* **930**, 167396 (2023).
25. Chisholm, M. F. et al. Atomic structures of interfacial solute gateways to θ′ precipitates in Al-Cu alloys. *Acta Materialia* **212**, 116891 (2021).
26. Chen, X. et al. Precipitation processes and structural evolutions of various GPB zones and two types of S phases in a cold-rolled Al-Mg-Cu alloy. *Materials & Design* **199**, 109425 (2021).
27. Niu, F. J. et al. The effect of pre-deformation on the precipitation behavior of AlCuMg(Si) alloys with low Cu/Mg ratios. *Journal of Alloys and Compounds* **823**, 153831 (2020).
28. Ringer, S. P., Yeung, W., Muddle, B. C.&Polmear, I. J. Precipitate

stability in Al-Cu-Mg-Ag alloys aged at high temperatures. *Acta Metallurgica et Materialia* **42**, 1715-1725 (1994).

29. Bai, S., Liu, Z., Ying, P., Wang, J.&Wang, A. Quantitative study of the solute clustering and precipitation in a pre-stretched Al-Cu-Mg-Ag alloy. *Journal of Alloys and Compounds* **725**, 1288-1296 (2017).
30. Chen, M.-C. et al. Quantitative evaluation of the effect of Ag-addition on the concurrently-existing precipitation kinetics in the aged Al-Cu-Mg(-Ag) alloys. *Materials & Design* **227**, 111766 (2023).
31. Zhou, Y., Liu, Z., Bai, S., Ying, P.&Lin, L. Effect of Ag additions on the lengthening rate of Ω plates and formation of σ phase in Al-Cu-Mg alloys during thermal exposure. *Materials Characterization* **123**, 1-8 (2017).
32. Howe, J. M. Analytical transmission electron microscopy analysis of Ag and Mg segregation to {111} θ precipitate plates in an Al-Cu-Mg-Ag alloy. *Philosophical Magazine Letters* **70**, 111-120 (1994).
33. Lityńska, L., Braun, R., Staniek, G., Dalle Donne, C.&Dutkiewicz, J. TEM study of the microstructure evolution in a friction stir-welded AlCuMgAg alloy. *Materials Chemistry and Physics* **81**, 293-295 (2003).
34. Ringer, S. P.&Hono, K. Microstructural evolution and age hardening in aluminium alloys: Atom probe field-ion microscopy and transmission electron microscopy studies. *Materials Characterization* **44**, 101-131 (2000).
35. Reich, L., Murayama, M.&Hono, K. Evolution of Ω phase in an Al-Cu-Mg-Ag alloy—a three-dimensional atom probe study. *Acta Materialia* **46**, 6053-6062 (1998).
36. Zhu, A., Starke, E. A.&Shiflet, G. J. An FP-CVM calculation of pre-precipitation clustering in AlCuMgAg alloys. *Scripta Materialia* **53**,

35-40 (2005).

37. Macchi, C., Tolley, A., Giovachini, R., Polmear, I. J.&Somoza, A. Influence of a microalloying addition of Ag on the precipitation kinetics of an Al-Cu-Mg alloy with high Mg:Cu ratio. *Acta Materialia* **98**, 275-287 (2015).
38. Bai, S., Liu, Z., Zhou, X., Xia, P.&Zeng, S. Mg-controlled formation of Mg-Ag co-clusters in initial aged Al-Cu-Mg-Ag alloys. *Journal of Alloys and Compounds* **602**, 193-198 (2014).
39. Teleshov, V. V., Kaputkin, E. Y., Golovleva, A. P.&Kosmacheva, N. P. Temperature ranges of phase transformations and mechanical properties of alloys of the Al-Cu-Mg-Ag system with various Cu/Mg ratios. *Metal Science and Heat Treatment* **47**, 139-144 (2005).
40. Zhang, J.-b. et al. Identification of thermal effects involved in DSC experiment on Al-Cu-Mg-Ag alloys with high Cu:Mg ratio. *International Journal of Minerals, Metallurgy, and Materials* **18**, 671-675 (2011).
41. Zhang, J., Zhang, Y., Zhu, B., Liu, R., Li, Z.&Li, X. Small-angle X-ray scattering investigation of aging behavior of Al-Cu-Mg-Ag alloys using synchrotron radiation. *Rare Metals* **31**, 537-540 (2012).
42. Lumley, R. N., Morton, A. J.&Polmear, I. J. Enhanced creep performance in an Al-Cu-Mg-Ag alloy through underageing. *Acta Materialia* **50**, 3597-3608 (2002).
43. Gazizov, M.&Kaibyshev, R. Precipitation structure and strengthening mechanisms in an Al-Cu-Mg-Ag alloy. *Materials Science and Engineering: A* **702**, 29-40 (2017).
44. Bai, S., Xu, H., Liu, Z., Yi, X., Zhao, J.&Wang, J. On the role of the solute partitioning and chemistry in initial precipitation of Ω plates. *Materials Science and Engineering: A* **766**, 138339 (2019).

45. Li, B. Q.&Wawner, F. E. Dislocation interaction with semicoherent precipitates (Ω phase) in deformed Al-Cu-Mg-Ag alloy. *Acta Materialia* **46**, 5483-5490 (1998).
46. Muddle, B. C.&Polmear, I. J. The precipitate Ω phase in Al-Cu-Mg-Ag alloys. *Acta Metallurgica* **37**, 777-789 (1989).
47. Auld, J. H. Structure of metastable precipitate in some Al-Cu-Mg-Ag alloys. *Materials Science and Technology* **2**, 784-787 (1986).
48. Knowles, K. M.&Stobbs, W. M. The structure of {111} age-hardening precipitates in Al-Cu-Mg-Ag alloys. *Acta Crystallographica Section B* **44**, 207-227 (1988).
49. Gazizov, M. R. et al. Precipitate/matrix incompatibilities related to the $\{111\}_{Al}$ Ω plates in an Al-Cu-Mg-Ag alloy. *Materials Characterization* **182**, 111586 (2021).
50. Gazizov, M. R., Boev, A. O., Marioara, C. D., Holmestad, R., Gazizova, M. Y.&Kaibyshev, R. O. Edge interfaces of the Ω plates in a peak-aged Al-Cu-Mg-Ag alloy. *Materials Characterization* **185**, 111747 (2022).
51. Yang, S. L., Zhao, X. J., Chen, H. W., Wilson, N.&Nie, J. F. Atomic structure and evolution of a precursor phase of Ω precipitate in an Al-Cu-Mg-Ag alloy. *Acta Materialia* **225**, 117538 (2022).
52. Kang, S. J., Kim, Y.-W., Kim, M.&Zuo, J.-M. Determination of interfacial atomic structure, misfits and energetics of Ω phase in Al-Cu-Mg-Ag alloy. *Acta Materialia* **81**, 501-511 (2014).
53. Garg, A.&Howe, J. M. Convergent-beam electron diffraction analysis of the Ω phase in an Al-4.0 Cu-0.5 Mg-0.5 Ag alloy. *Acta Metallurgica et Materialia* **39**, 1939-1946 (1991).
54. Yang, S. L., Wilson, N.&Nie, J. F. Revisit of the structure of Ω precipitate in Al-Cu-Mg-Ag alloys. *Scripta Materialia* **205**, 114204

(2021).

55. Wang, S. C.&Starink, M. J. Precipitates and intermetallic phases in precipitation hardening Al-Cu-Mg-(Li) based alloys. *International Materials Reviews* **50**, 193-215 (2005).
56. Kang, S. J., Zuo, J.-M., Han, H. N.&Kim, M. Ab initio study of growth mechanism of omega precipitates in Al-Cu-Mg-Ag alloy and similar systems. *Journal of Alloys and Compounds* **737**, 207-212 (2018).
57. Liu, X. Y., Li, M. J., Gao, F., Liang, S. X., Zhang, X. L.&Cui, H. X. Effects of aging treatment on the intergranular corrosion behavior of Al-Cu-Mg-Ag alloy. *Journal of Alloys and Compounds* **639**, 263-267 (2015).
58. Li, C. et al. Effect of solution treatment on precipitation and age-hardening response of an Al-4Mg-1Cu-0.5Si-0.4Ag (wt%) alloy. *Materials Science and Engineering: A* **599**, 64-68 (2014).
59. Balducci, E., Ceschini, L., Messieri, S., Wenner, S.&Holmestad, R. Thermal stability of the lightweight 2099 Al-Cu-Li alloy: Tensile tests and microstructural investigations after overaging. *Materials & Design* **119**, 54-64 (2017).
60. Wang, J., Yi, D., Su, X.&Yin, F. Influence of deformation ageing treatment on microstructure and properties of aluminum alloy 2618. *Materials Characterization* **59**, 965-968 (2008).
61. Ovri, H., Jägle, E. A., Stark, A.&Lilleodden, E. T. Microstructural influences on strengthening in a naturally aged and overaged Al-Cu-Li-Mg based alloy. *Materials Science and Engineering: A* **637**, 162-169 (2015).
62. Gazizov, M.&Kaibyshev, R. Effect of over-aging on the microstructural evolution in an Al-Cu-Mg-Ag alloy during ECAP at

300°C. *Journal of Alloys and Compounds* **527**, 163-175 (2012).

63. Balducci, E., Ceschini, L., Messieri, S., Wenner, S.&Holmestad, R. Effects of overaging on microstructure and tensile properties of the 2055 Al-Cu-Li-Ag alloy. *Materials Science and Engineering: A* **707**, 221-231 (2017).
64. Li, Y., Liu, Z., Bai, S., Zhou, X., Wang, H.&Zeng, S. Enhanced mechanical properties in an Al-Cu-Mg-Ag alloy by duplex aging. *Materials Science and Engineering: A* **528**, 8060-8064 (2011).
65. Ying, P. et al. Pre-Aging Effect on the Formation of Ω Phase and Mechanical Properties of the Al-Cu-Mg-Ag Alloy. *Metals* **12**, 1208 (2022).
66. Liu, X.-y., Wang, Z.-p., Li, Q.-s., Zhang, X.-l., Cui, H.-x.&Zhang, X.-l. Effects of pre-deformation on microstructure and properties of Al-Cu-Mg-Ag heat-resistant alloy. *Journal of Central South University* **24**, 1027-1033 (2017).
67. Deng, X. Precipitation strengthening of stress-aged Al-Cu-Mg-Ag alloy single crystals. *Materials Science and Engineering: A* **819**, 141458 (2021).
68. Hono, K., Sakurai, T.&Polmear, I. J. Pre-precipitate clustering in an Al-Cu-Mg-Ag alloy. *Scripta Metallurgica et Materialia* **30**, 695-700 (1994).
69. Gazizov, M.&Kaibyshev, R. Effect of pre-straining on the aging behavior and mechanical properties of an Al-Cu-Mg-Ag alloy. *Materials Science and Engineering: A* **625**, 119-130 (2015).
70. Zhao, Z., Xiao, N., Zhang, Z.&Wang, Z. Improved stress relaxation stability of a heat-resistant Al-Cu-Mg-Ag alloy with good mechanical properties by a pre-annealing/solution-aging treatment. *Journal of Alloys and Compounds* **961**, 171145 (2023).

71. Sadeghi-Nezhad, D. et al. The effect of cold rolling, double aging and overaging processes on the tensile property and precipitation of AA2024 alloy. *Journal of Materials Research and Technology* **9**, 15475-15485 (2020).
72. Tang, C., Luo, B., Bai, Z., Mo, W.&Deng, P. Effect of non-isothermal ageing on microstructure and mechanical properties of an Al-Cu-Mg-Ag alloy. *Materials Science and Engineering: A* **830**, 142315 (2022).
73. Wang, J. et al. Microstructure evolution and mechanical properties of the Al-Cu-Mg-Ag alloy during non-isothermal aging. *Journal of Alloys and Compounds* **942**, 169031 (2023).
74. Bergsma, S. C., Li, X.&Kassner, M. E. Effects of thermal processing and copper additions on the mechanical properties of aluminum alloy ingot AA 2618. *Journal of Materials Engineering and Performance* **5**, 100-102 (1996).
75. Alexopoulos, N. D., Velonaki, Z., Stergiou, C. I.&Kourkoulis, S. K. Effect of ageing on precipitation kinetics, tensile and work hardening behavior of Al-Cu-Mg (2024) alloy. *Materials Science and Engineering: A* **700**, 457-467 (2017).
76. Teleshov, V. V., Andreev, D. A.&Golovleva, A. P. Effect of chemical composition on the strength of alloys of the Al-Cu-Mg-Ag system after heating at 180-210°C. *Metal Science and Heat Treatment* **48**, 104-112 (2006).
77. Lumley, R. N.&Polmear, I. J. The effect of long term creep exposure on the microstructure and properties of an underaged Al-Cu-Mg-Ag alloy. *Scripta Materialia* **50**, 1227-1231 (2004).
78. Liu, X. Y. et al. Effect of aging temper on the thermal stability of Al-Cu-Mg-Ag heat-resistant alloy. *Materials & Design* **46**, 360-365 (2013).

79. So, H., Won, S.-J., Park, J., Oh, S. J., Kang, L.&Kim, K.-H. Mechanical properties and microstructural evolution in Al-Cu-Mg-Ag alloy with a Cu_xMg_x/10 content. *Materials Science and Engineering: A* **824**, 141573 (2021).
80. Bai, S., Ying, P., Liu, Z., Wang, J.&Li, J. Quantitative transmission electron microscopy and atom probe tomography study of Ag-dependent precipitation of Ω phase in Al-Cu-Mg alloys. *Materials Science and Engineering: A* **687**, 8-16 (2017).
81. Bai, S., Zhou, X., Liu, Z., Xia, P., Liu, M.&Zeng, S. Effects of Ag variations on the microstructures and mechanical properties of Al-Cu-Mg alloys at elevated temperatures. *Materials Science and Engineering: A* **611**, 69-76 (2014).
82. Bai, S., Yi, X.&Liu, Z. On the role of Ag additions on the initial solute hardening and competitive precipitation of Al-Cu-Mg alloys. *Journal of Alloys and Compounds* **945**, 169339 (2023).
83. Liu, X. Y., Wang, Z. P., Fu, B. G., Long, L., Zhang, X. L.&Cui, H. X. Effects of Mg content on the mechanical properties and corrosion resistance of Al-Cu-Mg-Ag alloy. *Journal of Alloys and Compounds* **685**, 209-215 (2016).
84. Bai, S., Zhou, X., Liu, Z., Ying, P., Liu, M.&Zeng, S. Atom probe tomography study of Mg-dependent precipitation of Ω phase in initial aged Al-Cu-Mg-Ag alloys. *Materials Science and Engineering: A* **637**, 183-188 (2015).
85. Røyset, J.&Ryum, N. Scandium in aluminium alloys. *International Materials Reviews* **50**, 19-44 (2005).
86. Jiang, L., Rouxel, B., Langan, T.&Dorin, T. Coupled segregation mechanisms of Sc, Zr and Mn at θ′ interfaces enhances the strength and thermal stability of Al-Cu alloys. *Acta Materialia* **206**, 116634

(2021).

87. Zhang, J.-Y. et al. Microalloying Al alloys with Sc: a review. *Rare Metals* **39**, 636-650 (2020).
88. Pan, S. et al. Micro-alloying effect of Er and Zr on microstructural evolution and yield strength of Al-3Cu (wt.%) binary alloys. *Materials Science and Engineering: A* **790**, 139391 (2020).
89. Zhang, X., Wang, H., Yan, B., Zou, C.&Wei, Z. The effect of grain refinement and precipitation strengthening induced by Sc or Er alloying on the mechanical properties of cast Al-Li-Cu-Mg alloys at elevated temperatures. *Materials Science and Engineering: A* **822**, 141641 (2021).
90. Gao, Y. H., Cao, L. F., Kuang, J., Zhang, J. Y., Liu, G.&Sun, J. Dual effect of Cu on the Al_3Sc nanoprecipitate coarsening. *Journal of Materials Science & Technology* **37**, 38-45 (2020).
91. Taendl, J., Orthacker, A., Amenitsch, H., Kothleitner, G.&Poletti, C. Influence of the degree of scandium supersaturation on the precipitation kinetics of rapidly solidified Al-Mg-Sc-Zr alloys. *Acta Materialia* **117**, 43-50 (2016).
92. Gao, Y. H., Kuang, J., Zhang, J. Y., Liu, G.&Sun, J. Tailoring precipitation strategy to optimize microstructural evolution, aging hardening and creep resistance in an Al-Cu-Sc alloy by isochronal aging. *Materials Science and Engineering: A* **795**, 139943 (2020).
93. Lefebvre, W., Masquelier, N., Houard, J., Patte, R.&Zapolsky, H. Tracking the path of dislocations across ordered Al_3Zr nano-precipitates in three dimensions. *Scripta Materialia* **70**, 43-46 (2014).
94. Seidman, D. N., Marquis, E. A.&Dunand, D. C. Precipitation strengthening at ambient and elevated temperatures of heat-treatable Al(Sc) alloys. *Acta Materialia* **50**, 4021-4035 (2002).

95. Gazizov, M., Teleshov, V., Zakharov, V.&Kaibyshev, R. Solidification behaviour and the effects of homogenisation on the structure of an Al-Cu-Mg-Ag-Sc alloy. *Journal of Alloys and Compounds* **509**, 9497-9507 (2011).
96. Jiang, L. et al. Length-scale dependent microalloying effects on precipitation behaviors and mechanical properties of Al-Cu alloys with minor Sc addition. *Materials Science and Engineering: A* **637**, 139-154 (2015).
97. Chen, B. A. et al. Effect of interfacial solute segregation on ductile fracture of Al-Cu-Sc alloys. *Acta Materialia* **61**, 1676-1690 (2013).
98. Chen, B. A. et al. Effect of solution treatment on precipitation behaviors and age hardening response of Al-Cu alloys with Sc addition. *Materials Science and Engineering: A* **530**, 607-617 (2011).
99. Gao, Y. H. et al. Stabilizing nanoprecipitates in Al-Cu alloys for creep resistance at 300°C. *Materials Research Letters* **7**, 18-25 (2018).
100. Gao, Y. H., Cao, L. F., Yang, C., Zhang, J. Y., Liu, G.&Sun, J. Co-stabilization of θ′-Al_2Cu and Al_3Sc precipitates in Sc-microalloyed Al-Cu alloy with enhanced creep resistance. *Materials Today Nano* **6**, 100035 (2019).
101. Bai, S., Yi, X., Liu, G., Liu, Z., Wang, J.&Zhao, J. Effect of Sc addition on the microstructures and age-hardening behavior of an Al-Cu-Mg-Ag alloy. *Materials Science and Engineering: A* **756**, 258-267 (2019).
102. Xue, H. et al. Highly stable coherent nanoprecipitates via diffusion-dominated solute uptake and interstitial ordering. *Nature Materials* **22**, 434-441 (2023).
103. Li, Y., Gao, G., Wang, Z., Di, H., Li, J.&Xu, G. Effects of the Mg/Si Ratio on Microstructure, Mechanical Properties, and Precipitation

Behavior of Al-Mg-Si-1.0 wt %-Zn Alloys. *Materials (Basel)* **11**, 2591 (2018).

104. Buchanan, K., Colas, K., Ribis, J., Lopez, A.&Garnier, J. Analysis of the metastable precipitates in peak-hardness aged Al-Mg-Si(-Cu) alloys with differing Si contents. *Acta Materialia* **132**, 209-221 (2017).
105. Wang, Y., Liao, H., Wu, Y.&Yang, J. Effect of Si content on microstructure and mechanical properties of Al-Si-Mg alloys. *Materials & Design* **53**, 634-638 (2014).
106. Biswas, A., Siegel, D. J.&Seidman, D. N. Compositional evolution of Q-phase precipitates in an aluminum alloy. *Acta Materialia* **75**, 322-336 (2014).
107. Mitlin, D., Morris, J. W., Radmilovic, V.&Dahmen, U. Precipitation and aging in Al-Si-Ge-Cu. *Metallurgical and Materials Transactions A* **32**, 197-199 (2001).
108. Mitlin, D., Morris, J. W.&Radmilovic, V. Catalyzed precipitation in Al-Cu-Si. *Metallurgical and Materials Transactions A* **31**, 2697-2711 (2000).
109. Barlow, I. C., Rainforth, W. M.&Jones, H. The role of silicon in the formation of the ($Al_5Cu_6Mg_2$) σ phase in Al-Cu-Mg alloys. *Journal of Materials Science* **35**, 1413-1418 (2000).
110. Cai, Q., Mendis, C. L., Wang, S., Chang, I. T. H.&Fan, Z. Effect of heat treatment on microstructure and tensile properties of die-cast Al-Cu-Si-Mg alloys. *Journal of Alloys and Compounds* **881**, 160559 (2021).
111. Li, F., Chen, S., Chen, K.&Huang, L. The role of Si on microstructure, mechanical and local corrosion behaviors of an Al-Cu-Mg-Si alloy with high Cu/Mg ratio. *Journal of Alloys and Compounds* **819**,

152977 (2020).

112. Liu, L., Chen, J. H., Wang, S. B., Liu, C. H., Yang, S. S.&Wu, C. L. The effect of Si on precipitation in Al-Cu-Mg alloy with a high Cu/Mg ratio. *Materials Science and Engineering: A* **606**, 187-195 (2014).
113. Gazizov, M., Marioara, C. D., Friis, J., Wenner, S., Holmestad, R.&Kaibyshev, R. Precipitation behavior in an Al-Cu-Mg-Si alloy during ageing. *Materials Science and Engineering: A* **767**, 138369 (2019).
114. Biswas, A., Siegel, D. J.&Seidman, D. N. Simultaneous segregation at coherent and semicoherent heterophase interfaces. *Physical Review Letters* **105**, 076102 (2010).
115. Gao, Y. H. et al. Segregation-sandwiched stable interface suffocates nanoprecipitate coarsening to elevate creep resistance. *Materials Research Letters* **8**, 446-453 (2020).
116. Gao, Y. H., Cao, L. F., Kuang, J., Zhang, J. Y., Liu, G.&Sun, J. Assembling dual precipitates to improve high-temperature resistance of multi-microalloyed Al-Cu alloys. *Journal of Alloys and Compounds* **822**, 153629 (2020).
117. Gao, Y. H. et al. Si-mediated reassembly of interfacially segregated Sc atoms in an Al-Cu-Sc alloy exposed to high-temperature creep. *Journal of Alloys and Compounds* **845**, 156266 (2020).
118. Gao, X., Nie, J. F.&Muddle, B. C. Effects of Si Additions on the Precipitation Hardening Response in Al-Cu-Mg(-Ag) Alloys. *Materials Science Forum* **217-222**, 1251-1256 (1996).
119. Gable, B. M., Shiflet, G. J.&Starke, E. A. The effect of Si additions on Ω precipitation in Al-Cu-Mg-(Ag) alloys. *Scripta Materialia* **50**, 149-153 (2004).

120. Abis, S., Mengucci, P.&Riontino, G. Influence of Si additions on the ageing process of an Al-Cu-Mg-Ag alloy. *Philosophical Magazine A* **70**, 851-868 (1994).
121. Li, C. et al. Enhanced age-hardening response of Al-4Mg-1Cu (wt.%) microalloyed with Ag and Si. *Scripta Materialia* **68**, 857-860 (2013).
122. Li, B. et al. Competition between precipitation and segregation of Sc and its effects on thermal stability of Al-Cu-Mg-Ag alloys. *Materials Letters* **297**, 129927 (2021).
123. Xu, H., Dong, Y., Bai, S.&Liu, Z. Effect of small Sn addition on the initial strengthening and microstructural evolution of an Al-Cu-Mg-Ag alloy. *Journal of Alloys and Compounds* **943**, 169167 (2023).
124. Ågren, J. Calculation of phase diagrams: Calphad. *Current Opinion in Solid State and Materials Science* **1**, 355-360 (1996).
125. Lu, Q. et al. Simultaneously enhanced strength and ductility of 6xxx Al alloys via manipulating meso-scale and nano-scale structures guided with phase equilibrium. *Journal of Materials Science & Technology* **41**, 139-148 (2020).
126. Schueller, R. D., Sachdev, A. K.&Wawner, F. E. Identification of a cubic precipitate observed in an Al-4.3Cu-2Mg/SiC cast composite. *Scripta Metallurgica et Materialia* **27**, 617-622 (1992).
127. Schueller, R. D., Sachdev, A. K.&Wawner, F. E. Interfacial structure of the cubic σ phase. *Scripta Metallurgica et Materialia* **27**, 1289-1294 (1992).
128. Samson, S. Die Kristallstruktur von $Mg_2Cu_6Al_5$. *Acta Chemica Scandinavica* **3**, 809-834 (1949).
129. Kilaas, R. Optimal and near-optimal filters in high-resolution electron microscopy. *Journal of Microscopy* **190**, 45-51 (1998).
130. Koch, C. Determination of core structure periodicity and point defect

density along dislocations.). Arizona State University (2002).

131. Liu, C. et al. In-situ STEM imaging of growth and phase change of individual $CuAl_X$ precipitates in Al alloy. *Scientific Reports* **7**, 2184 (2017).
132. Vlasov, E., Skorikov, A., Sánchez-Iglesias, A., Liz-Marzán, L. M., Verbeeck, J.&Bals, S. Secondary electron induced current in scanning transmission electron microscopy: An alternative way to visualize the morphology of nanoparticles. *ACS Materials Letters* **5**, 1916-1921 (2023).
133. Shen, R., Shao, Q., Ming, W., Xie, P.&Yang, Q. Automated, quantitative electron tomography of dislocation morphology combined with deep learning technology. *Materials Characterization* **207**, 113566 (2024).
134. Feng, Z. et al. TEM-based dislocation tomography: Challenges and opportunities. *Current Opinion in Solid State and Materials Science* **24**, 100833 (2020).
135. Niehle, M., Trampert, A., Rodriguez, J.-B., Cerutti, L.&Tournié, E. Electron tomography on III-Sb heterostructures on vicinal Si(001) substrates: Anti-phase boundaries as a sink for threading dislocations. *Scripta Materialia* **132**, 5-8 (2017).
136. Mychinko, M. et al. The Influence of size, shape, and twin boundaries on heat-induced alloying in individual Au@Ag core-shell nanoparticles. *Small* **17**, e2102348 (2021).
137. Li, M.-h. et al. Development of advanced electron tomography in materials science based on TEM and STEM. *Transactions of Nonferrous Metals Society of China* **24**, 3031-3050 (2014).
138. Diehle, P., Kovacs, A., Duden, T., Speen, R., Zagar Soderznik, K.&Dunin-Borkowski, R. E. A cartridge-based turning specimen

holder with wireless tilt angle measurement for magnetic induction mapping in the transmission electron microscope. *Ultramicroscopy* **220**, 113098 (2021).

139. Cerezo, A. et al. Atom probe tomography today. *Materials Today* **10**, 36-42 (2007).
140. Grandfield, K., Micheletti, C., Deering, J., Arcuri, G., Tang, T.&Langelier, B. Atom probe tomography for biomaterials and biomineralization. *Acta Biomaterialia* **148**, 44-60 (2022).
141. Thermal-Calc. Aluminium-based alloys databases. 2022 2023-11-24; Available online at: https://thermocalc.com/products/databases/aluminum-based-alloys/.
142. Kresse, G.&Furthmüller, J. Efficient iterative schemes for ab initio total-energy calculations using a plane-wave basis set. *Physical Review B* **54**, 11169-11186 (1996).
143. Kresse, G.&Joubert, D. From ultrasoft pseudopotentials to the projector augmented-wave method. *Physical Review B* **59**, 1758-1775 (1999).
144. Perdew, J. P., Burke, K.&Ernzerhof, M. Generalized gradient approximation made simple. *Physical Review Letters* **77**, 3865-3868 (1996).
145. Bourgeois, L., Dwyer, C., Weyland, M., Nie, J.-F.&Muddle, B. C. The magic thicknesses of θ′ precipitates in Sn-microalloyed Al-Cu. *Acta Materialia* **60**, 633-644 (2012).
146. Bouchet, J., Bottin, F., Jomard, G.&Zérah, G. Melting curve of aluminum up to 300 GPa obtained throughab initiomolecular dynamics simulations. *Physical Review B* **80**, 094102 (2009).
147. Hong, Q.-J.&van de Walle, A. Prediction of the material with highest known melting point fromab initiomolecular dynamics calculations.

Physical Review B **92**, 020104 (2015).

148. Yu, Z. et al. Effect of aging route on the precipitation behavior and thermal stability of Al-Cu-Mg-Ag alloy. *Journal of Materials Research and Technology* **23**, 2010-2019 (2023).
149. Zhou, X., Liu, Z., Bai, S., Liu, M.&Ying, P. The influence of various Ag additions on the nucleation and thermal stability of Ω phase in Al-Cu-Mg alloys. *Materials Science and Engineering: A* **564**, 186-191 (2013).
150. Li, K. et al. Quantitative measurement for the microstructural parameters of nano-precipitates in Al-Mg-Si-Cu alloys. *Materials Characterization* **118**, 352-362 (2016).
151. Nie, J. F.&Muddle, B. C. Strengthening of an Al-Cu-Sn alloy by deformation-resistant precipitate plates. *Acta Materialia* **56**, 3490-3501 (2008).
152. Nie, J. F.&Muddle, B. C. Microstructural design of high-strength aluminum alloys. *Journal of Phase Equilibria* **19**, 543-551 (1998).
153. Grong, Ø.&Shercliff, H. R. Microstructural modelling in metals processing. *Progress in Materials Science* **47**, 163-282 (2002).
154. Baldan, A. Review Progress in Ostwald ripening theories and their applications to the γ′-precipitates in nickel-base superalloys Part II Nickel-base superalloys. *Journal of Materials Science* **37**, 2379-2405 (2002).
155. Al-Obaisi, A. M., El-Danaf, E. A., Ragab, A. E.&Soliman, M. S. Precipitation Hardening and Statistical Modeling of the Aging Parameters and Alloy Compositions in Al-Cu-Mg-Ag Alloys. *Journal of Materials Engineering and Performance* **25**, 2432-2444 (2016).
156. Du, Q., Poole, W. J.&Wells, M. A. A mathematical model coupled to CALPHAD to predict precipitation kinetics for multicomponent

aluminum alloys. *Acta Materialia* **60**, 3830-3839 (2012).
157. Liddicoat, P. V. et al. Nanostructural hierarchy increases the strength of aluminium alloys. *Nature Communications* **1**, 63 (2010).
158. Wu, S. et al. Freezing solute atoms in nanograined aluminum alloys via high-density vacancies. *Nature Communications* **13**, 3495 (2022).
159. Li, Q., Qin, J., Jiang, D., Yi, D.&Wang, B. Precipitate coarsening and mechanical properties in 6082 aluminium alloy during long-term thermal exposure. *Journal of Alloys and Compounds* **909**, 164819 (2022).
160. Dai, P. et al. Thermal stability analysis of a lightweight Al-Zn-Mg-Cu alloy by TEM and tensile tests. *Materials Characterization* **153**, 271-283 (2019).
161. Zhu, S., Shih, H.-C., Cui, X., Yu, C.-Y.&Ringer, S. P. Design of solute clustering during thermomechanical processing of AA6016 Al–Mg–Si alloy. *Acta Materialia* **203**, 116455 (2021).
162. Abdelaziz, M. H., Doty, H. W., Valtierra, S.&Samuel, F. H. Static versus dynamic thermal exposure of transition elements-containing Al-Si-Cu-Mg cast alloy. *Materials Science and Engineering: A* **739**, 499-512 (2019).
163. Qian, F., Jin, S., Sha, G.&Li, Y. Enhanced dispersoid precipitation and dispersion strengthening in an Al alloy by microalloying with Cd. *Acta Materialia* **157**, 114-125 (2018).
164. Yang, C. et al. The influence of Sc solute partitioning on the microalloying effect and mechanical properties of Al-Cu alloys with minor Sc addition. *Acta Materialia* **119**, 68-79 (2016).
165. Gazizov, M. R. et al. The unique hybrid precipitate in a peak-aged Al-Cu-Mg-Ag alloy. *Scripta Materialia* **194**, 113669 (2021).
166. Li, J. et al. Solute clustering and precipitation in an Al-Cu-Mg-Ag-Si

model alloy. *Materials Science and Engineering: A* **760**, 366-376 (2019).

167. Gariboldi, E., Bassani, P., Albu, M.&Hofer, F. Presence of silver in the strengthening particles of an Al-Cu-Mg-Si-Zr-Ti-Ag alloy during severe overaging and creep. *Acta Materialia* **125**, 50-57 (2017).
168. Marioara, C. D. et al. Improving thermal stability in Cu-containing Al-Mg-Si alloys by precipitate optimization. *Metallurgical and Materials Transactions A* **45**, 2938-2949 (2014).
169. Torsæter, M., Ehlers, F. J. H., Marioara, C. D., Andersen, S. J.&Holmestad, R. Applying precipitate–host lattice coherency for compositional determination of precipitates in Al-Mg-Si-Cu alloys. *Philosophical Magazine* **92**, 3833-3856 (2012).
170. Du, Y. et al. An overview on phase equilibria and thermodynamic modeling in multicomponent Al alloys: Focusing on the Al-Cu-Fe-Mg-Mn-Ni-Si-Zn system. *Calphad - Computer Coupling of Phase Diagrams and Thermochemistry* **35**, 427-445 (2011).
171. Bai, S., Liu, Z., Zhou, X., Xia, P.&Liu, M. Stress-induced thickening of Ω phase in Al-Cu-Mg alloys containing various Ag additions. *Materials Science and Engineering: A* **589**, 89-96 (2014).
172. Bai, S., Huang, T., Xu, H., Liu, Z., Wang, J.&Yi, X. Effects of small Er addition on the microstructural evolution and strength properties of an Al-Cu-Mg-Ag alloy aged at 200°C. *Materials Science and Engineering: A* **766**, 138351 (2019).
173. Xia, Q.-k., Liu, Z.-y.&Li, Y.-t. Microstructure and properties of Al-Cu-Mg-Ag alloy exposed at 200 °C with and without stress. *Transactions of Nonferrous Metals Society of China* **18**, 789-794 (2008).
174. Fan, J., Yang, B., Wang, Y., Gao, M.&Guan, R. Enhancing the tensile

strength and heat resistance induced by high-density Ω phases in an Al-Cu-Mg-Ag alloy. *Journal of Materials Research and Technology* **18**, 3347-3357 (2022).

175. Song, M., Xiao, D.&Zhang, F. Effect of Ce on the thermal stability of the Ω phase in an Al-Cu-Mg-Ag alloy. *Rare Metals* **28**, 156-159 (2009).
176. Shohei, I.&Masami, A. Effect of additional Cu and Mg in Al-Mn-Si alloy on intergranular corrosion susceptibility after heating at 200°C. *Journal of Japan Institute of Light Metals* **59**, 108-113 (2009).
177. Song, Y.-f., Pan, Q.-l., Wang, Y., Li, C.&Feng, L. Elevated-temperature mechanical properties and thermal stability of Al-Cu-Mg-Ag heat-resistant alloy. *Journal of Central South University* **21**, 3434-3441 (2014).
178. Jabra, J. et al. The effect of thermal exposure on the mechanical properties of 2099-T6 die forgings, 2099-T83 extrusions, 7075-T7651 plate, 7085-T7452 die forgings, 7085-T7651 plate, and 2397-T87 plate aluminum alloys. *Journal of Materials Engineering and Performance* **15**, 601-607 (2006).
179. Tzeng, Y.-C., Chengn, V.-S., Nieh, J.-K., Bor, H.-Y.&Lee, S.-L. Microstructure and thermal stability of A357 alloy with and without the addition of Zr. *Journal of Materials Engineering and Performance* **26**, 5511-5518 (2017).
180. Liu, K.&Chen, X. G. Development of Al-Mn-Mg 3004 alloy for applications at elevated temperature via dispersoid strengthening. *Materials & Design* **84**, 340-350 (2015).
181. Yuan, W., Liang, Z., Zhang, C.&Wei, L. Effects of La addition on the mechanical properties and thermal-resistant properties of Al-Mg-Si-Zr alloys based on AA 6201. *Materials & Design* **34**, 788-792 (2012).

182. Liu, H., Pang, J., Wang, M., Li, S.&Zhang, Z. The effect of thermal exposure on the microstructure and mechanical properties of multiphase $AlSi_{12}Cu_4MgNi_2$ alloy. *Materials Characterization* **159**, 110032 (2020).
183. Wang, J. H.&Yi, D. Q. Preparation and properties of alloy 2618 reinforced by submicron AlN particles. *Journal of Materials Engineering and Performance* **15**, 596-600 (2006).
184. Rosalie, J. M.&Bourgeois, L. Silver segregation to θ′ (Al_2Cu)-Al interfaces in Al-Cu-Ag alloys. *Acta Materialia* **60**, 6033-6041 (2012).
185. Weng, Y. et al. Effect of Ag addition on the precipitation evolution and interfacial segregation for Al-Mg-Si alloy. *Acta Materialia* **180**, 301-316 (2019).
186. Kumar Makineni, S. et al. Enhancing elevated temperature strength of copper containing aluminium alloys by forming $L1_2$ Al_3Zr precipitates and nucleating θ" precipitates on them. *Scientific Reports* **7**, 11154 (2017).
187. Bourgeois, L., Zhang, Y., Zhang, Z., Chen, Y.&Medhekar, N. V. Transforming solid-state precipitates via excess vacancies. *Nat. Commun.* **11**, 1248 (2020).
188. Bourgeois, L., Dwyer, C., Weyland, M., Nie, J.-F.&Muddle, B. C. Structure and energetics of the coherent interface between the θ′ precipitate phase and aluminium in Al-Cu. *Acta Materialia* **59**, 7043-7050 (2011).
189. Bourgeois, L., Medhekar, N. V., Smith, A. E., Weyland, M., Nie, J. F.&Dwyer, C. Efficient atomic-scale kinetics through a complex heterophase interface. *Physical Review Letters* **111**, 046102 (2013).
190. Zhang, D.-l., Wang, J., Kong, Y., Zou, Y.&Du, Y. First-principles investigation on stability and electronic structure of Sc-doped θ′/Al

interface in Al-Cu alloys. *Transactions of Nonferrous Metals Society of China* **31**, 3342-3355 (2021).

191. Ding, L. et al. The structural and compositional evolution of precipitates in Al-Mg-Si-Cu alloy. *Acta Materialia* **145**, 437-450 (2018).
192. Salvati, E., Sui, T., Lunt, A. J. G.&Korsunsky, A. M. The effect of eigenstrain induced by ion beam damage on the apparent strain relief in FIB-DIC residual stress evaluation. *Materials & Design* **92**, 649-658 (2016).
193. Koblischka-Veneva, A.&Koblischka, M. R. Ion damage during preparation of nanostructures in magnetite by means of Focused Ion-Beam (FIB) milling. *Superlattices and Microstructures* **44**, 468-475 (2008).
194. Zhong, X. L., Haigh, S. J., Zhou, X.&Withers, P. J. An in-situ method for protecting internal cracks/pores from ion beam damage and reducing curtaining for TEM sample preparation using FIB. *Ultramicroscopy* **219**, 113135 (2020).
195. Weng, Y., Jia, Z., Ding, L., Muraishi, S.&Liu, Q. Clustering behavior during natural aging and artificial aging in Al-Mg-Si alloys with different Ag and Cu addition. *Materials Science and Engineering: A* **732**, 273-283 (2018).
196. Weng, Y., Jia, Z., Ding, L., Pan, Y., Liu, Y.&Liu, Q. Effect of Ag and Cu additions on natural aging and precipitation hardening behavior in Al-Mg-Si alloys. *Journal of Alloys and Compounds* **695**, 2444-2452 (2017).
197. Gable, B. M., Shiflet, G. J.&Starke, E. A., Jr. The Effect of Si Additions on the Nucleation of Ω in Al-Cu-Mg Alloys. *Materials Science Forum* **426-432**, 471-476 (2003).

198. Mukhopadhyay, A. K., Eggeler, G.&Skrotzki, B. Nucleation of Ω phase in an Al-Cu-Mg-Mn-Ag alloy aged at temperatures below 200°C. *Scripta Materialia* **44**, 545-551 (2001).
199. Liu, F., Liu, Z., Jia, P., Bai, S., Yan, P.&Hu, Y. Dynamic dissolution and texture evolution of an Al-Cu-Mg-Ag alloy during hot rolling. *Journal of Alloys and Compounds* **827**, 154254 (2020).
200. Mei, Z., Liu, Z., Bai, S., Wang, J.&Cao, J. Effects of yttrium additions on microstructures and mechanical properties of cast Al-Cu-Mg-Ag alloys. *Journal of Alloys and Compounds* **870**, 159435 (2021).
201. Liang, S. S. et al. Effect of Er and Si co-microalloying on mechanical properties and microstructures of AlCuMg alloys. *Journal of Materials Research and Technology* **24**, 430-439 (2023).
202. Marioara, C. D. et al. The effect of Cu on precipitation in Al–Mg–Si alloys. *Philosophical Magazine* **87**, 3385-3413 (2007).
203. Ardell, A. J. Precipitation hardening. *Metallurgical Transactions A* **16**, 2131-2165 (1985).
204. Yang, M. et al. Quantified contribution of β″ and β′ precipitates to the strengthening of an aged Al-Mg-Si alloy. *Materials Science and Engineering: A* **774**, 138776 (2020).
205. Esmaeili, S., Lloyd, D. J.&Poole, W. J. A yield strength model for the Al-Mg-Si-Cu alloy AA6111. *Acta Materialia* **51**, 2243-2257 (2003).
206. Li, Y., Shi, Z.&Lin, J. Experimental investigation and modelling of yield strength and work hardening behaviour of artificially aged Al-Cu-Li alloy. *Materials & Design* **183**, 108121 (2019).
207. Myhr, O. R., Grong, Ø.&Andersen, S. J. Modelling of the age hardening behaviour of Al-Mg-Si alloys. *Acta Materialia* **49**, 65-75 (2001).
208. Loucif, A., Figueiredo, R. B., Baudin, T., Brisset, F., Chemam,

R.&Langdon, T. G. Ultrafine grains and the Hall-Petch relationship in an Al-Mg-Si alloy processed by high-pressure torsion. *Materials Science and Engineering: A* **532**, 139-145 (2012).

209. Liu, H., Bellón, B.&Llorca, J. Multiscale modelling of the morphology and spatial distribution of θ′ precipitates in Al-Cu alloys. *Acta Materialia* **132**, 611-626 (2017).
210. Gao, L., Li, K., Ni, S., Du, Y.&Song, M. The growth mechanisms of θ′ precipitate phase in an Al-Cu alloy during aging treatment. *Journal of Materials Science & Technology* **61**, 25-32 (2021).
211. Torsæter, M., Lefebvre, W., Marioara, C. D., Andersen, S. J., Walmsley, J. C.&Holmestad, R. Study of intergrown L and Q′ precipitates in Al-Mg-Si-Cu alloys. *Scripta Materialia* **64**, 817-820 (2011).
212. Rockenhäuser, C., Rowolt, C., Milkereit, B., Darvishi Kamachali, R., Kessler, O.&Skrotzki, B. On the long-term aging of S-phase in aluminum alloy 2618A. *Journal of Materials Science* **56**, 8704-8716 (2021).
213. Gupta, A. K., Chaturvedi, M. C.&Jena, A. K. Effects of silicon additions on aging behaviour of Al-1.52Cu-0.75Mg alloy. *Materials Science and Technology* **5**, 52-55 (1989).
214. Wang, F. et al. Effect of Si addition on the microstructure and mechanical properties of Al-Cu-Mg alloy. *Journal of Alloys and Compounds* **585**, 474-478 (2014).
215. Liang, S. S. et al. Enhanced thermal-stability of AlCuMg alloy by multiple microalloying segregation of Mg/Si/Sc solute. *Materials Science and Engineering: A* **831**, 142235 (2022).
216. Schueller, R. D., Wawner, F. E.&Sachdev, A. K. Nucleation mechanism of the cubic σ phase in squeeze-cast aluminium matrix

composites. *Journal of Materials Science* **29**, 424-435 (1994).

217. Thronsen, E. et al. The effect of heavy deformation on the precipitation in an Al-1.3Cu-1.0Mg-0.4Si wt.% alloy. *Materials & Design* **186**, 108203 (2020).
218. Mukhopadhyay, A. K. Coprecipitation of Ω and σ phases in Al-Cu-Mg-Mn alloys containing Ag and Si. *Metallurgical and Materials Transactions A* **33**, 3635-3648 (2002).
219. Ghosh, K. S. Calorimetric studies of 2024 Al-Cu-Mg and 2014 Al-Cu-Mg-Si alloys of various tempers. *Journal of Thermal Analysis and Calorimetry* **136**, 447-459 (2019).
220. Kent, D., Schaffer, G. B.&Drennan, J. Age hardening of a sintered Al-Cu-Mg-Si-(Sn) alloy. *Materials Science and Engineering: A* **405**, 65-73 (2005).
221. Zhan, X. et al. Effects of non-isothermal aging on mechanical properties, corrosion behavior and microstructures of Al-Cu-Mg-Si alloy. *Journal of Alloys and Compounds* **819**, 152960 (2020).
222. Gao, Y.-Y., Qiu, F., Zhao, Q.-L.&Jiang, Q.-C. A new approach for improving the elevated-temperature strength and ductility of Al-Cu-Mg-Si alloys with minor amounts of dual-phased submicron/nanosized TiB_2-TiC particles. *Materials Science and Engineering: A* **764**, 138266 (2019).

Publication and award

Publication

(1) **Qiang Lu,** Jianchuan Wang, Hongcheng Li, Shenbao Jin, Gang Sha, Jiangbo Lu, Li Wang, Bo Jin, Xinyue Lan, Liya Li, Kai Li*, Yong Du*, Synergy of multiple precipitate/matrix interface structures for a heat resistant high-strength Al alloy[J]. Nature Communications, 2023, 14(1): 2959.

(2) **Qiang Lu**, Jianchuan Wang, Liya Li, Kai Li, Yong Du, Dominique Schryvers. Effect of Mg and Ag on the precipitation sequence of Al-Cu-Mg-Ag-Si alloy [J]. To be submitted.

(3) Mingjun Yang, Kai Li, **Qiang Lu**, Xinyue Lan, Ning Yan, Shuyan Zhang, Yong Du, Quantified effect of sample size and gas environment on precipitation of an aged Al-Mg-Si alloy[J]. Materials Characterization, 2021, 172 110829.

(4) Yao Xiao, Xin-yue Lan, **Qiang Lu**, Yong Du, Kai Li, In-situ evidence for rotation of Si particles with respect to grains in tensile-deformed Al−Si alloys[J]. Transactions of Nonferrous Metals Society of China, 2023, 33(6): 1655-1664.

(5) Yucheng Wang, Tong Yang, **Qiang Lu**, Kai Li, Zhixiu Wang, Yong Du, Grain size refinement and enhanced precipitation strengthening in a hot extruded 6xxx Al alloy without homogenization[J]. Materials Characterization, 2023, 198 112718.

(6) Tong Yang, Yi Kong, Kai Li, **Qiang Lu**, Yucheng Wang, Yong Du, Dominique Schryvers, Quasicrystalline clusters transformed from C14-MgZn2 nanoprecipitates in Al alloys[J]. Materials Characterization, 2023, 199 112772.

(7) Xinyue Lan, Kai Li, Jiong Wang, **Qiang Lu**, Tong Yang, Yao Xiao,

Yong Du, Preparation of ultra-large intermetallic particles in Al alloys for accurate determination of their mechanical properties[J]. Intermetallics, 2023, 152 107771.

Award

(1) Central South University President Innovation Scholarship, 2023.

(2) Central South University Outstanding Student, 2023.

(3) China Scholarship Council Scholarship, 2022.

(4) Outstanding Master's Thesis of Hunan Province, 2022.

(5) Outstanding Report Award at the 2022 International Conference on Nonferrous Metal New Materials, 2022.

(6) Outstanding Master's Thesis Award of the Chinese Nonferrous Metals Society, 2021.

Acknowledgement

The research work in this thesis was carried out under the guidance of Prof. Kai Li, Prof. Liya Li and Prof. Yong Du form the State Key Laboratory of Powder Metallurgy, Central South University, and Prof. Dominique (Nick) Schryvers form EMAT lab of Department of Physics, University of Antwerp. I am honored to have met the above four supervisors, who helped me a lot in my scientific research. Firstly, I would like to thank Prof. Yong Du for his support for the research topic. Secondly, I would like to thank Prof. Li Liya, my doctoral supervisor. Every time I asked for help from her, she would reply and solve it in time. Then, I would like to thank Prof. Kai Li, who took me into electron microscopy scientific research. I first met Prof. Li during my undergraduate studies and worked together to spend my master's and doctoral degrees. Every time I proposed new research ideas to Prof. Li, Prof. Li gave me unconditional support for experimental testing. Finally, I would like to thank Prof. Dominique (Nick) Schryvers, my supervisor during the joint PhD training at the University of Antwerp in Belgium. I am very grateful for Nick's guidance and help during my joint PhD training period. Every time I met Nick in the laboratory, he would kindly ask about the progress of the experiment and whether I needed help. When I reported that the in-situ heating chip was damaged, he immediately helped me find a new in-situ heating chip. It is such a blessing to have such four supervisors. I would like to express my highest respect to all the supervisors.

I would like to express my sincere gratitude to my senior colleagues Mingjun Yang, Haonan Chen, Xinyue Lan, Bo Jin, Sijing Liu, and Shiyi Wen for their care and assistance in my research work! I also want to thank Tong Yang, Liying Wu, Yi Gao, Yanrong Hao, Yao Xiao, Yucheng Wang,

Qiao Yan, Feiyue Zhou, Yuanfei Li, Wenting Jiang, Meifang Tang, and others for their help in study, work, and life. Similarly, I am grateful to Dr. Lars Riekehr, Dr. Saeid Pourbabak, Dr. Alexander Zintler, and others for their guidance and assistance in operating TEM and laboratory instruments during my study abroad at EMAT. I appreciate the help from my friends in Belgium, including Chuang Gao, Min Tang, Zezhong Zhang, Tong Zhang, Zehua Tao, Dawei Wang, Ruihua Han, Pengbo Li, Hui Shi, and Yun Ling, in daily life. I am grateful to the China Scholarship Council for funding my joint PhD training at the University of Antwerp, Belgium.

Finally, I would like to express my sincere gratitude to my parents and family for their support and help during my doctoral studies. Special thanks to my fiancée, Miss Min Yuan, for her support. Your encouragement is the driving force for me to continue moving forward whenever I encounter difficulties. Thank you all once again for everything you have done for me!

Qiang Lu

May 11, 2024